Universidad
Carlos III de Madrid

TESIS DOCTORAL

MODELING AND SIMULATION OF BACTERIAL BIOFILMS

Autor:

DAVID RODRIGUEZ ESPESO

Director/es:

ANA MARÍA CARPIO RODRIGUEZ

DEPARTAMENTO DE CIENCIA E INGENIERÍA
DE MATERIALES E INGENIERÍA QUÍMICA

Leganés, Junio de 2013

TESIS DOCTORAL

MODELING AND SIMULATION OF BACTERIAL BIOFILMS

Autor: DAVID RODRIGUEZ ESPESO

Director/es: ANA MARÍA CARPIO RODRIGUEZ

Firma del Tribunal Calificador: Firma

Presidente:

Vocal:

Secretario:

Calificación:

Leganés/Getafe, de de

Dedicated to all people who have trusted me

Acknowledgements

This work would not have been possible without the help and support of Professor Ana Carpio, who trusted me and gave me the chance to participate in this exciting project. I consider her one of the best ever advisors.

I want to remark the brilliant support of Dr. Esteban Martinez, from who I have learned most of my knowledge about biology.

I would like to express my sincere gratitude to Professor Victor de Lorenzo and Professor Angel Velazquez for his kind support and advising.

I greatly appreciate Professor Juan Ramón Arias for his collaboration and for providing valuable experimental advice in experimental set-up construction.

I specially thank Dr. Baldvin Einarsson for his support on programming and computation, which was invaluable for my PhD research studies.

I would like to thank Professor Luis Bonilla for being a source of scientific inspiration.

I would like to thank Professor Michael Brenner for hosting me in his group during a short visit to Harvard University.

I thank the Universidad Complutense de Madrid and Universidad Carlos III de Madrid for providing an adequate research environment.

I would like to thank all the wonderful people in Laboratory 30 at the CNB, whose friendship during the development of experiments was always inestimable.

From Confocal microscopy service in CNB, I would like to thank Silvia

Gutierrez, Ana Carla García and Susana Hernández for their support offered in my experiments.

I want to remark the great support given by Helena Monasterio, who encouraged me to keep going on my career as scientist.

I would like to thank my parents Jose Luis Rodriguez and Maria Jesus Espeso for their love and support. They taught me the real value of education and knowledge in this competitive world.

Abstract

The present thesis focus its efforts on developing a mathematical and experimental modelization of bacterial biofilms: bacterial colonies embedded into a polysaccharid matrix with a high resistance against removal processes, which result in a recurrent source of problems in other disciplines (medicine, engineering, etc). The behaviour of these organisms is highly dependant of the physical system in which they are present. So different case studies are faced here to show their complexity.

First the dynamics of biofilms in straight ducts is studied. Experiments are performed to obtain statistics about spreading patterns, and a hybrid model (combining a discrete approach for bacterial population with stochastical behaviour rules and a continuum description of outer fields ruling those probabilities) is presented to simulate the biofilm dynamics, obtaining a successfully prediction of the different patterns observed in real experiments (flat layers, ripples, streamers, mounds).

This part is completed by providing an alternative continuum description of the biofilm dynamics (by deducing a lubrication equation) and extending the scope of the model to the formation of biofilm streamers inside a corner flow, where biomass adhesion mechanism become relevant. Streamers cross the channel joining both corners as observed experimentally.

Additionally this thesis also includes a description of more complex dynamics observed in biofilms. An experimental description of biofilm dynamics under pulsatile flows at low Reynolds numbers show spiral patterns not reported yet, supported by a theoretical mechanism of formation based on the competence between flow dynamics and nutrient gradients. Quorum Sensing and differentiation mechanisms are also incorporated in a hybrid model to describe other kind of biofilms developed onto an agar-air interface, allowing similar geometries and cell distributions as in experiments reported previously.

Resumen

En esta tesis se aborda la modelización de biopelículas bacterianas, es decir, agregados bacterianos adheridos a superficies y envueltos en una matriz polimérica que ellas mismos producen. Estos organismos son extremadamente resistentes a agresiones de todo tipo, como antibióticos o agentes químicos, lo que les confiere una gran relevancia a nivel hospitalario, industrial o medioambiental. Su estudio se muestra especialmente complejo debido a que biopelículas formadas en distintas condiciones ambientales poseen distinta estructura, ya que involucran distintos comportamientos bacterianos.

Inicialmente consideramos biofilms en flujos. Tras un estudio estadístico de su crecimiento en canales rectos, proponemos un modelo híbrido que describe las células como entidades que viven en una red y desarrollan actividades con una cierta probabilidad, determinada por campos de concentración continuos. Simulaciones del modelo generan estructuras similares a las observadas experimentalmente: ondulaciones, filamentos, championes, y permiten determinar la influencia de distintos parámetros en la organización del biofilm. Estudiamos la posibilidad de describir estas estructuras con modelos continuos.

A continuación consideramos la influencia de la geometra de los canales en la forma del biofilm. Adaptamos el modelo híbrido anterior incluyendo mecanismos de adhesión y el efecto del flujo. Obtenemos filamentos que cruzan la corriente uniendo esquinas, similares a los observados experimentalmente. Al introducir un flujo pulsante, los filamentos se convierten en hilos que se enroscan en espiral. Documentamos este hecho experimentalmente y proponemos una explicación cualitativa como un balance de mecanismos de crecimiento y desplazamiento por el fluido. En los biofilms que crecen sobre superficies en contacto con el aire se activan mecanismos de diferenciación que determinan su forma. Incorporamos al modelo híbrido comportamientos de diferenciación celular por producción en cascada de autoinductores.

Contents

Chapter 1

Scope and motivation of this work

This chapter explains the origin of this thesis and the conditions in which it has developed. The last part discusses the structure of this work and the main contributions.

1.1 Origin of this work

Nowadays science and engineering are at a singular development point. Technology must give a qualitative jump, changing old approaches for novel ways to keep advancing scientific research, all originated by the change of scale from macroscopic to microscopic and nano scale. For this reason, many companies and research groups are working to face this technological challenge and keep innovating at the same level as past years.

Some classic examples of affected fields are computer, space and aeronautic technologies. Processors, memories and electronic devices must keep on decreasing their size and increasing their speed, but sizes are now so small that classical ways to proceed (experimental methods, approaches) are not effective anymore. This is the reason for which many companies are investing a large number of resources to continue improving their technology.

The origin of this work is precisely an effort of space and aeronautic fields to give a solution to their miniaturization processes. Companies of this sector use "MEMS" (micro-electromechanical systems) in many electronic applications: aerials, satellites or aircrafts are some of them. Miniaturization of these devices have brought a fast development of benefits and yields:

miniaturized systems give the chance to build smaller equipments (making them cheaper and more powerful), but have also brought heat dissipation problems (more compact equipments generate much more heat that must be cooled) which are not solved properly. As a result equipment sizes can not be reduced in practice because cooling systems are restricting the minimum size of the whole device. This is a major drawback that must be solved.

One way to face this problem is to find a way to improve the heat exchange rates by planning a more detailed design. In order to achieve this objective, engineers and researchers should have more accurate measurements of different variables, like temperature or wall stresses, to modify designs properly. Classic measurements of these variables are not effective in miniaturized systems because measurement devices often alter working conditions: the system restricts our ability to gather useful information without perturbing real conditions with our measurement devices.

A novel but promising technique to solve measurement problems would be the use of living bacteria used as biosensors. Properly modified by using genetic manipulation, bacteria could give local information of desired variables (like temperature or shear stress) without perturbing the internal flow of these devices, reducing the size of sensors to the bacterial size, which is around several micrometeres.

In the present work bacterial growth is explored. More precisely, the behaviour of bacterial aggregates called biofilms is studied and modelled under different physical conditions, in order to control their size and shape by combining both experimental and theoretical approaches. Such control would allow to get biofilm geometries suitable to be handled in devices such as MEMs.

In an attempt to establish a solid base for further developments in the field (i.e. future experiments, devices or manipulation techniques), this thesis tries to cover a variety of general cases in which biofilms appear in natural or human made environments. These cases were chosen specifically with the aim of showing the vast complexity that these organisms may exhibit and with the ambitious purpose of developing a full framework of study combining the powerful approach of mathematical modelling and the evidence of the experimental method.

1.2 Structure and contents of this thesis

This thesis is structured in nine chapters as described below.

The present chapter 1 motivates this work and its basic structure.

Chapter 2 allows the reader to obtain a short but precise background about research in biofilms, the state of the art in this field and some basic concepts needed to follow this work.

Chapter 3 describes the experimental study that was devised to understand more deeply the main relations between biofilm growth patterns and relevant physical parameters on surfaces present in straight channels and exposed to a constant fluid flow rate. A major scope in mind was to grow biofilms in a controlled way with the aim of being used as biosensors in MEMS. The experiments were performed at the CNB (Centro Nacional de Biotecnología) under the supervision of V. de Lorenzo and E. Martínez, and with the technical assistance of the team led by A. Velázquez and J.R Arias at the UPM (Universidad Politécnica de Madrid). A description of the whole series of experiments is performed, discussing material selection, procedures, results and conclusions. The main objective was to select ranges of values for the main parameters governing biofilm growth (such nutrient concentration or water flow) leading to a flat geometry and stationary growth. The results of these experiments were recorded by taking pictures of biofilm patterns with a fluorescence microscope. This allows to compare biomass distribution according to the governing parameters. An statistic way to interpret the images and obtain precise information on bacterial distribution and patterns is introduced.

Chapter 4 presents a hybrid model to simulate the behavior of bacterial biofilms in the experimental conditions described in the previous chapter by using a simple set of probabilistic rules for basic bacterial mechanisms informed by the status of some continuous fields, mainly the nutrient concentration field. For industrial applications, the availability of simple but accurate theoretical models able to predict the response of physical systems to be controlled is a must. That fact motivated the development of a mathematical model to perform reliable simulations in chapter 3. The model includes a novel erosion mechanism which allows the flow to shape the growing biofilm and a novel mechanism for EPS generation. Like previous models, it also includes a basic division and spreading mechanism. An elementary adhesion mechanism for cells floating in the surrounding current, plus a de-

activation mechanism are also proposed. A final case study of the different numerical simulations performed shows three-dimensional biofilm structures recurrent in experiments such as ripples, streamers, mushroom networks or flat layers, depending on the different values of the model parameters.

Chapter 5 generalizes the model exposed in chapter 4 to handle biofilm growth in a non straight geometry. More precisely, growth under a corner flow is studied, guided by the experiments performed by the research group from Harvard - Princeton universities led by Prof. Howard A. Stone. This chapter details a hybrid model combining stochastic laws to update the boundary of biofilm and hydrodynamic results computed solving Navier - Stokes equations for the outer fluid. Biofilm streamers crossing the current and reaching the opposite corner are produced, as in the experiments, in similar parameter regimes. The influence of the adhesion rates of floating cells on the evolution and detachment of streamerlike patterns is analyzed.

Chapter 6 studies biofilm development in slow pulsatile flows combining both theoretical and experimental approaches. Although these systems are quite common in fields such as medicine or in nature (human or animal circulatory system), the study of biofilm growth under these conditions was unexplored to our knowledge. The results provided in this chapter are surprising and might suggest an unexpected path for bacterial contamination and the outbreak of infections. Helicoidal biofilm filaments expand filling the tubes, promoted by the initial nucleation of planktonic bacteria close to changes of section (stenosis). Experimental observations are sustained by numerical simulations that suggest how different physical mechanisms work to develop such structures.

Chapter 7 expands our models to biofilms on surfaces (agar-biofilm-air systems), and takes a deeper look into other physical-chemical processes that occur inside biofilms, such as quorum sensing and cell differentiation. A stochastic model is proposed to simulate the coupling between bacterial growth, cell signalling and bacterial differentiation processes during the development of a *B.Subtilis* colony attached onto an agar-gel surface. Cell signaling and autoinduction mechanisms are hence devised to include the dynamics of cellular differentiation. Additionally, the biofilm is allowed to absorb fluids from agar to improve the description of biofilm geometries that naturally appear as the bacterial population increases.

Chapter 8 presents a continuum model in which the biofilm behavior described in 3 and 4 is approached as a fluid system governed by the lu-

brication theory and mass transfer laws, thus providing another point of view to study the biofilm dynamics presented in 4. A perturbation study of the biofilm is also included. Numerical simulations of this model were also computed, showing a reasonable qualitative concordance with the previous discrete model shown in chapter 4, but also some limitations that suggest a more general level set formulation.

Chapter 9 discusses a possible continuation for this work and summarizes the general conclusions drawn from the results obtained.

Finally a bibliography and some appendices are also included.

Chapter 2

Introduction to biofilms

The present chapter reviews partially the state of the art in the biofilm field. It explains basic concepts and facts that are kept in mind in the subsequent chapters. This thesis has a multidisciplinary nature: biology, mathematics and engineering are mixed together.

2.1 Background and basic concepts

Bacteria attached to surfaces are commonly known as biofilms [81]. Biofilms are the result of the natural evolution of bacteria: a survival strategy developed during 3.000.000.000 years to create homeostatic conditions to favor bacterial survival in a changing environment. Biofilms were discovered recently in historic terms [125], being nowadays a developing field.

The formation of bacterial biofilms in solid surfaces within aqueous environments is an effect of great importance in medical and industrial applications. Bacteria may attach themselves to solid surfaces of a different nature (tissue, plastic, metal, rocks...) and to each other changing their morphology [102] by mechanisms that need clarification. Biofilms created on solid surfaces contain bacteria which are extremely resistant to external aggressions, like antibiotics, chemicals or flows. Once formed, biofilms may grow and spread cells and thin film fragments, which will be carried by the flow and may in turn reattach themselves to other solid surfaces, colonizing them [102]

Biofilms are extremely important for humans, not only in medicine and industry but also for the environment [150, 125]. Biofilms are responsible for a large percentage of infections in humans, ranging from deadly illnesses,

e.g., cystic fibrosis and legionellosis, to life-threatening infections originating at artificial joints, pacemakers, or catheters [105, 136, 35]. Biofilm-induced damage causes substantial economic losses, due to biocorrosion of aircraft fuselages or metallic structures, biofouling of ship hulls [174] , efficiency reduction in heat exchange systems [44], pressure drops and clogs in water systems, food and water poisoning [97, 34], and so on. They also constitute a recurrent problem in drinking water systems [97].

Although biofilms are often undesirable, they may also be exploited to our benefit. Bioremediation processes may be designed to remove toxic pollutants [136, 143] and different beneficial applications on wastewater treatment processes have already appeared [109, 129, 172]. There are as well very interesting novel applications, such as the ones that use biofilms as electro-optical devices, in which the structure of the biofilm is essential [17].

The development of synthetic biology is paving the way for the use of biofilms as biosensors or bioindicators for monitoring the presence of certain chemicals in the environment [158, 160]. Attempts to engineer devices out of biofilms continue to take place: electro-optical devices have already been created [17] and some applications include the use of biofilms as biosensors in MicroElectroMechanical Systems (MEMS)[45, 68, 136]. MEMS are taking special relevance in fields such as electronics or computing, where miniaturization processes force industry to develop new tools and solutions in order to sustain the fast increase of technical features. In all of these, it is essential to control biofilm growth to produce a homogeneous thin layer of biofilm for a successful design. However, there are many variables influence the process of biofilm formation, like attachment to the surface [56], quorum sensing [3, 177], generation of EPS [173, 48], or interaction with the surrounding flow [42, 121, 151].

In most of industrial applications biofilms pattern formation should be avoided and its control is a must. If a total control of biofilms growth is desired on some specific parts of a device, such surfaces must have well-defined properties. In particular, a defined roughness pattern. Standardized manufacturing of substrates are necessary to ensure similar biofilm quality under analogous external conditions. Surfaces with an unknown microstructure are mechanically processed by means of milling machines before being used as substrates. The resulting roughness, determined by the milling cutters, is typically of the same order of magnitude as the size of the bacteria. Therefore, the effect of such roughness patterns on biofilm growth under different flow conditions must be accounted for.

The most appropriate model for a particular biofilm should take into account the specific bacteria (different types of bacteria differ from each other in the same way as animals belonging to different species are dissimilar, and may react in different ways under the same circumstances), the environment in which the biofilm is formed, the parameters that can be fitted to experiments, and the predictions to be made [166, 159]. A deep understanding of the dynamics and different processes taking place in experiments of submerged biofilm growth in micropipes (on surfaces whose roughness is of the same order of magnitude as the bacterial size) is a critical scope to be achieved. However modelization must be performed carefully, because fitting model parameters to practical set-ups seems to be a general problem with models for biofilms due to a lack of adequate experimental data [104, 124].

As a conclusion, it can be deduced that a deep understanding about biofilm development and their properties is essential in order to control them properly when used in different industrial and scientific systems, either to destroy them when unwanted or to better exploit them when beneficial. The ability to fine tune the thickness of a biofilm could have a profound impact on many applications that could bring plenty of technological improvements in almost all fields of science and engineering.

Below, we review a few aspects of biofilm study: the historic background, their structure, their life cycle and the main theoretical approaches to modelize them.

2.2 Biofilm history

The first scientific evidence of biofilm existence is due to Antonie Van Leeuwenhoek in 1680, who detected these structures while performing a detailed study of the dental plaque. In 1943, Zobell found a high increase of bacterial activity near several surfaces [181]. The studies of Jones and coworkers in 1963 [73] about polysaccharid matrices and William G. Characklis in 1973 about the resilience and resistance of such matrices [21] led to the work of William Costerton in 1978 [28], who isolated bacterial cells with a completely different bacterial development from those seen until that year in laboratories (suspended cells or "planctonic"). He named them biofilms [28]. Several circumstances prevented earlier discovery of biofilms. A key one was the standard methodology to treat bacteria. Until then, the same strain was used during

several generations keeping it in optimal growth conditions. This induces the natural genetic selection of bacteria unable to generate biofilms, which are the result a natural mechanism to survive in hostile environments.

Since Costerton's work in 1978, the field has developed continuously [102, 136, 169, 154, 49, 27, 7]. However, many issues concerning biofilm behavior and its responses to changes in the environment remain unsolved. Different bacterial species may create different types of biofilms depending on the growth conditions. Biofilms may stick on air-solid or air-liquid interfaces [20] forming wrinkled films. Submerged in a fluid, they tend to develop ripples and fingers. External and genetic factors play a very important role. The combination of physical, chemical and biological aspects make biofilms a multidisciplinary field of study.

2.3 Biofilm structure and characteristics

Biofilms can be defined as a large amount of microcolonies embedded inside a polysaccharid matrix attached to a solid surface. This matrix, formed by polysaccharids produced by bacteria, offers numerous advantages: it gives increased resistance against external aggressions (chemicals, high shear flows, radiation, etc.), can be used as a food reservoir and creates a friendly environment to reproduce [94].

Biofilms could be viewed as complex and adaptable systems able to evolve dynamically according to the biological and environmental conditions. The effect of these conditions will eventually determine its final architecture [159]. In nature, biofilms are highly diverse, from submerged biofilms attached to pyrite surfaces in acidic environments [43] to the complex biofilms forming the dental plaque [80].

Picture 2.1 shows a biofilm formed by bacteria genetically modified inserting the green fluorescent protein (GFP). This protein becomes fluorescent when exposed to UV-light, allowing to locate the biofilm fragments attached to the surface.

Biofilms are characterized by their high bacterial concentration, even in hostile environments. Densities larger than 10^6 cells/cm^2 were detected in biofilms attached on alpine spring rocks whereas the concentration of suspended cells on water does not reach 20 cells/ml [53]. Not all biofilm cells are active to reproduce [97]. The structure of the biofilm depends on the

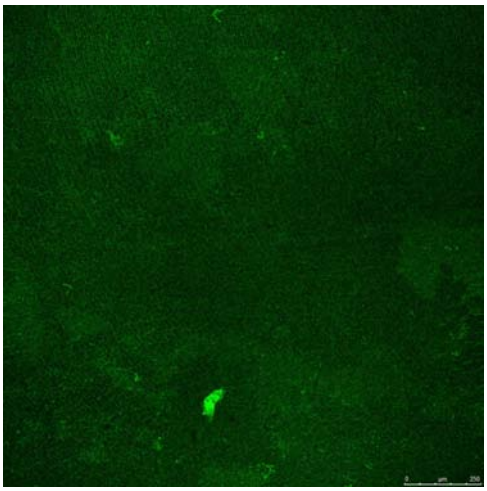

Figure 2.1: *Biofilm grown a polycarbonate surface. Image taken with a confocal microscope Leica TCS-SP5 (used lens: Plan Apo CS100x/1.4NA oil)*

external flow in which they are submerged [10]. Its internal structure varies greatly depending on the external conditions. Factors like turbulence [117], the nutrient concentration [62], the energy source type [125], the microorganism nature [89] or the presence of other microorganisms in the environment [117, 142] modify its final distribution, morphology and growth patterns.

All biofilms produce an EPS (exopolysacharid) matrix that maintains cells together [48]. The morphology of a biofilm is governed by the EPS matrix, which is normally composed of polysaccharides, proteins, DNA and water [12]. Although the nature and morphology of this matrix depends on many environmental conditions (ie, nutrient source, growth conditions, etc.), the external flow of the medium seems to be especially relevant for its final structure [125, 114]. It subjects cells in the upper part of the colony to higher shear forces and these cells may be detached from the colony.

At low flow, the biofilm structure tends to grow in volume, porosity, surface heterogeneity and generate different configurations like mushroom and mounds [25, 35]. Typical macrocolonies consist of mushroomlike towers separated by fluid-filled voids carrying nutrients and oxygen, although flat structures are also possible. Oppositely, high shear stresses generated by turbulent flows make biofilms grow thinner, more uniform, compact and with increased density [159]. Depending on the hydrodynamic conditions, the nutrient availability, the nutrient source, and the bacterial strain, cir-

cular colonies, streamers, ripples, rolls, streamlined patches or mushroom networks [126, 125] are observed. A reversible evolution from one pattern regime to another by increasing or decreasing the nutrient concentration and the shear force has been observed experimentally in Ref. [150]. However, [151] reported that biofilm monolayers might be produced under low-shear flow (laminar conditions), while filamentous and streamer-types were formed in turbulent situations. So, the conditions that direct the final biofilm structure might be influenced by a combination of parameters.

The structural behaviour of a biofilm suggests that the strongest part is at the base (the region close to the substratum), evolving gradually into a more flexible material in its upper part (to absorb elastically any admissible mechanical energy fluctuation) [10]. The biofilm inner structure is similar to a porous catalyzer [11]. It has a network of holes and channels through which liquids can circulate freely using convection or internal diffusion depending on flow conditions [31]. At the same time, this matrix acts as a physical barrier [29] to protect the biofilm against other microorganisms and offers a mass transfer resistance or chemical protection against toxic and harmful compounds [137, 108]. In fact, biofilms are structures of high complexity with a great number of internal variables, being some of them unknown.

Wild biofilms tend to grow as multispecies colonies to make possible the degradation of complex substrates [84], creating different levels depending on the nature of the different bacteria (heterotroph at the surface, anaerobic, reductive, nitrifying and methanogenics elsewhere). All of them are distributed according with the oxygen and nutrient availability. It has also been observed [142] that multispecies bacterial groups display an improved resistance against external threats (chemicals, shear stress, and so on).

Biofilms have the ability to communicate with each other by using which is known as autoinducers [53] in a process called quorum sensing. Autoinducers are special chemical molecules segregated by bacteria when a limiting cellular density has been reached that activate certain genetic expressions associated with different behaviour, like virulence, morphology or spreading. Different evidences [125] indicate the existence of interspecies bacterial cell signalling with different purposes, like eliminating competitors or gregary relationships.

2.4 Biofilm life cycle

The life cycle of biofilms has been largely studied [102, 53]. The main developmental stages are: colonization, growth, spread, maturation and death. A scheme of the biofilm life cycle is shown in figure 2.2.

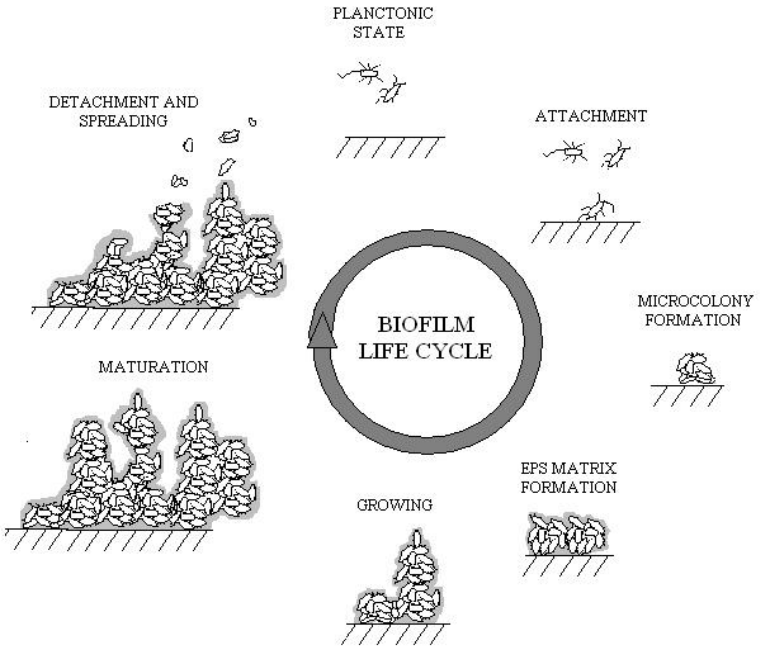

Figure 2.2: *Life cycle of a biofilm. Planktonic cells adhere to a surface and suffer changes in their phenotype. A microcolony is formed. Vertical growth reduces accessibility to nutrients and oxygen and a fraction of cells starts to produce EPS matrix. The matrix intensifies mass transfer, and strengthens the aggregate, leading to the formation of a macrocolony. As the macrocolony ages and its size increases, surface cells detach. They are carried by the flow, ready to colonize new surfaces.*

The colonization of new surfaces is a critical stage of the bacterial development. By using chemical species, bacteria have the ability to detect concentration gradients (which are related with the presence of a surface) [88, 27]. Microorganisms use cilia or flagella to reach the surface, trying to attach on it. The attachment process is force balance between different types. Bacteria must overcome repulsive electrostatic forces by establishing other interactions (Van der Waals or attractive electrostatic). If the balance

force is favorable, bacteria attach to the surface and establish an irreversible bond. Otherwise, they will be repelled, trying to colonize other zones. The attachment process induces several changes in the morphology of bacteria and their behavior, marking the onset of the development of a biofilm: loss of flagella or cilia, changes in cell phenotype, start of reproduction process to create a microcolony and secretion of exopolysaccharid matrix (EPS).

The generation of the EPS matrix offer numerous advantages, such as the promotion of colony vertical growth or an improvement in the access to oxygen and carbon, creating an ideal ambient for bacterial growth, multiplying their number exponentially and allowing the appearance of bacterial macrocolonies [102, 173]. Environmental physical conditions modify its main characteristics, generating different geometric structures optimized to improve nutrient obtention and mechanical resistance to external shear stress. In fact, the EPS matrix was shown to determine biofilm cohesive strength. The shear force created as the fluid flows over its surface seemed to be the principal physical force acting on the biofilm. Biofilms grown under higher shear were observed to adhere more strongly and have a stronger EPS matrix than those created at low shear.

If aerobic bacteria receive sufficient amounts of carbon and oxygen, they divide and proliferate on the surface forming microcolonies that constitute the germ of a biofilm and may eventually merge. The metabolism of the cells near the biofilm surface restricts the diffusion of oxygen and carbon to bacteria at the bottom of the colony. A fraction of cells in the biofilm begin to produce exopolysaccharides, forming the EPS matrix. This promotes vertical growth of the colony, improves access to oxygen and carbon, and gives rise to a macrocolony [102, 173].

Once the biofilm has reached a certain concentration and its structure is well defined, quorum sensing processes activate the spreading mechanism. This mechanism consist of a set of different strategies to release bacteria to the flow in order to colonize new surfaces and ensure the strain survival [27, 15, 150]. Some examples are flow detachment (self-weakening structure) or surface expansion produced by dragging mechanisms, like rippling, rolling or darting [102, 126] (see figure 2.3).

If nutrient concentration is not enough to sustain all bacteria, cells start dying until an equilibrium between deaths, availability of nutrients, cellular growth and spread is reached. Series of experiments (see Refs. [126, 125, 150], for instance) were performed to assess the influence of hydrodynamic condi-

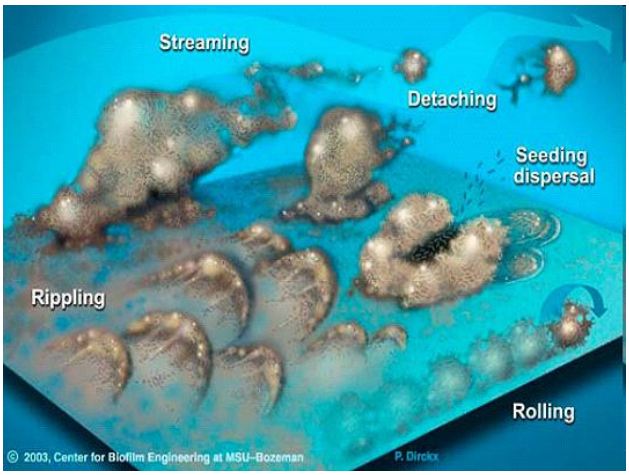

Figure 2.3: *Ilustration of several biofilm spreading mechanisms. Taken from Center for Biofilm Engineering MSU-Bozeman webpage*

tions and nutrients on biofilm structure for specific bacterial strains. Patches, ripples, streamer were found. Ripples appeared in turbulent and laminar regimes. Streamers were believed to be typical of turbulent regimes. Recent experiments carried out in curved pipes with sections of a few hundred microns [134] have produced streamers in laminar flows, raising new issues about the mechanisms leading to streamer and pattern formation in submerged biofilms. These experiments show that biofilm behaviour is not fully understood, and more efforts must be applied in order to enlighten the complex physical-chemical mechanism behind this casuistic.

2.5 Mathematical models

There is an increasing interest in the modeling of biofilms from the mathematical point of view. A good model should constitute a useful tool to predict the behaviour of biofilms and hence to control them properly. As the knowledge in this field increases, models have to be updated and become increasingly complicated. Nevertheless, this increase in complexity has not given always good results when comparing model predictions with experimental data [104, 159, 115]. General models describing biofilm dynamics can be classified in four groups [38] according to their description of bacteria [166, 104, 159]: continuum, individual based (IbM), cellular automata (CA) and hybrid models.

- Continuum models treat the biofilm as a continuum material, typically a gel, polymer or viscous fluid [76, 26, 169]. They are often two-phase models comprising the fluid containing the nutrients and the biofilm [38]. Interphases are treated as interfaces where properties change, being defined through boundary conditions. Mass transport equations with nonlinear bacterial reaction terms are the most widely used representation. The solutions of these models are in most cases numerical, being the boundary and interfacial conditions a critical issue in the solution of the system. When available, thin film approximations may be more effective [138]. These models have often a major drawback. They often fail to account for the fact that biofilms are alive and their material properties and morphology are governed by bacterial responses to environmental changes. For example, the film may harden or become less viscous, disaggregate or expel bacteria or film fragments in response to physical changes in the flow, nutrient concentration, presence of chemicals harmful to the bacteria, etc.

- IbM models consider microorganisms as hard spherical particles that evolve according to reaction-diffusion equations for nutrients and oxygen coupled with bacterial growth and spreading of biomass [118]. As different processes (diffusion of nutrients, reproduction, etc.) take place in different dimensional scales, these models are highly sensible to the grid size. Big sizes result in big deviations while small sizes may lead in a too hard computational effort. IbM models propose so far postulate too many hypothetical laws of uncertain range of validity and contain too many parameters with unknown values. There are some hybrid models combine discrete descriptions of the cells with continuous descriptions of other relevant fields [124],[120] to circumvent these backdraws. Some hybrid variants include the EPS matrix as an incompressible viscous flow, which embeds the discrete microbial cells [2]. A hybrid model trying to account for the effect of the flow is proposed in Ref. [41].

- CA models distribute biomass over a cellular grid and allow its cells to change with appropriate probabilities according to a set of simple rules [62, 123] (like feeding, reproduction, death, etc.). These models are appealing because the rules can be motivated from biological

principles, preconceived assumptions are kept to a minimum, and computer simulations turn out to be simpler and less costly than for the two other approaches. Available CA models already include a few bacterial mechanisms and activities in a reasonable way. However, the description of more complex mechanisms, such as microbe attachment to surfaces [56, 88], quorum sensing to form biofilms [3, 177], generation of EPS matrix [154, 173], and interaction with the surrounding flow [126, 121], remains unclear. There also exist the inconvenient that evolution rules are not rigorous laws that describe the physical system, but simplified rules based on experimental data whose calibration depends on the required accuracy and the experience of the researcher.

- Hybrid models combine discrete descriptions of the cells with continuous descriptions of other relevant fields [124],[120] to circumvent these drawbacks. Some hybrid variants include the EPS matrix as an incompressible viscous flow, which embeds the discrete microbial cells [2]. A hybrid model trying to account for the effect of the flow is proposed in Ref. [41].

Despite progresses made during the last ten years, the detailed description of microbial physiology in biofilms is not yet understood. There is not a perfect model: the preference for a particular type of model will depend on the context. In the industrial community [104] new models are needed continuously, looking always for simplicity and easy to handle when are used on industrial applications.

With the aim of facing this challenge, the next chapter presents a set of experiments designed to describe the biofilm growth dynamics at the bottom of a plane surface inside a straight duct in a laminar regime. It was considered a priority to gather experimental information by performing real experiments to gain intuition on the system to be modeled. The geometry was chosen with the idea of using biofilms in MEM type devices, which usually contain straight channels with plane surfaces.

Chapter 3

Design of a biofilm-water industrial device, experimentation and image analysis

In the previous chapter a brief introduction to the study of biofilms was provided. Biofilms are complex and dynamic living structures which respond to a high number of internal and external factors, by mechanisms poorly understood. This reason makes it necessary to retrieve experimental data in order to get complementary information on the parameters involved in the process and their influence in the system dynamics.

One of the main objectives of this chapter is to devise a procedure to control the shape of a growing biofilm with the purpose of getting a thin layer inside a channel exposed to a flow. This would be another step in the development and use of biofilms as biosensors in high technology applications like MEMs [14]. The design of MEMs is one of the most promising technological fields [68]. Modified properly, biofilms could be used as biosensors [68], to give local hydrodynamic information inside microchannels about scalar or vectorial fields (like temperature or shear stress) that could be used to improve heat transfer performance of those devices [130]. This application is only viable if biofilm growth can be controlled to produce thin uniform layers, to avoid any disruption of the fluid flow inside the channels and to give reliable information about the measured variables at the wall (so layers must be as thin as possible).

As said before, biofilm development depends on a variety of factors (like

growth conditions) that must be fixed when a experimental set-up is implemented. There are critical variables, such as the substratum material or the nutrient source, which should be studied beforehand. The performed experiments were divided into two sets. A first set of experiments was performed at zero Reynolds number Re. They were designed to choose basic parameters for further experiments: the test sample material or the nutrient source were two of them. The second set of experiments was done at non-zero Reynolds number to check the influence of the flow on biofilm growth. Biofilm evolution was photographed using a fluorescence microscope. A mathematical procedure to quantify the information provided by the images was introduced.

This chapter is divided in four parts. Section 3.1 discusses the materials and methods for the experiments. Section 3.2 summarizes the results obtained, introducing the quantification methods and illustrating them. Section 3.3 collects our conclusions.

3.1 Materials and methods

Conventional laboratory materials were avoided, as we intended to approximate our experimental set-up to an industrial scaled plant. All materials used here were industrial-type materials, which implies not having the best conditions for operation and handling (materials, roughness, maintenance, sterilization methods, etc.) but gives a more precise information about what would be the behaviour of biofilms in such conditions.

3.1.1 Bacterial Strains, media and reagents

There are many bacterial strains that could be selected to perform a theoretical or experimental study. Depending on the selected strain the results may be different because of the singular nature of each bacteria. With this fact in mind, the main criteria to select the bacterial species were a large availability of previous information in the literature and a wide potential as a tool for industrial and scientific applications. *Pseudomonas Putida* was the bacterial species chosen to perform most part of this work. The *Pseudomonas* genus is the model choice for studies of biofilms in flows, whereas *B.Subtilis* is a standard choice for biofilms on surfaces.

P.Putida (see picture 3.1) is a gram negative bacteria belonging to the

class of flagellated heterotroph bacillus. It can endure temperatures between 20^oC and 42^oC, being widely spread over numerous media. It is greatly resistant to hazardous chemical products, like organic chlorinated products, having the ability to use them as a nutrient source. This application makes it valuable for biodegradation of chemical compounds in controlled media like waste water or bioremediation of land or water damaged by oil spills or containing high concentrations of metals (mines) or nitrogen (farms). In spite of its resistance to antibiotics and disinfectant agents, *P.Putida* is not a pathogenic agent, but an opportunist bacterium able to colonize any media in favorable conditions [107, 36, 71]. All of these properties make it a perfect candidate for industrial purposes.

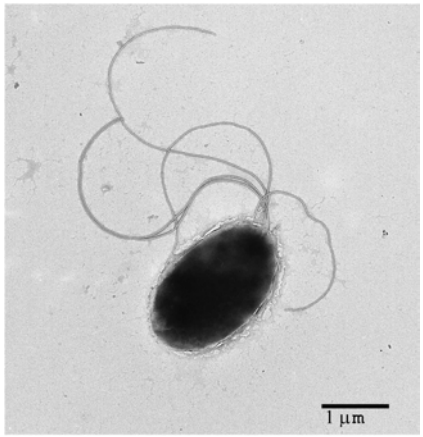

Figure 3.1: *Pseudomonas putida image. Picture taken with a transmission electron microscope. Taken from CNB webpage.*

Among all *P.Putida* strains, *P. putida mt-2* [79] or its fluorescently labeled derivative (mt-2-GFP) were selected to follow biofilm development. *P.Putida* mt-2-GFP was generated by a site-specific insertion at an intergenic region of a miniTn7-gfp2 cassette [78, 85]. Bacteria were grown either Luria-Bertani media (also known as LB, it contains 10 g/l of tryptone, 5 g/l of yeast extract and 5 g/l of NaCl) or M9 minimal medium (see [135] for more details) supplemented with glycerol 2 g/l as the sole carbon source. Antibiotics, when required, were added at the following final concentrations gentamicin (Gm) 10 $\mu g/ml$; chloramphenicol (Cm) 30 $\mu g/ml$.

3.1.2 Experimental setup

Experiments at $Re = 0$

Experiments at $Re = 0$ were designed as a fast set of experiments to decide whether polycarbonate was a good material for growing biofilms and which nutrient source was better to grow Pseudomonas Putida. Both nutrient sources (M9+0.2% glycerol and LB Media) were tested to get optimal results. No special setup was required for those tests.

The substratum has a big influence in the attachment and development of biofilms. Key factors to take into account are the electrostatic charge interaction between bacteria and surfaces [170], [57], the roughness of the surface, that may provide protection against shear forces [5, 60], and the physical nature of the surface [57]. There are several physical theories that try to explain this initial attachment step, like the zeta-potential and collision theory [163, 98, 65].

As a consequence, the selection of the material for the plates is essential to obtain a good attachment, especially when chemical or physical treatments are envisaged. An inadequate material choice could generate problems, such as partial or total surface degradation, when applying conventional cleaning and sterilization methods (UV irradiation, sodium hypochlorite, or ethanol cleaning). Furthermore, for industrial applications the cost of the plate fabrication should be as low as possible. Different bibliographic sources led to polycarbonate as a reasonable material choice [9, 83, 178, 171].

The roughness of the surface plate was another important parameter to take into account. Small holes on the plate might enhance the biofilm occupied surface area [119]. The numerical simulations using cellular automata models described in Chapter 4 suggested that roughness patterns of the same order of magnitude as the bacterial size (but slightly larger, to be able to accommodate them) could shelter them from the shear forces exerted by the flow current and would be less likely to be wiped out and colonizes new regions more easily [130]. So, polycarbonate plates were milled to obtain different roughness patterns with averaged dimensions from 2 to 4 μm, similar to the size of the bacteria.

Small square polycarbonate plates ($70 \times 50 \times 6$ mm) were initially made to test the adhesion of *P. putida mt-2* onto this material at $Re = 0$ (see picture 3.2). These plates were shaped with one channel (5 mm deep) with different

Figure 3.2: *A* $70 \times 50 \times 6$ *mm polycarbonate sample test*

milling speed configurations in an EMCO Concept MILL 105 milling machine. This machine consists of a computerized mill which allows create customized fabrication programs to create whatever shape is needed for different kind of materials. A customized program was created to give polycarbonate the desired shape and dimensions. Polycarbonate plates were sterilized by UV irradiation at 254 nm during 30 minutes to avoid cross-contamination with other bacterial strains. To test biofilm formation on those plates, they were introduced into Petri dishes (90 mm diameter), covered with 80 ml of M9 + 0.2% glycerol and incubated at room temperature for 24 h.

Experiments at Re $\neq$ 0

Once basic variables regarding optimum experimental conditions were selected, a setup to perform experiments at non zero Reynolds values was designed.

Experiments at $Re \neq 0$ requested an adaptable setup, with a simple but powerful design, easy to handle and operate and with a minimum cost. Different experimental configurations are found in the literature [97, 117, 16, 18]. One of the simpler configurations are the *chemostat reactors*.

These equipments act basically as a continuous stirred tank reactor (CSTR) in which all conditions are fixed at certain values. They consist of a tank

which is stirred continuously and it is operated at steady state: there is an inflow and a outflow for a recirculation loop in the setup and it has a fresh component inflow and a drain to control undesired compounds. The other variables are also fixed, so this kind of setup allows to measure the influence of only one or two variables in a very complex system which depends on many magnitudes. These setups also include several measurement devices to control or modify different variables. In the case of this experimental setup, the recirculation flow, the drain and fresh component flow, the temperature and the volume should be controlled.

The user has the possibility to make different experiments under controlled conditions, changing only the desired parameters. Under these conditions, biofilms are expected to grow and spread over time in the presence of an erosion effect that will reduce the amount of biofilm until a final pseudo-stationary equilibrium is reached (under this equilibrium, biofilm acquires a macroscopic distribution over the channel as a function of the main parameters such as flow or nutrient). The experiments performed at different growth conditions, measuring the effect of Reynolds number and surface roughness will be described later. The experimental setup, the main design criteria and the operative methods are described below.

A picture of the complete system is shown in Figure 3.3. An additional layout scheme may be found in Figure 3.4. The dimensions of the whole device were scaled up to millimetres to facilitate its handling and to use an specific channel geometry and size so that a simulation of real conditions inside industrial MEMs could be reproduced.

Following the previous design criteria, the main vessel was dimensioned as a continuously aerated reactor with a 2 l volume. The nutrient concentration of the system is controlled only in the main tank, since it comprises 90% of the volume of the whole circuit (modifications in the setup are performed by modifying the concentration in the vessel). The apparatus was designed as a continuous stirred tank reactor (CSTR) to reach a steady state (no change of the nutrient concentration fixed at 0.1 g/l and waste products along time). To estimate all the variables mass balances were applied to biomass, nutrient, and oxygen and set constant the inflow, volume of the tank, and steady state nutrient concentration. See appendix D for more details.

Fresh air is introduced into the vessel by using a small compressor (AQUACLEAR 10) with a particle filter to supply oxygen to the mixture at 1 l/min. The introduction of air in the vessel also avoids the contamination by sus-

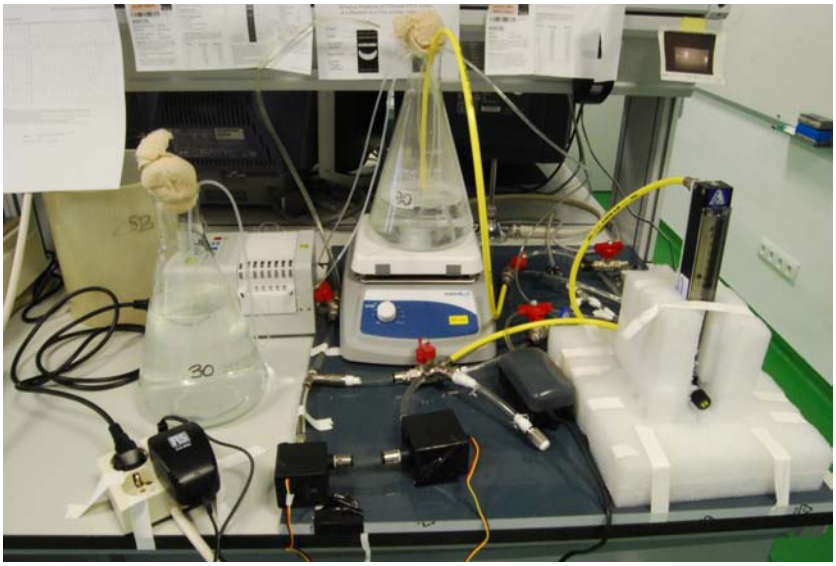

Figure 3.3: *Experimental essay set-up for* $Re \neq 0$ *conditions*

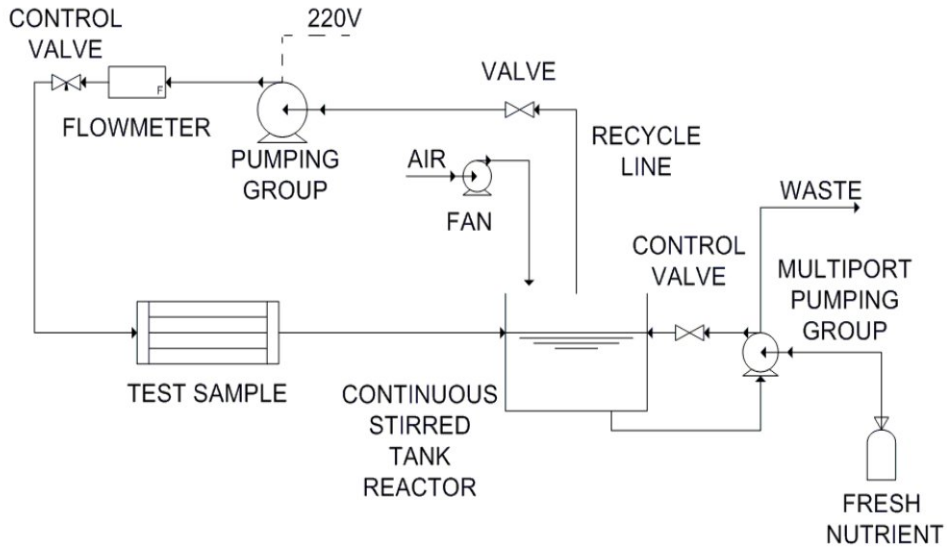

Figure 3.4: *Lay-out design of the installation for* $Re \neq 0$

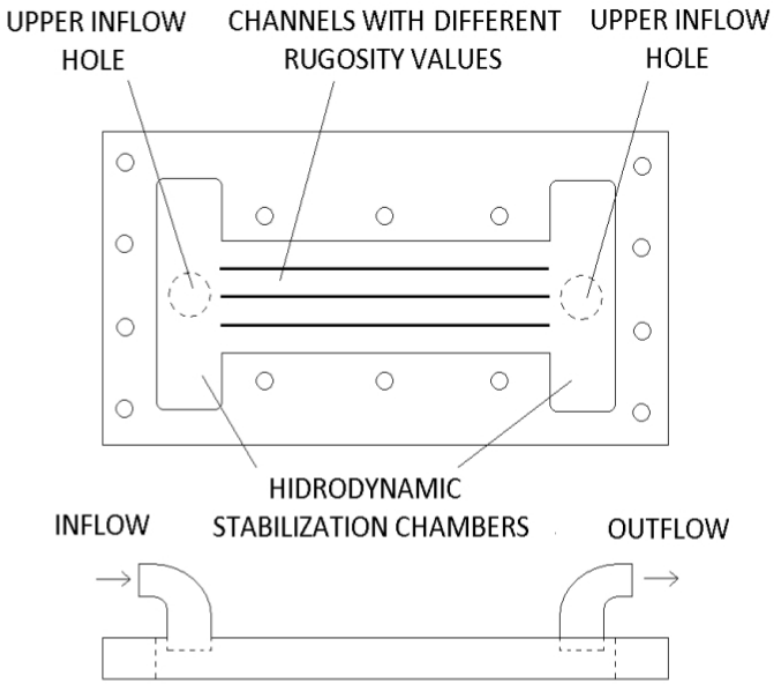

Figure 3.5: *Schematic lay-out design of the $Re \neq 0$ test sample*

pended particles as there is a positive pressure inside. There is also a recirculation loop consisting of a pumping group (EK-DCP 2.2) to force water flow through the circuit and a rotameter (ANAME P-150 mm) to know and regulate the incoming flow.

Polycarbonate test sample plates are connected after the rotameter, then closing the whole hydraulic circuit. These plates (with main dimensions of $162 \times 50 \times 5.4$ mm, see figure 3.6) were fabricated with an EMCO Concept MILL 105 milling machine. They were milled with four rectangular channels of $100 \times 5 \times 5.4$ mm at different milling speeds (see appendix E for more details). A further analysis of the mechanized samples performed with a Leica-DCM3D reflection confocal microscope (50xLWD lens) showed that the rugosity obtained in the samples was in the range of 2-4 μm. The plates were composed of four channels and had two stabilization chambers to control the Reynolds number of the inflow (Fig. 3.5). The system was closed with a polycarbonate screwed lid and sealed with a silicon joint to avoid leaking. A multiport pump controls the inflow of fresh nutrient source and outflow of waste from main reactor to get a constant value the concentration

of waste products and available nutrients inside the reactor.

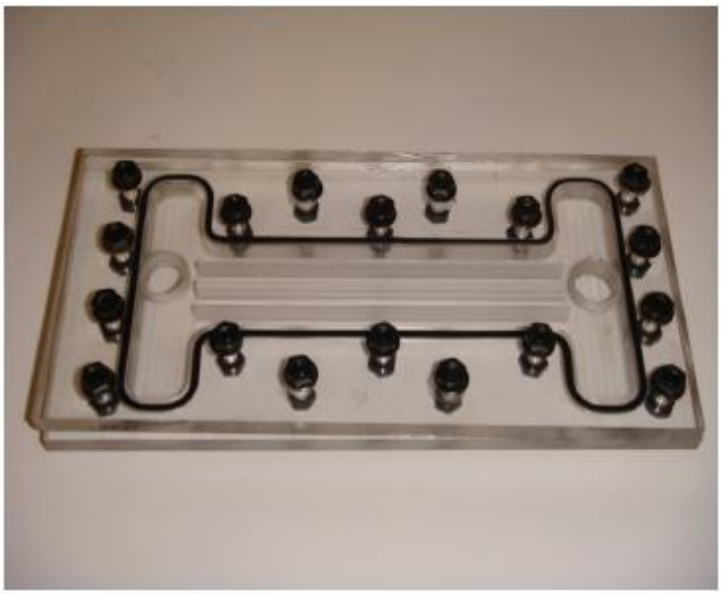

Figure 3.6: *Polycarbonate test sample designed to essay experiments at Re ≠ 0*

A multiport pump (ISMATEC IP-C 8) controls the inflow of nutrient M9 with 1% glycerol at 1.7 ml/min, and the outflow of waste products out of the main reactor. The steady state concentration of glycerol in the circuit is expected to be around 0.2%.

The system was designed to ensure sealing and sterilization: gentamicin was added into the vessel to prevent any contamination with other bacterial strain. Additionally, a sterilization process was performed before each experiment by pumping in 700 ml of ethanol 70% through the experimental system during 30 minutes. Then, it was washed with the circulation of 1 l of sterile water during 30 minutes to completely remove the ethanol out of the circuit. After this step, the system was buffered with M9 supplemented with 0.2% glycerol medium.

Once the setup was ready to be used, the same start-up procedure was followed for all repetitions: First, cells from overnight cultures were used to inoculate the CSTR at an OD_{600} of 0.0025, connecting the two pumps at maximum flow during 10 seconds to ensure a homogeneous distribution

of bacteria throughout the circuit. Second, the pumps were stopped for 15 minutes to promote bacterial attachment onto the plate. After that, the pumps were connected at the chosen flow rates depending on the selected Re number, and the system was incubated for four days at room temperature. Images were taken daily during the four days with a high-resolution confocal Leica TCS SP5 fluorescence microscope equipped with a CCD camera. Different 2D pictures were obtained for each channel at random places to have an overall view of the biofilm distribution within a channel. Before microscopic inspection, the plate sample was cleaned with 400 ml of fresh M9 medium to reduce the fluorescence background produced by non-attached cells. Two different experiments were performed for each different Reynolds number (100, 400 and 1000).

3.1.3 Biofilm quantification methods

Crystal violet assay

Crystal violet assay procedure was the chosen method for biofilm quantification in $Re = 0$ experiments, which is described next. Briefly, inocula for biofilm experiments were grown aerobically (180 rpm) at 30^oC overnight. The OD_{600} of the cultures was adjusted to 0.0025 and allowed to grow at room temperature for 24 h without shaking. Biofilms were grown either on 96-well polystyrene plates or onto polycarbonate plates custom-made with different channels at different milling configurations. A sample of the medium was removed and OD_{600} measured to estimate planktonic cells in the culture. The wells or plates were then washed three times with water to remove all non-adhered cells, and stained with 0.1% crystal violet for 30 minutes (see picture 3.7).

The dye was removed and the wells washed three further times with water, dried and the remaining stain dissolved with 33% acetic acid and the absorbance measured at 595nm (biofilm formation). In order to obtain a more quantitative estimate of biofilm formation we also calculated the biofilm index as the ratio of biofilm formation to planktonic cell density (biofilm formation/OD_{600}). Additional information about this procedure may be found in [50].

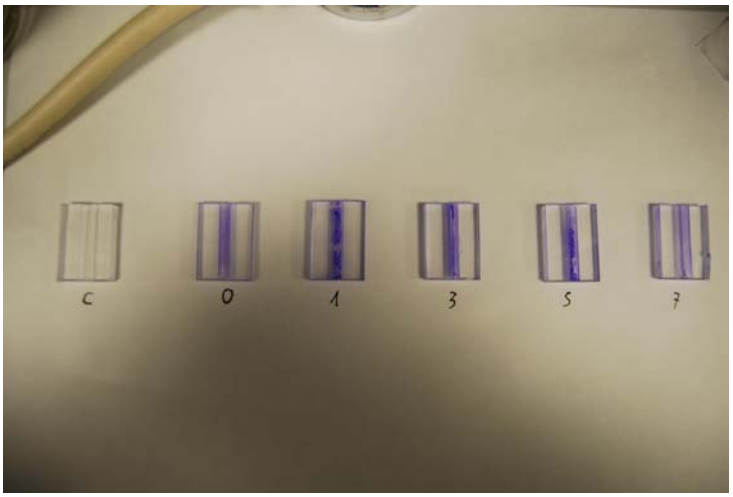

Figure 3.7: *Dyed polycarbonate plates with Violet Crystal*

Image processing

Image processing of the obtained pictures during $Re \neq 0$ experiments was the chosen method to obtain useful information about the biofilm behaviour during the experiments. A custom image treatment process was designed specifically to measure three properties related to biofilm thickness and distribution (intensity, percentage of occupied area and cluster number). This method, although is not as exact as performing direct measures, might be a faster option when trying to obtain an indirect measurement of biofilm geometric characteristics. Photos were organized in 3 groups based on the different essayed Reynolds number (100, 400 and 1000). For each group, a set (224 images) of 672 x 480 pixel size pictures were processed for each day. Images from the microscope were previously treated with Adobe Photoshop CS5 version 12.0 x64, and then further processed using MATLAB (The Mathworks).

All pictures were processed following several steps, which are indicated next. An example of this treatment is showed in 3.8. Pictures were gray-scaled, RBG images (3.8A), were converted into a 8-bit gray-scale image with light intensity values in each pixel ranging from 0 to 255 (3.8B), then a filter was applied to clean the images by reducing the average background noise found in them (3.8C), and finally they were converted into a binary data matrix by setting a threshold (3.8D). We set up the same threshold value for all pictures taken the same day with the same conditions manually

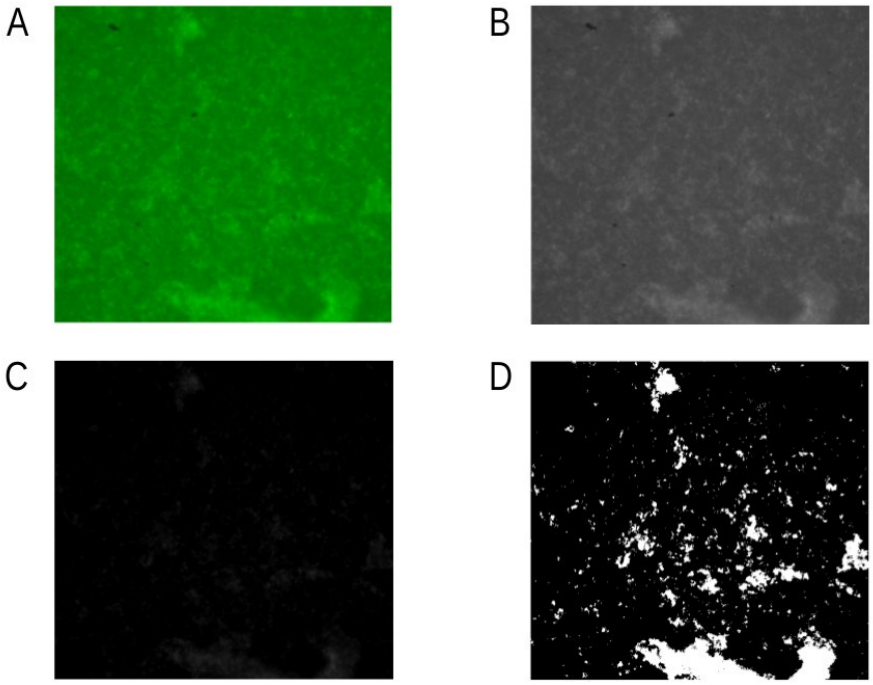

Figure 3.8: *Image treatment method applied to analyse the images from the microscope. (A) Original RGB picture obtained from the microscope. (B) Grayscaled image. (C) Image after the application of an intensity filter which removes background noise, defining shapes more accurately. (D) Binarized matrix result once an arbitrary threshold value (20 in the picture) was set to the image to support the mathematical handling of the images, such as detection of objects.*

[64, 176]. Establishing a critical intensity to gray-scaled pictures serves to define a value above which pixels with an intensity value larger than it are set to 1 while the rest is set to 0. The final result is a $M \times N$ logical matrix that matches the original picture pixel dimension and whose values are only one or zero.

The variable intensity represents the average thickness of a biofilm in a picture. Higher intensity values are associated to thicker values of biofilm. It is calculated (using grayscaled pictures without the binarization process) as the average of the intensity values of each pixel (these values range between

0 and 255) for the whole picture. For a set of N_P pictures all taken under the same conditions, if i_k is the intensity of a pixel inside a picture j with a size of $M_j \times N_j$ pixels, the average intensity I is defined as follows:

$$I = \frac{1}{N_p} \sum_{j=1}^{N_p} \left(\frac{1}{M_j \times N_j} \sum_{k=1}^{M_j \times N_j} i_k \right). \tag{3.1}$$

The percentage of area occupied by a biofilm was obtained as the average ratio between all non-zero pixels and the total number of pixels of the picture j with size $M_j \times N_j$ for all pictures after removing average intensity value of each picture background. This property gives an approximated idea of the heterogeneity of the sample: smaller values are related with more or less homogeneous biofilm layers of a certain thickness. Nevertheless larger values are linked with a heterogeneous growth of the biofilm, indicating the presence of mounts and holes over the biofilm layer. $\hat{P}_i$ equals 1 if the considered pixel is a nonzero value and equals zero otherwise. For a set of N_P pictures taken with the same conditions the value of the area is:

$$A = \frac{1}{N_p} \sum_{j=1}^{N_p} \left(\frac{1}{M_j \times N_j} \sum_{i=1}^{M_j \times N_j} \hat{P}_i \right). \tag{3.2}$$

The number of clusters denotes the degree of aggregation and roughness of a biofilm (small values would indicate a compact and relative smooth biofilm surface). This parameter has been calculated by counting the number of logical objects in the binary matrix created considering a logical object a group of pixels with nonzero value surrounded by null pixels (biofilm clusters of any shape). If N_P is the total number of taken pictures for a certain case and n_i represents the number of clusters found in a singular picture in that case, then the cluster number N is defined as:

$$\hat{N} = \frac{1}{N_p} \sum_{i=1}^{N_p} n_i \tag{3.3}$$

3.2 Results and discussion

3.2.1 Experiments at $Re = 0$

First, a series of experiments were performed using 96-well polystyrene plates to select an appropriate medium to study biofilm formation of *P. putida mt-*

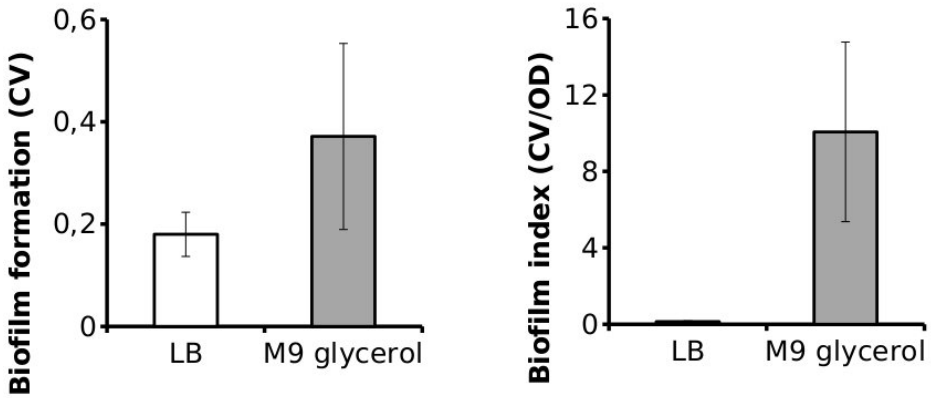

Figure 3.9: *Analysis of biofilm formation in different carbon sources. LB medium (white) was used as a rich nutrient medium while M9 plus* 0.2% *glycerol (black) was set as poor nutrient medium.*

2. Biofilm formation was tested after 24 hours of growth on LB (rich nutrient medium) and M9 with 0.2% glycerol as carbon source (poor nutrient medium). As shown in 3.9, the amount of biofilm produced (left) and biofilm index (right) were higher using M9 supplemented with 0.2% glycerol. These data suggest that the poor medium seems to be the optimum choice for our experimental settings.

Our second step was to verify the attachment of *P. putida mt-2* to the new fabricated milled polycarbonate plates using M9 supplemented with 0.2% glycerol as growth medium. A qualitative view of the crystal violet stained plates is shown in figure 3.10. A quantitative result is depicted in figure 3.11 showing that *P. putida mt-2* attaches well to all polycarbonate plates independently of the different milling speeds used.

3.2.2 Experiments at $Re \neq 0$

The use of biofilms for industrial applications will require a total control of their geometric patterns, looking for special geometries that gather all the demanded properties for the respective application. For instance, thin homogeneous layers would be useful in MEMS design, see [162]. This singular architecture would allow the measurement of experimental variables (temperature or shear fields) and avoid the disturbance of the hydrodynamics of the flow, which would be extremely useful to improve the design of MEM de-

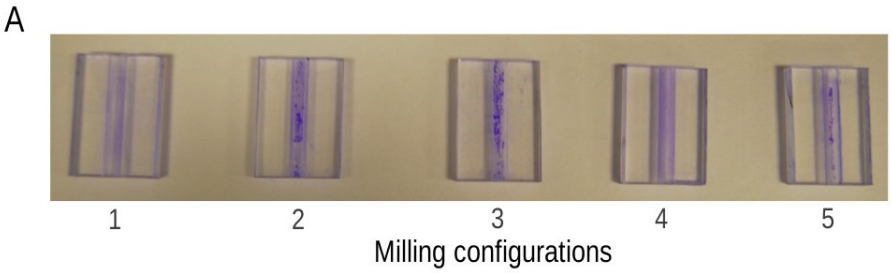

Figure 3.10: *Example of biofilm attachment quantification onto polycarbonate plates in experiments at* $Re = 0$ *by using a crystal violet process. Stained cells are measured by controlling absorbance at 595 nm (CV).*

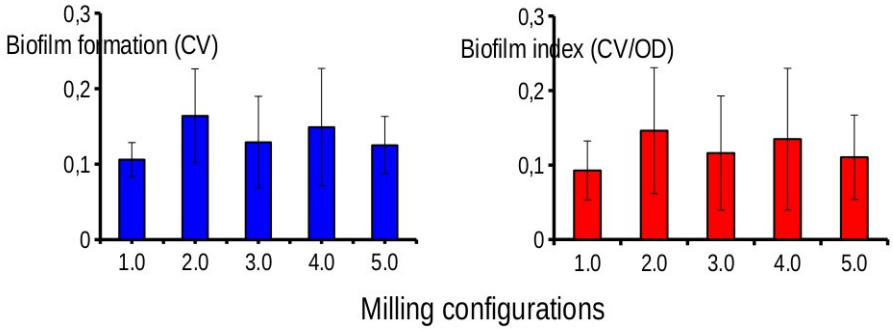

Figure 3.11: *Biofilm formation and Biofilm index results for the different polycarbonate plates made with different milling configurations and quantified by using violet crystal for experiments at* $Re = 0$*. The experiments were performed growing the cells on polycarbonate plates in M9 plus* 0.2% *glycerol for 24 h at room temperature. Polycarbonate plates were made with different milling configurations and all of them showed a roughness range within 2-4* μm*. Biofilm index calculation was performed by normalizing the amount of crystal violet stained cells normalized by the planktonic cells, in both media. In both cases, figures represent the average of four biological experiments with eight technical replicates each, the error bars means the standard deviation.*

vices. One of the main scopes in this chapter was to study biofilm formation under conditions that would be found in real MEM devices and to analyze the range of Reynolds numbers that leads to the formation of biofilms with a desired geometry.

Experiments were planned to study the influence of hydrodynamics on biofilm patterns distribution over time by applying different Reynolds numbers. To do that, we selected three different Re numbers (100, 400, and 1000) in which MEMS cooling systems commonly operate by regulating the circulating flow with the rotameter. The images obtained (3.12) show different biofilm pattern configurations depending on the Reynolds number. At $Re = 100$ small patches lead to the formation of larger accumulations of biofilm at day three, but they are removed by the flow at day four, remaining mostly colonies near the walls (see Fig. 3.12A). Experiments at $Re = 100$ showed a disperse colony configuration, suggesting that with this value of Reynolds number there might exist a limited mass transfer which promote the formation of these structures, as shown in [159].

At $Re = 400$, small colonies appear at day 2 and evolve into a homogenously distributed layer of biofilm which spreads along the whole surface of the plate at day four. A few big spots can also be observed (Fig. 3.12B). Some local patterns might indicate the presence of eddies in the current, which could suggest that waves and rippling mechanism may be already present at this Re. Shear forces within this Re seem to dominate over growth mechanisms: pictures show an effective erosion of all small colonies of biofilm and only a thin layer with a few compact spots remains attached to the bottom of the surface at day 4.

At $Re = 1000$, experiments show the generation of a higher amount of biofilm than in the other cases, and the biofilm is spread throughout the channel (see Fig. 3.12C and 3.12D). The high amount of biofilm present in the panoramic photographs at $Re = 1000$ might indicate the presence of an enhanced mass transfer of nutrients and oxygen in the biofilm exposed to these conditions. Because of Reynolds number in the plate is expected to be around 1000 (laminar regime), the hydraulic circuit geometric design of the experimental device might be responsible of some effects (such as vorticity) that could promote turbulence in the fluid and hence a larger bacterial population. Also, biofilm thickness tends to increase on the borders of the channel, as it can be seen in Fig. 3.12C and 3.12D. This is consistent with the fact that the vorticity near the corners of a duct tends to increase, giving rise to a more complex bacterial population distribution in these zones

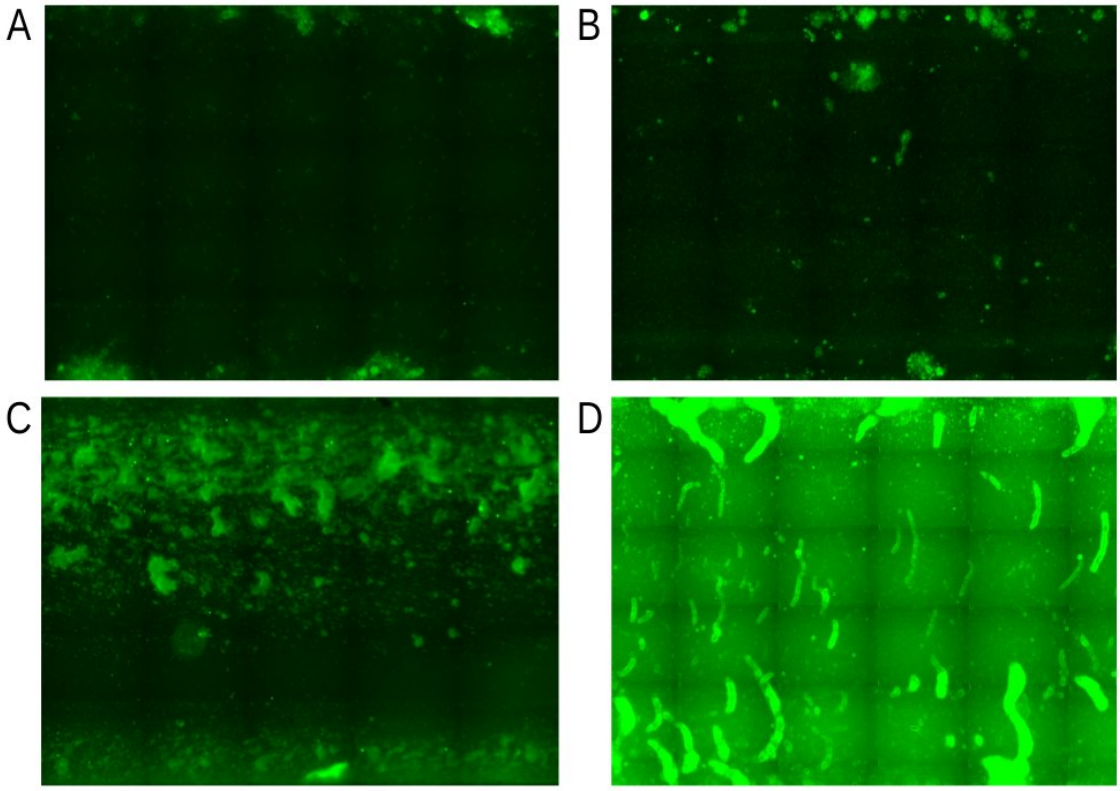

Figure 3.12: *Biofilm pictures obtained at different Reynolds number. (A)* $Re = 100$. *(B)* $Re = 400$ *(C) and (D)* $Re = 1000$. *The pictures were taken at day four in channel 2.*

[134, 152]. In one of the biological repetitions at $Re = 1000$, a ripple and a wave configuration are clearly seen (Fig. 3.12D). The differences observed in both $Re = 1000$ experiments (Fig. 3.12C and 3.12D) may indicate the influence of other variables relevant for biofilm development. Since the experiments were repeated at room temperature during different months of the year, temperature deviations (1-6^{o}C) could have led to different growth patterns. Temperature is another interesting parameter that we will explore in future experiments.

Image treatment is a very useful tool to obtain quantitative information regarding biofilm distribution and patterns, as it is shown in other works [64, 63] where an image treatment software is developed to measure different parameters of biofilms such as the overall distribution, percentage of occupied area, etc. However, because we wanted to obtain specific information andoptimize the handling of the different set of pictures, we decided to program ourselves a software to analyze the pictures in order to extract quantitative parameters to compare the different Reynolds numbers tested. Fig. 3.13A shows the percentage of biofilm occupied area at different days. This value increases with growing Reynolds numbers. The evolution with time of this parameter shows different behaviors depending on the Reynolds number number. At Re=100 the percentage of occupied area decreases with time, at Re=400 that value seems to be constant, while at Re=1000 shows a maximum value at day three.

The number of clusters (see Fig. 3.13B) decreases with time at $Re = 100$. For $Re = 400$ and $Re = 1000$ it stabilizes at a constant value as time increases.

The intensity parameter tends to a constant value for $Re = 100$, while at $Re = 400$ and $Re = 1000$ it increases with time. Comparing different Re numbers, larger Re numbers lead to larger intensity values (Fig. 3.13C).

The analysis of 2D panoramic images within these conditions, does not allow to quantify distances in the Z-axis. However, qualitative information can be inferred by comparing their intensity profiles (see Fig. 3.14). A contour image can be plotted, representing the value of each processed pixel by its intensity. Higher intensities are linked with a larger amount of light taken from the camera, which is associated with a higher amount of biofilm in that area. The intensity profiles at different Re allow for qualitative comparison among different pictures.

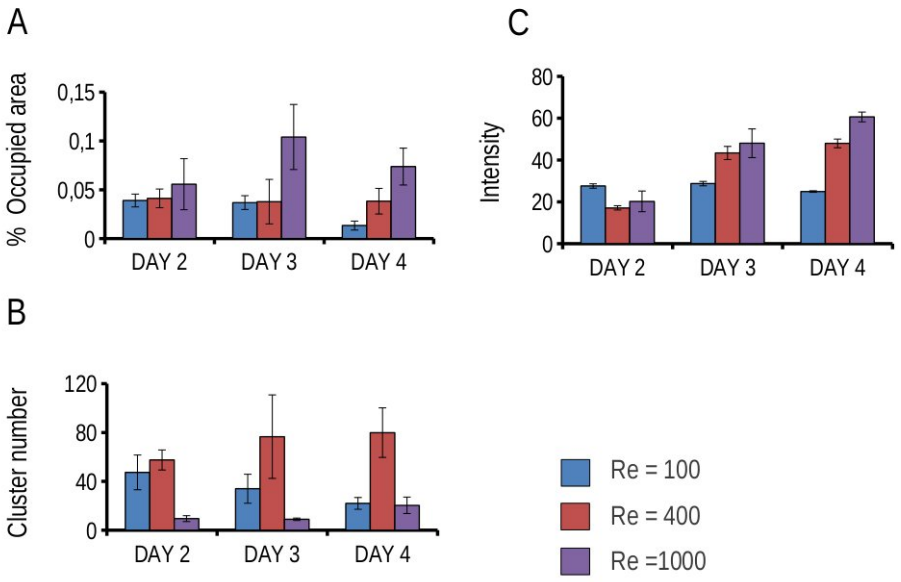

Figure 3.13: *Average results after image treatment at different Reynolds number at different days. (A) % Area occupied is calculated as the number of nonzero pixels /total number of pixels. (B) The number of clusters represents the total number of sets containing only nonzero pixels surrounded by pixels with zero value. (C) Intensity (Average of the light intensity value of each pixel in each photo). Values were obtained for each Re number and day, and two different experiments per Re number were used to calculate the average and standard deviation.*

3.3 Conclusion

We have designed an industrial setup to study biofilm formation in a flow cell under different hydrodynamic conditions. The experiments show different biofilm development depending on the *Re* number. Hydrodynamic conditions seem to generate different biofilm structures derived from reaching a balance between the availability of nutrients, growth rate, death rate and erosion caused by the hydrodynamic effect.

At a low Reynolds numbers ($Re = 100$ in our specific device), intensity values are small and the observed heterogeneity tends to be bigger than at larger Reynolds numbers.

On the contrary, increased Reynolds numbers seem to promote an en-

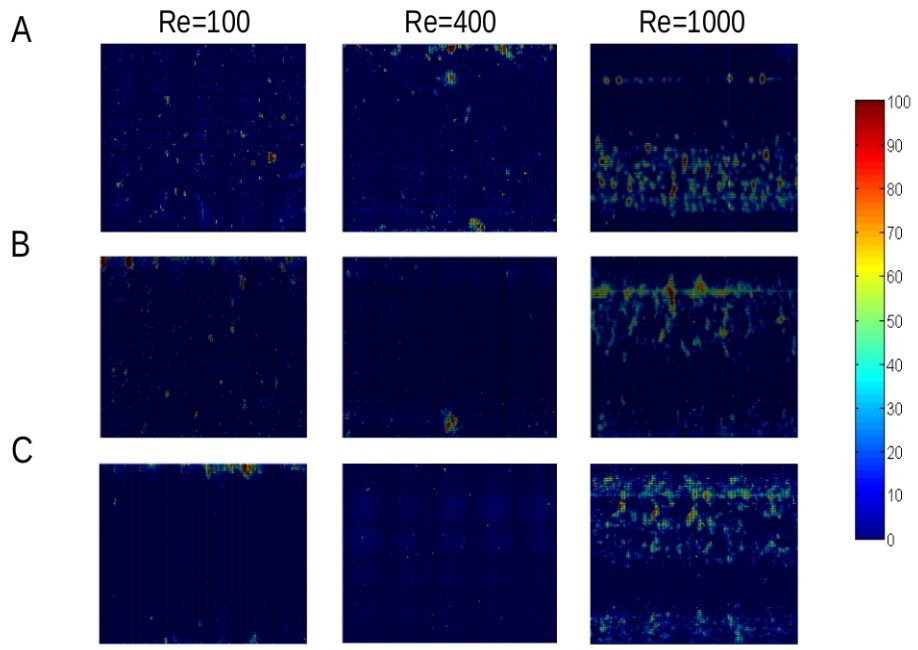

Figure 3.14: *Intensity profile pictures obtained for the different biofilm images. (A) Day 2. (B) Day 3. (C) Day 4. The vertical bar to the right represent the color code intensity values for biofilm formation. The scale is indicated as percentage of the maximum obtained value in each picture.*

larged mass transfer rate (favoring high bacterial densities), and smooth out biofilm irregularities, making its surface more homogeneous as shown by the percentage of occupied area, intensity and cluster number (Fig. 3.13). Larger Reynolds numbers (about 1000 in our specific devices) produce biofilms adequate for industrial applications that require homogeneous biofilm covers, but are not adequate when we wish to minimize biofilm thickness (as they yield the maximum thickness of all tested conditions). Depending on the application and the desired biofilm properties, the selected Reynolds number will vary.

The standard deviation values indicate a reasonable dispersion of the data. This behavior agrees with the fact that analyzing images leads to a high heterogeneity of samples depending on what pictures have been selected for processing: pictures focusing on valleys or biofilm peaks will lead to a high dispersion value, but their effect will be eventually averaged out

if they are an exception in the set of pictures. The potential of image processing to analyze the geometry of biofilm patterns provides an alternative way to calibrate biofilm theoretical models. Especially relevant could be the case of cellular automata models, in which all the parameters are completely numeric and many times they do not have a physical equivalent parameter. Our experimental work generates a set of geometric numerical data obtained from real experiments that we could use to explore the range of parameters in cellular automata models that results into specific geometric patterns. If a connection between those numerical values and the physical conditions could be established, it would help to predict other behaviors without performing additional and expensive experiments.

Based in the fact that experimental information may be used to set a realistic theoretical framework, we decided to model mathematically the conditions tested in these experiments. Because bacteria depend on many parameters not fully understood and that the information gathered in the experiments similar to those described in this chapter may fit naturally a probabilistic description, the next chapter will be dedicated to develop a hybrid model able to predict biofilm spreading patterns observed in experiments.

Chapter 4

A hybrid model to describe biofilm growth in a straight duct

The previous chapter explains the design, assembly, start up and operation of an experimental set up to gather laboratory data regarding the effect of some physical variables in the biofilm growth patterns. It was inferred that by controlling a few parameters we are able to generate flat homogeneous biofilm layers, which may be useful for industrial purposes. A standardized manufacture of substrates should ensure similar roughness patterns and hence similar biofilm quality under analogous external conditions. The effect of roughness on the tests were not conclusive as all tests were performed in a similar roughness range. However, roughness could be a key factor for the industrial use of biofilms. The presence of cavities in the surface of these devices (as a result of the mechanical milling process) with the same order of magnitude than bacterial size (in the range 2-3 μm) might have a positive or negative influence on biofilm growth. A theoretical model would be useful to gain insight on the effect of different parameters on biofilm growth when experiments fail to provide conclusive evidence. Available models have not taken into account important parameters, such as roughness. All surfaces have a roughness, but most models which simulate spreading biofilm patterns do not take into account this factor. This seems to be a flaw: roughness should affect biofilm patterns, as it allows bacteria to grow safe and apart from shear forces produced by the flow.

In this chapter, a hybrid model is proposed to describe the growth and evolution of a biofilm in presence of a flow on rough or smooth surfaces. Bacteria are seen as creatures living in a grid that may perform different

tasks (reproduction, detachment, attachment) with a certain probabilities, informed by the status of continuous fields, such as the nutrient concentration or the fluid velocity and pressure. There are other choices that could describe biofilm dynamics in a more complex way. However, it is not the purpose of this work to give a full description of all physical and chemical processes involved, yet poorly understood. Instead, a simple model that reproduces the basic behavior of a bacterium is developed.

The stochastic approach allows scientists more freedom to design rules without knowing the processes in detail. Using a simple set of probabilistic rules for each process, a simple mathematical description may be obtained at a reduced computational cost, yet useful to approach the real behavior of biofilms.

The chapter is divided in six parts. Section 4.1 introduces the geometry and conditions in which biofilms are grown, and summarizes the expected evolution [102]. Section 4.2 presents the hybrid model, explaining the different bacterial mechanisms taken into account. Section 4.3 contains the nondimensionalization process and discusses the key parameters to be controlled during the numerical simulations. Section 4.4 explains the adaptation of the model to perform simulations in a 3D lattice. Section 4.5 details the numerical simulations of the model and discusses the relation between experiments and the theoretical simulations. Finally, the chapter is summarized with some conclusions in section 4.6.

4.1 Geometry and basic ideas

This model describes the formation and evolution of a biofilm in a simple way based on reference [102] and in line with the experiments described at the end of the previous chapter. The physical domain consists of a duct with a rough bottom surface (the roughness has the same order of magnitude as the bacterial size) and with a rectangular cross-section filled with water, nutrients and oxygen. It is assumed that a small quantity of biofilm is already attached to the bottom of the channel. This biofilm seed receives nutrients and oxygen from the surrounding flow circulating along the pipe in the x direction, and suffers erosion due to the shear stress exerted by the fluid. A longitudinal section of the rectangular pipe is taken and a study of the biofilm evolution is performed (see figure 4.1). This model will be extended to three dimensions in following sections.

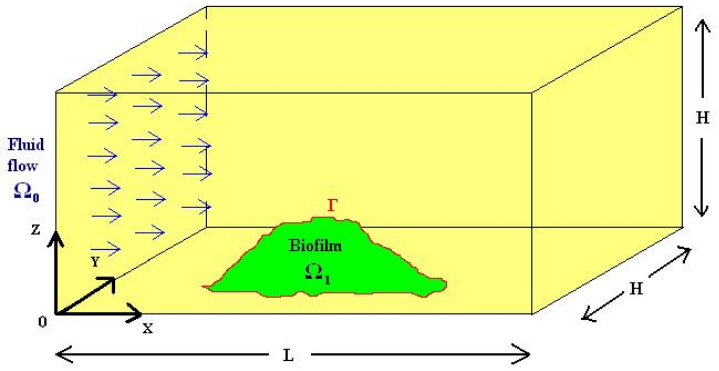

Figure 4.1: *Channel filled with fluid and biofilm attached to the bottom.*

Bacteria are considered as living entities that may perform a certain number of activities depending on external factors. They may divide and spread, generate an EPS matrix, deactivate, detach from the biofilm, and so on. Aerobic bacteria need oxygen and a carbon source to survive. Bacteria choose to carry out one activity or another according to the levels of nutrient and oxygen available at their location and the shear force exerted by the flow.

The basic activities performed by bacteria are selected to generate patterns and reproduce behaviors reminiscent of those observed in real biofilms. The true biological processes are yet largely unknown, but the idea is to choose simple rules motivated by experimental observations trying to mimic some observed behaviors. Whenever a better understanding of the cellular processes is available, the proposed rules can be updated to reflect that knowledge. The selection of processes considered here provides insight into the role of different parameters in the structure of cellular aggregates, together with basic understanding of the way some competing cellular mechanisms may act and interact. This information might be incorporated in more refined models or used for calibration in experiments.

In the present model, the flow influences detachment and attachment processes, the concentration boundary layer outside the biofilm, the EPS matrix generation and cell reproduction through it, allowing the biofilm-fluid interface to move as a result of erosion, adhesion, mass production and spreading. However, possible motion of cells or cell blocks due to the flow is neglected here. It would be included in the next chapter. Here, the fluid is crudely

taken into account through a couple of parameters: the shear force on the biofilm surface (taken to be constant to simplify) and the thickness of the concentration boundary layer. Concentrations are computed solving simplified reaction-diffusion equations in the biofilm and the concentration boundary layer. The approach to incorporate bacterial mechanisms in each time step of the biofilm evolution will be described below, and is inspired by the current biological knowledge.

The evolution of biofilms is believed to be as follows [102]. Planktonic bacteria suspended in the water flow reach the substratum and attach to it. Once they are attached, if bacteria receive sufficient amounts of carbon and oxygen they will divide and start spreading on the surface forming microcolonies that constitute the germ of a biofilm and may eventually merge. During biofilm formation bacteria suffer morphological and metabolic changes, such as loss of their flagella and EPS secretion, to generate more complex structures called macrocolonies. Bacterial cells depend on the nutrients and oxygen available in the environment to survive. In fact, they adapt their metabolism according to the concentrations of these components. The biofilm surface restricts the diffusion of oxygen and carbon to bacteria at the bottom of the colony. As reproduction has a high cost in terms of energy, only cells with a large availability of nutrients and oxygen may reproduce (these cells will be located mainly in the upper part of the biofilm). The other fraction of cells will deactivate following different kind of mechanisms (which are out of the scope of this model) or produce exopolysaccharides (EPS), forming a rigid polymeric matrix. This matrix promotes vertical growth of the colony improving access to oxygen and carbon, hardens the biofilm structure to protect the colony against the external flow and finally gives rise to a macrocolony. Macrocolonies can adopt different geometries depending on different external and internal factors.

Typical macrocolonies consist of mushroom-like towers separated by fluid-filled voids carrying nutrients and oxygen, although flat structures are also possible. Experimental data shows that rich carbon sources seem to favor mushroom-like colonies, while poor sources may result in almost flat biofilms. Depending on the hydrodynamic conditions, circular colonies, streamers, ripples, rolls, streamlined patches, etc. can be observed [126]. Two examples of ripple (picture 4.2) and patch (picture 4.3) configuration are included.

The liquid flow generates in the biofilm a shear stress derived from viscous forces acting on the boundary layer close to the interphase. Cells attached to the upper part of the colony are exposed to higher shear forces, having a

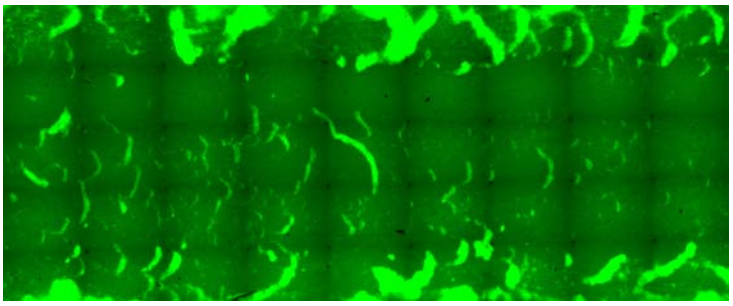

Figure 4.2: *Ripple configuration shown by a biofilm grown in a channel attached to the bottom and exposed to a flow.*

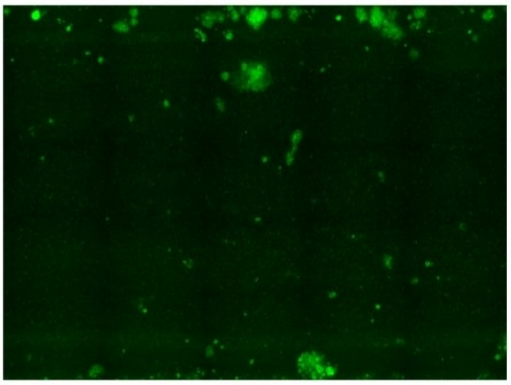

Figure 4.3: *Patch configuration shown by a biofilm grown in a channel attached to the bottom and exposed to a flow.*

larger probability to be detached from biofilm and carried away with the current. As it is expected, final configuration of biofilm will be a balance between hydrodynamic forces, reproduction speed, deactivation and EPS processes.

4.2 Mathematical approach

The biofilm system described above is modeled with a cellular automata model informed by the continuous fluid and concentration fields. In CA models, space is represented by a grid of square tiles (see [62, 123] and references therein). To describe a roughness of the same order of magnitude as the size of bacteria, the size of the tiles is chosen to be similar to the size

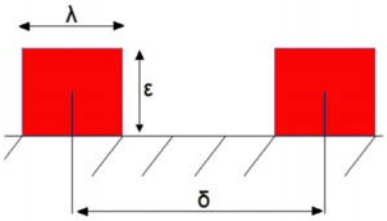

Figure 4.4: *Roughness parameters in CA model*

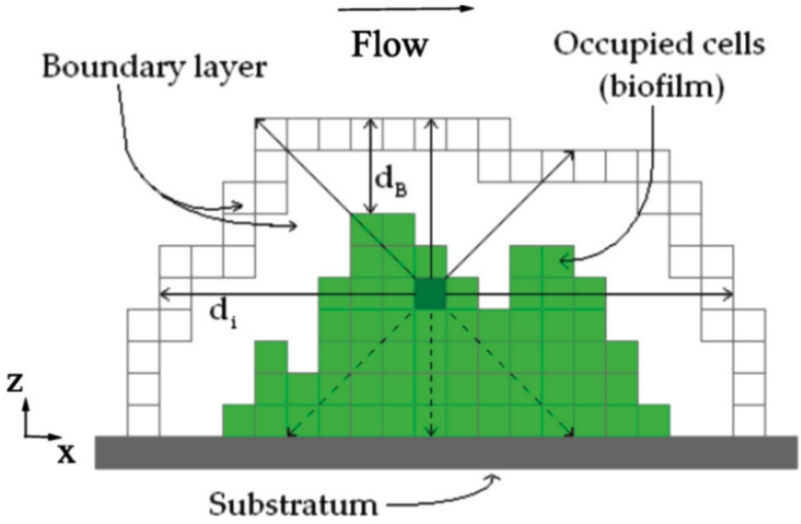

Figure 4.5: *Coordinate reference system in CA model*

of one bacteria (microns) [130]. Notice that the size of the envisaged tubes are in the order of a few hundred microns. Each tile is filled with either one bacterium, water or bottom surface material, and its status may change from one time step to the next according to the rules governing the different processes. Each individual bacterium evolves according to the nutrient and oxygen presence it feels, to its affinity to the carbon source, to the flow strength it feels, and to its location in the biofilm. Roughness is modeled by rectangular steps on the bottom, characterized by their height ϵ, the length of the peaks λ, and the distance between them δ (see figure 4.4). A 2D longitudinal section representing a rectangular pipe (x=length,z=height) (see Fig. 4.5) is discretized in square tiles taking the roughness pattern into account. The determine the nature of each of them.

Biofilm is only expected to adhere to the bottom substratum, which can be achieved by choosing the material properly. In most simulations, the initial condition of the biofilm will be an initial seed that is already attached to the substratum. In the last simulations we will allow for adhesion of floating cells, a point that will be studied further in next chapter.

Time is discretized in time steps whose size is determined in terms of the time for a bacterial reproduction cycle (in our experiments, this value is approximately 23 minutes). To modelize properly the different bacterial behaviors the model is structured as a modular cellular automata model. Its structure is organized in submodels describing the different mechanisms that govern biofilm formation and the evolution which we want to describe. Each submodel deals with a distinctive bacterial mechanism: cellular division and spreading to neighboring tiles, generation of an EPS matrix and decay, and cell detachment and adhesion. For each individual bacterium, at each time step, a probability for all of these events will be assigned, that usually depends on the concentration of oxygen and nutrients, the fluid flow, the biofilm cohesion, or the number of neighboring cells containing biomass and their location. The sub-models cover the following aspects of biofilm formation and evolution:

- Dynamics of dissolved components (nutrients, oxygen) outside the biofilm and inside. Experiments are usually designed in such a way that their concentrations are almost constant outside the biofilm. Inside, they are governed by reaction-diffusion equations, but a quasisteady approximation thereof might suffice because the diffusion and reaction of dissolved components are likely to be faster than the rates of biological processes [2, 42, 75].

- Generation of EPS matrix [154, 173] and decay. Each bacterium has a probability to produce EPS matrix depending on its location, the concentration of substrate and oxygen [154, 49, 173] and the hydrodynamical shear stress. Bacteria synthetizing EPS are unable to reproduce. The cohesion of the biofilm depends on the EPS matrix, which in turn affects mechanisms such as detachment [150]. Cell deactivation and decay mechanisms for low concentrations may generate inerts playing a role in biofilm adhesive properties.

- Detachment of isolated bacteria or biofilm erosion and detachment of biofilm fragments. Each cell has a probability to detach from the biofilm

depending on its location, the number and location of neighboring bacteria, the hydrodynamic shear stress and the cohesion of the biofilm. Detached bacteria are carried by the flow and may eventually reattach themselves. Biofilm fragments attached to the rest of the film by a few cells may also be eroded if the connection to the substratum breaks off.

- Reproduction and spreading. Each bacterium has a probability to reproduce depending on its location and the available oxygen and nutrients [62]. New bacteria fill neighboring empty tiles or shift existing bacteria with a certain probability.

- Adhesion of floating cells. The bacteria carried with the flow may attach either to existing biofilm parts or to uncolonized parts of the substratum with a certain probability that depends on the flow and the affinity between the bacterial strain and the surface [56, 88].

4.2.1 Dissolved components

The evolution of a biofilm depends on the availability of carbon sources and oxygen. The concentrations of oxygen c_o and substrate c_s are governed by a reaction-diffusion system of PDEs with different domains (fluid and porous biofilm): outside the biofilm, concentrations solve uncoupled convection-diffusion equations. Inside the biofilm, the convection due to the flow disappears, but coupling reaction terms representing nutrient and oxygen uptake by cells must be included. A boundary layer of thickness d_B is formed at the interface. The model is completed with boundary conditions at the walls of the duct and the bulk/boundary layer interface [42].

Nutrient concentration gradients result from a combination of nutrient transport from the bulk fluid through a concentration boundary layer adjacent to the biofilm-fluid interface and nutrient uptake by the cells. The thickness of the concentration boundary layer characterizes the external mass transport and depends on the flow regime. Experimental measurements of the nutrient concentration gradients and the boundary layer thickness for different flows are presented in Refs. [31, 179].

The thickness d_B is shown to depend on the bulk velocity of the flow in Ref. [31] (it seems to be inversely proportional to it). Additional experimental studies show that transport outside cell aggregates is larger than inside

them [175]. Outside the boundary layer, advection dominates the transport, while inside the aggregates diffusion is the controlling factor. This motivates the assumption that transport through the cellular aggregate and the boundary layer occurs by diffusion with the same effective diffusion coefficient for the boundary layer and the biofilm [62, 175].

Instead of solving the full reaction-diffusion system, a quasi-steady approximation is implemented because the diffusion and reaction rates of dissolved components are faster than biological process rates [2, 42, 75]. Experiments are usually designed to keep the concentration constant within the fluid. Choosing the concentration values at the bulk/boundary layer interface C_o, C_s as control parameters, the concentrations of nutrients and oxygen inside the region containing the biofilm and the boundary layer [62] are governed by the equations (4.1) and (4.2):

$$D_s \Delta c_s = k_2 \frac{c_s}{K_s + c_s} \frac{c_o}{K_o + c_o} \tag{4.1}$$

$$D_o \Delta c_o = \omega k_2 \frac{c_s}{K_s + c_s} \frac{c_o}{K_o + c_o} \tag{4.2}$$

with zero flux conditions at the substratum. The diffusion constants D_s and D_o are assumed to be the same for the biomass and the boundary layer. The right hand sides represent the nutrient and oxygen uptake kinetics. Here, ω is the stoichiometric coefficient of the oxygen reaction, k_2 the uptake rate of the nutrient, K_o the Monod half saturation coefficient of oxygen, and K_s the Monod half saturation coefficient of the carbon source. The values of all these parameters depend on the bacteria species forming the biofilm. The use of Monod laws makes sense provided that values of the concentrations remain small. Otherwise, inhibition terms should be incorporated. It is assumed that oxygen is in excess, which is often the case. The concentration of nutrients c_s becomes the limiting concentration c_l, that is, the one that penetrates a shorter distance into the biofilm and therefore constrains division and survival of cells and biofilm growth thereof. The system is reduced to:

$$D_s \Delta c_s = k_2 \frac{c_s}{K_s + c_s} \tag{4.3}$$

For submerged biofilms, nutrients and oxygen are both provided by the surrounding flow. Biofilms grown on air-solid surfaces [20] might take oxygen from the air and the substratum, and nutrients from the substratum. In those cases, oxygen and nutrients might become limiting factors in different regions.

At each time step, (4.3) is solved to reflect changes of nutrient uptake caused by the new biofilm geometry. In the simulations showed in this chapter, it has been computed numerically the solution of the nonlinear boundary value problem for the concentration by using an iterative relaxation scheme with local error control. Solutions for the elliptic problem are constructed as stationary solutions of the diffusion problem. In the tests presented here, error tolerance is set to 10^{-3}. Nevertheless there is a simpler analytical formula which approaches the concentration distribution inside the biofilm (usually by underestimating it), adapted to its boundary and with a reasonable qualitative dependence on the parameters (see [62]). Instead of numerically solving (4.1)-(4.2) inside the biofilm, an approximation may be found assuming zero-order uptake kinetics (the right hand sides are replaced by just constants k_2, and ωk_2, respectively) and a flat one dimensional biofilm (z axis). The system uncouples and may be solved explicitly the resulting one dimensional equations to get ((4.4)) and ((4.5)):

$$c_s = \left(C_s^{1/2} - \sqrt{\frac{k_2 d^2}{2D_s}} \right)^2 , \tag{4.4}$$

$$c_o = \left(C_o^{1/2} - \sqrt{\frac{\omega k_2 d^2}{2D_o}} \right)^2 , \tag{4.5}$$

where d is the distance from the surface to the biofilm (penetration distance). These formulas are adapted to 2D geometries following [62]:

$$c_s(cell) = \left(C_s^{1/2} - \sqrt{\frac{k_2}{2D_s} \left[\frac{1}{8} \sum_{i=1}^{8} \frac{1}{d_i(cell)^2} \right]^{-1}} \right)^2 , \tag{4.6}$$

$$c_o(cell) = \left(C_o^{1/2} - \sqrt{\frac{\omega k_2}{2D_o} \left[\frac{1}{8} \sum_{i=1}^{8} \frac{1}{d_i(cell)^2} \right]^{-1}} \right)^2 , \tag{4.7}$$

where d_i(cell) are penetration distances between the cell and the bulk/boundary layer interface in the directions joining the cell with its eight neighbors (see picture 4.6).

The distances to the boundary layer interface in each of the 8 directions are calculated assuming variable diffusion contributions in all directions. Once the values of the parameters have been fixed, values of both

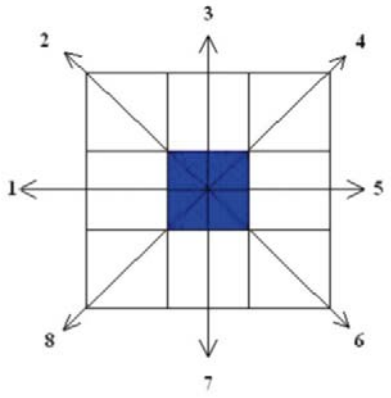

Figure 4.6: *Allowable directions on 2D cellular automata model*

concentrations may be compared to decide which one is the limiting concentration c_l(cell), that is, the one that penetrates less deeper into the biofilm and therefore constrains division and survival of cells and biofilm growth thereof.

Although this formula may produce useful qualitative predictions at a much lower computational cost if plugged into the stochastic description, here we include the results obtained by solving the full nonlinear equations for concentration field. The result of these calculations will be a nutrient/oxygen concentration matrix that will be updated each time step whose elements are concentration values in every tile of the simulation grid.

4.2.2 EPS matrix generation

In small colonies, most bacteria reproduce again and again. As the size of the biofilm grows, nutrients and oxygen become scarce in inner parts of the biofilm because the distance to the interphase increases (and the mass transport rate becomes smaller). This forces a fraction of bacterial population in the biofilm to switch their metabolic processes and start producing EPS matrix with a certain probability [102, 160], giving the colony additional benefits explained in previous chapters. Experiments show that as bacteria are deeper in the biofilm, their chances to produce EPS increase. The EPS matrix also spreads over the neighboring bacteria making their reproduction harder.

The nature of the surrounding flow also influences EPS generation: the stronger the shear stress due to the flow is, the more resistant the EPS matrix is [125, 150]. Biofilms grown at low Reynolds numbers tend to be carried away with the flow if the Reynolds number is increased in a short period of time. Biofilms grown at large Reynolds numbers in turbulent regimes are difficult to remove, and expand easily as the Reynolds number is decreased or the availability of carbon improves [3] (switching to a richer source or increasing the nutrient concentration).

The probability for a cell to produce EPS matrix depends on the availability of nutrients and oxygen at the cell position and the shear exerted by the flow. The EPS matrix is generated with the following probability law ((4.8)):

$$P_{eps}(\mathcal{C}) = R(Re)\left(1 - \frac{c_l(\mathcal{C})}{c_l(\mathcal{C}) + K_l}\right), \tag{4.8}$$

where R(Re) $\in (0,1)$ and c_l represents the limiting concentration in each cell taken from the concentration matrix. These matrices are updated once a time step has been completed to reflect the change in the biofilm geometry. The parameter $R(Re) \in (0,1)$ is an increasing function of the Reynolds number Re.

Cell decay may be taken care of by deactivating cells in which the concentration falls below a critical value. Concentrations in each cell $\mathcal{C}$ are stored in a linked list of cells. These lists are updated once a time step has been completed, to reflect the change in the biofilm geometry.

As expected [102], the probability (4.8) takes small values when the biofilm thickness does not surpass a threshold (the limiting concentration is large enough) and increases as the cell is deeper into the biofilm (the limiting concentration will decrease). At each time step and for each cell, a random number $s \in (0,1)$ is generated. When $s < Peps(C)$, the cell will generate the EPS. After several steps, the fraction of cells generating the EPS matrix stabilizes to a certain value, which may be used to determine R(Re) by comparison with experimental measurements.

Whereas $R(Re)$ controls the percentage of cell generating the EPS matrix, the factor involving the concentration governs the spatial distribution of these cells in the biofilm. The amount and nature of the EPS matrix produced determines the cohesion (strength) of the biofilm. Parameters representing the biofilm cohesion can be measured [150, 134] and introduced

in the erosion probability law (4.10). However, it may be useful to have a rough idea of its spatial variations and their effect to infer how the presence of weaker regions may affect biofilm evolution or to input this information in macroscopic models. The EPS matrix diffuses and accumulates in different ways in different biofilms [154, 49]. Here we test a local measure, σ of the biofilm cohesion which takes into account the number of neighbors and their nature:

$$\sigma(\mathcal{C}) = \frac{\sigma_0(Re)}{8} \sum_{i=1}^{8} \sigma_i(\mathcal{C}) \tag{4.9}$$

where

$$\sigma_i(cell) = \begin{cases} 0 \text{ if neighbour } n_i \text{ is not present,} \\ \alpha \text{ if neighbour } n_i \text{ is present, but does not produce EPS matrix,} \\ 1 \text{ if neighbour } n_i \text{ produces EPS matrix,} \end{cases}$$

and $n_1(cell)$, $n_2(cell)$,...,$n_8(cell)$ denote the eight neighbour locations for the cell under study (see Figure 4.6) and σ_0, $\alpha \in (0, 1)$. These parameters represent the strength of the EPS matrix generated by the bacteria and the strength of the attachment between standard bacteria. When deactivated cells are present an additional constant α should be used for them. Other options are possible as well: $\sigma(\mathcal{C})$ might be modulated by the variations of the concentration of the EPS matrix, governed by equations similar to those described in the previous section when the matrix diffuses easily. The parameters σ_0 and α represent the strength of the EPS matrix generated by the bacteria and the strength of the attachment between standard bacteria. In practice, σ_0 seems to increase with Re [121, 125, 150]. These parameters depend on the type of bacteria and must be fitted experimentally. $\alpha = 1/2$ has been selected in the showed computer experiments. Figure 4.23 includes the variable cohesion in the erosion mechanism.

For specific bacteria forming biofilms on air-agar interfaces in the absence of flow, there are detailed measurements of the fractions of cells generating EPS and related chemicals. Precise visualizations of their spatial distribution within the biofilm are available too [20]. Regions with large availability of nutrients contain normal cells. As the concentration of nutrients decreases, the percentage of cells generating EPS matrix increases, and they may even deactivate. In that specific case, the EPS matrix production is known to be triggered by cell production of several chemicals. The author could not find any evidence of such detailed studies for biofilms in flows yet, but the laws

described here might be updated to incorporate such knowledge if it ever becomes available.

4.2.3 Detachment and erosion by the flow

Surface cells are subject to shear forces exerted by the flow, which may detach them from the biofilm [125, 151]. In principle, cells sheltered by other cells are somehow protected from erosion. Exposed cells will detach with a probability depending on the number and location of their neighbors relative to the motion of the fluid, the biofilm cohesion, which is controlled by EPS matrix generation, and the force due to the flow felt by them, which depends on the Reynolds number. The Reynolds number, Re, is computed using the hydraulic diameter of the ducts and the average velocity, which are known.

The hydrodynamical stress on a cell may be compensated by the forces exerted by its neighbors, depending on their number and distribution. According to the geometry depicted in Figure 4.5, hydrodynamic shear forces are mostly oriented in the x direction. Figure 4.6 illustrates the location of possible neighbors. Each of them adds a certain force (which depends on their relative position) with a component opposite to the direction of the flow. The eight neighboring tiles will be numbered clockwise, starting with the western direction, so that n_1, n_2, n_3, n_4, n_5, n_6, n_7, n_8 denote the neighbors located to the west, northwest, north, northeast, east, southeast, south, and southwest, respectively. If the cell has a western neighbor, n_1 , it is partially shielded from the flow and is unlikely to be carried away. The strongest resistance against the flow is exerted by the eastern neighbor n_5. Next in magnitude are the resistance forces due to adjacent cells n_4 and n_6 located in the northeast and southeast directions, and then n_3 and n_7 in the north and south directions. Neighbors n_2 and n_8 in the northwest and southwest directions add little resistance. The magnitude of the local force acting on a cell C can be described by:

$$\tau(\mathcal{C}) = \tau(Re)(1 - \beta\chi_1(\mathcal{C}))(1 - \sum_{i=2}^{8} e_i\chi_i(\mathcal{C})). \tag{4.10}$$

Here, $\tau(Re)$ represents the shear force due to the flow. Solving Navier-Stokes equations outside the biofilm at each step to evaluate it is too costly especially in turbulent regimes. Small biofilms growing at the wall are being studied here. Therefore, it is approximated by the shear force at the bottom of an

unperturbed rectangular tube. The shear stress at the substratum surface is evaluated from the velocity profiles as $\tau = \mu \frac{du}{dz}$, where μ is the fluid viscosity. For laminar flows, $\tau(Re)$ is known explicitly: u is given by the Hagen-Poiseuille expression. In general, it can be estimated as:

$$\tau(Re) = \frac{f \rho u^2}{2}. \tag{4.11}$$

where u is the known average flow velocity, ρ the fluid density and f the friction factor given by $\frac{16}{Re}$ for laminar flows and $\frac{0.0791}{Re^{0.25}}$ for turbulent flows (see Refs. [67, 68]). Notice that the roughness Reynolds number $Re_r = \frac{\rho u e}{\mu}\sqrt{\frac{f}{8}}$ is expected to be small, e being the height of the roughness elements. $\tau(Re)$ is multiplied by a factor that takes into account the geometry of the biofilm and the local support provided by neighboring cells depending on their distribution. The function $\chi_1(\mathcal{C})$ in Eq. (4.10) take the value 1 whenever the cell $\mathcal{C}$ has a neighbor located at the position n_i , and vanish otherwise. The factors and weights have been chosen to account for the fact that the fluid flows in the x direction. The weights satisfy:

$$\begin{cases} e_i \in \ (0,1), \\ \sum_{i=2}^{8} e_i = 1. \end{cases}$$

and $\tau(Re) \in (0, 1)$, so that the sign $\tau(Re)$ is not reversed. The factors and weights have been chosen to account for the fact that the fluid flows in the x direction. They represent the added resistance against the flow due to neighboring cells depending on their position. In the simulations shown here their values were set to $e_5 = \frac{5}{17}$,$e_4 = e_6 = \frac{3}{17}$,$e_3 = e_7 = \frac{2}{17}$, and $e_2 = e_8 = \frac{1}{17}$.

$\beta(Re)$ takes values close to 1. If $\beta(Re) = 1$ is set, and $\tau(\mathcal{C}) = 0$ whenever the cell has a western neighbor. As it departs from 1, the probability of a cell being eroded in the presence of the western neighbor n_1 grows. This may be more likely as Re increases.

Once the shear and cohesion parameters have been introduced, the probability for cell erosion (4.12) can be defined following [62]:

$$P_e(\mathcal{C}) = \frac{1}{1 + \frac{\tau(\mathcal{C})}{\sigma(\mathcal{C})}} = \frac{\tau(\mathcal{C})}{\tau(\mathcal{C}) + \sigma(\mathcal{C})} \tag{4.12}$$

Whenever $\tau(\mathcal{C}) = 0$, we set $P_e(\mathcal{C}) = 0$. Here, $\tau(\mathcal{C})$ is given by Eq. (4.10), and $\sigma(\mathcal{C})$ represents the biofilm strength (cohesion parameter $\sigma(\mathcal{C})$ varying in accordance with the local EPS generation production). At each time step and for each cell, a random number $r \in (0, 1)$ is generated. When $r < P_e(\mathcal{C})$,

the cell detaches from the biofilm. Erosion due to the flow may occur as detachment of single cells or of whole clusters of bacteria with a thinning connection to the rest of the biofilm.

While programming the erosion mechanism it was considered to let two cells be connected if they are neighbors in the grid via any of the eight neighboring directions. This was done for several reasons: Consistency with division is desired, as cells divide in each of the eight directions. Further, if the four main directions would only be let connect cells, then newly formed cells with only diagonal connections would break off immediately. Both versions were coded and simulations showed that qualitatively the behavior of the system is unchanged. The difference is that with connections in only-four main directions the erosion is a little stronger for the reasons mentioned above.

4.2.4 Reproduction and spreading

The mechanism for cell reproduction is similar to that in Ref. [62], except for the detail that here EPS producers and deactivated cells do not undergo cellular division in the same step. At each time step, and once checked which cells produce the EPS matrix or are deactivated, the remaining cells C will divide with probability:

$$P_d(\mathcal{C}) = \frac{c_l(\mathcal{C})}{c_l(\mathcal{C}) + K_l}, \tag{4.13}$$

where c_l denotes the limiting concentration and K_l its saturation coefficient in the Monod law. The concentration is computed at the beginning of each step as described in Sec. III A. Changes in concentration due to newborn cell consumption or cell switching to EPS generation within the same step have been neglected.

At each time step, and for each cell not generating the EPS matrix, a random number $p \in (0, 1)$ is computed. If $p < P_d(\mathcal{C})$, the cell will divide. The newborn cell must be located somewhere in the grid, so when neighboring grid tiles are empty, the daughter cell is placed in any of the empty tiles with equal probability. Otherwise, the new cell will shift one of the neighbors. The cell offering the minimal mechanical resistance is chosen, that is, the one lying in the direction of shortest distance from the reproducing cell to the biofilm boundary-bulk layer. The same rule should be applied to the shifted cell: it either occupies adjacent empty tiles with equal probability or

shifts a neighboring cell in the direction of smallest mechanical resistance. However, to reduce the computational cost neighboring cells are shifted in the same direction. This process is repeated until all the displaced cells have been accommodated.

4.2.5 Cellular adhesion

The adhesion mechanism assumes known the number of bacterial cells that are floating in the flow and the adhesion rate. Let $N_f(t)$ be the number of cells carried by the flow at time step t. The number of cells that will attach to the bottom surface at time t will be a fraction of the number of floating cells, larger or smaller depending on the Reynolds number, the type of surface, and the bacteria species. By raising the Reynolds number the probability of hitting the surface is increased. Whether the bacteria successfully attach or not will rely on the interaction between the specific type of bacteria and the surface being used. Thus, the number of attached cells will be:

$$N(t) = [\gamma N_f(t)] \tag{4.14}$$

where [ ] denotes the integer part and γ is a parameter which measures the likeliness of that specific bacterium to attach to that surface. It can be seen as an adhesion rate. Bacterial likeliness to attach to a surface depends on the type of flow and the nature of the substratum [56]. In laminar flows the main mechanism driving particles to the wall seems to be Brownian motion [52]. This usually results in low deposition rates for laminar flows. As the Reynolds number increases, turbulent effects play a role and the particle deposition rate increases linearly with the Reynolds number for small Stokes numbers [52]. It has been experimentally observed that the residence time of bacteria hitting a wall increases with shear [88] and that biofilm accumulation tends to be larger for larger flows [39]. Thus, $\gamma(Re)$ is likely to increase with Re.

To decide where these cells are going to be attached, a number to any surface compartment is assigned (of either substrate or biofilm, both are considered together), producing a list of S numbers. Then, N random integers between 1 and S are generated. New cells are located at those positions. This assumes equal probability for all the surfaces as adhesion sites.

Numerical tests implementing this mechanism are shown in Figs. 4.19 and 4.21. Whenever precise information on preferential adhesion sites is

available, as in Ref. [134], the adhesion strategy should be changed to account for that fact.

4.3 Nondimensionalization and parameters

Nondimensionalizing the model is essential to identify the minimum number of independent parameters or to be able to distinguish what is large and what is small. Results can also be useful in other situations with different variable values. All the introduced probabilities are dimensionless. Dimensions enter the model mainly through the concentration, length, and time scales.

- Length: The basic distance considered in the model is the size of a bacteria a, about 1 or 2 micrometers. It is set equal to 1 in the tests.

- Time: In the model, time is not given explicitly. It appears in the number of time steps carried out at each simulation. A simple estimate for the time step size can be given: in the most favorable conditions for bacterial reproduction, the concentration is so high that the probability of reproduction is approximately 1. In these conditions, the bacterial population will double in a single time step. An upper bound for the time step, which allows one to relate computational T and experimental times is the minimum doubling time:

$$t = \frac{ln(2)}{\nu_{max}}, \tag{4.15}$$

  where ν_{max} is the growth rate, which is a known parameter for some bacterial species and nutrients.

- Concentration: The concentration field is calculated by solving a boundary value problem for the limiting concentration, which involves a number of constants with their units that must be nondimensionalized. Making the changes of variables:

$$\hat{c}_l = \tfrac{c_l}{K_l} \ , \ \hat{C}_l = \tfrac{C_l}{K_l} \ , \ F_l = \tfrac{k_l a^2}{2 D_l K_l} \ , \ \delta_B = \tfrac{d_B}{a} \ , \ \hat{x} = \tfrac{x}{a},$$

  a dimensionless expression for the concentration may be obtained:

$$\hat{\Delta}\hat{c}_l = 2F_l \frac{\hat{c}_l}{\hat{c}_l + 1}, \tag{4.16}$$

The four parameters a, k_l, D_l, K_l are reduced to one: F_l, which is analogous to the Thiele modulus.

The main controlling parameter is therefore F_l, which measures the ratio of the uptake rate to the diffusional supply. Typical values for bacteria commonly used in flows, like *Pseudomonas aeruginosa* or *Pseudomonas putida*, and standard nutrients produce values in the range $10^{-8} - 10^{-2}$. Notice that in all the formulas introduced in previous sections, only the quotient $\frac{\hat{c}_l}{\hat{c}_l+1}$ is involved. All combinations of parameter which produces the same value of F_l for fixed values of the remaining parameters produce the same results.

For fixed bacterial strains, nutrients, surfaces, and flows, the parameters a, ϵ, λ, δ, C_s , C_o , D_s , D_o , ω, Re, ρ, μ, and $N_f(t)$ are usually known. The parameters describing the bacterial kinetics for the particular choice of nutrient k_2 , K_s , K_o , and ν_{max} are only available in some cases. In general, they have to be measured. The same happens with the average cohesion $\sigma_0(Re)$ or the adhesion rate $\gamma(Re)$. The boundary layer thickness $d_B(Re)$ may be estimated experimentally for a given flow regime. $\sigma_0(Re)$ and α in Eq. (4.9) might be calibrated using experimental measurements on the percentage of biofilm cells generating the EPS matrix and its cohesion. The specific values of $e_2, e_3, ..., e_8$ in Eq. (4.10) are not too relevant. Replacing them by other positive values respecting the symmetry produces similar results. The dependence on temperature in the model is implicit through the uptake rates, the density and viscosity of the fluid, and the diffusivities.

4.4 Full tridimensional cellular automata model

The model can be extended to three dimensions with simple changes. Biofilms grow on the bottom of a rectangular pipe carrying a flow containing nutrients, as shown in Fig. 4.7. Space is partitioned in a grid of cubic tiles, of size a. Again, each of them is filled with one bacterium, fluid, or substratum. Bacteria reproduce, spread, detach, decay, and generate an EPS matrix according to the rules described in Sec. 4.2, with the changes included below.

The probabilities for EPS generation and cell division are still given by Eqs. (4.8) and (4.13), respectively. Quotients $\frac{\hat{c}_l}{\hat{c}_l+1}=\frac{c_l}{c_l+K_l}$ are involved, where the dimensionless limiting concentration field is computed by solving numerically the three-dimensional version of the nonlinear boundary value problem for the concentration. A relaxation method to compute numerically the so-

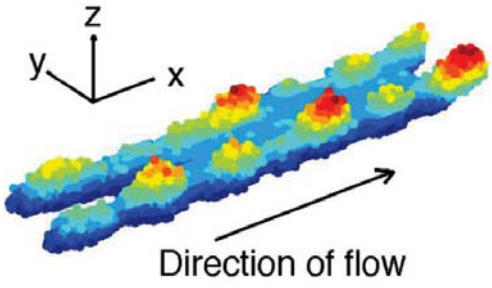

Figure 4.7: *Three dimensional geometry for the hybrid model.*

lutions is used.

The erosion probability has the form of Eq. (4.12), where $\tau(\mathcal{C})$ is given by Eq. (4.10) with $\sum_{i=2}^{8} e_i\chi_i(\mathcal{C})$ replaced by $f(C)$:

$$f(\mathcal{C}) = \frac{1}{2}f_y(\mathcal{C}) + \frac{1}{4}\left[f_{y+1}(\mathcal{C}) + f_{y-1}(\mathcal{C})\right],$$

$$f_{y-1} = \frac{1}{19}\sum_{i=9}^{17} w_i\chi_i(\mathcal{C})$$

$$f_{y+1} = \frac{1}{19}\sum_{i=18}^{26} w_i\chi_i(\mathcal{C}) \tag{4.17}$$

$$f_y = \frac{1}{17}\sum_{i=2}^{8} w_i\chi_i(\mathcal{C})$$

$\tau(Re)$ represents the shear at the bottom wall. This assumes that the patterns remain near the wall. Explicit formulas for laminar flows are available in ducts with rectangular section [67], and approximations for turbulent flows can be found in Ref. [100]. Numerical simulations in Figs. 4.9 - 4.13 set $\tau(Re)$ equal to a constant to simplify. The functions $\chi_i(\mathcal{C})$ take the value 1 whenever the cell has a neighbor located at the position n_i ,respectively, and vanish otherwise. n_i, $i = 1, ...26$, denote the neighbors of the cell under study n_0 (see Fig. 4.8). The weights w_i are chosen to account for the fact that the fluid flows mostly in the x direction.

In our simulations, the weights w_i are slightly larger for neighbors located in the intermediate slice of the cube, which contains the cell whose neighbors

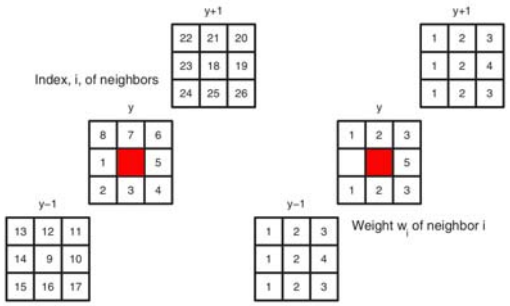

Figure 4.8: *Location of the different neighbours in three dimensions.*

are being tracked. The weights are equal for neighbors occupying the same position in each of the two lateral slices. Figure 4.8 illustrates the numbering of neighbors and the weights which have used in our simulations. The local cohesion in Eq. (4.8) may be constant or take the form:

$$\sigma(\mathcal{C}) = \frac{1}{3}\left[\sigma_{y+1}(\mathcal{C}) + \sigma_y(\mathcal{C}) + \sigma_{y-1}(\mathcal{C})\right] \tag{4.18}$$

where $\sigma_y(\mathcal{C})$ is given by Eq. (4.9) applied to the slice containing the cell. $\sigma_{y+1}(\mathcal{C})$ and $\sigma_{y-1}(\mathcal{C})$ are given by a similar formula, but replacing 8 in Eq. (4.9) by 9 and summing up over all the neighbors in the lateral slices.

4.5 Numerical results

In this section, we illustrate the evolution of several initial biofilm geometries (flat layers, scattered peaks) under different initial conditions (concentrations, shear stress) in order to analyze the influence of the controlling parameters and the interaction between competing mechanisms. First, the evolution of a biofilm seed for constant biofilm cohesion σ is studied, considering only the growth and erosion mechanisms for different shear and nutrients on either flat or rough surfaces. Next, the adhesion mechanism on uncolonized surfaces is implemented and finally the EPS generation mechanism influence will be analyzed. Notice that all parameter values used to obtain the simulations do not correspond to any specific bacterium neither nutrient choice, since adequate experimental data for parameter calibration are not available yet.

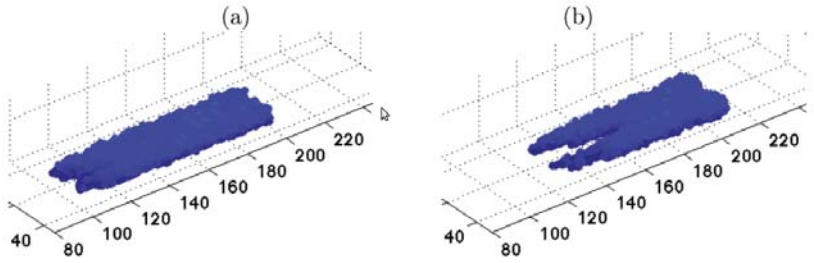

Figure 4.9: *An initially flat and homogeneous biofilm is eroded by the current. Snapshots are taken at steps* $T = 20$ *and* $T = 60$*. After* 200 *steps all the cells have been eroded. Dimensionless parameter values:* $\hat{C}_l = 2.25$, $F_l = 0.04$, $\delta_B = 5$, $\frac{\tau(Re)}{\sigma} = 5$, *and* $\beta = 1$.

The initial bacterial seed in all the tests will be the same for 3D simulations: a small piece of biofilm containing $110 \times 20 \times 4$ cells. 2D simulations are also studied and compared with 3D results. Almost all the simulations start from an initial biofilm seed containing 110×4 cells. We usually fix F_l (which corresponds with to a specific choice of nutrient and bacterium) and analyze the influence of the concentration or the flow. A well-defined qualitative behavior is observed in all the simulations. In order to illustrate properly the observed phenomenology, both 2D or 3D pictures will be used through this section.

The first numerical experiments show the effect of the ratio $\frac{\tau(Re)}{\sigma}$ as a control parameter to observe the influence of the flow. Specific three-dimensional patterns for constant concentrations and $\frac{\tau(Re)}{\sigma}$ ratios appear as a result of two erosion processes observed in the simulations: sloughing of large fragments and smooth erosion of surfaces. When the shear is large enough compared to the biofilm cohesion ($\frac{\tau}{\sigma}$ large) and the limiting concentration is not too high, the initial layer of biofilm remains almost flat and homogeneous while it is slowly washed out (see Fig. 4.9). Cells are eroded from the front, but may grow downstream. Biofilms that are not strong enough have been experimentally observed to be washed out on glass surfaces in Ref. [150]. This happens typically to biofilms created at lower Reynolds number when the shear is increased.

Decreasing the ratio $\frac{\tau(Re)}{\sigma}$ or increasing slightly the concentration, the initial biofilm seeds develop ripplelike patterns that advance downstream with the flow, as in Fig. 4.10. Ripples anchor and become streamerlike struc-

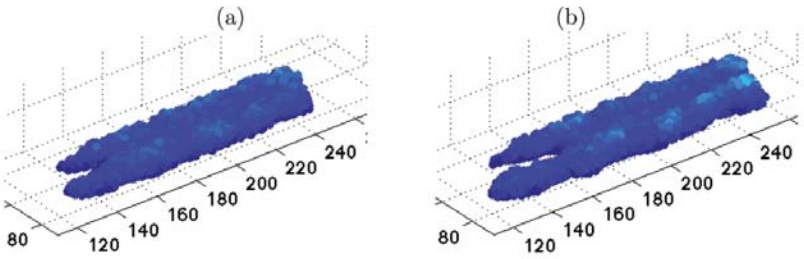

Figure 4.10: *A flat and homogeneous biofilm seed develops ripplelike patterns moving downstream with the flow. Snapshots are taken at steps $T = 50$ (a) and $T = 80$ (b). A peak located at grid position* 200 *clearly migrates to position 220. Same parameter values as in Fig. 4.9 except* $\frac{\tau}{\sigma}(Re) = 2$.

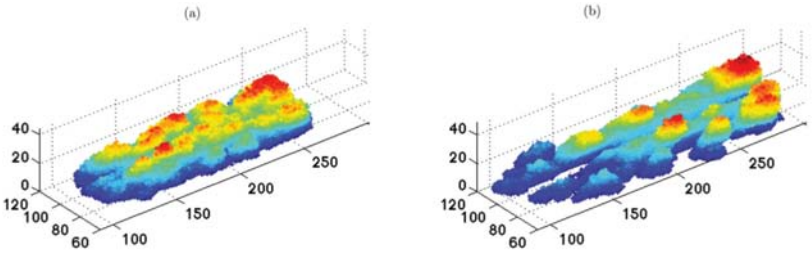

Figure 4.11: *A flat and homogeneous biofilm seed generates streamerlike structures. Same parameter values as in Fig. 4.10 except* $\frac{\tau}{\sigma}(Re) = 1.5$. *Snapshots are taken at steps* $T = 80$ *(a) and* $T = 160$ *(b) (75089 alive cells).*

tures (fingers or peaks elongated in the direction of the flow) for smaller $\frac{\tau(Re)}{\sigma}$ or larger concentrations [see Figs. 4.11 and 4.12(a)]. Fingers that become too large may detach. Ripples travelling downstream on top of lower layers of biofilm have been reported for both laminar and turbulent flows in Refs. [125, 152]. Networks of streamers being eroded and leaving small ripples behind have been experimentally observed in Ref. [125]. Low enough ratios $\frac{\tau(Re)}{\sigma}$ or large enough concentrations lead to networks of mounds or towers separated by voids, as in Figs. 4.12(b) and 4.13, where F_l is increased so that towers are more clearly noticed with fewer cells. Similar patterns are commonly observed in nature in low shear environments (see Ref. [148]).

The evolution of the cellular aggregates reproduced in these three-dimensional simulations includes only growth and erosion processes, but seems to mimic somehow the observed geometric patterns that some biofilms develop in na-

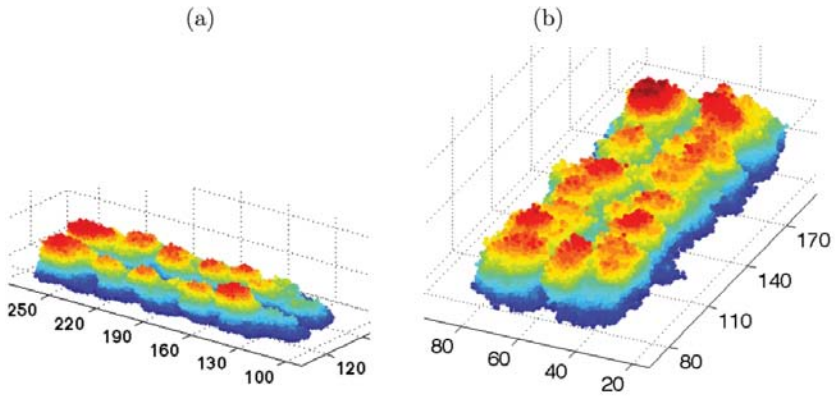

Figure 4.12: *(a) Increasing the outer concentration in Fig. 4.10 streamerlike structures are also found. Snapshot taken at* $T = 80$ *for* $\hat{C} = 3$ *(71 516 alive cells). (b) Further decreasing* $\frac{\tau(Re)}{\sigma}$ *in Fig. 4.11 mounds are generated. Snapshot taken at* $T = 70$ *for* $\frac{\tau(Re)}{\sigma} = 0.5$ *(88 815 alive cells).*

ture. Although the precise mechanisms producing different ripples or streamers observed in real biofilms are (in both laminar and turbulent regimes) uncertain, these results suggest that the mechanical effects derived from the interaction about biofilm mechanical resistance, the bacterial reproduction rate and the erosive effect of shear stress produced by the surrounding fluid are relevant. Cell displacement due to the flow, decay, and cell adhesion should also be considered to gain insight into the processes that trigger real pattern formation.

The patterns which are observed in the simulations depend on the different parameters that can be set in each simulation: F_l, δ_B, $\hat{C}_l$, and $\frac{\tau}{\sigma}$. When only growth processes are taken into account, vertical fingers are formed if the growth dynamics is constrained by the limiting concentration (see Refs. [124, 120]). If a large enough concentration reaches most cells, biofilms tend to be flatter. A wide variety of intermediate regimes may also be observed, going from sorts of dendritic or porous patterns, especially in two dimension simulations. These remarks only apply in static or very slow flows.

These conditions may be reached by modifying some of the key parameters that govern the concentrations, which are shown next:

1. Decreasing F_l reduces nutrient-oxygen uptake by the cells and increases the average values of the limiting concentration field for a fixed biofilm

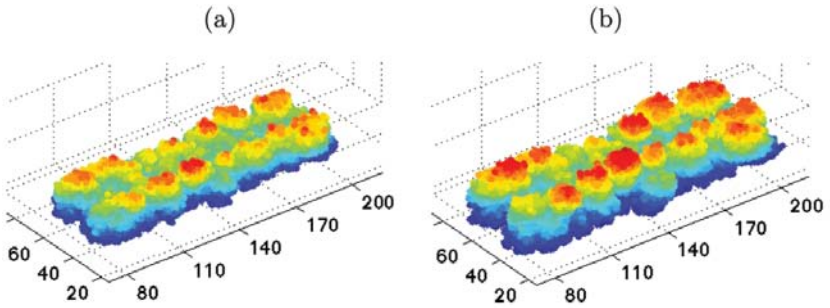

Figure 4.13: *A biofilm seed forms a group of mounds. Same parameter values as in Fig. 4.12(b) except* $F_l = 0.08$. *Snapshots are taken at steps* $T = 70$ *(a) and* $T = 100$ *(b) (63534 alive cells).*

geometry, δ_B and $\hat{C}_l$. F_l depends on the nutrient type and the bacterial species through uptake rates, saturation, and diffusion coefficients. Therefore, for specific choices of bacteria and nutrients is fixed. The threshold concentration to hinder fingering can only be reached if the limiting concentration in the fluid $\hat{C}_l$ is large enough depending on F_l and the biofilm thickness.

2. Decreasing the boundary layer thickness δ_B also increases the concentration field for a fixed biofilm geometry, F_l and $\hat{C}_l$. However, concentrations that are large enough uniformly can only be reached if the limiting concentration in the fluid $\hat{C}_l$ is large enough. In practice, δ_B decreases with the flow velocity. Raising the flow velocity might increase everywhere the concentration field and favor flatter biofilms.

3. Choosing $\hat{C}_l$ large enough depending on the biofilm geometry, F_l and δ_B, the system may end up with flatter biofilms. Their thickness will increase with time, unless we are able to choose a current strong enough to keep them thin. However, that might in turn generate patterns by a different mechanism, or just wash out the biofilm on smooth surfaces.

However, as the ratio $\frac{\tau}{\sigma}$ grows, the erosion mechanism modifies the picture. It may modify or suppress patterns or create additional ones depending on the values of $\frac{\tau}{\sigma}$ and δ_B. Notice that a strong erosion does not require necessary large flows: a weak biofilm cohesion might be enough to allow a slow flow to erode a biofilm structure. In general, the growth rate induced by the available nutrient concentration may reduce or overcome erosion effects as it

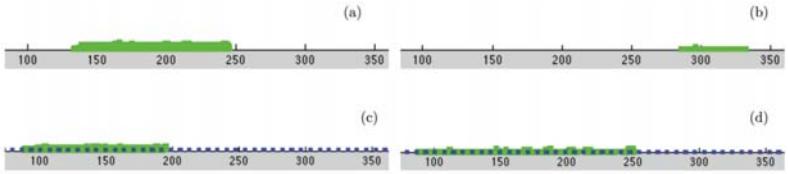

Figure 4.14: *(a), (b) Snapshots showing a biofilm being washed out over a flat substratum for large enough* $\frac{\tau(Re)}{\sigma}$ *. (c), (d) On a rugose surface, with steps characterized by peak height* $\epsilon = 2$*, length* $\lambda = 2$*, and interpeak distance* $\delta = 5$*, the biofilm front is anchored and the biofilm expands colonizing new regions downstream. Dimensionless parameter values:* $\frac{\tau(Re)}{\sigma} = 5$*,* $F_l = 0.04$*,* $\hat{C}_l = 1.5$*,* $\delta_B = 5$*, and* $\beta = 1$*. Time between snapshots: 450 time steps.*

can be seen in Figs. 4.12(a) or 4.18(b).

Two-dimensional simulations produce similar results to three-dimensional simulations although the patterns tend to be more branchy. The numerical parameter thresholds separating flat biofilms, wavy biofilms, mounds, and streamerlike or mushroomlike patterns are shifted. Depending on F_l and $\hat{C}_l$, some of the regimes observed in 3D case as $\frac{\tau}{\sigma}$ is varied may almost vanish in the 2D case.

Roughness adds another variable that interacts with the growth and erosion mechanisms. It is represented by the peaks depicted in Fig. 4.4. Some roughness patterns may prevent the washing out effect described before as $\frac{\tau}{\sigma}$ increases. In Figs. 4.14(c) and 4.14(d), 2×2 square peaks with an interpeak space of five tiles help the biofilms remain attached to surfaces they have already colonized and expand onto neighboring downstream regions. The biofilms are washed out on a smooth surface, see Figs. 4.14(a) and 4.14(b). By reducing the spacing between peaks to two tiles it can be seen a similar behavior with less cells and flatter biofilms, since cells have less space to reproduce. Increasing the spacing to ten tiles, the evolution is similar. However, biofilms contain more biomass since cells have more space to divide and spread. If this spacing increases further, the sheltering effect of roughness decreases. If the depth of the steps increases, nutrients become too scarce to sustain the cell population, hindering biofilm survival. Considering several biofilm peaks as initial data instead of flat layers, a similar evolution is seen. Biofilms are washed out on a flat substratum. Surface roughness of the same order of magnitude as the bacterial size helps the peaks to colonize

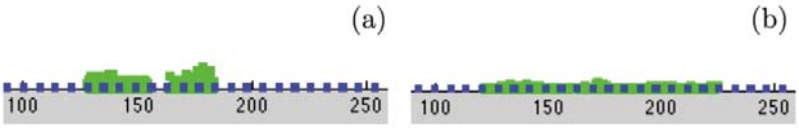

Figure 4.15: *Same as Fig. 4.14 starting from two small colonies, which merge and expand helped by roughness, downstream but also slightly upstream. On a flat substratum they are washed out.*

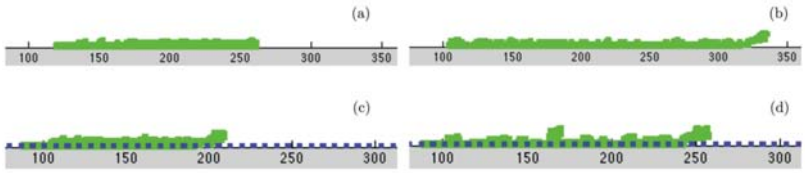

Figure 4.16: *Ripplelike structures form on an initially flat seed: (a), (b) over a flat substratum; (c), (d) on a rugose surface with steps characterized by peak height* $\epsilon = 2$*, length* $\lambda = 2$*, and interpeak distance* $\delta = 5$*. Dimensionless parameter values:* $\frac{\tau(Re)}{\sigma} = 2$*,* $F_l = 0.04$*,* $\hat{C}_l = 1.5$*,* $\delta_B = 5$*, and* $\beta = 1$*. Time between snapshots: 800 time steps.*

neighboring regions and merge, producing more uniform covers, as in Fig. 4.15. Biofilms succeed in expanding upstream. Other roughnesses may have different effects.

Decreasing the ratio $\frac{\tau(Re)}{\sigma}$ a new regime is found in which ripplelike patterns are observed. Newborn cells accumulate downstream, forming ripples and a floating finger at the rear of the biofilm, which eventually reattaches allowing the biofilm to expand downstream [see Figs. 4.16(a) and 4.16(b)]. More limited upstream expansion may also occur. Roughness anchors the front of the biofilm, fostering colonization of downstream regions, as in Figs. 4.16(c) and 4.16(d). Thicker biofilms with more noticeable ripples seem to be formed. Further decreasing $\frac{\tau(Re)}{\sigma}$, fingers aligned with the flow develop, which detach when they surpass a certain size. Figures 4.17(a) and 4.17(b) show the biofilm evolution on a flat substratum. For smaller $\frac{\tau(Re)}{\sigma}$, branchy biofilm towers separated by fluid grow on the initial biofilm, as in Fig. 4.18(a). When $\hat{C}_l$ is increased, mushrooms are more easily formed and become denser and merge for higher values of $\hat{C}_l$, as in Fig. 4.18(b).

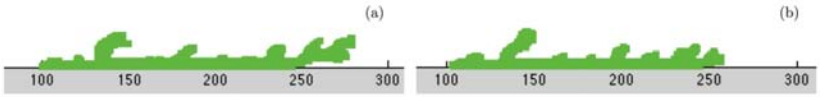

Figure 4.17: *Fingers curved with the flow develop in a biofilm over a flat substratum. (a) Time step $T = 300$. (b) Time step $T = 500$. The trailing finger has eroded, it will grow again later. The biggest finger at the front detached but has grown again. An intermediate finger has also detached, leaving room for another one at its back to grow. Dimensionless parameter values: $\frac{\tau(Re)}{\sigma} = 1$, $F_l = 0.04$, $\hat{C}_l = 1.5$, $\delta_B = 5$, and $\beta = 1$.*

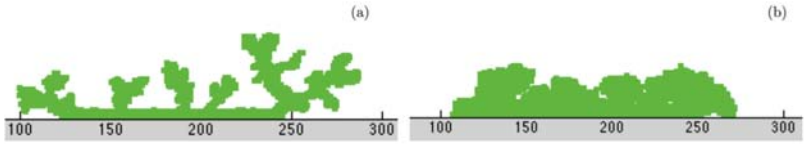

Figure 4.18: *(a) Same as Fig. 4.17 for smaller $\frac{\tau(Re)}{\sigma} = 0.25$. An expanding network of biofilm branches infiltrated with fluid is formed. (b) Same as Fig. 4.17 increasing the limiting concentration to $\hat{C}_l = 2.7$. The biofilm expands forming dense mushrooms separated by narrow channels that eventually merge.*

All the previous numerical simulations set $\beta = 1$ in fig. 4.17. That assumes that cells only feel the influence of the flow in the x direction. The previous simulations have been repeated for $\beta \in (0.9, 0.99)$ finding an increasing chance of long biofilm layers splitting in smaller patches, which may eventually be washed out, and a reduction in the maximum height of the patterns. Otherwise, similar trends are observed provided the concentration is large enough to compensate for the increased erosion. In fig. 4.19(a), an initially flat biofilm seed breaks into separated patches. Increasing the concentration, the biofilm splits in patches that evolve into streamerlike patterns (see fig. 4.19c. Decreasing $\frac{\tau(Re)}{\sigma}$, a stable network of biofilm towers separated by fluid channels develops in fig. 4.19(d).

Figure 4.19(b) shows the effect of roughness, compared to Fig. 4.19(a). In practice, as Re grows turbulent effects may be important and the model should allow for a degree of erosion in the z direction. As Re increases, β(Re) should probably diminish, enhancing erosion by the flow. However, there are

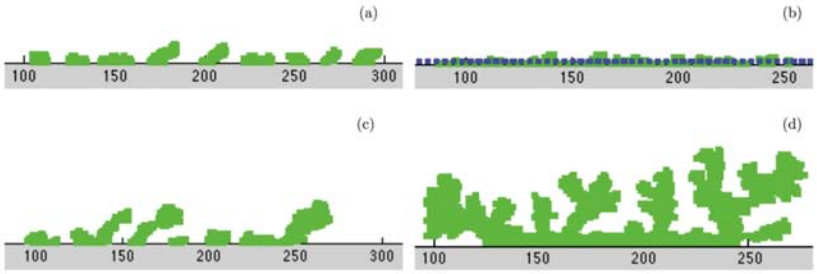

Figure 4.19: *Evolution of a flat biofilm seed when* $\beta \neq 1$. *(a)* $\frac{\tau(Re)}{\sigma} = 2$, $\hat{C}_l = 1.5$, $\beta = 0.99$, $\delta_B = 5$, $F_l = 0.04$, *and* $T = 600$. *The biofilm breaks into patches that generate small peaks. (b) Same parameters as in panel (a) except* $\frac{\tau(Re)}{\sigma} = 5$, *on a rough surface. Fingers are eventually eroded, leaving a thin biofilm behind. (c) Same parameters as in panel (a) with increased* $\hat{C}_l = 1.8$. *Streamerlike structures are formed, which detach when they become too large. (d) Same parameters as in panel (c) with smaller* $\frac{\tau(Re)}{\sigma} = 0.25$. *An expanding network of biofilm branches develops.*

a number of overlapping competing effects with uncertain outcomes. The thickness of the concentration boundary layer $\delta_B(\mathrm{Re})$ should also decrease, augmenting the concentration of nutrients and growth rates thereof. In case floating cells are present, adhesion rates might equally increase with Re, leading to larger biofilm accumulation [39].

An adhesion mechanism was also introduced in the model to check possible effects in biofilm patterns. Figure 4.20 shows the evolution of an uncolonized substratum under a flow carrying nutrients and suspended bacteria. The initial state is the same in all the trials, a clean surface. The densities of bacteria, oxygen, and nutrients carried by the flow are also the same in all the figures. The ratio $\frac{\tau(Re)}{\sigma}$ and the number of attached cells N vary. For high enough adhesion rates the biofilm may cover completely the bottom of the pipe provided the rate of adhesion of bacteria is high enough compared to the erosion effects [see Fig. 4.20(a)]. Biofilm patches form, which eventually merge. After some time, the substratum is fully covered by wavy biofilm layers of increasing thickness. Otherwise, only patches or isolated peaks grow [see Fig. 4.20(b)]. It has been experimentally observed in Ref. [131] that low adhesion rates at low Reynolds numbers lead to patchy configurations (see Fig. 4.3). Larger adhesion rates at larger Reynolds numbers have produced rippled biofilm layers (see Fig. 4.2).

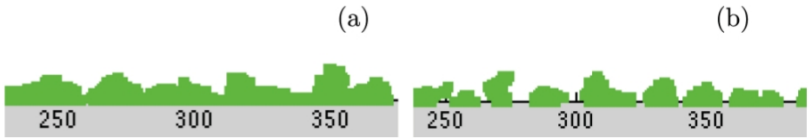

Figure 4.20: *(a) Biofilm growth at large adhesion rates. A wavy biofilm carpet is formed when* $\frac{\tau(Re)}{\sigma} = 2.5$ *and* $N = 80$*. (b) Biofilm grown at smaller adhesion rates. Scattered patches are generated when* $\frac{\tau(Re)}{\sigma} = 1$ *and* $N = 10$*. Other dimensionless parameter values are* $\hat{C}_l = 1.5$*,* $\beta = 0.99$*,* $F_l = 0.04$*, and* $\delta_B = 5$*. Snapshots are taken at time step* 75*.*

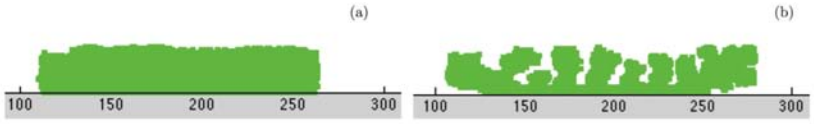

Figure 4.21: *(a) Biofilm for a small boundary layer thickness* $\delta_B = 1$*. A flat biofilm seed evolves into a thickening dense biofilm. (b) Biofilm evolution for an increased boundary layer thickness* $\delta_B = 3$*. A mushroom network develops. Other dimensionless parameter values are* $\frac{\tau(Re)}{\sigma} = 2$*,* $\hat{C}_l = 1.5$*,* $\beta = 1$ *and* $F_l = 0.04$*. Snapshots are taken at time steps* 25 *and* 75*, respectively.*

The length scales in the patterns when erosion effects are low seem to be governed by the average concentration the cells feel. Low concentrations seem to increase the distance between patterns. Raising F_l and δ_B produces that effect. Figures 4.21(a) and 4.21(b) show the effect of δ_B. For small δ_B , flat dense biofilms may be formed [see Fig. 4.21(a)]. Small F_l would have a similar effect. Increasing F_l or decreasing $\hat{C}_l$, protuberances appear again. For larger δ_B , fingers are formed at increasing distances (see Figs. 4.17, 4.18, 4.22(b), or 4.23(a), which includes also adhesion). Figures 4.12(b) and 4.13 illustrate variations in the patterns with F_l . Taking only into account erosion and growth, the boundary layer thickness δ_B is shown in Ref. [62] to control the distance between patterns for fixed F_l . Notice that in Ref. [62], $\tau(\mathcal{C})$ in Eq. (4.10) is set equal to a constant and the resulting fingers do not see the direction of the flow. In static flows, the distance between fingers is shown to increase as the availability of nutrients diminishes in Ref. [124]. Additionally, the erosion mechanism can generate, suppress, or modify

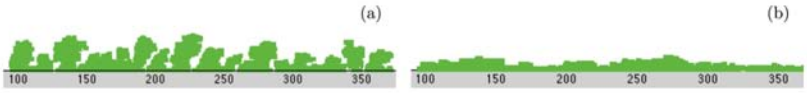

Figure 4.22: *(a) Variations of the boundary layer thickness including adhesion. (a) Biofilm evolution after 50 time steps when* $\delta_B = 3$*. A network of biofilm towers separated by fluid is grown. (b) Biofilm evolution after 50 time steps when* $\delta_B = 7$*. The surface is covered by a wavy carpet of biofilm. Other dimensionless parameter values are* $\frac{\tau(Re)}{\sigma} = 2$*,* $N = 60$*,* $\hat{C}_l = 1.5$*,* $\beta = 0.99$ *and* $F_l = 0.04$*.*

patterns. It can erode and curve the fingers that would grow in the absence of flow or change initial distances between fingers. Some of them may detach when they surpass a certain size, leaving just a few or only one at the end, or they may detach and grow in turn. Adhesion mechanisms further modify the picture; see Fig. 4.22(b), where peaks have been replaced by wavy layers.

In the previous figures, the cohesion parameter σ is set equal to a constant. The remaining figures incorporate the EPS generation mechanism for σ given by Eq. (4.9) in the absence of floating cells. Compare Figs. 4.16 and 4.17 to Figs. 4.23(a) and 4.23(b). Resulting biofilms are more rigid. As $\frac{\tau(Re)}{\sigma_0(Re)}$ is further reduced, biofilm towers are stronger and do not deviate in the direction of the flow [see Fig. 4.23(c)]. In these figures, σ varies locally, depending on the number of bacteria generating the EPS matrix, and the values given to the parameters σ_0 and α, representing the strength of the EPS matrix and standard attached cells of a specific bacteria species. The percentage of cells producing the EPS matrix remains stable during the biofilm evolution and might be used to calibrate σ_0 and α, since this is a parameter that can be measured experimentally in real biofilms. Matrix generation affects growth and local consistency. The thresholds separating different pattern regimes are apparently shifted.

In general, the role of the controlling parameters once the type of bacterium and nutrient is fixed seems to be the following. In the absence of floating cells, the parameter F_l appears to regulate the critical thickness for the biofilm to survive and the regimes for patterns. Small F_l due to small uptake rates may result in mostly flat patterns. Large F_l due to small diffusivities may result in mostly towerlike structures. Once F_l is fixed, δ_B has a similar effect and the ratio between the shear due to the flow and the

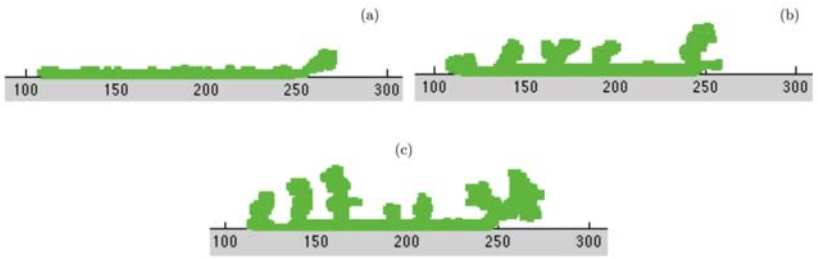

Figure 4.23: *Tests including the EPS generation mechanism. The constant cohesion parameter σ is replaced by a self-adjusted variable cohesion parameter σ given by Eq. (4.9): (a) Small ripples are formed when $\frac{\tau(Re)}{\sigma_0} = 2$ and $R(Re) = 0.4$. (b) Peaks curved in the direction of the flow develop on more compact biofilms when $\frac{\tau(Re)}{\sigma_0} = 0.5$. (c) Vertical towers appear when $\frac{\tau(Re)}{\sigma_0} = 0.25$. The symmetry of the (Re)(Re) pattern shows a decreasing dependence on the flow direction. Other dimensionless parameter values: $\hat{C}_l = 1.5$, $\delta_B = 5$, $\beta = 1$, $F_l = 0.04$, and $T = 150$.*

biofilm cohesion determines the degree of erosion of the biofilm by the flow. It competes with the concentration to determine the patterns. For low concentrations, the system switch from vertical to curved fingers, then ripples, and finally homogeneous biofilms as the ratio of the shear to the biofilm cohesion increases. As the concentration grows, the transition between these regimes occurs at larger ratios. Usually, we end up with a mixture of bacterial towers infiltrated with networks of channels, unless the concentration is too large and bacteria fill all the available space. Adhesion of floating cells may change the pattern regimes. Low adhesion rates may produce patchy biofilms whereas large adhesion rates may generate wavy biofilm layers, depending on erosion and growth. One must keep in mind that biofilm evolution depends on how many mechanisms are relevant in the time scale which is considered and what all the values of the main controlling parameters are.

4.6 Conclusions

A stochastic model is proposed for submerged biofilm growth on rugose surfaces in 2D and 3D. Cell behavior is governed by a set of probabilistic rules. The included behaviors were cell division, spreading, EPS generation, cell detachment, cell deactivation, and adhesion. Different patterns are generated as a result of the collective behavior of cells acting according to those rules,

being able to gain an insight into the interplay of the competing mechanisms considered. Additionally several combinations of mechanisms producing patterns similar to structures observed in real biofilms were identified.

The proposed framework for studying the behavior of cell aggregates is quite flexible and may be used to test mechanisms for cell behavior or may be combined with more refined descriptions of biofilm evolution. The parametric study it has been performed reproduces some qualitative trends already observed in other groups' experiments [126, 125, 150] and in the experiments already shown in this work. This model does not account yet for mechanical processes like cell displacement within the biofilm or movement of biofilm blocks due to external forces, which are thought to be relevant in the formation of real biofilm streamers. A proper calibration of the different numeric parameters to experimental results is needed to perform realistic predictions. Further work on this issue is needed to assess its effect on the observed patterns.

In absence of floating cells, the evolution of a biofilm seed depends on a main set of parameters: the ratio of uptake rates to diffusional supply, the ratio of the shear due to the flow to the biofilm cohesion, the thickness of the concentration boundary layer, and the values of the concentrations in the outer fluid. Erosion and growth mechanisms alone are able to generate biofilm structures moving downstream.

When the nutrient type and the bacterial species are fixed, different patterns are generated as the shear due to the flow or the concentrations of oxygen and nutrients inside the flow vary: networks of ramified towers separated by fluid channels, vertical fingers, streamerlike structures, ripplelike patterns traveling downstream, flat biofilms, and so on. For slow or static flows, fingering is avoided when the limiting concentration reaches easily all biofilm cells.

Erosion affects the growth of fingers: they may deviate in the direction of the flow or their heights may be severely reduced. Thickening flat biofilms may be eroded and kept thin. Strong erosion does not require large flows. Small biofilm cohesion is enough. For most nutrients, by increasing the ratio of the shear due to the flow to the biofilm cohesion a more homogeneous and thinner biofilms are found, which may be eventually washed out, depending on the concentration.

Surface roughness of the same order of magnitude as the bacterial size

may anchor the biofilm and promote its survival and expansion. Other types of roughness may hinder biofilm growth. Roughness also fixes bacteria on the surface, preventing the dragging effect downstream.

Adhesion of floating cells can change qualitatively the nature of the observed patterns. For small adhesion rates, patchy biofilms may be formed on clean surfaces. Nevertheless for larger adhesion rates, wavy uniform covers may appear depending on the remaining parameters.

The insight gained into the influence of different variables in the evolution of biofilms may be useful to control their structure, either to destroy them or to use them to our advantage in different technological, medical, and environmental problems. However, there are many different biofilm systems in which processes of a different nature take place. The experiments performed in chapter 3 and the theoretical model developed refer to one specific bacterial strain (*P.Putida*). Other bacteria which do not behave like *P.Putida* because they have developed other natural strategies to survive in the environment. Moreover, the same bacteria may vary their behavior depending on the flow geometry.

The following chapter addresses a different geometry in which the flow is not straight anymore. We consider a channel with two 90^o turns, and now the flux itself carries a fixed concentration of bacterial cells that attach to surfaces. Now the biofilm is exposed to a flow with net velocity components in the three directions of space, and is also influenced by new incoming cells carried by the flow. The discrete model developed in the current chapter will be modified to take into account the new situation with additional stochastic rules and a more detailed treatment of the flow. Computational results will be contrasted with experimental data gathered from literature.

Chapter 5

Modeling and simulation of biofilm streamers developed under a corner flow

Chapter 4 develops a hybrid model which describes the dynamics of a biofilm attached onto a straight duct. Different patterns arise naturally on the biofilm surface, such as mushrooms, ripples or streamers. But there are many situations in which the fluid flow does not follow exactly a straight profile. Surfaces in nature are usually curved (stones, soil grains, etc.) and human made systems susceptible to be colonized by biofilms (such as cooling systems, pipes, medical devices, etc.) often show changes of directions in order to accomplish their function, turning an eventual straight duct into a complex circuit with lots of changes of directions and bifurcations. This situation involves a variation in the flow hydrodynamics, which forces biofilms to behave in a different way. The biofilm will suffer the effect of a fluid flow which moves in three dimensions. A more general situation arises when we take into account attachment of floating bacteria to surfaces driven by the flow.

The recent development of microfluidics has provided detailed studies of biofilm dynamics in the microscale. For instance, the growth of biofilms in corner microflows is quite well documented [133, 6, 37, 134]. Biofilm formation seems to be triggered by the adhesion of floating cells and other substances released by other bacterial colonies into the flow that act on a faster time scale than growth processes. Notice that biofilms are actually a mixture of living cells embedded in a exopolysaccharide matrix (EPS) which contains many different kind of metabolic by-products, generically named *"biomass"*: in fact, biofilm streamer formation may be included in a more general group

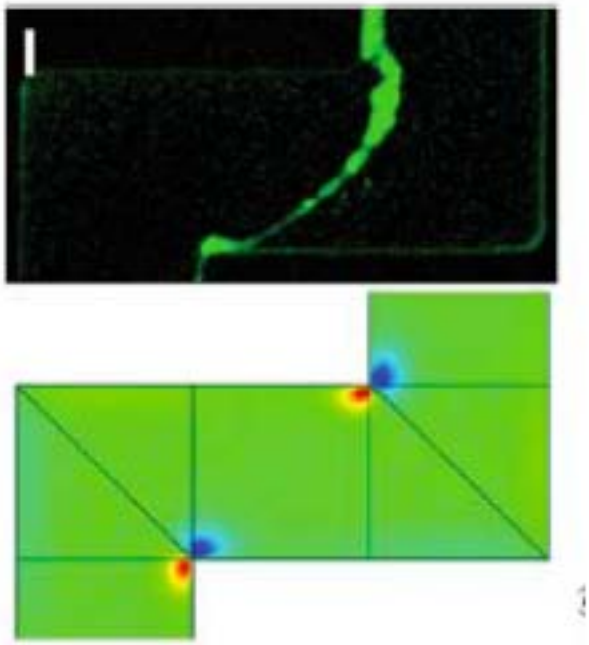

Figure 5.1: *(Up) Biofilm streamer matching both corners in the channel. Image taken with a confocal microscope. (Down) Numerical simulations of the secondary flow raising these structures in a curved channel. Pictures taken from [134]*

of physical processes where adhesion mechanism drives an agglomeration process of matter to create different geometries. So the mechanical properties of the biomass (living cells, EPS, debris) and the adhesion mechanisms of suspended particles blocks driven by the flow seems to be relevant, allowing the growth of the streamer to the opposite corner crossing the streamlines, see Figure 5.1. The situation is quite different from the interaction of already grown elastic biofilm filaments with fast flows investigated numerically in [155].

In this chapter a hybrid model that combines a discrete description of the biomass with the continuous descriptions of external flow and concentration fields is presented and adapted to the geometry of corner microflows. Stochastic rules are formulated for biomass adhesion, erosion, motion and cell division (similar to those described in chapter 4) informed by the continuous fields, that are approximated using a finite difference discretization

strategy designed to reduce the computational cost. Recall again that the growing biofilm (biomass) is considered as a mixture of cellular aggregates (living cells) and a generic material (EPS, debris,etc.) with known cohesive properties.

The chapter is structured as follows. Section 5.1 describes the hybrid model. Section 5.2 states the equations for the continuous flow and concentration fields. Section 5.3 details the discretization procedure. Section 5.4 collects the rules for biomass behavior. Section 5.5 illustrates the numerical results and discusses the insight gained on biofilm formation. Section 5.6 summarizes the chapter with some conclusions.

5.1 Hybrid description of biofilms in microflows

Hybrid models combine discrete descriptions of the biomass with continuous descriptions of additional relevant fields. From a computational point of view, biomass is considered as a mixture of bacteria and organic matter allocated on a grid which may behave in different ways in response to external conditions with a certain probability. The external factors that influence their behavior are typically the flow conditions and the availability of oxygen and nutrients for bacteria, that are continuous fields governed by partial differential equations. The status of these fields at the tile location determine whether biofilm particles are going to attach, detach, reproduce or move, with a certain probability. The true mechanisms for these behaviors being yet largely unknown, the probability rules are motivated by observations of biofilm behavior, and may be updated in the measure more biological information becomes available. Additional factors such as quorum sensing or EPS generation are neglected here. The biofilm cohesion resulting of EPS generation is assumed to be uniform and known. The growing biofilm is seen both as an aggregate of cells and a material with cohesive properties.

In a microflow setting, the basic length scale is taken to be the average size of one bacterium, which is of the order of microns: 1-2 $\mu\, m$. Each tile of the computational grid has that size, and can be filled with either fluid, solid substratum or biomass cluster. As model case of study the growth of streamers in corner microflows is fixed, that is well documented experimentally [134, 133, 37]. The computational region is described in Fig. 5.2. A pressure driven flow circulates through the ducts with maximum velocities of about 1 mm/s. The central straight fragment is $N \times M \times L\ \mu\, m$. Stream-

ers grow mostly in the $N/3 \times M \times L$ μm region between corners. In real experiments, usual values for N,M and L are 600, 200 and 100 μm. In the numerical tests selected here, those sizes are divided by 2 to reduce the computational cost.

An initial biofilm seed is placed on the left corner at the bottom, see Figure 5.2. According to [58, 133], the presence of secondary vortices in that area favors adhesion of particles to the wall, becoming a preferential adhesion site. Biomass will be attached to that seed, eroded, moved or divided according to stochastic rules described below. These rules for biomass behavior use the values of flow fields outside the aggregate and the values of nutrient and oxygen concentration fields everywhere.

5.2 Continuous fields

In a biofilm, bacteria evolve in response to environmental conditions, such as the availability of nutrients and oxygen or the flow regime. Let us denote by Ω_f the region occupied by fluid and by Ω_b the region occupied by biofilm. The surrounding fluid is governed by the incompressible Navier-Stokes equations:

$$\rho \mathbf{u}_t - \mu \Delta \mathbf{u} + \mathbf{u} \cdot \nabla \mathbf{u} + \nabla p = 0 \quad \mathbf{x} \in \Omega_f, t > 0 \tag{5.1}$$

$$\operatorname{div} u = 0 \quad \mathbf{x} \in \Omega_f, t > 0 \tag{5.2}$$

where $\mathbf{u}(\mathbf{x}, t)$ is the velocity and $p(\mathbf{x}, t)$ the pressure. ρ and μ stand for the density and viscosity of the fluid. The non-slip condition on the velocity holds at the biofilm/fluid interface Γ.

For aerobic bacteria the evolution of the concentrations of nutrients and oxygen must be controlled[130]. One of them becomes usually the limiting concentration $c(\mathbf{x}, t)$, that is, the one restricting cell growth. The concentration is advected by the fluid velocity outside the biofilm, and diminishes inside the biofilm due to a nonlinear source term representing cell consumption. It evolves with time according to:

$$c_t(\mathbf{x}, t) - D_f \Delta c(\mathbf{x}, t) + \mathbf{u} \cdot \nabla \mathbf{c} = 0 \quad \mathbf{x} \in \Omega_f, t > 0, \tag{5.3}$$

$$c_t(\mathbf{x}, t) - D_b \Delta c(\mathbf{x}, t) = -k \frac{c(\mathbf{x}, t)}{c(\mathbf{x}, t) + K} \quad \mathbf{x} \in \Omega_b, t > 0. \tag{5.4}$$

D_f and D_b represent the diffusivities of the limiting concentration in the fluid and biofilm, respectively. k is the uptake rate of the selected limiting

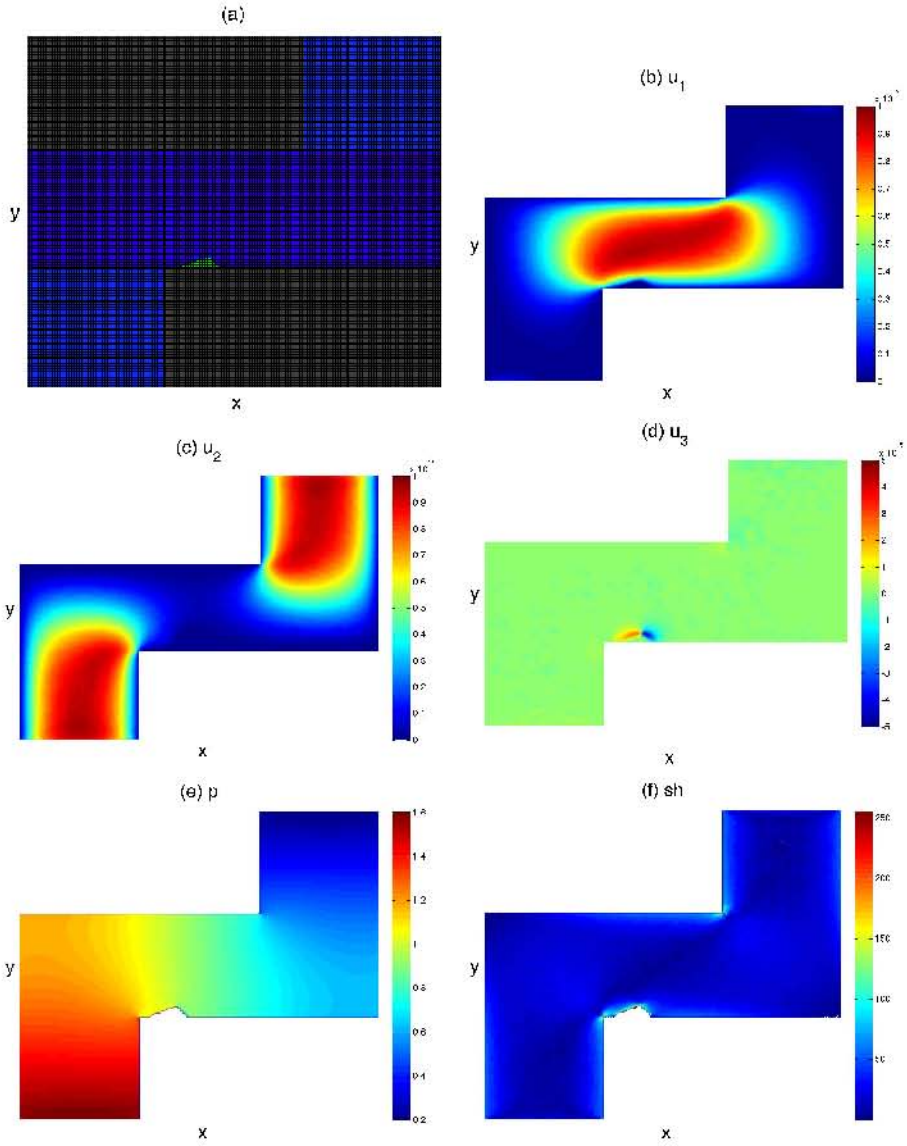

Figure 5.2: *Initial status of a central slice of the tubes: (a) Computational grid. (b),(c),(d) Velocity components around the initial biofilm seed. (e) Pressure field. (f) Shear rate.*

concentration for the chosen bacteria. K is the half-saturation concentration. The source term $r(c) = k\frac{c}{c+K}$ is a Monod law. It should be corrected incorporating inhibition terms if concentrations became too large. At the biofilm/fluid interface, transmission conditions (continuity of concentrations and fluxes) are imposed.

A procedure to approximate numerically these velocity and concentration fields in our grid framework is described in the next section.

5.3 Discretization of the continuous fields

The velocity and pressure fields will be approached first. We intend to compute the evolution of biofilms for a relatively long time. Since velocities and pressures have to be approximated each time the biofilm boundary is slightly moved, a reasonable compromise between precision and computational cost is required.

The cubic grid of bacterial size step provides a basic discretization mesh. This suggests resorting to finite difference schemes to avoid the cost of remeshing the fluid domain any time the biofilm boundary changes. It could be inserted in this primitive mesh finer cubic meshes if required. However, in practice, only the average values of the flow fields in the original cubic tiles are needed by our bacterial cells.

Now nondimensionalization of the equations is performed by setting $x' = \frac{x}{X}$, $\mathbf{u}' = \frac{\mathbf{u}}{U}$, $t' = \frac{tU}{X}$, where U is the maximum velocity in the tubes before the biofilm starts to grow. There are several choices for X. Here X is taken to be the size of one bacteria, that is, the size of the grid tiles. The spatial step dx in this length scale becomes one. The dimensionless pressure is $p' = \frac{p}{U^2\rho}$. The resulting Reynolds number $Re = \frac{XU\rho}{\mu} << 1$ for the flows which are considered, with $\rho \sim 10^3 \frac{Kg}{m^3}$, $\mu \sim 10^{-6}\, Pa \cdot s$, $X \sim 10^{-6}\, m$ and $U \sim 10^{-3} \frac{m}{s}$. For computational purposes is convenient to work with the rescaled time $t'' = \frac{t'}{Re\, dx^2}$.

From now on the primes are dropped for ease of notation and work with dimensionless variables. The velocity and pressure of the fluid around the initial biofilm seed are the stationary laminar fields computed using a standard finite element package. They are stored as initial data for the finite difference evolution.

A low cost prediction of the evolution of the velocity and pressure fields

is provided by second order slight artificial compressibility schemes [23, 86]. The basic scheme is:

$$\frac{\mathbf{u}^{\ell+1}-\mathbf{u}^{\ell-1}}{2dt}+\mathbf{u}^{\ell}\cdot\nabla\mathbf{u}^{\ell}=-\nabla p^{\ell}+\frac{1}{Re}\Delta\mathbf{u}^{\ell}$$
$$\frac{p^{\ell+1}-p^{\ell-1}}{2dt}=-c_0^2\mathrm{div}\mathbf{u}^{\ell}.$$

The superscript m denotes the value of the fields at time $t^{\ell}=t_0+\ell\,dt$, dt being the time step. The spatial derivatives may be discretized with centered finite differences on the standard grid or a staggered grid [23, 86]. Changes in the flow around the initial biofilm seed are very slow. So at each stage, few cells have attached or detached. Hence, this may be considered a quasi-steady evolution driven by the slow changes in the biofilm boundary. With the velocity of the interface being much smaller than the fluid velocity, the velocity of the fluid on the biofilm boundary is set to be equal to zero anytime the flow is updated around it.

The above prediction of velocities and pressures can be improved using second order implicit gauge schemes [167, 86], if necessary, at a higher cost. The velocity field is split as $\mathbf{u}=\mathbf{a}-\nabla\phi$, for a gauge variable ϕ. The field $\mathbf{a}$ satisfies:

$$\mathbf{a}_t+\mathbf{u}\cdot\nabla\mathbf{u}=\frac{1}{Re}\Delta\mathbf{a}$$

and the gauge variable ϕ:

$$\Delta\phi=\mathrm{div}\,\mathbf{a}.$$

zero Neumann o Dirichlet boundary conditions can be chosen for $\mathbf{a}$ at the wall of the tubes and the biofilm/fluid interface:

$$\frac{\partial\phi}{\partial\mathbf{n}}=0,\quad\text{or}\quad\phi=0.$$

This yields boundary conditions for $\mathbf{a}$:

$$\mathbf{a}=\mathbf{u}_{\text{walls}}+\nabla\phi.$$

The initial distribution for ϕ is obtained solving:

$$-\frac{1}{Re}\Delta\phi=p,$$

with the selected boundary conditions for ϕ, p being the initial pressure distribution around the initial biofilm seed.

In this new framework, $\mathbf{a}$ and ϕ are calculated as the biofilm evolves by means of an iterative scheme [167, 13]. $\mathbf{a}$ is updated first:

$$\frac{\mathbf{a}^{\ell+1}-\mathbf{a}^{\ell}}{dt}+\mathbf{u}^{\ell+1/2}\cdot\nabla\mathbf{u}^{\ell+1/2}=$$
$$\frac{1}{Re}\Delta(\mathbf{a}^{\ell+1}+\mathbf{a}^{\ell}),\mathbf{a}^{\ell+1}=\mathbf{u}_{\text{walls}}^{\ell+1}+\nabla(2\phi^{\ell}-\phi^{\ell-1}).$$

By extrapolation, $\phi^{\ell+1}$ is approximated above as $2\phi^{\ell}-\phi^{\ell-1}$. $(\mathbf{u}\cdot\nabla\mathbf{u})^{\ell+1/2}$ is also evaluated by extrapolation: $(\mathbf{u}\cdot\nabla\mathbf{u})^{\ell+1/2}=3/2(\mathbf{u}\cdot\nabla\mathbf{u})^{\ell}-1/2(\mathbf{u}\cdot\nabla\mathbf{u})^{\ell-1}$.

Next, ϕ is updated :

$$\Delta\phi^{\ell+1}=\operatorname{div}a^{\ell+1},$$

with the selected zero boundary conditions at the walls. The spatial derivatives may be discretized using centered differences in a standard grid. However, if Dirichlet conditions are chosen for ϕ, is convenient to discretize divergences and gradients so that the discrete divergence of the discrete gradients agrees with the discrete laplacian. This means forward approximations for gradients of ϕ and backward approximations for divergences of $\mathbf{a}$. If Neumann boundary conditions are chosen for ϕ, a unique solution is selected imposing zero mean.

To compute $\mathbf{a}^{\ell+1}$ and $\phi^{\ell+1}$ two linear systems must be solved. To avoid relabelling all the unknowns to write the equations in matrix form, some iterative relaxations schemes are used. Convergence is quite fast since the solutions change very little from one stage to the next. At the end of the time step, the velocity and the pressure in the fluid are defined by:

$$\mathbf{u}^{\ell+1}=\mathbf{a}^{\ell}-\nabla\phi^{\ell+1},\quad \phi^{\ell+1/2}=\frac{\phi^{\ell+1}-\phi^{\ell}}{dt}-\frac{1}{2Re}\Delta(\phi^{\ell+1}+\phi^{\ell}).$$

The values of the fluid pressure and stresses are needed to be known at the biofilm/fluid interface. They are computed by extrapolation from values inside the fluid:

$$s_0=3s_1-3s_2-s_3.$$

Artificial compressibility schemes handle easily slowly moving interfaces. Gauge schemes may have some trouble with them because ϕ tends to concentrate large gradients at interfaces and walls. This effect worsens as the size of the computational region and the pressure increase. This may produce larger errors at the fluid/biofilm interface any time it is moved. Therefore, anytime the interface is moved, first artificial viscosity schemes are applied to obtain a few corrections of the flow around the object, and then use the gauge method to refine those corrections.

Discretizing the equations for the concentration is much simpler. Concentration equations are nondimensionalized setting $x' = \frac{x}{X}$, $c' = \frac{c}{K}$, $\mathbf{u}' = \frac{\mathbf{u}}{U}$ and $t' = \frac{tU}{X}$ to obtain (dropping the primes):

$$\frac{UX}{D_f}(c_t(\mathbf{x},t) + \mathbf{u}\cdot\nabla\mathbf{c}) - \Delta c(\mathbf{x},t) = 0 \quad \mathbf{x}\in\Omega_f, t>0, \tag{5.5}$$

$$\frac{UX}{D_b}c_t(\mathbf{x},t) - \Delta c(\mathbf{x},t) = -\frac{kL^2}{KD_b}\frac{c(\mathbf{x},t)}{c(\mathbf{x},t)+1} \quad \mathbf{x}\in\Omega_b, t>0. \tag{5.6}$$

A common explicit finite difference scheme for heat equations works. The velocity is already computed using the schemes describe above. For Pseudomonas strains and standard nutrients, the diffusion coefficients D_f, D_b are usually of order $10^{-9}\ \frac{m^2}{s}$. X has been set equal to the bacterial size, of order $10^{-6}\ m$. In corner microflow experiments U is about $10^{-3}\ \frac{m}{s}$. Therefore, the coefficients $\frac{UX}{D}$ are expected to be of order one (or smaller, for smaller U). The parameter $F = \frac{kX^2}{KD_b}$ is analogous to the Thiele modulus and measures the ratio of the uptake rate to the diffusional supply. It governs the chemistry of the system, in the same way the Reynolds number Re controls the flow. Typical values for bacteria commonly used in flows, like Pseudomonas Aeruginosa or Pseudomonas Putida, and standard nutrients produce values in the range $10^{-8} - 10^{-2}$.

5.4 Stochastic rules for cell behavior

Biomass attach, detach, move, divide and spread according to the concentration and flow fields they feel at their location. Floating biomass is carried by the fluid. The flow characteristics select preferential adhesion sites on the walls where biofilm seeds may be nucleated [134, 133]. Biofilm nucleation may be successful or not depending on the surface nature and the bacterial strain. The flow also determines the strength of the biofilm [88, 150]. Once

a biofilm seed is formed, biomass accumulation is a balance between cell increase due to adhesion and growth processes, and loss of biomass due to erosion [151]. The flow shapes the biofilm [37, 151], not only by determining transport and diffusion of nutrients inside the biofilm, and bacterial growth thereof, but also by carrying new floating biomass particles that attach to it, by detaching fragments, and by moving blocks [6, 37, 151]. Biomass variations due to adhesion and erosion take place on a faster time scale than growth processes [37].

We describe below the stochastic rules for adhesion, erosion, motion and growth processes, having in mind the model case of bacterial streamers in laminar corner microflows.

5.4.1 Adhesion

Biomass carried by the flow that hit a surface may attach to it [88]. In a laminar corner flow, cells are driven to the walls by small vortices at corners [58]. Once a biofilm seed is sticking out from the wall, bacteria and particles swimming with the flow may hit it, and stick to it at a certain rate [37]. There seem to be several overlapping adhesion mechanisms driven by the flow.

Continuous adhesion of biomass at the corner region is taken care of by attaching N_s biomass tiles at each step at the seed surface, inside a limited region where the vortices are expected to be relevant. The new cells are distributed between the tiles located at the seed/fluid interface giving more probability to the sites with more neighboring tiles already occupied by biomass. Later, attached biomass particles will eventually be eroded or moved by the erosion or motion mechanisms.

At each step, N_b biomass particles are attached to the biofilm surface sticking out from the corner, as in [130]. Again, the new particles are distributed between the tiles located at the seed/fluid interface giving more probability to the sites with more neighboring tiles already occupied by those. A hanging biomass particle does not seem as likely as a biomass particle sustained by several neighbors for the successful adhesion of a new tile.

The adhesion policy can be modified to attach more biomass at the back of the biofilm (more protected from the flow, where streamlines merge, particles carried by them may concentrate and be sheltered) or to attach biomass following a wavy probability profile representing a non uniform distribution

of biomass in the flow (flocks of bacteria).

N_s and N_b depend on the density of biomass particles floating in the fluid. N_s is affected by the likeliness of the specific bacterial strain selected to adhere to the material the walls are made of.

5.4.2 Erosion

Biomass tile $\mathcal{C}$ located on the surface of the biofilm may detach due to shear forces exerted by the flow [125, 151]. A probability for biomass detachment was proposed in [62]:

$$P_e(\mathcal{C}) = \frac{1}{1 + \frac{\gamma}{\tau(\mathcal{C})}} = \frac{\tau(\mathcal{C})}{\tau(\mathcal{C}) + \gamma}. \tag{5.7}$$

γ is a measure of the biofilm cohesion. It is assumed to be known, and constant. $\tau(\mathcal{C})$ measures the shear force felt by tile $\mathcal{C}$. It was taken to be constant in [62], resulting in fingers that do not see the direction of the flow. Here, the magnitude of the shear force due to the flow at the tile location $\tau_f(\mathcal{C})$ is used, but modified by a geometrical factor that accounts for the local sheltering role of neighboring tiles [130]:

$$\tau(\mathcal{C}) = \tau_f(\mathcal{C})(1 - \beta\chi_1(\mathcal{C}))(1 - f(\mathcal{C})). \tag{5.8}$$

$\tau_f(\mathcal{C})$ in our numerical experiments is usually set equal to the shear rate at location $\mathcal{C}$ multiplied by the fluid viscosity μ. The shear rate is defined as the rate of change of shear stress [47]:

$$\sqrt{\frac{1}{2}\big((4u_1^2 + 4u_2^2 + 4u_3^2) + 2(u_1 + u_2)^2 + 2(u_1 + u_3)^2 + 2(u_2 + u_3)^2\big)}.$$

As for the geometrical factor, it varies according to the main component of the flow. For the component in the x direction:

$$f(\mathcal{C}) = \frac{1}{2}f_y(\mathcal{C}) + \frac{1}{4}(f_{y+1}(\mathcal{C}) + f_{y-1}(\mathcal{C})), \tag{5.9}$$

$$f_{y-1}(\mathcal{C}) = \frac{1}{19}\sum_{i=9}^{17} w_i\chi_i((\mathcal{C}), \quad f_{y+1}(\mathcal{C}) = \frac{1}{19}\sum_{i=18}^{26} w_i\chi_i((\mathcal{C})), \tag{5.10}$$

$$f_y(\mathcal{C}) = \frac{1}{17}\sum_{i=2}^{8} w_i\chi_i((\mathcal{C})). \tag{5.11}$$

Each fixed tile of the grid has 26 neighbors n_i, numbered starting with the y-slice that contains the tile. Inside each slice, neighbors are numbered

clockwise, beginning with the one in the negative x direction. $\chi_i((\mathcal{C})$ is equal to 1 when the $i-$th neighbor location of biomass tile $\mathcal{C}$ is occupied by a biomass tile, and vanishes otherwise. $w_i \in (0,1)$ are weights that depend on the neighbor location, satisfying the restriction $f(\mathcal{C}) \leq 1$ not to reverse signs. $\beta \in (0,1)$ is the sheltering weight assigned to the neighbor in the negative x direction, taken usually equal to 1. To check erosion effects by the y and z components of the flow, this geometrical factor is changed accordingly. In practice, erosion in the three directions are checked.

At each step and for each biomass tile on the biofilm boundary, a random number $r_1 \in (0,1)$ is generated. When $r_1 < P_e(\mathcal{C})$, the biomass tile detaches from the biofilm. Erosion due to the flow may occur as detachment of single cells or of whole clusters of biomass with a thinning connection to the rest of the biofilm. After eroding biomass, the connectivity of the final aggregate is checked and all the biomass clusters with no connection to the wall are removed.

5.4.3 Motion

Shear forces exerted by the flow on the biofilm surface are believed to detach biomass. Normal forces on biomass surface may move them. The motion of a biofilm block may be seen as the result of the collective motion of individual biomass tiles or small fragments of the aggregate.

Probabilities for biomass motion in the x, y, z directions are defined as follows:

$$P_x(\mathcal{C}) = \frac{1}{1+\frac{\gamma}{|F_x(\mathcal{C})|}} = \frac{|F_x(\mathcal{C})|}{|F_x(\mathcal{C})|+\gamma}, \tag{5.12}$$

$$P_y(\mathcal{C}) = \frac{1}{1+\frac{\gamma}{|F_y(\mathcal{C})|}} = \frac{|F_y(\mathcal{C})|}{|F_y(\mathcal{C})|+\gamma}. \tag{5.13}$$

$$P_z(\mathcal{C}) = \frac{1}{1+\frac{\gamma}{|F_z(\mathcal{C})|}} = \frac{|F_z(\mathcal{C})|}{|F_z(\mathcal{C})|+\gamma}. \tag{5.14}$$

γ is again a measure of the biofilm cohesion. F_x is the force exerted by the flow in the x direction (on cell walls normal to the x direction) weighted with a geometrical factor accounting for neighbor protection similar to the one used in 5.4.2. F_y and F_z are its counterparts in the y and z direction. The forces are calculated using the values of the fluid stress tensor σ at the biomass tile location: $\sigma \cdot \mathbf{n}$ for the chosen normal vector $\mathbf{n}$.

At each step and for each biomass tile on the biofilm boundary, random numbers $m_1, m_2, m_3 \in (0, 1)$ are generated. When $m_1 < P_x(\mathcal{C})$, the tile moves in the x direction and pushes its neighbors in that direction too. When $m_2 < P_y(\mathcal{C})$ or $m_3 < P_z(\mathcal{C})$, the cell moves in the y or z directions and pushes its neighbors in those directions too. Motion is in the positive or negative sense depending on the signs of F_x, F_y, F_z. In practice, for the flows under study, motion seems to be driven by the variations of pressure between biofilm walls. The contribution of the velocity seems to be small because of its small values and the small viscosity.

5.4.4 Growth

Alive cells in the biomass $\mathcal{C}$ will divide with probability [62]:

$$P_d(\mathcal{C}) = \frac{c(\mathcal{C})}{c(\mathcal{C}) + K}, \tag{5.15}$$

where c denotes the limiting concentration and K its half-saturation coefficient in the Monod law. The concentration is previously computed as described in Section 5.2 and stored before the division status of all alive cells is checked. The effect of newborn cell consumption is neglected at this stage.

For each cell a random number $d \in (0, 1)$ is computed. When $d < P_d(cell)$, the cell divides. The daughter cell is allocated in any of the empty adjacent grid tiles with equal probability. If all are occupied, the newborn cell will shift one of the neighbors. There different strategies to implement this idea. Here, the cell offering the smallest mechanical resistance is chosen, that is, the one lying in the direction of shortest path from the reproducing cell to the interface biofilm/fluid. The shifted cell should be moved following the same rule: it fills empty neighboring tiles with equal probability or shifts adjacent cells in the direction of minimal mechanical resistance. The process is iterated until all displaced cells have been accommodated.

5.4.5 Time scales

Flow effects are felt by the biofilm in shorter time scales than growth effects [37]. The stochastic rules (section 5.2) are coupled to the continuous fields in the following way. At each basic step, the adhesion, erosion and motion processes described in subsection 5.4.1 are implemented, see subsections 5.4.2 and 5.4.3. The erosion probabilities at the biofilm surface are checked and the cells and fragments to be detached are removed. Then, the probabilities for biomass motion are calculated, displacing the affected tiles and their

neighbors. Finally, the specified number of new biomass tiles are attached onto the surface of the biofilm. Once the new biofilm shape is calculated, the continuous fields are updated by solving the equations (5.1) and (5.3)-(5.4) using the discretizations described in 5.3. At a time τ, the process is repeated. τ may be seen as some kind of average successful adhesion time. This is done until times of order of the minimum doubling time $T = \frac{\ln(2)}{\nu_{max}}$ are reached, where ν_{max} is the growth rate for the selected bacterial strain and nutrient source (in the range of 20 min). At time T the division status of all alive biofilm cells is checked and newborn cells are allocated.

5.5 Numerical simulations

Numerical tests of biofilm growth have been performed using the model geometry described in section 5.1. The results for sizes $N = 300\ \mu\, m$, $M = 100\ \mu\, m$ and $L = 50\ \mu\, m$, half usual experimental sizes is discussed below. A pressure driven flow with maximum velocity of order 1 $\frac{mm}{s}$ circulates through the ducts. The density of the liquid is $10^3\ \frac{Kg}{m^3}$ and its viscosity $\mu = 10^{-3}\ Pa \cdot s$. The bacterial size, and the tile size thereof, is taken to be $2\,\mu\, m$. γ is a measure of the biofilm cohesion that might be estimated from the biofilm Young modulus. Values in the range $70 - 140\ Pa$ are given in [133]. To reduce the computational cost, it is adjusted so that the biofilms involve a small number of cells. For a particular choice of nutrient and bacteria, $T = \frac{\ln(2)}{\nu_{max}}$. In [37] the doubling time is about 6.5 hours. The adhesion time τ can be estimated from images in [133] to be about 1 bacteria per second. Each step of the adhesion-erosion-motion motion process occurs in a time scale τ. In step of the growth process takes place on a time scale T.

As long as enough biomass tiles are attached to the seed (to avoid detachment of the streamer) and the biofilm 'body' (to resist increasing erosion while crossing the current), the biofilm is seen to grow into the current, elongate with it, bend when it reaches the curve, approach the opposite corner, and merge with the additional biofilm seed that should be growing there. Figure 5.3 shows a successfully grown streamer after 12600 steps of the adhesion-erosion-motion process. One step of the growth process doubles its size, see Figure 5.3(c).

The biofilm grows into the region of minimum shear rate, that joins the two corners. Once it is formed, pressure variations move the thread downstream, curving it in a similar way to the threads observed in the experiments and leaving a thin joint with the seed. It reaches the opposite corner from

behind, at it seems to happen in the experimental photographs [134]. The observed effective adhesion rate is the balance between the biomass tiles that attach and detach at each step, and varies during biofilm growth. It is usually larger before the biofilm tries to cross the main stream and decreases as it tries to reach the opposite corner while changing its shape.

The number of biomass tiles to be computationally attached depends on the selected biofilm cohesion. Too large N_a produce expanding balls. Too small adhesion rates N_a to the streamer body produce an elongated thread close to the wall, that eventually feels the corner flow and eventually starts to gain cells on the top, but may not receive enough biomass tiles to survive the increased erosion and detaches, see Figures 5.4 (b) and (c). Small adhesion rates N_s at the seed break off the connection between streamer and seed, see Figure 5.4 (a). Too large adhesion rates N_s at the seed favor expansion parallel to the bottom substratum. If N_a is not large enough for the selected cohesion, the biofilm reaches the rightmost wall as shown in Figure 5.5 (a). It thickens when growth effects become relevant and expands over the bottom, unable to cross. Increasing N_a, the biofilm may cross to the opposite corner sustained by a wide basis. Depending on the ratio of N_a to N_s for the selected γ, narrower or wider streamers that open like fans over the corner are seen.

When the cohesion parameter γ is increased the computational adhesion rates N_a and N_s must be reduced to see similar behaviors. The failed streamer in Figure 5.5 (a) crosses successfully to the opposite corner sustained by a wider basis when γ is slightly increased in Figure 5.5 (b), (c).

If the biofilm cohesion is too small, the biofilm seed is eroded and eventually washed out. No biofilm grows. If the initial adhesion rates are large enough for the considered cohesion, a sort of fan expands into the main stream, see Figure 5.5. The fan becomes narrower as the adhesion rates are reduced.

Growing similar streamers in a region with dimensions $n = 600\ \mu m$, $m = 200\ \mu m$ and $\ell = 100\ \mu m$ would involve about 35000 biomass tiles and 46000 steps of the adhesion-erosion-motion process. For effective adhesion rates of a one biomass tile per second, that corresponds to a time of 12 hours, within the experimental range.

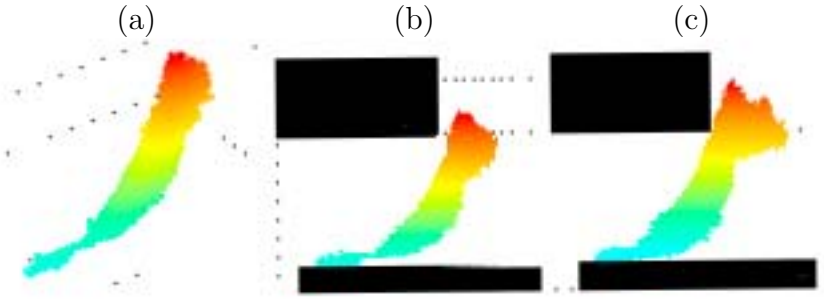

Figure 5.3: *Streamer grown for* $\gamma = 15\,Pa$ *at step* 12600 *of the adhesion-erosion-motion process.* $N_s = 1$ *around the initial seed and* $N_a = 4$ *along the biofilm body. The biofilm is merging with another seed growing at the opposite corner, which has been ignored in the plot: (a) front view, (b) side view, (c) thickening of the biofilm after one step of the growth process. when the outer limiting concentration is* $C = 0.75K$*,* K *being the half-saturation rate for the limiting concentration. The number of biomass tiles increases from* 4611 *to* 8058*. Iterating the procedure, the duct eventually clogs. The distance between dotted lines is 40* μm*.*

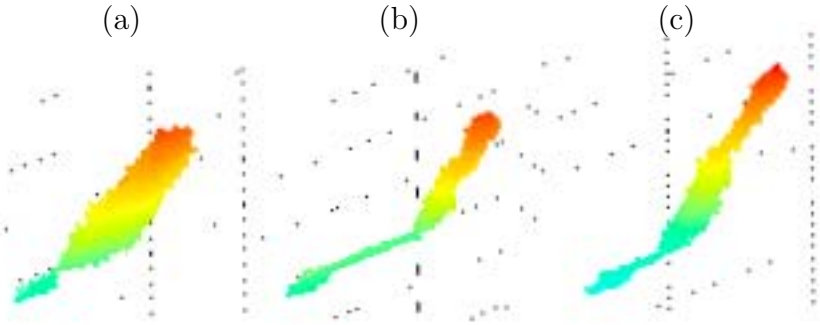

Figure 5.4: *Varying the number of attached cells, streamers fail to reach the corner. They detach and grow repetitively. (a) Decreasing* N_s *to* 0.5 *(one biomass tile attached each two steps) the connection of the streamer to the seed breaks off after step* 9700 *with* 4792 *biomass tiles. (b) Decreasing* N_a *to* 2 *the streamer elongates, bends and detaches repetitively. The image corresponds to step* 42600*, just before the fourth detachment, with* 1373 *biomass tiles. (c) Decreasing* N_a *to* 3 *the streamer becomes too thin and the top part encounters resistance to join the corner. It finally breaks off at step* 15600*, with* 2151 *biomass tiles. Other parameters as in Figure 5.3.*

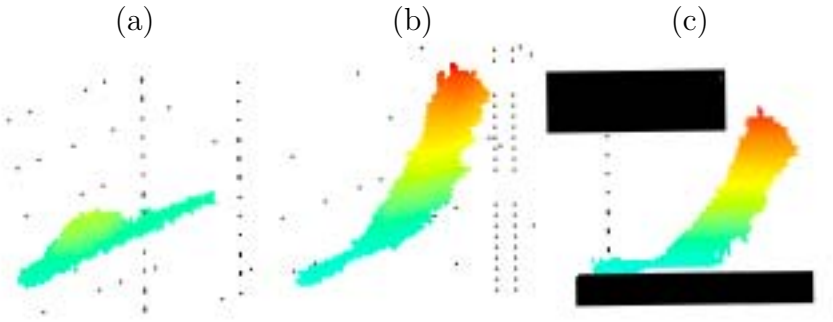

Figure 5.5: *Stable streamers crossing to the opposite corner may fail to be formed not just because they detach before growth effects sustain them. Snapshot (a) shows a streamer that remains mostly parallel to the substratum until it reaches the wall at step* 3200 *with* 3242 *biomass tiles.* $\gamma = 15\,Pa$, $N_a = 3$ *and* $N_s = 2$. *Increasing* γ *to* $20\,Pa$, *the biofilm is strong enough to cross the current and wide streamers are formed. (a) and (b) show the front and lateral views of a streamer at step* 15000, *with* 4702 *biomass tiles.*

5.6 Conclusions

In this chapter biofilm development in a corner microflow has been discussed. A hybrid model combining discrete probabilistic rules for the biofilm phase and a finite difference solver for the incompressible Navier-Stokes equations in a quasisteady laminar regime has been proposed and compared with experimental results presented in [133, 6, 37].

The model seems to reproduce the behavior observed in the experiments. Initial biofilm seeds planted past a corner may develop into streamers reaching the opposite corner. The streamer configuration shows a strong dependence of the adhesion rate and the biofilm cohesion. Small cohesions compared to the shear rate exerted by the flow forbid the development of streamers. The initial seed is washed out. Increasing the cohesion for a fixed corner flow, we see streamerlike patterns that vary depending of the number of biomass tiles attached to the seed and the biofilm body. They either grow parallel to the bottom wall, or start to bend when they feel the corner flow. In this later case, they may detach for low adhesion rates or cross the mainstream and reach the opposite corner for large adhesion rates. Growth processes act in a longer time scale and may thicken the biofilm blocking the channel.

So far we have studied biofilm patterns in flows driven by a constant pressure drop. The flow is stationary, except for the slow variation of the

biofilm boundary, which makes it quasi-stationary. In the next chapter we will study biofilm development in pulsatile flows. Such flows are common in Nature, starting with the human body, and in medical or biological applications, where the use of peristaltic pumps is generalized.

Chapter 6

Development of spiral biofilms in slow pulsatile flows

Biofilm dynamics depends of many factors. One of the most relevant for their spread through the environment are the hydrodynamic conditions of the media in which they are immersed [117]. Not all bacteria show the same spreading behavior under similar conditions, though there may be some common trends that should be identified. For instance, filamentous biofilms are ubiquitous in Nature and may largely disrupt the environment they grow in. As discussed in previous chapters, biofilm formation and evolution was documented in a series of experimental papers [126, 125, 151, 152, 150] for laminar and turbulent flows at moderate and relatively large Reynolds numbers under different nutrient conditions. A rich variety of biofilm patterns and spread mechanisms, such as ripples, streamers, mounds, mushrooms, rolling and darting, were observed in straight ducts. The development of microfluidic devices has stimulated research on biofilm growth at very low Reynolds numbers [134, 133, 88, 58, 37]. The disruption of flow caused by biofilm streamers in sharply curved devices has been shown to have undesirable consequences for environmental and medical systems. In these microfluidic studies, flow motion is driven by a constant pressure gradient caused by placing the culture reservoir above the collection disk [37]. We have discussed and modeled all these patterns in previous chapters. Biofilm dynamics in slow pulsatile flows remains unexplored, although pulsatile and peristaltic flows are typical of many medical and biological systems, starting with the human body [70, 144].

In this chapter, biofilm formation in slow pulsatile flows is studied. The pulsatile flow is produced by a roller pump, that sets flow in motion by peristalsis: rolls strain periodically the tubes pushing the fluid forward [168].

Such pumps are commonly used in medical and biological systems to produce slow flows that do not harm cells. They are widely used in other fields in which no contact between the pump and the propelled fluid is required for different reasons, such as to obtain a complete sterile system, to keep the purity of the transported fluids or to avoid any damage to the equipment. In flow circuits that remind of small circulatory systems, we have discovered the formation of long helicoidal bacterial threads wrapped around the tube walls, see Figure 6.1. They often originate as spiral biofilms at stenosis or at joints with small diameter variations.

These helicoidal biofilms are brittle, with a tendency to split into rings if perturbed. They collapse slowly if the flow stops, reappearing when the flow is restored. To our knowledge, such spiral bacterial filaments have not been reported before. Formation and eventual detachment of such biofilms in medical and biological systems may provide unexpected mechanisms for the outbreak of infections and bacterial contamination. These experimental observations are sustained with numerical studies of particle distributions in these geometries and an analysis of the growth process on a curved surface under a pulsatile flow. The resulting biofilms wrap around circular tubes and expand remaining near the walls, without interfering with the mainstream, but providing an unexpected mechanism for medical device associated infections and bacterial contamination.

This chapter is structured as follows. Section 6.1 describes the materials, setup configurations and the methodology used to perform the experiments that produced spiral biofilms. Section 6.2 discusses the experimental results. Section 6.3 details the numerical simulations. Finally, section 6.4 summarizes the chapter with some conclusions.

6.1 Materials and methods

6.1.1 Bacterial strains, media and reagents

P. putida KT2440-GFP [79] and *P. putida EM371-mCherry* were selected to perform the different essays. *P.Putida*KT2440-GFP was generated by a site-specific insertion at an intergenic region of a miniTn7-gfp2 cassette [78, 85]. Bacteria were grown overnight in M9 glucose 0.2% at room temperature.

A M9 minimal medium (see [135] for more details) supplemented with glucose 0.2 % was chosen as a nutrient source for biofilm growth.

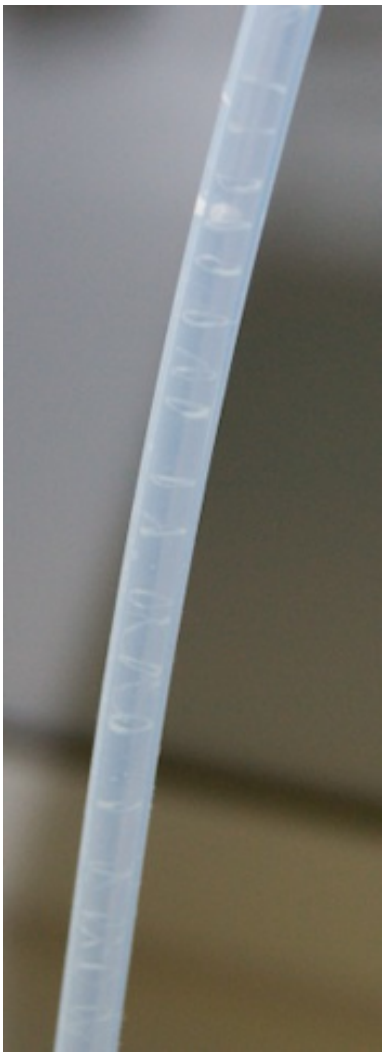

Figure 6.1: *Helicoidal biofilm filaments with Pseudomonas putida KT2440-GFP wrapped around a translucent silicon tube with an inner diameter of 2mm. Photograph taken after* 4 *days of pulsatile flow generated by a peristaltic multiport pump ISMATEC IP-C 8 set at 0.15 ml/min. Spirals are visible to the naked eye. Photographs are taken with a Nikon D60 camera (objective Nikon DX AF-S nikkor 18-55 mm 1:3.5-5.6 GII ED.) and no image manipulation.*

6.1.2 Experimental setups

The basic set up consists of a nutrient reservoir, a roller pump and a collection flask joined by tubes with maximum inner diameters of 2 mm. Different lay-outs of tube networks of increasing complexity were employed. The first ones are reminiscent of circuits found in nature (human body circulatory system) or engineered installations (drinking water piping system, industrial cooling systems). The last one is a standard flow cell system used in biology laboratories to study bacterial dynamics.

The initial lay-outs were designed to investigate the effect of the radius of the tubes and the presence of tube connectors on biofilm growth. Four configurations were explored, see Figure 6.2. The first one consists of a single tube connecting the circuit. Nutrients are suctioned from the reservoir by the pump and flow along the tube towards the waste collector. A second configuration has a T junction that splits the original tube in two branches which merge again in another T junction downstream. The position of the T is rotated 90^o at the joints, see Figure 6.2(up). The third configuration contains a couple of straight connectors that first reduce and then increase the diameter of the tube. A fourth configuration splits the tube in three branches using several T connectors, which merge again downstream, see the lower design in Figure 6.2.

In the previous configurations, bacteria were injected directly in the middle of the lines. The final setup was a cell quantification device, similar to the ones used in biological experiments [110], where bacteria are injected inside the flow cells through the enter ports inside each channel. Nutrients are suctioned by a roller multiport pump and distributed along two different lines. Bubble traps are placed between the pump and the flow cells to avoid the pass of bubbles that may be generated during the pumping process. The lines split into three smaller ducts which enter the channels present in the flow cell. At the exit of the flow cell the three ducts merge in one drain tube that ends in the waste flask, see Figure 6.3.

6.1.3 Roller pump

The liquid is pushed through the circuit using a multiport roller pump *ISMATEC IP-C 8*, see Figures 6.4 and 6.3. Roller pumps are based on a peristaltic mechanism [168, 70]. They push the fluid forward by straining the duct containing the fluid with the rollers. A proper modulation of the frequency of rotation of the rollers will achieve different flow rates. The pump connection tube, a 1.65mm inner diameter elastic tygon tube (R3607, VWR), is periodically flattened in some zones by a train of rolls with a diam-

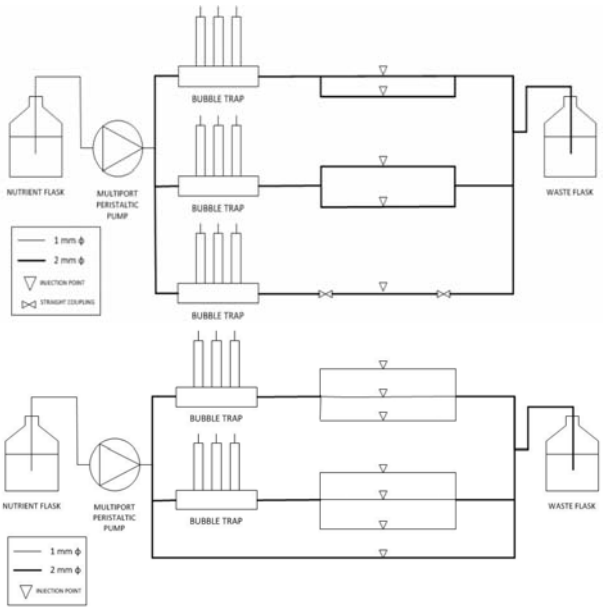

Figure 6.2: *Experimental setups to test the effect of changes in diameter and presence of junctions in nets of tubes on biofilm growth.*

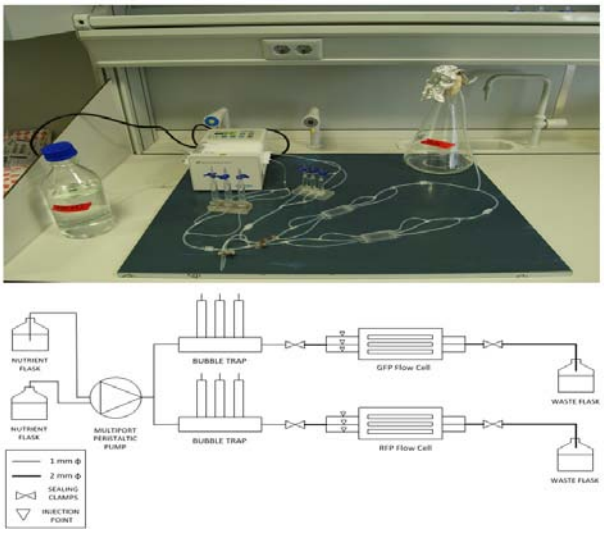

Figure 6.3: *Experimental setup of a parallel flow cell circuit to grow biofilms (up) and squematic lay-out showing the connectivity between each part of the essayed flow cell setup (down).*

Figure 6.4: *Inner structure of the roller pump. The upper part of the tubes containing the fluid is placed on the rollers, being periodically strained by them. This peristaltic mechanism forces fluid motion.*

eter of 1.8 mm, creating small fluid packs which are forced to advance in the direction of the rotor. The geometry of the pump generates a dynamic distribution of zones with high pressure (fluid packs) and low pressure (strained tube zones). When the rollers advance along the tubes, the fluid packets are forced to occupy the empty space left behind the forward rod and are pushed by the rod which advances from behind. Empty gaps will be filled with fluid coming from both sides of the rods, generating flow oscillations in the axial direction of the tube with a magnitude directly related with the spatial step performed by the rotor and the geometry showed by the strained tubes. The free section of the duct in strained zones may be completely closed or not, which may cause flow fluctuations between fluid packets and influence reflux processes usually present in these pumping mechanisms.

Flow rate/time curves have been computed by filming the advance of liquid/air interfaces in tubes of different diameters in different situations: empty tubes being filled, advance of injected bubbles, height variations at the collector. The results suggest an oscillatory time dependence of the flow rate. For instance, when the pump is adjusted to 0.15 ml/min, the velocity of the flow reaches a value of 3.183 and 0.795 mm/s for inner tube diameters of 1 and 2 mm respectively. Expected Reynolds value for both cases are 3.183 and 1.591. Two superimposed periods of about 0.1 and 0.8 seconds are identified. The largest period is determined by tube contact with rollers. The shortest one may be related to the mechanical advance of the rotor. The shape of the flow pulses is similar to those observed in systems such as the

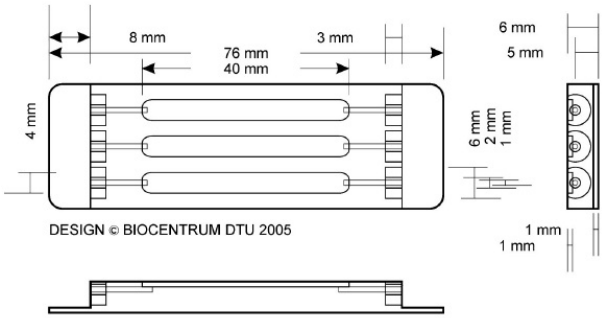

Figure 6.5: *Flow cell scheme designed by BioCentrum-DTU.*

human circulatory system, with long impulses and sudden drops of flow rate.

Additional information on the spatial variation of the volume velocity inside tubes with inner diameter of 2mm was obtained injecting violet crystal as an ink tracer. The profiles suggested a Poiseuille like distribution in the bulk of the flow, with small vortices hitting the walls after narrow connectors. Particle imaging velocimetry (PIV) showed static spiral like patterns on the walls. No obvious evidence of backward flow was observed in the bulk fluid, suggesting that, if present, it must be confined to the wall and be of small order of magnitude. We will comment later on additional facts that suggest some kind of reflux in the system.

6.1.4 Materials

The multiport roller pump ISMATEC IP-C 8 uses 1.65 mm flexible Tygon tubes (R3607, VWR) to suction the fluid from the nutrient reservoir. Those tubes are connected to the networks described above using polypropylene T-Junctions (EW-30623-66, 1/16", Cole Parmer). Peroxide cross-linked silicone tubes (VWR) are used for the main networks. Inner diameters are typically 1-2 mm. Biofilm spiral growth was only observed in silicone tubes, that are translucent. When replaced by transparent PVC ducts no spirals were observed. No spirals grew on the transparent Tygon tubes either.

Polycarbonate flow cells (made by BioCentrum-DTU, see [110]) were used to grow biofilm samples for the lay-out depicted in Figure 6.3. Their structure is shown in figure 6.5. Flow cells were covered with a 24×50 cover slip (Menzel-Glaser) and sealed with silicone glue.

6.1.5 Growth conditions

A similar start-up procedure was designed for all cases. The assembled system was first sterilized by introducing in the circuit a solution of 1 % sodium hypoclorite at a flow rate of 1.5 ml/min during a period of time at least of 5 hours. Then the circuit was cleaned with 1 l of sterilized water and afterwards buffered with the nutrient solution. $200\mu l$ aliquots of selected bacteria (with an $OD_{600} = 0.2$, the initial bacterial seed is around $4{\cdot}10^7$ bacteria) were injected in the circuit with a $500\mu l$ syringe. In the initial layouts, bacteria were injected directly in the middle of each line properly marked (in order to know the initial injection point). In the flow cell setup, bacteria were injected inside the flow cells through the enter ports inside each channel. Injection sites were clamped by both sides as shown in figures 6.2 and 6.3. Bacteria were left to attach during 30 minutes. Finally, clamps were removed and the multiport pump was connected at a typical rate of 0.15 ml/min to start the experiments. The duration of the experiment was 2 days for the initial setups and 7 days for the final one.

Systems were checked periodically: for the first configurations shown in figure 6.2, growth was controlled by taking pictures every 1 hour, excluding the night hours. For the flow cell setup the system was monitored at days 1, 4 and 7, performing stops at checking days to inspect the results in the microscope.

6.2 Experimental results

In the flow cell setup, the flow carries downstream bacteria grown at the flow cells. Helicoidal growth was found in straight tube configuration after a section reduction, and its presence was also observed in some branches of the T-Juncions (see photograph 6.6). These structures end up filling all the available length of the tube in which they grow, downstream, but also upstream. Figure 6.7 shows spiral biofilm expansion when bacteria are injected in the middle of the tubes. The initial injection itself drives cells to the walls in this case and generates initial nucleation sites for the threads.

The helix step increases with the diameter of the tubes (Fig. 6.8), which also suggest a velocity dependence because of both diameter and velocity are related for a fixed flow rate inside a tube by a quadratic relation. Figures 6.1 and 6.8(up) show spirals inside tubes of 2mm of diameter. On the contrary, a shorter helix step was observed in a branch of 1mm diameter in the

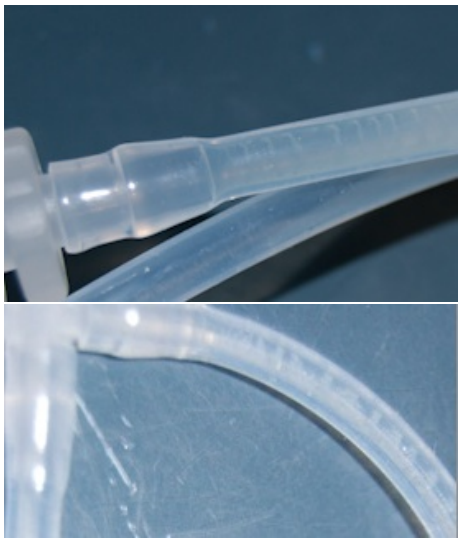

Figure 6.6: *Spiral filaments nucleated on different types of section adaptors: (up) Helix generated at a straight tube adaptor inside a* $2mm$ *tube. The tube collects detached bacterial cells from biofilm growing upstream inside flow cells. The combination of hydrodynamics and bacterial growth promote the formation of these structures. (down) Spiral nucleated at a branch of a T-junction inside a* $1mm$ *tube before the entering port of a flow cell. Either by swimming or due to backflow, bacteria travel upstream from the flow cells, attach and eventually form spiral biofilms. Images taken after 4 days in a flow cell setup. Photographs were taken with a Nikon D60 camera (objective Nikon DX AF-S nikkor 18-55 mm 1:3.5-5.6 GII ED.) and no image manipulation.*

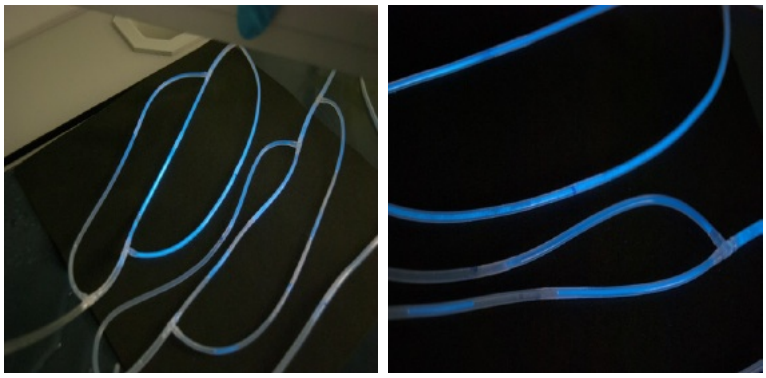

Figure 6.7: *When bacteria are injected in the middle of the tubes, spiral biofilms spread upstream and downstream, as shown by their glowing when exposed to UV-light. Blue color is produced by some metabolic by-products secreted by bacteria to catch iron molecules. Photograph taken 4 days after injection. Photographs were taken with a Nikon D60 camera (objective Nikon DX AF-S nikkor 18-55 mm 1:3.5-5.6 GII ED.) and no image manipulation.*

experiment performed in the second setup, as shown in Fig. 6.8(down).

Spiral structures were not formed in all the lines with T-junctions, and neither in straight tube configuration without any section reduction. Small bubbles at the entrance or exit of the T junctions seemed to reduce the expected flow rate in some lines, diminishing the the amount of nutrients supplied to bacteria and the velocity of the flow in those areas. In straight tubes, the absence of obstacles in the line prevented the formation of streamers although bacteria adhered slowly to the entire tube surface.

Different streamer densities (see figure 6.9) were found in different experiments depending on which zone streamers were situated: spiral streamers seemed to grow as a simple helix through the tube at straight zones before high curvature zones in the tubes or with small changes of section. On the contrary, high curvature zones or tube section next to sharp changes of section (T-Junctions or tube couplers) were observed to be filled with a complex helicoidal structure composed by several helix rolled simultaneously, with a helix step much smaller.

Biofilm spiral growth was only observed in silicone tubes, that are translucent. When replaced by 2mm transparent PVC ducts (VWR) no spirals were observed. No spirals grew in the Tygon tubes either. The observation is con-

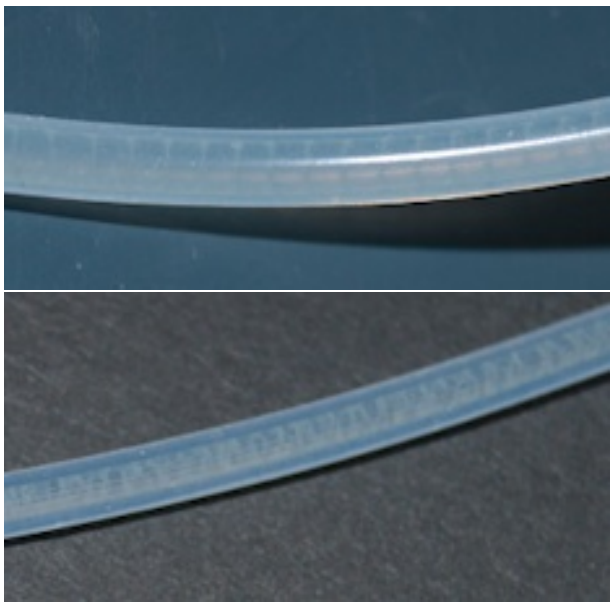

Figure 6.8: *Different diameter tubes promote different helicoidal size step. (up) Spiral inside a 2mm inner diameter tube. (down) Spiral inside a 1mm inner diameter tube. Photographs were taken with a Nikon D60 camera (objective Nikon DX AF-S nikkor 18-55 mm 1:3.5-5.6 GII ED.) and no image manipulation.*

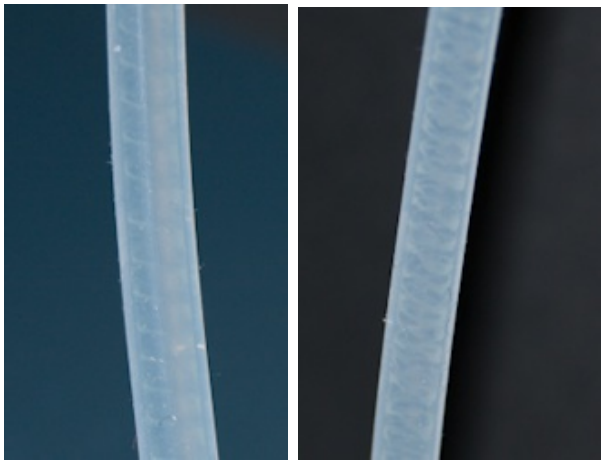

Figure 6.9: *Different spiral biofilm densities are observed depending on the geometry of the circuit in which they are growing. Periodic single helicoidal filaments (left) are generated when the changes of section inside the tubes are small. However, by using an adaptor with a sharp change of section or the presence of a high curvature in the tube is enough to generate a more denser and messy spiral structure. Photographs were taken after* 4 *days with a Nikon D60 camera (objective Nikon DX AF-S nikkor 18-55 mm 1:3.5-5.6 GII ED.) and no image manipulation.*

sistent with the fact that the selected bacterium adopt a net negative charge in its membrane. PVC tubes tends to adopt a negative charge on their surface due to the presence of fluorine molecules in its polymeric structure, avoiding the attachment of bacteria. On the contrary silicone is charged positively and hence bacteria may approach and attach to the surface more easily.

The growth process was observed to proceed as follows. An initial bacterial shot multiplies and increases the cellular density inside the ducts. Tubes are filled gradually with a flat layer of biofilm at the bottom. White lines in tangential section of the inner tube wall seem to appear at random places on the tubes, suggesting that bacteria may be taking advantage from natural shelters formed by the small rugosity voids present in the silicon of the tube produced during the fabrication process to further increase their cell density forming ringlike structures. As the cellular density increases, biofilm filaments (streamers) generated at specific nucleation points grow into the flow and are curved following a spiral trajectory.

In fact, the dynamics of the system revealed a nucleation zone at the end of one tee 17 hours after the beginning of the experiment, but a complete developed spiral biofilm zone is only visible to the naked aye in a period not shorter than 24 hours for the essayed conditions. This zone, which initially seemed to be similar to a thick spider web, evolved gradually forming an initial spiral biofilm.

Helicoidal structures showed to be quite brittle, see Figure 6.10. Once pumping is disconnected, they collapse gradually, disappearing completely in an interval of $1-2$ hours. Small movements in the tubes produce vibrations that disintegrate the spirals too. However, these structures seemed to be a stable biofilm configuration for these type of systems: once spirals were first grown and afterwards discomposed by motion of the tubes, spiral biofilms appeared again after an additional lapse of time agreeing with the bacterial growth time ($24-48$h).

Diameter variations in the tube network seem to be relevant for the generation of this kind of structures. In straight lines without changes of section nor bifurcations, a flat layer of biofilm grew at the bottom of the duct, but no spiral biofilms were found. This fact suggests that bacteria may actually need the presence of a perturbation in the duct to start the formation of streamers, which would eventually form the spiral structures observed. Perturbations would act as nucleation sites, enhancing local mass and momentum transfer because of formation of local eddies which would increase the growth rate

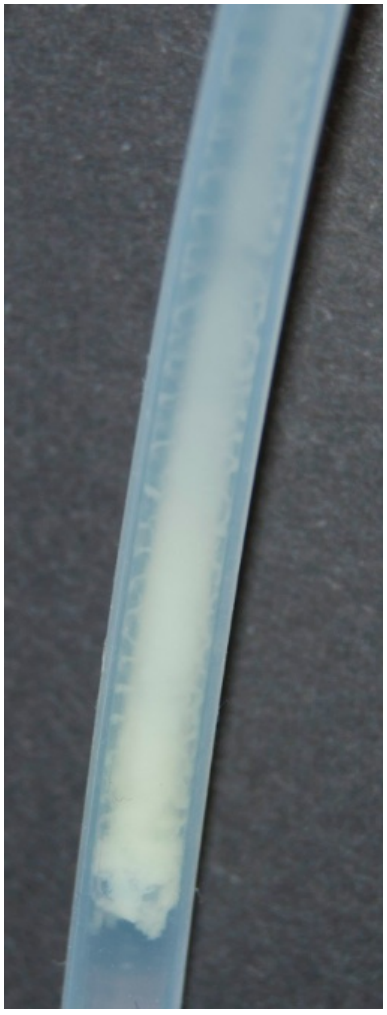

Figure 6.10: *Spiral biofilms live on the walls of the tubes. In this Figure, part of the brittle biofilm has been destroyed by a bubble formed in the tube. Cells are being carried downstream by the flow, that appears to be divided in two regions. The inner region carries the detached mass of cells downstream, without interfering with the outer wall region in which the spirals live. Photographs were taken after* 4 *days a Nikon D60 camera (objective Nikon DX AF-S nikkor 18-55 mm 1:3.5-5.6 GII ED.) and no image manipulation.*

and shear force on these zones and hence promoting the formation of spreading structures such as streamers, as showed in [159].

Several authors have pointed out the possibility of reflux in peristaltic systems [156, 157, 70]. Our experiments use a peristaltic pump that produces a pulsatile flow in the tube network. As said before, flow studies with ink or PIV did not show obvious reflux in selected configurations. However, bacterial spirals managed to grow upstream in some occasions. Additional tests adding disinfectant in the waste reservoir in the layouts shown in figure 6.2 from the beginning did not generate any spirals, which would suggest that either the disinfectant diffuses or is suctioned upstream from the waste and inhibits bacterial growth at early developmental stages. The presence of reflux in experiments using similar setup configurations has to be considered carefully, since it might change the chosen experimental conditions and hence invalidate the results of some biological experiments whenever chemicals are placed in the waste reservoir.

6.3 Numerical simulations

A link between the observed helicoidal structures and the geometry of the channels can be established analyzing the mass and momentum transfer between the biofilm and the flow. The Reynolds number (dimensionless parameter measuring the ratio of inertial to viscous forces) is expected to be about 1 - 3. Therefore, the flow is laminar in straight areas. The primary flow follows streamlines parallel to the walls, with a Poiseuille-like velocity profile that grows radially from the walls of the tubes to the center of the circular section. Our filaments often nucleate at stenosis. Connectors and T-junctions of about 0.8mm of diameter join tubes of 1 mm and 2 mm of diameter. Secondary flows superimposed to this primary flow develop at the joints between tubes of different diameters.

The presence of joints between tubes of different diameters or connectors (about 0.8mm of diameter joining $1-2$ mm inner diameter tubes) combined with the hydrodynamic resultant of both axial and radial velocity component imposed by the peristaltic flow seems to promote the nucleation of the spiral filaments at stenosis. Figure 6.11 shows streamlines computed with the finite element package COMSOL. The fluid circulates through the narrow passage at higher speed. It expands into the wider duct slowing down and forming small vortices that drive particles to the walls. This mechanism drives particles to the walls. Any irregularity breaking the symmetry selects one or

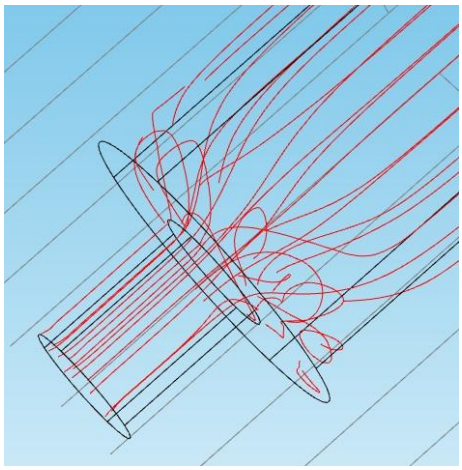

Figure 6.11: *Streamline expansion after a stenosis.*

several areas as nucleation sites of biofilm seeds.

Once a biofilm seed is generated, it grows following concentration gradients. Biofilms often expand into slow flows forming fingers or streamers. The pulsatile flow may prevent this behavior keeping the biofilm on the walls. Figure 6.12 shows variations in the magnitude of the velocity along the axis. It increases and decreases periodically. Sudden increases of the velocity may erode the upper part of the aggregate and detach fragments, forcing the biofilm to expand over the surface.

Biofilm consumption depletes the concentrations of nutrients and other chemicals downstream, see Figure 6.13 (left). The shear rate due to the flow is larger in the upper part, affecting especially the front, as shown in Figure 6.13 (right). As a result, an initially symmetric aggregate will elongate. Figure 6.14 illustrates the same phenomenon in an ellipsoidal seed. Cellular division and spread should be faster in the direction orthogonal to the tube axis, producing ring-like threads. However, the growing edges are shaped by the orthogonal flow and the rings become spirals. Making an analogy with helical motion, it is well known that particles advancing on a circle forms spirals when a perpendicular force acts on them. The step of the resulting helices is given by the time required to draw one circle times the linear velocity in the orthogonal direction. One may conjecture that, in our case, the helix step should somehow be related with the time a biofilm filament takes to grow forming a ring around the tube and the flow velocity.

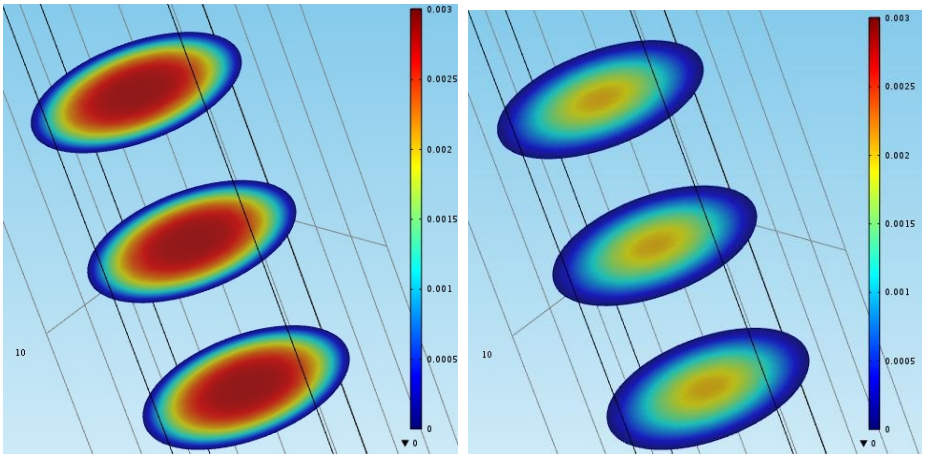

Figure 6.12: *Axial velocity field at times* 1.6 *s (left) and* 1.8 *s (right) for a pulsatile flow with period* $T = 0.8$ *s in a tube of* 2 *mm of diameter.*

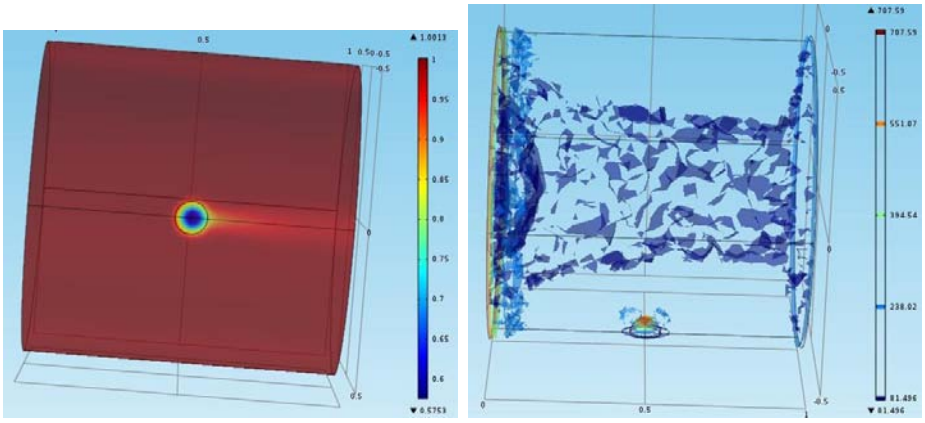

Figure 6.13: *(Left) Circular biofilm patch consumes nutrient and depletes the nutrient concentration downstream. (Right) The shear due to the flow erodes more the upper front and back sides of the biofilm.*

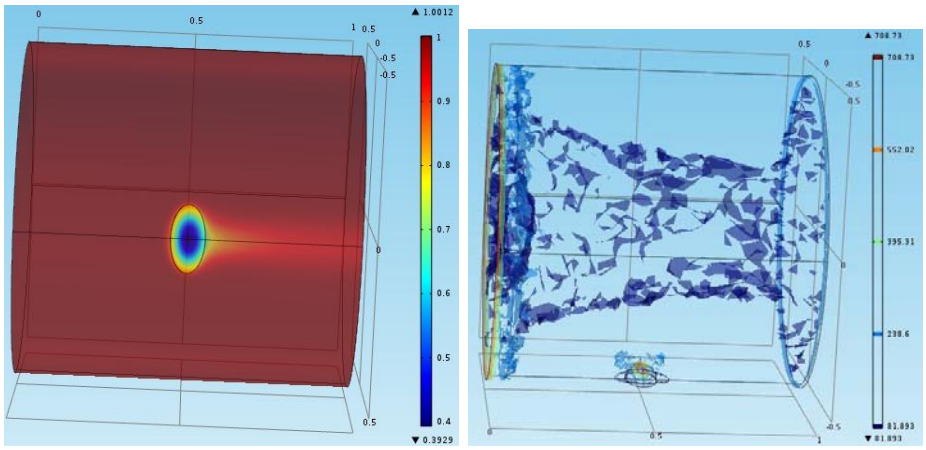

Figure 6.14: *(Left) Ellipsoidal biofilm patch consumes nutrient and depletes the nutrient concentration downstream. (Right) The shear due to the flow erodes more the upper front and back sides of the biofilm.*

When the tubes are curved, inertial effects due to curvature may become relevant and cause helicoidal motion [8]. In our case, the Dean number (dimensionless number expressing the ratio of the viscous force acting on a fluid flowing along a curved duct to the centrifugal forces) is too small [74] for the curvature to generate spirals on its own. However, inertial effects may drive suspended plancktonic cells to the walls forming rings in some areas, see Figure 6.15. The change of diameter in those regions would trigger spiral arrangements, as before.

Curvature may produce new nucleation areas for spiral filaments. Once formed, the pulsatile flow will push the filaments near the wall. The presence of an helicoidal filament in the flow seems to attract particles to spiral downstream, see Figure 6.16. Cell transport seems to suffice at initiating helicoidal filaments, which will thicken in a longer time scale by growth processes.

6.4 Conclusions

Understanding bacterial aggregation in flows is of paramount importance for many fields, where biofilm formation may be damaging or profitable. We show that by performing a set of experiments and supporting these results with numerical simulations (solving flow equations with a finite difference computational package), biofilms expand forming spirals in slow pulsatile

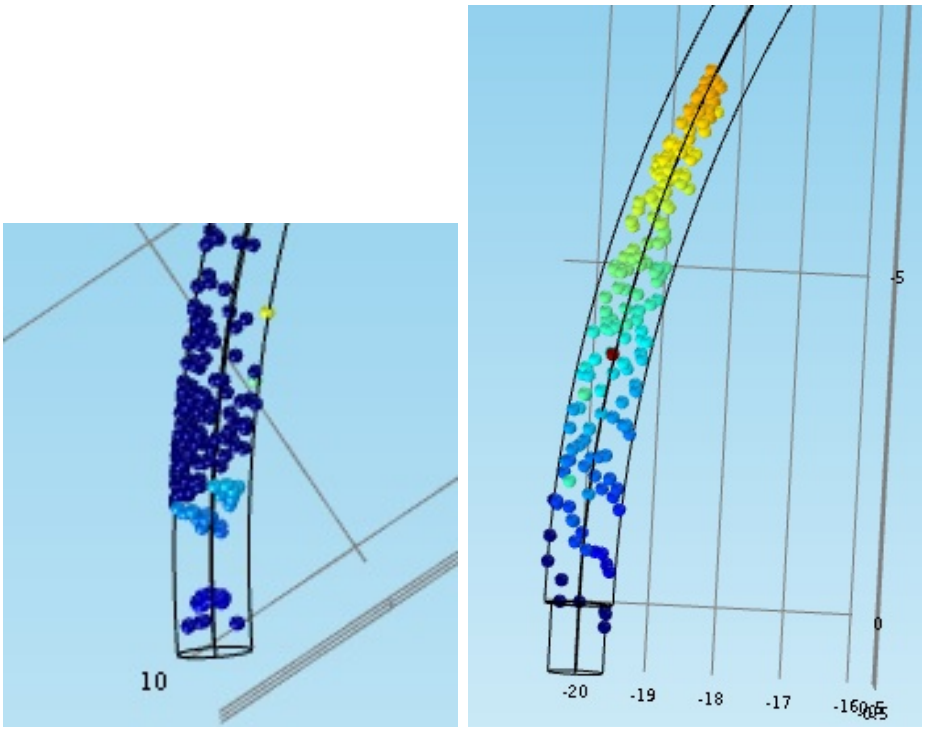

Figure 6.15: *Curvature effects. In absence of diameter variations, particles issued from the entrance of this* 1 *mm diameter tube hit the walls forming a ringlike structure (Left). In the presence of diameter variations, previously observed spiral arrangements persist (Right).*

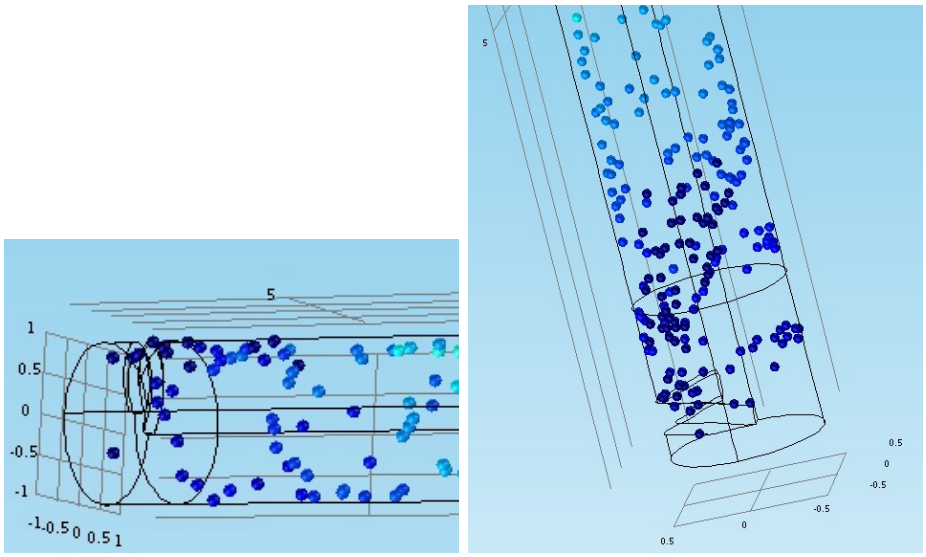

Figure 6.16: *An helicoidal indentation is made at the entrance of two tubes with diameters* 2 *mm (Left) and* 1 *mm (Right). Streamer gathers particles from bulk liquid by adhesion process and thicken its size*

flows generated by peristaltic pumps in circuits whose structure reminds of small circulatory systems, with presence of stenosis in the form of narrow connectors and T-junctions. Circuits with a similar structure appear often in medical, experimental and biological systems, since peristaltic pumps are a common choice to avoid harming cells or prevent contact between the fluids and the pumping device.

Helicoidal biofilms colonize the whole tube they grown in. They are brittle and collapse when the flow stops or the tubes are moved, but they persistently reappear and may become an unexpected mechanism to promote hospital-acquired infections and bacterial contamination. Spiral biofilms seem to nucleate after diameter variations and may be enhanced by curvature. Whether the presence of a pulsatile flow is essential to their formation and development has yet to be elucidated.

Spiral biofilms have been observed in situations in which laminar spiral flows may occur. Stable helical blood flows that are observed in vivo in several vessels, may play a beneficial role in vascular haemodynamics reducing turbulence in the arterial tree. Laminar spiral flows are common in blood vessels, due to the presence of natural junctions [146], to illness (stenosis,aneurysms) [147], or to surgery (grafs, bypasses) [103]. Curved geometries

and diameter variations are known to trigger spiral particle trajectories in a variety of flows, such as peristaltic flows and flows through stenosis or curved ducts [8, 69, 74, 140, 157]. However, our flows seem to be too slow for spiral flows to appear. The only effect of diameter variations, changes of curvatures or periodic pressure drops is to enhance cell attachment to walls and create preferential nucleation sites. Diameter variations prompt the appearance of helicoidal streamers attached to walls, that spiral downstream aided by the periodicity of the flow, bacterial growth processes, and, possibly, slight changes of curvature.

This chapter completes our study of biofilms in flows. The next chapter deals with biofilms grown on surfaces. This fact deactivates some of the bacterial mechanisms we have enforced so far and activates new ones, such as differentiation processes.

Chapter 7

A hybrid description of differentiation processes in biofilms on surfaces

In previous chapters we have studied biofilm growth in different hydrodynamic environments (straight ducts, curved ducts, corner flows, pulsatile flows, etc.). However, not all biofilms are submerged in a liquid. Many biofilms grow on solid/air interfaces too, and the physics involved is different. Furthermore, bacteria often show additional behaviors to the ones we have already considered, such as bacterial communication or self-inducting metabolic changes [30]. It is commonly accepted that biofilms are able to generate molecular signals as cell-cell communication mechanisms to activate gene expressions that unleash different survival strategies adapted to the environmental conditions. These communication processes, still poorly understood, might be one of the key issues to clarify the different community behaviors observed in bacterial colonies on surfaces [125].

In this chapter we will focus our efforts on describing simple differentiation processes for biofilms grown in a solid - gas interphase. Section 7.1 introduces basic concepts. Section 7.2 describes the physical framework, together with the assumed hypothesis and the mathematical formulation: a stochastic model similar to those developed in previous chapters, but involving concentrations that interact in cascade. Numerical results illustrating the expansion of biofilms with wavy borders, with differentiated cells distributed spatially as observed in experiments [30] are showed in section 7.3. Section 7.4 presents the conclusions.

7.1 Self-induction and differentiation concepts

It is known since 1970s that some extracellular inducers may induce genetic expression in some bacteria [20]. Subsequent research in the following decades has clarified autoinduction processes [106] The basic approach relies on the idea that the same organism that is sensible to certain chemical inducers is also responsible of producing those compounds, creating a self-feeding loop which regulates both the genetic expression and the generation of autoinductor, see picture 7.1).

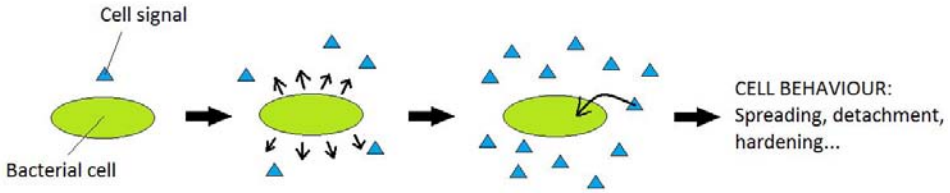

Figure 7.1: *Schematic picture of an autoinduction process*

This idea was developed further during 1990s, when Fuqua et al. [51] started to talk about "*quorum sensing*" mechanisms as a possible way through which bacteria may count their population previously to unleashing different behaviours such as virulence or spreading mechanisms. An example found in Nature about quorum sensing mechanisms and autoinduction processes is described in [165]. The squid *Euprymna Scolopes* shows bioluminiscence in the presence of high population densities of the bacteria *Vibrio Fischeri*, which do not show bioluminiscence when are found at low densities in the environment.

These concepts established a solid base to study different behaviors observed in bacteria, such as the differentiation processes observed in some bacterial strains. Differentiation is a mechanism through which some bacteria inside a population suffer physiological changes, developing different phenotypes even though they have the same genotype. This change leads to the development of "specialized" cells with certain characteristics which perform some specific tasks that seems to increase the chance of survival of the whole colony.

Differentiation processes have been observed to depend on the local conditions around each cell, in particular, the state of the neighbours and the

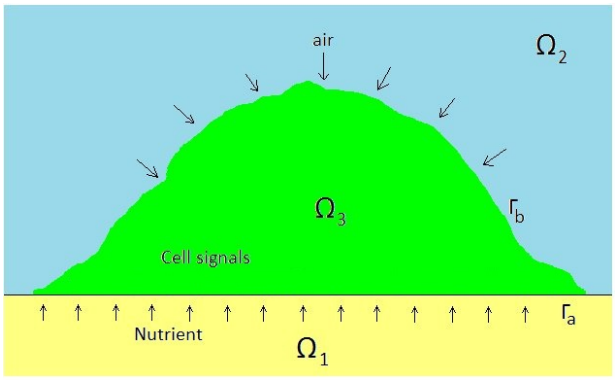

Figure 7.2: *Scheme of the simulated system*

local chemical composition found around them [95, 161, 145]. A well known example of differentiation process is provided by *"Bacillus subtilis"*, where initial biofilm cells may differentiate in four well defined cell types [20].

Although there are experimental works that define and quantify these processes for *B.Subtilis* [91], there is a lack of theoretical models to analyze and simulate computationally the behaviour observed in the laboratory. The aim of this chapter is to develop a mathematical model for a growing biofilm of *B. Subtilis* taking into account the differentiation process that is observed during its development in the experiments, trying to obtain similar results regarding geometry, spatial distribution and relative quantities between differentiated cells.

7.2 Model and simulations

7.2.1 Physical geometry

We simulate the development of a *B. Subtilis* biofilm patch (subdomain Ω_3) attached to an agar-gel surface (subdomain Ω_1) and exposed to the atmosphere (subdomain Ω_2) (see picture 7.2). To perform their metabolic activities, the biofilm obtains nutrients from the gel and oxygen from the air and eventually from water suctioned from agar. In this model only bacterial mechanisms such as reproduction and differentiation are considered.

The reproduction process demands oxygen and nutrients to generate new

biomass. Newborn cells are reallocated inside biofilm by pushing existing cells in the direction of minimum mechanical resistance. The chemical reaction may be written as:

$$Nutrient + \omega Oxygen \longrightarrow Biomass \tag{7.1}$$

where ω is the oxygen stoichiometric coefficient which denotes how many moles of oxygen are being consumed for each mole of nutrient.

The differentiation mechanism deploys a set of chemical compounds that trigger the phenotypic changes. Two autoinductors relate the four types of differentiated cells present in the development of *B. Subtilis* colonies, see Picture 7.3. Following [20], the scheme is the following:

Relevant autoinductors:

- **comX**: It is a molecule related with quorum sensing mechanisms in *B. Subtilis* [59, 96]. It is produced by all cells in the biofilm (except those which are not metabolically active).

- **Surfactine**: It is produced to foster the spread of the biofilm colony acting as a lubricant which allows bacteria to diffuse over the surface. It also acts as an autoinductor in normal bacteria, changing its phenotype to become EPS producers.

Type of cells:

- **Normal cells**: They perform all metabolic activities and generate comX. They are sensible to all autoinductors and may be deactivated due to a lack of nutrients or oxygen. They may turn into surfactine generators or EPS cells when the threshold concentration of these respective compounds is reached.

- **Surfactine producers**: They generate surfactine. They do not reproduce (see [20] for more details), neither are sensitive to other autoinductors, but they may be inhibited by the presence of EPS cells in their neighbourhood.

- **EPS cells**: The produce EPS matrix. They are able to reproduce and are not sensitive to other autoinductors.

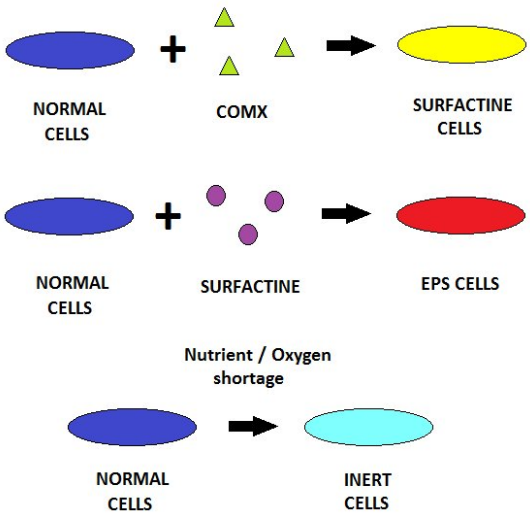

Figure 7.3: *Differentiation scheme of the different type of cells and the different autoinductors*

- **Inert cells**: Also known as "spores". They are deactivated, not performing any metabolic activity (no reproduction, no differentiation process). Normal cells become spores when there is a severe lack of nutrients or oxygen in the local environment of the cell.

The dominating mass transport mechanism in the system is the diffusion produced by the presence of chemical concentration gradients of the chemical compounds (oxygen, nutrients and autoinductors) between the biofilm phase and the other subdomains (gel and air).

Biofilms are expected to grow in size, increasing the concentration of the different autoinductors as the population grows. At certain point, bacteria will start the differentiation process that will evolve as the size of the colony changes.

7.2.2 Mathematical description

A hybrid model has been chosen in order to take into account the inherent randomness of individual bacterial behaviors observed in the experiments and the need of considering local interactions around each cell to fully describe the differentiation process. Cells are regarded as creatures living in

a grid, that reproduce or differentiate with certain probability, informed by the status of the concentration fields nearby. This choice implies that our system is discrete in space and time, and all performed activities by bacteria are described in terms of their probability of happening. The spatial step chosen for this description was the size of one bacterium (around 2 μm) to be able to consider individual interactions among bacteria.

The equation that describes the dynamic of all chemical compound i inside the biofilm is:

$$c_{i,t} - D_i \Delta^2 c_i = b_i \tag{7.2}$$

where the index i denotes the considered chemical specie, D_i is the diffussion coefficient and b_i the source term involved in each case. The kinetics of all chemical reaction processes which are considered in the source term have been described by using modified Monod type kinetics (for simplicity). These expressions with their respective boundary conditions are described next for each chemical species.

Nutrient and oxygen

Kinetics

Both elements are consumed at the same rate, which is always described by the minimum available concentration of nutrient/oxygen:

$$b_n = -k_{rep} \frac{c_n}{c_n + K_n} \frac{c_o}{c_o + K_o} \tag{7.3}$$

$$b_o = -k_{rep} \cdot \omega \cdot \frac{c_n}{c_n + K_n} \frac{c_o}{c_o + K_o} \tag{7.4}$$

where k_{rep} is the uptake rate of the nutrient, ω is the stoichiometric coefficient ratio for nutrient-oxygen reaction and K_o, K_n the half-saturation coefficients. If we consider the oxygen in excess, nutrient kinetics dominates the chemical process and then those expressions may be reduced to:

$$b_n = -k_{rep} \frac{c_n}{c_n + K_n} \tag{7.5}$$

Boundary conditions

Nutrients flow through the agar - biofilm interface (Γ_a) into the biofilm phase from the agar-gel phase. It is considered that nutrient concentration at

that phase is constant during the simulation time. No penetration conditions are imposed on the biofilm - air interface (Γ_b):

$$\begin{cases} c_n(x,y,0) \mid_{\Gamma_a} = c_{n,0}, \\ \frac{dc_n}{dz} \mid_{\Gamma_b} = 0. \end{cases} \tag{7.6}$$

Oxygen diffuses through air - biofilm interface (Γ_b) to the biofilm phase. The concentration on the boundary is set to be constant to an initial fixed value. No penetration conditions are imposed on Γ_a:

$$\begin{cases} c_o \mid_{\Gamma_b} = c_{o,0}, \\ \frac{dc_n}{dz} \mid_{\Gamma_a} = 0. \end{cases} \tag{7.7}$$

Eventually, the biofilm will get also oxygen from the water extracted from agar [138], and we change the boundary condition on Γ_a to $c_n(x,y,0) \mid_{\Gamma_a} = c'_{o,0}$. This avoids a necrotic region in the biofilm core.

comX

Kinetics

This autoinductor will be produced by all cells except inert cells. Its shape has the form:

$$b_{comX} = \begin{cases} k_{\mathrm{comX}} \left(1 - \frac{c_{\mathrm{comX}}}{c_{\mathrm{comX}} + K_{\mathrm{comX}}}\right) & \text{if cell type = normal} \\ 0 & \text{if cell type = Inert} \end{cases}$$

where index k_{comX} is the comX production kinetic constant. This shape of the comX source term predicts saturation limit in comX generation as the environment is being filled with comX molecules.

Boundary conditions

comX diffuses through the biofilm phase. No penetration conditions are imposed in both Γ_a and Γ_b.

$$\begin{cases} \frac{dc_{comX}}{dz} \mid_{\Gamma_a} = 0 \\ \frac{dc_{comX}}{dz} \mid_{\Gamma_b} = 0 \end{cases} \tag{7.8}$$

Surfactine

Kinetics

This autoinductor will be produced only by surfactine generator cells:

$$b_{surf} = \begin{cases} k_{\text{surf}} \left(1 - \frac{c_{\text{surf}}}{c_{\text{surf}}+K_{\text{surf}}}\right) & \text{if cell type = surfactine} \\ 0 & \text{if cell type = EPS, normal, inert} \end{cases}$$

where index k_{Surf} is the surfactine production kinetic constant. As in the case of comX, the shape of the surfactine source term predicts a saturation limit in the production of surfactine when the enviornment is being saturated with its molecules.

Boundary conditions

Surfactine diffuses as in the comX case through the biofilm phase. No penetration conditions are imposed in Γ_a andΓ_b.

$$\begin{cases} \frac{dc_{Surf}}{dz} \mid_{\Gamma_a} = 0 \\ \frac{dc_{Surf}}{dz} \mid_{\Gamma_b} = 0 \end{cases} \tag{7.9}$$

EPS

Kinetics

This autoinductor will be produced only by EPS generator cells.

$$b_{EPS} = \begin{cases} k_{\text{EPS}} \left(1 - \frac{c_{\text{EPS}}}{c_{\text{EPS}}+K_{\text{EPS}}}\right) & \text{if cell type = EPS} \\ 0 & \text{if cell type = normal, surfactine, inert} \end{cases}$$

where index k_{EPS} is the EPS production kinetic constant. The shape of the source term has the same structure as in both surfactine and comX cases. EPS concentration over a certain threshold C^*_{EPS} allow the water absorption mechanism to be activated.

Boundary conditions

The EPS matrix diffuses as in the comX case through the biofilm phase. No penetration conditions are imposed in Γ_a and Γ_b.

$$\begin{cases} \frac{dc_{EPS}}{dz} \mid_{\Gamma_a} = 0 \\ \frac{dc_{EPS}}{dz} \mid_{\Gamma_b} = 0 \end{cases} \tag{7.10}$$

In the simulation, a complete reproductive cycle of a bacterium was set as the time step of the model (which is typically in the order of minutes). Hence it is possible to neglect transient states associated with diffusion processes because these effects are much faster than the chosen temporal step size and the movement of the wall is governed by growth mechanism. This makes it possible to describe mass transport phenomena of any chemical compound i with the classic Poisson equation:

$$D_i \Delta c_i + b_i = 0 \tag{7.11}$$

As said previously, hybrid models set probabilistic laws to describe cell behavior at every time step. In this model, reproduction and differentiation processes are the main metabolic activities that a bacterium may perform. The probabilistic laws are expressed by means of Monod type expressions:

- **Reproduction and spread**

  A cell $\mathcal{C}$ will reproduce depending of the availability of nutrients and oxygen present in its local environment. The probabilistic law is given by:

  $$P_{rep}(\mathcal{C}) = \frac{c_l}{c_l + K_{rep}} \tag{7.12}$$

  where c_l is the limiting concentration of nutrient or oxygen (the minimum of both values) and K_{rep} the value for which the probability of reproduction is 0.5. If we want to consider both oxygen and nutrients, the probability of division becomes:

  $$P_{rep}(\mathcal{C}) = \text{Min}\left(\frac{c_n(\mathcal{C})}{c_n(\mathcal{C}) + K_n}, \frac{c_o(\mathcal{C})}{c_o(\mathcal{C}) + K_o}\right), \tag{7.13}$$

  In previous chapters, any time a cell divided, a new one was placed in the direction of minimal mechanical resistance, shifting its neighbors if necessary in the same direction. This mechanism seemed to work adequately for biofilms in flows. As remarked in [138], biofilms on surfaces that expand using that mechanism are rather 'solid' and expand very slowly. Other biofilms show a more 'fluid' aspect due to water absorption from the substratum. For 'fluid' biofilms we modify the spread mechanism by including creation of water cells that push their

neighbors, in the same way as dividing cells do. Each grid tile occupied by a cell has a probability of being filled with water that pushes the cell around:

$$P_w(\mathcal{C}) = \frac{p(\mathcal{C})}{p(\mathcal{C}) + K_p}. \tag{7.14}$$

$p(\mathcal{C})$ is the value of an inner pressure field at the cell $\mathcal{C}$. A continuous model for the water absorption process is formulated in [138], together with a perturbation analysis that produces simple analytical expressions for the pressure fields in thin biofilms. We may feed those expressions for the pressure field into this probability.

- **Surfactine generator conversion**

A cell will change their phenotype from normal cell to surfactine generator if the local concentration of comX reaches a certain threshold called C^*_{comX}. With this, the probability is given by:

$$P_{surf}(\mathcal{C}) = \frac{c_{comX}(\mathcal{C})}{c_{comX}(\mathcal{C}) + K_{comX}} \tag{7.15}$$

where $c_{comX}(\mathcal{C})$ is the local concentration of comX and K_{comX} the value for which the probability of transformation is 0.5. When there are EPS neighbour cells, they will exert an inhibition mechanism due to the natural activity of EPS on surfactine, decreasing the chance of conversion. This is expressed as:

$$P_{surf}(\mathcal{C}) = P_{inhib}\frac{c_{comX}(\mathcal{C})}{c_{comX}(\mathcal{C}) + K_{comX}} \tag{7.16}$$

with $P_{inhib} = \frac{\text{Number of EPS neighbours}}{\text{Total number of neighbours}}$

If a cell is surrounded by all EPS cells, there is no any chance of conversion to surfactine generator type.

- **EPS cell conversion**

Normal cells will have the chance of turning into EPS productor cells if the local concentration of surfactine reaches a certain threshold C^*_{Surf}.

We assume that active cells $\mathcal{C}$ not secreting surfactin become EPS producers with probability:

$$P_{\mathrm{EPS}}(\mathcal{C}) = \frac{c_{\mathrm{surf}}(\mathcal{C})}{c_{\mathrm{surf}}(\mathcal{C}) + K_{\mathrm{surf}}} \left(1 - \frac{c_n(\mathcal{C})}{c_n(\mathcal{C}) + K_n}\right), \tag{7.17}$$

being $c_{Surf}(\mathcal{C})$ the local concentration of surfactine and K_{surf} the value for which the probability of transformation is 0.5.The probability increases with the availability of surfactin and the scarceness of nutrients.

- **Spore conversion**

  Each kind of cell may suffer a shortage of nutrient or oxygen, triggering a sporulation mechanism that will try to preserve bacteria in a "deactivated" state until better environmental conditions are present. To reflect this, all cells with a local concentration of nutrient or oxygen below a certain threshold C^*_{lim} become spores.

For each process described above and for each time step, a random number r between 0 and 1 will be generated. The process with take place if:

$$r < P_{event} \tag{7.18}$$

The constants affecting the probability laws (K_i) are numeric constants that should be calibrated with experimental data to have a real description in the simulations that do not have to match with saturation constants used in the source term, which are related with a chemical saturation limit. However here these numeric parameters have been chosen to be the same as the values for saturation constants.

7.3 Results and discussion

Several simulations were performed to illustrate the qualitative behavior of the model and its limitations. Simulations suggest a dynamic evolution of the biofilm according with the experimental data [20]. The geometric distribution of each type of cell agrees qualitatively with those taken from [20]. Relative proportions for each type of cell were adjusted by fitting numeric

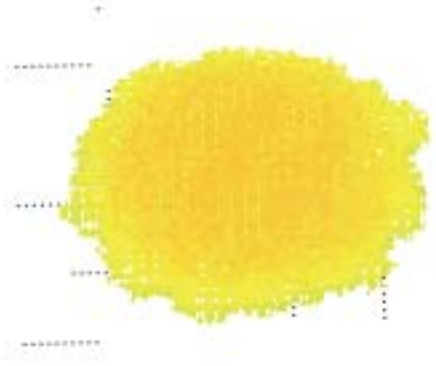

Figure 7.4: *Growing biofilm colony with 8989 cells.*

parameters, but there should be an experimental calibration to improve these values.
The initial small round cluster grows in size in a radial way. As the size of the biofilm increases, the concentration of comX increases until the threshold level C^*_{comX} is reached. At this point bacteria start to differentiate. First, surfactine generators appear, secreting surfactine, which eventually triggers differentiation of cells into EPS producers when the surfactine threshold concentration C^*_{surf} is reached. As the number of EPS cells to increases, the rate of differentiation into surfactine generators decays due to an inhibition mechanism induced by the EPS cells over surfactine. As the biofilm increases its thickness, scarcity of nutrients is felt in the upper part due to the high resistance to mass transfer across the increasing thickness. This effect induces the appearance of spores in the upper part, slowing down the growth of the biofilm.

The current model does not reproduce all observed geometries generated by *B.Subtilis* biofilms, see picture 7.7. The wrinkles and the radial geometry of the colony with an compact inner part and smooth fine layer surrounding it (similar to an egg) suggests other physical mechanisms linked with fluid transport from the inner part to the outer part and possible buckling due to elastic compression.

7.4 Conclusions

In this chapter a 3D hybrid model is proposed to describe the growth dynamics of a small cluster of *B. Subtilis* biofilm on an agar-gel surface. This

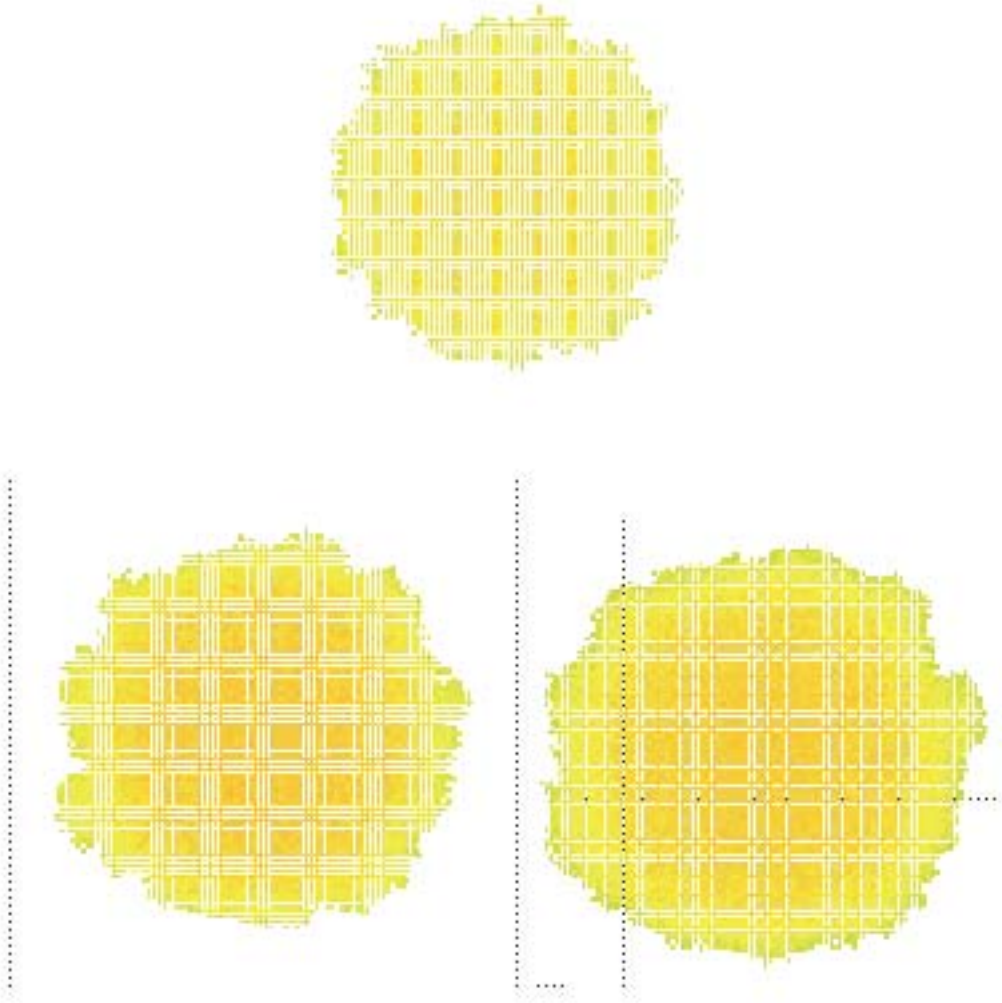

Figure 7.5: *Expansion of an initially circular biofilm seed. Top views.*

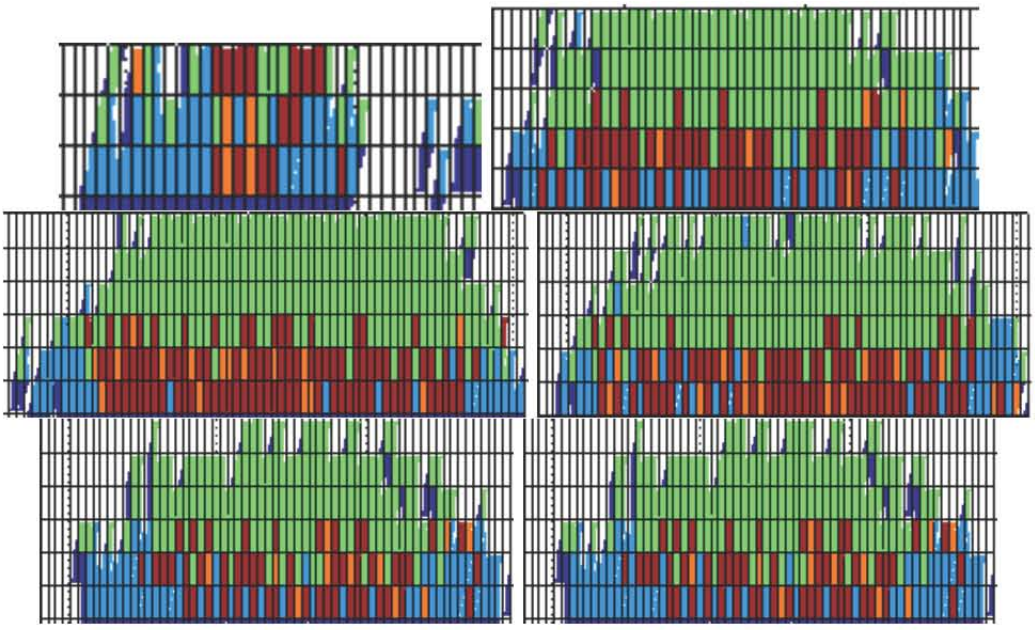

Figure 7.6: *Slices of the distribution of cell types. Blue cells are normal. Green cells are inert. Brown cells are EPS matriz producers. Orange cells are surfactine producers.*

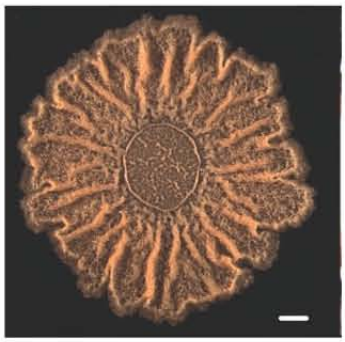

Figure 7.7: *Radial geometry found in B. Subtilis biofilms. Taken from [20]*

model estimates the concentration field of all involved chemicals by solving Poisson equations with their specific boundary conditions and parameters. Probabilistic laws are defined in terms of local concentrations to simulate reproduction and differentiation processes happening on individual bacteria.

The simulated differentiation cascades contain *comX* and *Surfactine* as main autoinductors which regulate the transformation of normal cells into surfactine producers and EPS cells respectively, imposing certain thresholds for these compounds. Additionally a shortage of nutrients /oxygen leads to a sporulation process. Nutrient/oxygen driven expansion is too slow and too many cells are deactivated in the upper part and the core of the biofilm. Considering extraction of water from agar into the biofilm, we create water cells inside and allow for oxygen uptake through the agar/biofilm interface. This fosters a faster expansion and reduces the number of inert cells.

Simulations agree qualitatively with observed experimental data [20] in the sense that the spatial distribution of the different types of differentiated cells is similar. Also, the geometry of the expanding biofilm is not too different: a round patch with wavy borders expanding in the radial direction. There two facts that could be improved though. First, the observed bacterial colonies become wrinkled after a certain time. This has been related to macroscopic buckling effects as the size of the colony grows. Second, biofilm colonies are observed to contain channels that drive water and nutrients from the agar surface inside the biofilm, like small circulatory networks. They might be caused by erosion of weak biofilm regions by the inner biofilm fluids. In the initial stages of the biofilm development, oxygen may come mainly from air creating a necrotic region near the surface, that will deactivate and become weak. Easy to erode by the suctioned fluids. These effects should be incorporated in the model for a better description of the structure of the colonies.

The hybrid models that are used here have limitations and the probability laws are completely heuristic. It would be convenient to develop additional models based on mass and momentum transfer laws to check under which physical assumptions the different geometric patterns observed in biofilm development appear and which would be the order of magnitude of the numerical parameters used in this discrete description in order to check its validity. An attempt to put in practice this idea for biofilms in flows is described in next section.

Chapter 8

Continuum modeling and perturbation analysis of a biofilm-fluid system

In previous chapters a description of biofilms using a hybrid discrete-continuous approach has been proposed. However, that approach is based on stochastic laws which describe the reality more accurately depending on how complete is the description of the system physics provided. These models also include several numeric constants which do not have a physical meaning themselves and must be calibrated previously to approach experimental results with numerical predictions. The overall insight provided about biofilms as physical systems is then not complete.

Another approaches may be able to offer complementary information about biofilm evolution. Biofilm patterns are affected by combinations of physical variables such as the flow velocity or the reproduction kinetics. Continuous models may be a good choice because they are based on PDEs which describe momentum, heat and mass transfer processes dynamically.

This chapter discusses possible physical approaches that could be used to describe biofilms dynamics previously to decide about a particular PDE system of equations, see section 8.1. The next step will be to simplify the selected approach to obtain a reduced model in section 8.2). Section 8.3 presents a perturbative study and a discretization method. Finally, section 8.4 ends this chapter discussing conclusions and perspectives for improvement.

8.1 Introduction

Biofilm patterns depend on the way in which their mechanical structure is strained due to different forces acting on the biofilm - fluid interphase. Biofilms are believed to be soft material with properties between a fluid and a solid [90, 141]. This fact allows to use both approaches to describe biofilm properties and behavior.

8.1.1 Biofilm as a solid material

If biofilms are considered like a common solid material, they can be characterized by measuring mechanic properties that are obtained in standardized experiments. Strain - Stress curves (see picture 8.1) are necessary to get basic parameters used in solid mechanics theory: Young Modulus, Poisson coefficient or Shear Modulus are some of these parameters needed to define completely from a mechanic point of view. Several experiments measure these variables, as for example those found in [19] and [87].

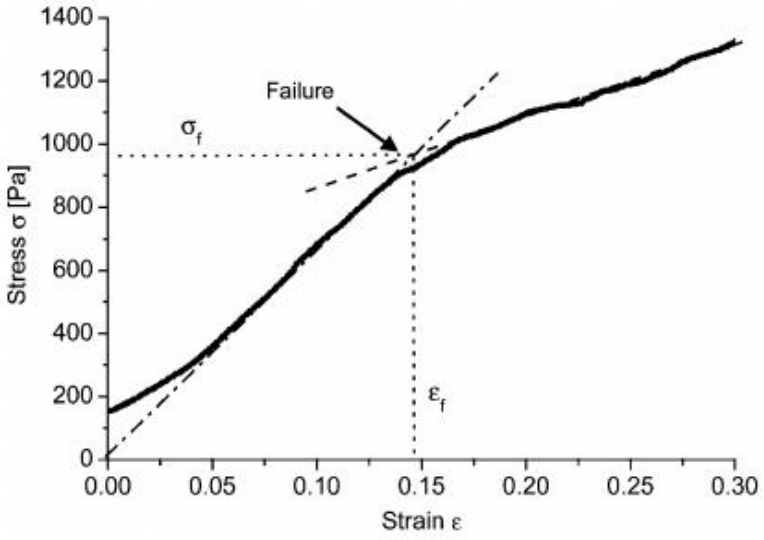

Figure 8.1: *Stress - Strain curve obtained in a biofilm experiments [82] for pseudomonas aeruginosa at a constant deformation speed of 1 $\mu m/s$*

Rheology studies are also necessary in order to measure the dependance of the mechanical stress and strain with time. Once experiments (i.e. [66,

87]) determine the creep and relaxation curves (see picture 8.3), a fitting procedure with available theoretical models is performed. There are several models, but most of them are based in the approximation that the mechanical behavior of the solid is similar as if it was composed by the assembly of several mechanical devices (springs and dashes) in serial or parallel configuration (see picture 8.2). These elements can be predefined (Voight elements, Kelvin elements) or it can be a combination of them (standard linear solid model). This similarity is based on the assumption that each element has a singular behavior when they are strained, and an adequate combination of them can approximate the real behavior of whatever solid.

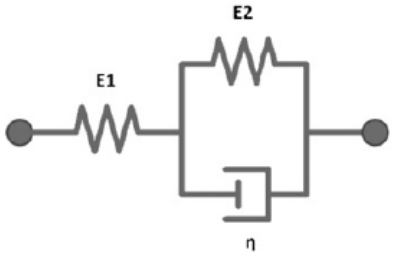

Figure 8.2: *Voight element scheme. It consists on a dash and a spring in parallel, together with another spring in series.*

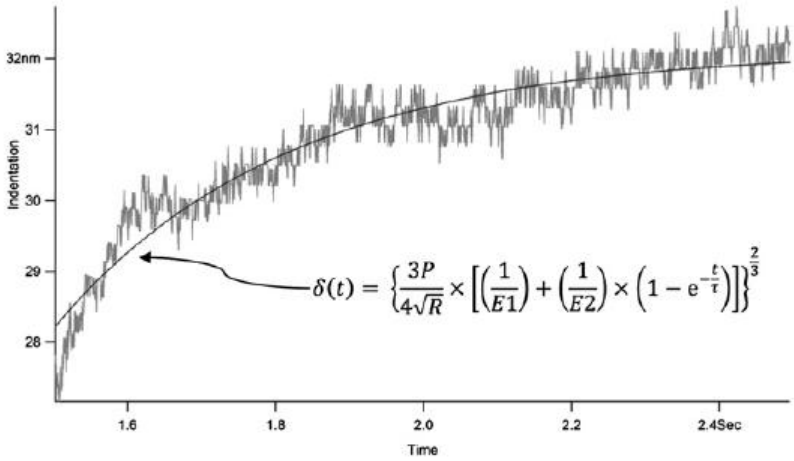

Figure 8.3: *Creep curve obtained in a biofilm indentation experiment ([87]) and theoretical fitting with standard linear solid model*

There may be also other parameters that could affect biofilm mechanics such as the temperature or the chemical composition, which forces to use additional equations to show that dependence. A classic example might be the state equations proposed by Johnson and Cook [72] or Klopp et al. [77]. With these variables and relations, simulations of mechanical straining by using finite element methods can be carried away to predict biofilm dynamics.

However, there are major problems when trying to generalize these variables and models for the overall field: they are function of other conditions that affect biofilm structure: hydrodynamics of the external flow, nutrient availability or genetics generate variability in these parameters, which convert the task into a very complicated objective.

8.1.2 Biofilm description as biomaterials

The description of biofilm structure and composition as a solid is a first trial in the objective of describing biofilm behavior as a specific type of solid material with a biological nature. Although biofilms behave in fact as a whole living organism, it is known that they are formed by a mixture of living bacteria and a polymeric material that protect them, allowing to consider the whole as a common material with certain properties.

By applying this approach. biofilms could be classified as an specific type of biomaterials, understanding as biomaterials an specific type of materials (natural or artificial) in contact with biological systems that try to fulfill certain tasks [128]. Their nature is very extensive, including almost all type of complex chemical compounds created by living beings (proteins, biofluids, inorganic structures like shells, etc.) or human made compounds (teflon, silicone, titanium alloys, etc.).

The gelly nature and the biological origin of biofilms led several researchers to classify them as biogels. Biofilms may be considered to be highly porous polymer gels [24] and diffusion studies demonstrated gel-like characteristics [32]. This material is composed by an organic polymeric matrix (biopolymer) filled with fluid whose properties depend on its internal composition and structure.

This definition fits with the real basic structure of a biofilm: it has been widely observed that biofilms can be considered as clumps of cells separated

by intersticial voids and channels [33, 99, 101], and the nature of the filling fluid (the ratio between water and other metabolic products produce by bacteria) will affect the mechanics of displacement and the stress field evolution.

The mechanical properties of biofilms are also affected by both environmental and genetical conditions, a wide variety of behaviors being possible. Viscous liquid, viscoelastic solid, viscoplastic solid or viscoelastic liquid are typical choices used to describe biofilms [153, 22]. Attending to this, biogels are expected in general to be a viscoelastic material, with a nonlinear creep or relaxation curves when they are tested [122]. Their mechanical properties will depend on time if enough stress is applied. Creep will affect in different ways the biofilm structure, being possible an irreversible recovering of the initial state: viscoelastoplastic behaviors have to be taken into account in the biofilm description [164].

Biofilm solid mechanics is an area that is currently being developed. The complex interaction of many variables in the overall behavior of the biofilm makes difficult a full description: only a few in situ rheological tests have been done [22, 112]. In those experiments, mechanical properties of biofilms both as a liquid (viscous properties) and as a solid (elastic properties) were measured. However, there is a large list of experiments which try to define and characterize the biofilm mechanics, though shear or elastic constants [153, 132, 1], morphology [149], or other variables that affect them like nutrient concentration and hydrodynamics [151].

8.1.3 Biofilm description as an hydrogel

Specially interesting are other materials that can be structurally similar to biofilms, and particularly hydrogels. Their properties [4] are quite similar to biogels. They are also composed by polymeric chains filled with fluid (water) and their mechanical behavior is similar. All the models developed for them describing the stress distribution and displacement fields could be a good approach to perform further investigations on biofilm fields. Picture 8.4 show similarities in their inner structure between hydrogels and EPS matrix of biofilms.

There are several authors [82] which established similarities between biofilms and hydrogels. Although hydrogels are characterized by existence of chemical bonds between solvent and polymeric structure, in biofilms these bonds are expected to have a physical nature (like reversible adsorption forces), being

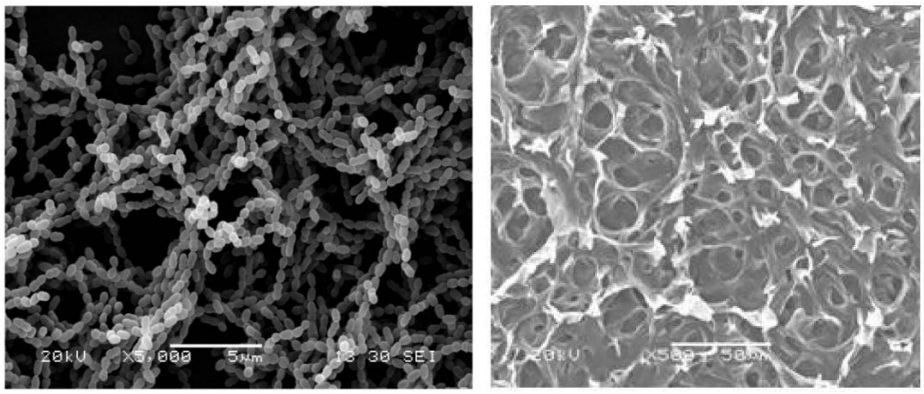

Figure 8.4: *Comparation between a biofilm EPS matrix structure (left) and hydrogel inner structure (right). The existence of a structural similarity might suggest a similar mechanical behaviour. Images taken from [127] y [55] respectively.*

weaker and more temporal. However, these bonds may be strong enough to show a behavior similar to the hydrogels.

This kind of approach is promising, but there are certain difficulties that have to be overcome. Some of them are related with the unavailability of experimental equipments. As biofilms have very specific properties, special adaptations in conventional solid mechanics equipments and instruments are needed in order to perform the experiments [19, 87]. There is also the problem of the heterogeneity shown by biofilms: they are living organisms that adapt themselves to the environment to survive, so their mechanical properties will be directly linked with many external (flow, antibiotics, etc.) and internal variables (bacterial strain, biofilm age, etc.). Trying to design a general set of experiments which deals with such variability of behaviors makes the experimentation stage a very complicated step that must be studied very carefully.

8.1.4 Fluid description of a biofilm

The description of the biofilm evolution dynamics (which involves the study of boundary geometries adopted by the biofilm - fluid interphase) by using a solid mechanics approach is a powerful method able to obtain accurate results. However, its numerical implementation is quite complex and rigid: although the biofilm structure may be described by using finite element method, the description of outer fluid would need another type of computational methods such as finite volumes or finite differences. There is also the fact that coupling both problems is not trivial, as the boundary geometry is evolving with time. The excessive required computational effort forces us to assume certain reasonable hypothesis that allow us to solve the problem in a faster and simpler way.

It has been already pointed out in chapter 7 that some biofilms behave more like solids, whereas other biofilms behave more like fluids. This section assumes that the target biofilm-fluid system is not a solid-fluid system but a two-phase fluid system. This allows us to use the same computational methodology for the whole system through the distinction of both subdomains separated by a dynamic interface.

For simplicity, we consider a 2D representation of the overall domain Ω, in which the biofilm is represented by a subdomain Ω_1. The biofilm is attached to a smooth surface by its lower part and exposed to a fluid composed by a mixture of water, nutrients and oxygen (subdomain Ω_0) which flows through a rectangular channel of length L and height H under certain hydrodynamic conditions. The fluid phase Ω_0 exerts a shear stress on the biofilm interface, straining the subdomain Ω_1 as a result of the boundary Γ displacement (which separates both subdomains). Additionally, the biofilm boundary Γ is pushed normally due to biologic chemical reactions performed by bacteria to increase their population. Those reactions are fed by the availability of nutrients and oxygen present in the fluid flow Ω_0. Both oxygen and nutrients will permeate through the interface into the biofilm subdomain due to gradient forces by molecular diffusion mechanism. The overall problem consists of calculating the behavior and evolution of this system during the time when the initial conditions of all involved variables (concentration fields for oxygen and nutrients, hydrodynamic conditions, initial geometry for Ω_1 and transport and mechanic properties of each phase) are known. It is also quite desirable to know the asymptotic behavior of the system under certain conditions. Picture 8.5 shows an illustrative scheme of this system.

The overall description is a two-phase dynamic system. Both phases are considered as fluids, described by Navier-Stokes equations (mass and momentum conservation). Mass conservation is described by convection-diffusion and diffusion-reaction processes that rule mass transport inside the fluid and biofilm phase respectively. The PDE system of equations is completed with their respective boundary conditions: no penetration and no slip on the channel walls and continuity of shear forces and concentration fields through interface Γ, which couple both phases and close the description of the system.

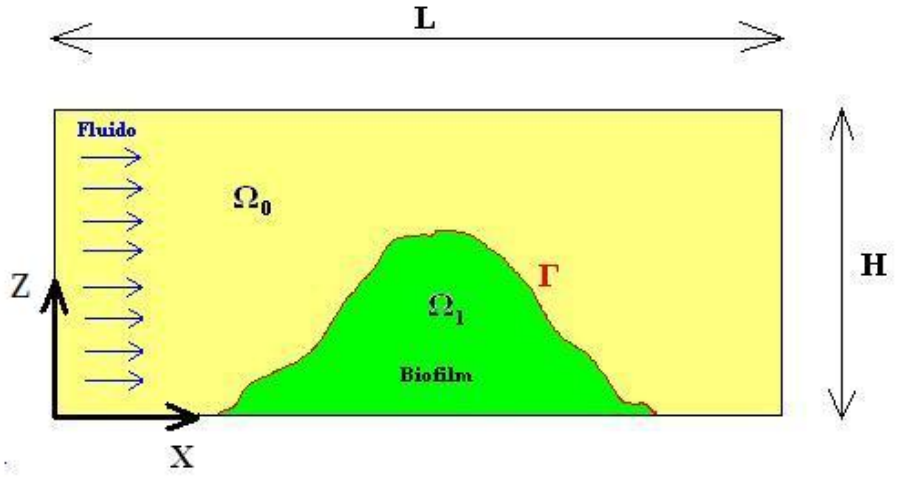

Figure 8.5: *Channel with biofilm. The domain is divided into two subdomains* Ω_0 *(water and nutrients) and* Ω_1 *(biofilm) separated by a free boundary* Γ *which evolves during the time*

Each phase has its physical properties. The biofilm phase has a density ρ_b and viscosity μ_b, and diffusion coefficient for nutrients $D_{s,b}$. The fluid phase has a density ρ_f, a viscosity μ_f and a diffusion coefficient for nutrients $D_{s,f}$. Surface tension effects are also considered. They will be included in the interface force balance.

Variables and operators

For ease of the reader, we list below all the variables and operators involved in the theoretical development presented in the next section:

h: Biofilm thickness. Dynamic variable which changes through the space and time.

$\vec{n}$: Biofilm surface normal vector defined in terms of arc length and biofilm thickness.

$$\vec{n} = \frac{1}{[1+(\partial_x h)^2]^{1/2}} \begin{pmatrix} -\partial_x h \\ 1 \end{pmatrix}$$

$\vec{t}$: Biofilm tangent surface vector defined in terms of arc length and biofilm thickness.

$$\vec{t} = \frac{1}{[1+(\partial_x h)^2]^{1/2}} \begin{pmatrix} 1 \\ \partial_x h \end{pmatrix}$$

p: Biofilm - fluid interface pressure.

τ_b, τ_f: Biofilm and fluid shear stresses.

$\mathbf{T}$: Biofilm and fluid stress tensors for both interface sides.

$$\mathbf{T}_b = \begin{pmatrix} p_b & \tau_{xz,b} \\ \tau_{xz,b} & p_b \end{pmatrix}$$
$$\mathbf{T}_f = \begin{pmatrix} p_f & \tau_{xz,f} \\ \tau_{xz,f} & p_f \end{pmatrix}$$

κ: Boundary curvature defined in terms of the first and second derivative of the biofilm thickness.

$$\kappa = \frac{\partial_x^2 h}{[1+(\partial_x h)^2]^{3/2}}$$

$\vec{\nabla}_s \sigma$: Surface tension gradient vector.

$$\vec{\nabla}_s \sigma = \vec{\nabla}\sigma - \vec{n}\left(\vec{n} \cdot \vec{\nabla}\sigma\right) = \begin{pmatrix} \partial_x \sigma - \frac{(\partial_x h)^2 \partial_x \sigma - \partial_x h \partial_z \sigma}{1+(\partial_x h)^2} \\ \partial_z \sigma - \frac{\partial_z \sigma - \partial_x h \partial_x \sigma}{1+(\partial_x h)^2} \end{pmatrix}$$

Full biofilm - fluid partial differential system of equations

The PDEs system which describes the two phase problem is presented here. In both phases, mass and momentum conservation equations apply. Nutrient concentration equations are also necessary for both biofilm and fluid phases.

The system of equations is completed by defining their respective boundary conditions.

FLUID FLOW PHASE EQUATIONS (Ω_0)

Conservation of mass

Applied to the incompressible and homogeneous fluid yields the incompressibility condition:

$$\nabla \cdot \vec{V_f} = 0 \qquad [kg/m^3 min] \tag{8.1}$$

where V_f is the fluid velocity

Conservation of nutrients

$$C_{s,f}|_{\Omega_0} = cte \qquad [kg/m^3 min] \tag{8.2}$$

where C_s is the concentration of substrate (or nutrient). It is assumed that the concentration of nutrients is well mixed through all the volume. This implies a constant concentration in all the subdomain Ω_0.

Momentum conservation

$$\frac{\partial \vec{V_f}}{\partial t} + \vec{V_f} \cdot (\nabla \vec{V_f}) = -\frac{1}{\rho_f} \nabla p_f + \nu_f \nabla^2 \vec{V_f} \qquad [kg/m^2 min^2] \tag{8.3}$$

where ρ_f is the density of the fluid and p_f its pressure.

These equations must be supplemented with boundary and initial conditions.

Boundary conditions

The velocity field at $x = 0$ and $x = L$ does not have y component, and it is known. No slip and no penetration conditions are imposed on the walls of the channel. Conservation laws yield relations for velocities in fluid phase (V_f) and biofilm phase (V_b), and for the pressure at Γ. An additional numerical boundary condition is imposed at the interface to avoid singularities.

$$\begin{cases} \vec{V_f}(0,z,t) = (u_0(z), 0) \\ \vec{V_f}(L,z,t) = (u_\infty(z), 0) \\ \vec{V_f}(x,H,t) = (0,0) \\ \vec{V_f}|_{z=0} = (\beta\partial_z u, 0) \ \text{ if } (x,z) \notin \Gamma \text{ (used to avoid numerical singularities)} \\ \vec{V_f}|_\Gamma = \vec{V_b}|_\Gamma \ \text{ if } (x,z) \in \Gamma \\ V_f(x,z,0)|_{\Omega_0} = (v_{0x}, v_{0z}) \\ p(0,z,0) = p_0 \\ p(L,z,0) = p_\infty \ \text{ or } \ \tau\vec{n}|_{x=L} = -p_\infty \vec{n}|_{x=L} \end{cases} \tag{8.4}$$

BIOFILM PHASE EQUATIONS (Ω_1)

To simplify, the biofilm is assumed to be a Newtonian fluid with transport and viscosity coefficients:

$$\begin{cases} D_{s,b} = constant & [m^2/min] \\ \mu_b(x,z) = constant & [kg/m\ min] \end{cases} \tag{8.5}$$

Conservation of Biomass

The biofilm biomass changes because there is a chemical reaction which converts a fraction Y of the metabolized nutrients into biomass, varying the position of the boundary Γ. A source term is added to take this into account:

$$\frac{\partial \rho_b}{\partial t} + \nabla \cdot \rho_b \vec{V_b} = \frac{\gamma}{Y} \frac{C_s}{C_s + K_s} \qquad [kg/m^3 min] \tag{8.6}$$

where ρ_b is the biofilm density, γ/Y is a constant ratio taking into account biomass generation kinetics and K_s is the Monod saturation constant.

Conservation of nutrients

Oxygen balance equations should be included as well but we consider that oxygen is in excess with respect to the nutrient. This assumption implies that the limiting chemical species will be the nutrient, and then its mass transport equation will regulate the whole system. The nutrient will be transported

through the biofilm phase by a diffusion mechanism at the same time that it is reacting chemically with the oxygen in the whole biofilm domain:

$$\frac{\partial C_s}{\partial t} = D_{s,b}\nabla^2 C_s - \gamma \frac{C_s}{C_s + K_s} \qquad [kg/m^3 min] \tag{8.7}$$

where ρ_b is the density of biofilm, C_s the concentration of nutrients and K_s the Monod constant for the nutrient half-saturation and γ the bacterial nutrient consumption kinetic constant.

Momentum conservation

$$\frac{\partial \vec{V_b}}{\partial t} + \vec{V_b} \cdot (\nabla \vec{V_b}) = -\frac{1}{\rho_b}\nabla p_b + \nu_b \nabla^2 V_b \qquad [kg/m^2 min^2] \tag{8.8}$$

where ν_b is the kinematic viscosity of the biofilm.

Boundary conditions

These equations must be supplemented with boundary and initial conditions. As in the previous case, no slip and no penetration conditions hold on the walls and stress equilibrium applies at the interface Γ.

$$\vec{V_b}(x, 0, t) = (0, 0) \tag{8.9}$$

$$(T_{ij}|_f - T_{ij}|_b)|_\Gamma \cdot n_j|_\Gamma = -\sigma\kappa n_j|_\Gamma \text{ i,j=fluido,biofilm} \tag{8.10}$$

The concentration is known at the interface Γ and there is a no flux at the walls.

Concentration field boundary conditions for the nutrient

$$\begin{cases} C_s(x, z, t)|_\Gamma = C_0 \\ \frac{\partial C_s}{\partial z}|_{z=0} = 0 \end{cases} \tag{8.11}$$

Initial conditions

$$\begin{cases} \vec{V_b}(x,z,0) \\ C_s(x,z,0) \end{cases} \tag{8.12}$$

The solution of this system of equations governs the behavior of the biofilm (subdomain dynamics) and the flow displacement field. In this section the study of the evolution of the interface Γ is a priority because it governs the patterns formed by the biofilm due to the mechanisms of erosion and biofilm growth. The above mathematical formulation is clearly disadvantageous, since the interface position appears implicitly in the problem through the boundary conditions regarding force balance and velocity fields on the Γ interface. This fact makes a perturbative study much harder to develop and make it necessary to reformulate the problem.

Obtaining an expression which describes the evolution of the boundary itself (as a function of the height) would be advantageous when using perturbation methods. For this reason, the **PDE system for the biofilm phase will be reformulated** and handled to reach a simple and useful equation able to describe the movement of the interface Γ.

8.1.5 Reduced equations for the biofilm

In this section we rewrite the equations for the biofilm phase producing an equation for its moving boundary Γ.

- Momentum conservation equation in x-axis

$$\rho\left(\partial_t u + u\partial_x u + w\partial_z u\right) = -\partial_x p + \mu\nabla^2 u \tag{8.13}$$

- Momentum conservation equation in z-axis

$$\rho\left(\partial_t w + u\partial_x w + w\partial_z w\right) = -\partial_z p + \mu\nabla^2 w \tag{8.14}$$

- Biomass conservation equation

$$\partial_x u + \partial_z w = \frac{\gamma}{\rho_b}\frac{c_s}{c_s + K_s} \ (\rho_b = cte) \tag{8.15}$$

- Mass flux through the interface as a function of the velocity field

$$j = \rho_f(\vec{v_f} - \vec{v_i}) \cdot \vec{n} = \rho_b(\vec{v_i} - \vec{v_b}) \cdot \vec{n} \tag{8.16}$$

- Chemical species conservation equation

$$\frac{\partial c_s}{\partial t} + \partial_x(uc_s) + \partial_z(wc_s) = D_s\nabla^2 c_s - \gamma\frac{c_s}{c_s + K_s} \tag{8.17}$$

Here, u stands for the fluid velocity in x direction, w for the fluid velocity in z direction, c is the concentration of nutrients, p is the pressure, t is denotes time. Notice that $v_{f,n}$, $v_{b,n}$ and v_i are the respective normal components of velocity field of water (index f), the velocity of the biofilm phase (index b) and interface velocity (index i). The respective boundary conditions are:

z=0

$$w = 0 \tag{8.18}$$

$$u - \beta\partial_z u = 0 \tag{8.19}$$

$$-D_s\frac{\partial c_s}{\partial z} = 0 \tag{8.20}$$

Boundary condition (8.19) is added instead no slip condition (u=0) to avoid singularities when PDE system is integrated. It was proposed by Huh and Scriven [67] and by Dussan and Davis [40]). Other conditions are no penetration of biofilm and no mass flux of nutrient through the wall. On z=h(x,t) we have:

z=h(x,t)

$$w = \partial_t h + u\partial_x h \tag{8.21}$$

$$c_s = c_0 \tag{8.22}$$

$$j(\vec{v}_{b,n} - \vec{v}_{f,n}) - (\mathbf{T_b} - \mathbf{T_f})\cdot\vec{n} = \kappa\sigma\vec{n} - \vec{\nabla}_s\sigma \tag{8.23}$$

$$\tau_b = \mu_b\partial_z u \tag{8.24}$$

where (8.23) is the stress equilibrium taken from Oron, Davis and Bankoff [113]. Equation (8.21) is the typical dynamic evolution boundary condition on velocities. Eq.(8.17) gives the value of C at the boundary. There are other boundary conditions that can be applied instead of (8.22) when the concentration in fluid phase is not assumed to be constant:

$$D_f \partial_z c_f = D_b \partial_z c_b \tag{8.25}$$

Equation (8.23) is a force balance per unit area at the upper boundary (z=h(x,t)). This condition can be split into two conditions for tangential and normal components of the force acting over the biofilm surface. More details, see appendix A:

Normal component:

$$-\left(\frac{1}{\rho_b}+\frac{1}{\rho_f}\right)\left(\gamma\frac{c_s}{c_s+K_s}\frac{\int_0^L h dx}{\int_0^L \sqrt{1+(\partial_x h)^2}dx}\right)^2-\left[(p_b-p_f)-\frac{2(\tau_{xz,b}-\tau_{xz,f})\partial_x h}{1+(\partial_x h)^2}\right]$$

$$=\frac{\partial_x^2 h}{[1+(\partial_x h)^2]^{3/2}}\sigma \tag{8.26}$$

Tangential component:

$$(\tau_{xz,b}-\tau_{xz,f})\frac{1-(\partial_x h)^2}{1+(\partial_x h)^2}=\frac{\partial_x\sigma+\partial_z\sigma\partial_x h+\partial_z\sigma(\partial_x h)^3+\partial_x\sigma(\partial_x h)^2}{1+(\partial_x h)^2} \tag{8.27}$$

8.1.6 Nondimensionalization

In this section equations will be nondimensionalized. All nondimensionalized variables are written below in the next table:

Variable	Dimensional	Dimensionless
z	h_0	Z
x	h_0/ϵ	X
u	U_0	U
w	$U_0\epsilon$	W
t	$h_0/U_0\epsilon$	T
-	K/C_0	K'
τ_0	$\mu U_0/h_0$	τ_i
Π_0	$\mu U_0/(h_0\epsilon)$	Π
c	$C_0\epsilon$	C
σ	$\mu U_0/\epsilon$	Σ
-	U_0h_0/ν	Re (Reynolds)
-	$\gamma/(\rho U_0/h_0)$	Da_U (Damkhler)
-	$\gamma/(C_0D/h_0^2)$	Da_D(Damkhler)
-	$(\gamma^2h_0^2/\rho_f)/(\mu U_0/h_0)$	ξ
-	h_0U_0/D	Sh(Sherwood)

With these definitions the main set of equations is nondimensionalized as follows. Details of how equations (8.36) and (8.37) have been obtained can be seen in appendix A. The deduction of equation (8.31) is found in appendix B. Equations (8.28) and (8.29) can be obtained immediately from text of Bankoff and Davis [113]:

$$\epsilon Re(\partial_t U + U\partial_X U + W\partial_Z U) = -\partial_X P_b + \partial_Z^2 U + \epsilon^2\partial_X^2 U \tag{8.28}$$

$$\epsilon^3 Re(\partial_T W + U\partial_X W + W\partial_Z W) = -\partial_Z P_b + \epsilon^2\partial_Z^2 W + \epsilon^4\partial_X^2 W \tag{8.29}$$

$$\epsilon(\partial_X U + \partial_Z W) = Da_U\frac{C}{\epsilon C + K'}\epsilon \tag{8.30}$$

$$\epsilon Sh[\partial_T C + \partial_X(CU) + \partial_Z(CW)] = \epsilon^2\partial_X^2 C + \partial_Z^2 C - Da_D\frac{C}{C + K'} \tag{8.31}$$

Boundary conditions:

Z=0

$$W = 0 \tag{8.32}$$

$$U - \beta_0 \partial_Z U = 0 \tag{8.33}$$

Z=H(X,T)

$$W = \partial_T H + U \partial_X H \tag{8.34}$$

$$Q = \int_0^H U dZ \tag{8.35}$$

$$-2\xi \left(\frac{C}{\epsilon C + K'} \right)^2 \left(\frac{\int_0^L H dX}{\int_0^1 \sqrt{1 + \epsilon^2 \left(\partial_X H \right)^2} dX} \right)^2 \epsilon^2 \tag{8.36}$$

$$- \left[(P_b - P_f) - \frac{2(\tau_b - \tau_f)\partial_X H}{1 + \epsilon^2 (\partial_X H)^2} \right] \epsilon = \frac{\partial_X^2 H \Sigma}{[1 + \epsilon^2 (\partial_X H)^2]^{3/2}} \epsilon$$

$$(\tau_b - \tau_f) \frac{1 - \epsilon^2 (\partial_X H)^2}{1 + \epsilon^2 (\partial_X H)^2} \tag{8.37}$$

$$= \frac{\partial_X \Sigma + \partial_Z \Sigma \partial_X H + \partial_Z \Sigma (\partial_X H)^3 \epsilon^2 + \partial_X \Sigma (\partial_X H)^2 \epsilon^2}{1 + \epsilon^2 (\partial_X H)^2}$$

$$\tau_f = \partial_Z U \tag{8.38}$$

The original system of equation has been simplified and nondimensionalized, but there is still the inconvenient that biofilm-fluid boundary Γ is an implicit variable that cannot be obtained directly by solving these equations. We should perform costly calculations to solve a highly non linear system of partial differential equations, but we are only interested in studying the evolution of the boundary. This handicap is overcome in the next section.

8.2 Thin film approximation. Lubrication equation

Biofilms tend to colonize surfaces, trying to occupy all the available surface if the conditions are favorable. They are also influenced by the surrounding fluid and by other forces like surface tension or the gravity force. These factors make much more favorable an increment of size of the colonies in a direction tangential to the surface instead of a growth in the orthogonal direction. For this reason, a reasonable approximation may be applied to simplify the equations: let assume that variations along the film are much more gradual with time than those normal to it, and that variations are slow in time. This approximation is called the "*long-scale approximation*" [113]. The essential information which provides is that considering the x axis scales with a wavelength λ, and the length in z axis scales with h_0, we can define that a perturbation is long-scale if:

$$\epsilon = \frac{2\pi h_0}{\lambda} \lll 1 \tag{8.39}$$

With this criterion, a perturbation analysis is performed to simplify the system of equations at the same time that information can be gathered about the stability of the system. By performing reasonable simplifications based on balance of different terms and substituting several expressions into a single equation, this method will yield an evolution equation for the biofilm-fluid interface. Once this expression is reached a deep analysis of the system by developing classic stability studies and numeric calculations may be performed.

8.2.1 Approximation

An expansion of different main variables in series of ϵ is proposed to analyze how the system will respond respond to a small perturbation:

$$U = U_0 + \epsilon U_1 + \epsilon^2 U_2 + ... \tag{8.40}$$

$$W = W_0 + \epsilon W_1 + \epsilon^2 W_2 + ... \tag{8.41}$$

$$P_b = P_{b,0} + \epsilon P_{b,1} + \epsilon^2 P_{b,2} + ... \tag{8.42}$$

$$C = C_0 + \epsilon C_1 + \epsilon^2 C_2 + ... \tag{8.43}$$

Equations (8.40), (8.41), (8.42) and (8.43) may be substituted inside the rest of the equations described in the previous section. Only ϵ terms will be retained. The system of equations becomes:

$$\partial_Z^2 U = \partial_X P_b \tag{8.44}$$

$$\partial_Z P_b = 0 \tag{8.45}$$

$$\partial_T H + \partial_X Q = \frac{Da_U}{K'} \int_0^H C dZ \tag{8.46}$$

$$Q = \int_0^H U \cdot dZ \tag{8.47}$$

$$C = \frac{\cosh\left(\sqrt{\frac{Da_D}{K'}} Z\right)}{\cosh\left(\sqrt{\frac{Da_D}{K'}} H\right)} \tag{8.48}$$

$$J = Da_U \frac{C}{\epsilon C + K'} \int_0^L H dX \tag{8.49}$$

Notice that the variables written above without index should have index 0 when applying the expansion in series. In order to simplify notations they have been omitted.

For more details about expression (8.48) and equation(8.46), see appendix B and C respectively.

Boundary conditions

Z=0

$$W = 0 \tag{8.50}$$

$$U - \beta_0 \partial_Z U = 0 \tag{8.51}$$

Z=H

$$W = \partial_T H + U\partial_X H \longrightarrow \partial_X W = 0 \tag{8.52}$$

$$(P_b - P_f) - 2(\tau_b - \tau_f)\partial_X H = -\partial_X^2 H\Sigma \tag{8.53}$$

$$\tau_b - \tau_f = \partial_X \Sigma \tag{8.54}$$

$$\tau_b = \mu_b \partial_Z U \longrightarrow \partial_Z U = \tau_f + \partial_X \Sigma \tag{8.55}$$

Now the new system of equations will be handled properly. The first step will be to differentiate the expression (8.53) to get an equation valid for $\partial_X P_b$, which will be substituted in eq. (8.44). For simplicity, the expression will not be written in its expanded shape:

$$\partial_Z^2 U = \partial_X P_b \tag{8.56}$$

Integrating the previous expression twice with respect to Z:

$$U = \partial_X P_b \frac{Z^2}{2} + A_1 Z + A_2 \tag{8.57}$$

Boundary conditions will be applied to get the constants A_1 and A_2:

Boundary conditions:

Z=0

$$U - \beta_0 \partial_Z U = 0 \longrightarrow A_2 = \beta_0 A_1 \tag{8.58}$$

Z=H

$$\partial_Z U = (\tau_f + \partial_X \Sigma) \longrightarrow A_1 = (\tau_f + \partial_x \Sigma) - \partial_X P_b H \tag{8.59}$$

So:

$$U = \partial_X P_b \left[\frac{Z^2}{2} - ZH - H\beta_0 \right] + (\tau_f + \partial_X \Sigma)(Z + \beta_0) \tag{8.60}$$

Equation (8.60) gives the velocity field. The flow can be calculated by integration:

$$Q = \int_0^H U dZ = \partial_X P_b \left[-\frac{1}{3} H^3 - \beta_0 H^2 \right] + (\tau_f + \partial_X \Sigma) \left(\frac{1}{2} H^2 + \beta_0 H \right) \tag{8.61}$$

In the other hand, by differentiating with respect to X the result of (8.53) and by substituting (8.54) the following expression may be obtained:

$$\partial_X P_b = \partial_X P_f + 2\partial_X^2 \Sigma \partial_X H - \partial_X^3 H \Sigma - \partial_X^2 H \partial_X \Sigma + 2\partial_X \Sigma \partial_X^2 H \tag{8.62}$$

And finally by substituting equation (8.61) in (8.46) taking into account the previous expression:

$$\begin{aligned} &\partial_T H + \partial_X \left[(\tau_f + \partial_X \Sigma) \left(\frac{1}{2} H^2 + \beta_0 H \right) \right] \\ &-\partial_X \left[\partial_X P_b \left(\frac{1}{3} H^3 + \beta_0 H^2 \right) \right] \\ &= \frac{Da_U}{K'} \frac{1}{\sqrt{\frac{Da_D}{K'}}} \int_0^H C_0 dZ \end{aligned} \tag{8.63}$$

Additionally, by taking into account the deduction of **appendix C** to rewrite the second term, the boundary evolution equation can be finally written as:

$$\begin{aligned} &\partial_{\mathbf{T}} \mathbf{H} + \partial_{\mathbf{X}} \left[(\tau_{\mathbf{f}} + \partial_{\mathbf{X}} \mathbf{\Sigma}) \left(\frac{\mathbf{1}}{\mathbf{2}} \mathbf{H^2} + \beta_{\mathbf{0}} \mathbf{H} \right) \right] \\ &-\partial_{\mathbf{X}} \left[\partial_{\mathbf{X}} \mathbf{P_b} \left(\frac{\mathbf{1}}{\mathbf{3}} \mathbf{H^3} + \beta_{\mathbf{0}} \mathbf{H^2} \right) \right] \end{aligned} \tag{8.64}$$

$$= \frac{\mathbf{Da_U}}{\mathbf{K'}} \frac{\mathbf{1}}{\sqrt{\frac{\mathbf{Da_D}}{\mathbf{K'}}}} \tanh\left(\sqrt{\frac{\mathbf{Da_D}}{\mathbf{K'}}}\mathbf{H}\right)$$

8.2.2 Perturbative study

The equation obtained for the interface allows us to study its behavior when it is excited with small perturbations. The main objective is then to deduce stationary points, periodic structures and parameter ranges in which the boundary becomes unstable.

It is convenient to develop all the terms of the expression. However, if (8.62) is substituted in (8.64), it can be seen that there are still some terms which difficult the perturbative study. If this equation could be simplified by assuming some reasonable hypothesis, it could be transformed into a more simple expression. A reasonable hypothesis that may be applied is to assume that the shear stress produced by the flow in the biofilm interface is constant (τ_f=constant) when the flow is in a steady state. The mechanism for change will be the biofilm growth rate produced by the chemical reaction. It can be also assumed that the surface tension on the biofilm interface (Γ) is constant at every point: (Σ=constant and $\beta_0 = 0$). With these hypotheses, the evolution equation (8.64) can be simplified:

$$\partial_{\mathbf{T}}\mathbf{H} + \frac{\tau_{\mathbf{f}}}{\mathbf{2}}\partial_{\mathbf{X}}\left[\mathbf{H^2}\right] - \left(\partial^{\mathbf{2}}_{\mathbf{X}}\mathbf{P_f} - \partial^{\mathbf{4}}_{\mathbf{X}}\mathbf{H\Sigma}\right)\frac{\mathbf{H^3}}{\mathbf{3}} - \left(\partial_{\mathbf{X}}\mathbf{P_f} - \partial^{\mathbf{3}}_{\mathbf{X}}\mathbf{H\Sigma}\right)\partial_{\mathbf{X}}\left[\frac{\mathbf{H^3}}{\mathbf{3}}\right]\partial_{\mathbf{X}}\mathbf{H}$$

$$+\partial_{\mathbf{X}}\mathbf{H}\left[-\left(\partial_{\mathbf{X}}\mathbf{P_f}\frac{\mathbf{H^2}}{\mathbf{2}} - \partial^{\mathbf{3}}_{\mathbf{X}}\mathbf{H\Sigma}\frac{\mathbf{H^2}}{\mathbf{2}}\right) + \tau_{\mathbf{f}}\mathbf{H}\right] = \tag{8.65}$$

$$\frac{\mathbf{Da_U}}{\mathbf{K'}}\sqrt{\frac{\mathbf{K'}}{\mathbf{Da_D}}}\tanh\left(\sqrt{\frac{\mathbf{Da_D}}{\mathbf{K'}}}\right)\mathbf{H}$$

The resulting expression is not linear, so a linearization process will be convenient prior to the study:

$$H = H_0 + \hat{H} \tag{8.66}$$

For ease of the reader we set:

$$\gamma = \sqrt{\frac{Da_D}{K'}} \tag{8.67}$$

$$\zeta = \frac{Da_U}{K'}\sqrt{\frac{K'}{Da_D}} \tag{8.68}$$

Using a Taylor series:

$$\tanh(\gamma H) \approx \tanh(\gamma H_0) + \frac{tanh(\gamma H_0)'}{1!}(\hat{H} - \gamma H_0) + \mathcal{O}(\hat{H}^2) \tag{8.69}$$

$$= \tanh(\gamma H_0) + \gamma(1 - \tanh(\gamma H_0)^2)(\hat{H} - \gamma H_0) + \mathcal{O}(\hat{H}^2)$$

$$\tanh(\gamma H) \approx \tanh(\gamma H_0) - \gamma^2 H_0 + \gamma^2 H_0 tanh(\gamma H_0)^2 + \tag{8.70}$$

$$\gamma\left[1 - tanh(\gamma H_0)^2\right]\hat{H}$$

The constants may be regrouped into two parameters L_1 and L_2:

$$L_1 = \tanh(\gamma H_0) - \gamma^2 H_0 + \gamma^2 H_0 tanh(\gamma H_0)^2$$

$$L_2 = \gamma\left[1 - tanh(\gamma H_0)^2\right]$$

Substituting previous expressions in (8.64) we find:

$$\partial_T(H_0 + \hat{H}) + \frac{\tau_f}{2}\partial_X\left[(H_0 + \hat{H})^2\right] - \left(\partial_X^2 P_f - \partial_X^4(H_0 + \hat{H})\Sigma\right)\frac{(H_0 + \hat{H})^3}{3}$$

$$- \left(\partial_X P_f - \partial_X^3(H_0 + \hat{H})\Sigma\right)\partial_X\left[\frac{(H_0 + \hat{H})^3}{3}\right]$$

$$+\partial_X(H_0 + \hat{H})\left[-\left(\partial_X P_f \frac{(H_0 + \hat{H})^2}{2} - \partial_X^3(H_0 + \hat{H})\Sigma\frac{(H_0 + \hat{H})^2}{2}\right) + \tau_f(H_0 + \hat{H})\right]$$

$$= \zeta(L_1 + L_2\hat{H})$$

Neglecting terms larger than $\hat{H}^1$ the following equation holds:

$$\partial_T\hat{H}+\frac{\tau_f}{2}\partial_X\left[2H_0\hat{H}\right]-\left(\partial_X^2P_f-\partial_X^4\hat{H}\Sigma\right)\frac{H_0^3+3H_0^2\hat{H}}{3}-\left(\partial_XP_f-\partial_X^3\hat{H}\Sigma\right)\partial_X\left[H_0^2\hat{H}\right]$$

$$+\partial_X\hat{H}\left[-\left(\partial_XP_f\frac{H_0^2+2H_0\hat{H}}{2}-\partial_X^3\hat{H}\Sigma\frac{H_0^2+2H_0\hat{H}}{2}\right)+\tau_f(H_0+\hat{H})\right]=\zeta(L_1+L_2\hat{H})$$

Additional calculations are performed to simplify the equation:

$$\partial_T\hat{H}+\tau_fH_0\partial_X\hat{H}-\left(\partial_X^2P_f-\partial_X^4\hat{H}\Sigma\right)\frac{H_0^3+3H_0^2\hat{H}}{3}-\left(\partial_XP_f-\partial_X^3\hat{H}\Sigma\right)H_0^2\partial_X\hat{H}$$

$$+\partial_X\hat{H}\left[-\partial_XP_f\frac{H_0^2}{2}+\tau_fH_0\right]=\zeta(L_1+L_2\hat{H})$$

$$\partial_T\hat{H}+\tau_fH_0\partial_X\hat{H}-(\frac{1}{3}H_0^3\partial_X^2P_f+\partial_X^2P_fH_0^2\hat{H}-\partial_X^4\hat{H}\Sigma\frac{H_0^3}{3}-\partial_X^4\hat{H}\Sigma H_0\hat{H}+H_0^2\partial_XP_f\partial_X\hat{H}$$

$$-H_0^2\Sigma\partial_X^3\hat{H}\hat{H})+\partial_X\hat{H}\left[-\partial_XP_f\frac{H_0^2}{2}+\tau_fH_0\right]=\zeta(L_1+L_2\hat{H})$$

This final expression is found:

$$\partial_{\mathbf{T}}\hat{\mathbf{H}}+\tau_{\mathbf{f}}\mathbf{H_0}\partial_{\mathbf{X}}\hat{\mathbf{H}}-\left(\frac{\mathbf{1}}{\mathbf{3}}\mathbf{H_0^3}\partial_{\mathbf{X}}^{\mathbf{2}}\mathbf{P_f}+\partial_{\mathbf{X}}^{\mathbf{2}}\mathbf{P_f}\mathbf{H_0^2}\hat{\mathbf{H}}-\partial_{\mathbf{X}}^{\mathbf{4}}\hat{\mathbf{H}}\mathbf{\Sigma}\frac{\mathbf{H_0^3}}{\mathbf{3}}\right.$$

$$\left.+\mathbf{H_0^2}\partial_{\mathbf{X}}\mathbf{P_f}\partial_{\mathbf{X}}\hat{\mathbf{H}}\right)+\partial_{\mathbf{X}}\hat{\mathbf{H}}\left(-\partial_{\mathbf{X}}\mathbf{P_f}\frac{\mathbf{H_0^2}}{\mathbf{2}}+\tau_{\mathbf{f}}\mathbf{H_0}\right)=\zeta(\mathbf{L_1}+\mathbf{L_2}\hat{\mathbf{H}}) \qquad (8.71)$$

This is the linearized expression of the evolution equation. A planar wave type perturbation is introduced in the system to check how it responds:

$$\hat{H} = A_0 e^{ikx+\lambda t}$$

Introducing that expression in the equation that must be satisfied, we find:

$$\partial_T A_0 e^{ikx+\lambda t} + \tau_f H_0 \partial_X A_0 e^{ikx+\lambda t} - (\frac{1}{3} H_0^3 \partial_X^2 P_f + \partial_X^2 P_f H_0^2 A_0 e^{ikx+\lambda t} -$$

$$\partial_X^4 A_0 e^{ikx+\lambda t} \Sigma \frac{H_0^3}{3} + H_0^2 \partial_X P_f \partial_X A_0 e^{ikx+\lambda t}) \tag{8.72}$$

$$+\partial_X A_0 e^{ikx+\lambda t} \left(-\partial_X P_f \frac{H_0^2}{2} + \tau_f H_0 \right) = \zeta (L_1 + L_2 A_0 e^{ikx+\lambda t})$$

Regroupping terms:

$$e^{ikx+\lambda t} \left[\left(\lambda A_0 - \partial_X^2 P_f H_0^2 A_0 + k^4 A_0 \Sigma \frac{H_0^3}{3} - \zeta L_2 A_0 \right) + \right.$$

$$\left. \left(\tau_f H_0 k A_0 - H_0^2 \partial_X P_f k A_0 - \frac{H_0^2}{2} \partial_X P_f A_0 k + H_0 \tau_f A_0 k \right) i \right] \tag{8.73}$$

$$= \partial_X^2 P_f \frac{1}{3} H_0^3 + \zeta L_1$$

The variables will be renamed to handle them more easily when in the subsequent calculations:

$$F_1 = \lambda A_0 - \partial_X^2 P_f H_0^2 A_0 + k^4 A_0 \Sigma \frac{H_0^3}{3} - \zeta L_2 A_0$$

$$F_2 = \tau_f H_0 k A_0 - H_0^2 \partial_X P_f k A_0 - \frac{H_0^2}{2} \partial_X P_f A_0 k + H_0 \tau_f A_0 k$$

$$G = \partial_X^2 P_f \frac{1}{3} H_0^3 + \zeta L_1$$

Substituting and regrouping:

$$e^{ikx+\lambda t}\left(F_1+F_2 i\right)=G \tag{8.74}$$

$$e^{\lambda t}\left(\cos(kx)+i\sin(kx)\right)\left(F_1+F_2 i\right)=G \tag{8.75}$$

$$e^{\lambda t}\left[\left(F_1\cos(kx)-F_2\sin(kx)\right)+\left(F_2\cos(kx)+F_1\sin(kx)\right)i\right]=G \tag{8.76}$$

The next relations must be satisfied if the equation is satisfied:

$$\begin{cases} e^{\lambda t}\left[F_1\cos(kx)-F_2\sin(kx)\right]=G \\ e^{\lambda t}\left[F_2\cos(kx)+F_1\sin(kx)\right]=0 \end{cases} \tag{8.77}$$

From the second equation of (8.77) a value for λ can be obtained:

$$F_2\cos(kx)=-F_1\sin(kx) \tag{8.78}$$

$$\lambda=\partial_X^2 P_f H_0^2-k^4\sigma\frac{H_0^3}{3}+\zeta L_2 \tag{8.79}$$

$$+\left(-\tau_f H_0 k+H_0^2\partial_X P_f k+\frac{H_0^2}{2}\partial_X P_f k-H_0\tau_f k\right)cotan(kx)$$

In order to get consistency on the solution, several constrains must be fulfilled:

- $\lambda=cte$

$$F_2=0\longrightarrow -\tau_f H_0 k+H_0^2\partial_X P_f k+\frac{H_0^2}{2}\partial_X P_f k-H_0\tau_f k=0 \tag{8.80}$$

$$\longrightarrow H_0=\frac{4}{3}\frac{\tau_f}{\partial_X P_f}$$

- $H=0$ must be a solution, so:

$$L_1=0\longrightarrow \tanh(\gamma H_0)-\gamma^2 H_0+\gamma^2 H_0 tanh(\gamma H_0)^2=0 \tag{8.81}$$

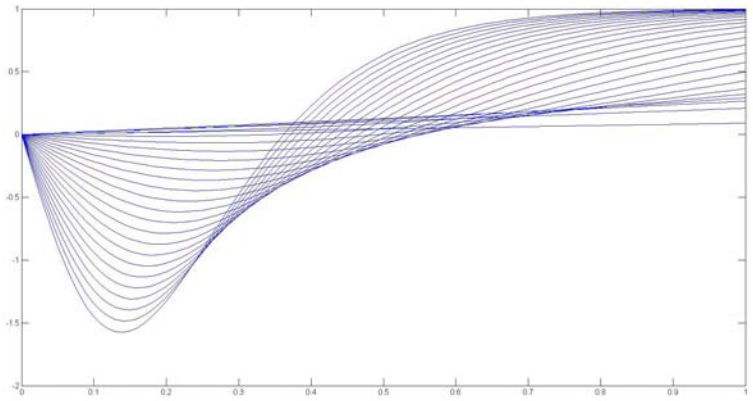

Figure 8.6: *Plot of F(H_0) (Y-axis) vs H_0 (X-axis) for different γ values (from 0.1 to 5 in this picture). The different solutions provided by different γ values (greater values of gamma match with more negative values in the first part of the curve) cut the X-axis once at least. The trivial solution is also satisfied.*

This expression may be modified conveniently to obtain additional information. So calling: $F(H_0) = \tanh(\gamma H_0) - \gamma^2 H_0 + \gamma^2 H_0 tanh(\gamma H_0)^2$, a plot $F(H_0)$ vs H_0 for different values of γ (see picture 8.6) is drawn:

This equation has at least one solution for each value of H_0 different than trivial solution, which is also attained.

Depending on the sign and value of λ the introduced perturbation will be stable or not. The system will be unstable for positive values of λ. The stability limit will be:

$$\lambda = \partial_X^2 P_f H_0^2 - k^4 \Sigma \frac{H_0^3}{3} + \zeta\gamma \left[1 - tanh(\gamma H_0)^2\right] \tag{8.82}$$

It can be deduced that the system will be stable depending on the term balance. Assuming a constant pressure drop along the domain, a wave will be propagated through the space-time plane depending on the balance between the surface tension term and chemical reaction term. The chemical reaction has actually an amplifying effect, having the chance to destabilize the whole system.

Nevertheless these conclusions have a limited applicability due to the sin-

gular structure of the equations. Another approaches would be needed to handle these equations in a more global way.

8.3 Numerical simulations

In this chapter a numerical algorithm to test the behavior of the equation for the interface is implemented. All the performed simulations were carried in 1-D for simplicity, although a natural extension to several dimensions may be applied. By solving numerically the equation we can observe which type of phenomena appear and predict other unexpected behaviors difficult to observe by using a theoretical approach.

A short theoretical introduction about the possible numerical methods applicable in this case will be given. Their numerical implementation will be shown next. Finally the results of the numerical simulations and the respective conclusions will be detailed.

8.3.1 Numerical schemes and discretization

Recalling the evolution equation to be discretized and reorganizing terms, it can be written in this form:

$$H_t + F(H)_x = G(H_{xxx}, H) + S(H(x,t)) \tag{8.83}$$

By applying the chain rule we get:

$$H_t + \frac{\partial F}{\partial H}\frac{\partial H}{\partial x} = G(H_{xxx}, H) + S(H(x,t)) \tag{8.84}$$

This type of expressions corresponds to a non-linear hyperbolic equation with a lubrication term (G) plus a reaction term (S). Non homogeneous hyperbolic equations are specially relevant in science because they appear in many problems such as shallow water description, boiling fluids or chemical reaction processes.

The solution of this equation is a wave-type solution propagated through the space and time at a finite speed, but with some numerical corrections due to the presence of a source term and a dissipative lubrication term. The numerical solution of this equation and its stability will be conditioned by different constrains. Positivity must be preserved: the measured magnitude is a positive height measured from the solid surface. A negative height has no physical sense in this case. It is also compulsory to have a good prediction of the wave front position at each time step. For these reasons each term has been discretized by using different methods that take into account the

physics of the system and their qualitative effect on the solution.

Convective term

Convective terms are discretized by using hyperbolic conservative schemes. A hyperbolic conservative equation has a convective term which controls the dynamic of the solution over the time. The wavefront and the propagation speed will be affected by the influence of this term in the equation.

Take as an example a generic 1-D hyperbolic conservation equation:

$$H_t + F(H)_x = 0 \tag{8.85}$$

with

$$H(t = 0, x) = H_0 \tag{8.86}$$

By applying the chain rule the equation may be expressed as:

$$H_t + a(H)H_x = 0 \tag{8.87}$$

where $a(H) = F(H)'$ is the convective term. The equation (8.85) is conservative because its integration (see (8.88)) results into a conservation law: the variation of H with time is equal to the difference between its input and and output through the x-axis.

$$\frac{d}{dt}\int_a^b H(x,t)dx = -\int_a^b F(H(x,t))_x dx = F(H(a,t)) - F(H(b,t)) \tag{8.88}$$

It is also relevant the fact that it is not required any spatial smoothness condition to build the solution of a hyperbolic equation if the conservation law is preserved. The solution only depends on the initial condition $H_0(x_0)$. Even when the initial condition is not continuous, the construction of the solution is still possible. See [92] for more details.

This feature introduces the concept of "*weak solution*": if $H(x,t)$ is not differentiable, this is not strictly a solution of the PDE but it can satisfy the integral form of the equation. Then it is said to satisfy a conservative form of it. A more rigorous approach to define the concept of weak solution would

be the next one. Consider a smooth test function with compact support ϕ (it vanishes out of a support set) in the interval $[x_1, x_2] \times [t_1, t_2]$, with $\phi \in C_0^n(\mathbb{R} \times [0, \infty))$. By multiplying both terms of this equation and integrating along all dimensions by parts the result is:

$$\int_0^\infty \int_{-\infty}^\infty [\phi_t H + \phi_x F(H)] dx dt = -\int_{-\infty}^\infty \phi(x, 0) H(x, 0) dx \tag{8.89}$$

The function $H(x, t)$ is a weak solution if (8.89) is satisfied for each $\phi \in C_0^n(\mathbb{R} \times [0, \infty)$.

In order to have a good idea about how solutions may behave we will see what happens if $a(H)$ is constant in (8.87). In that case, the solution is well known:

$$H(x, t) = H_0(x - at) \tag{8.90}$$

This solution is constant through each trajectory $x_0 = x - at$, which are known as "*characteristics*" of the equation. Now consider the analysis of (8.87) with $a(H) = H$, which turns the equation into the "non viscous Burgers equation":

$$H_t + HH_x = 0 \tag{8.91}$$

How will the characteristics behave when the initial value problem is solved? In this case the characteristics are solutions of $x'(t) = a(x(t)) = H(x(t), t)$, $x(0) = x_0$. It is still valid that the solution along the characteristics is constant, $H(x(t), t) = H(x(0), 0)$.

Depending on the initial data, singularities (discontinuities at a finite time due to nonlinearity) may appear and result in the fact that characteristics could be used to calculate solutions only before the singularity. By considering discontinuous initial data we can have an idea about how to solve the situation.

Let us consider piecewise constant initial conditions:

$$H(x, 0) = \begin{cases} H_l \text{ if } x < 0 \\ H_r \text{ if } x > 0. \end{cases}$$

The form of the solution gives rise to two different cases which correspond to the so-called **Riemann problem**. The weak solutions are built in a different way:

I) $H_l > H_r$. In this case (see picture 8.7), there is only one unique weak solution:

$$H(x,t) = \begin{cases} H_l \text{ if } x < st \\ H_r \text{ if } x > st \end{cases}$$

with $s = \frac{H_l + H_r}{2}$ the speed at which the discontinuity (shock wave) is propagated.

The characteristics converge in the shock wave, so it is not possible the propagation of any unstability. The information is propagated at the shock wave speed. It can be also observed that this solution is weak only if s may be described as above. In fact it can be demonstrated [92] that for a general convection function the shock wave propagation speed can be calculated (for scalar functions) by using the **Rankine-Hugoniot condition**:

$$s = \frac{F(H_l) - F(H_r)}{H_l - H_r} \tag{8.92}$$

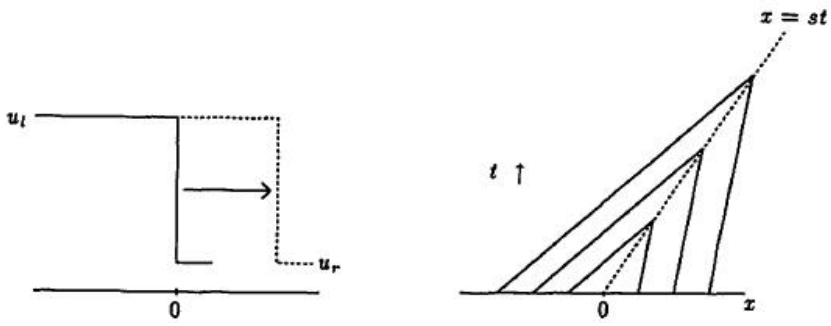

Figure 8.7: *Case I: $H_l > H_r$ (left), and characteristics of the equation (right). The unique reliable solution is a shock wave propagating at speed s. Possible perturbations decay in the solution. Taken from [92]*

II) $H_r > H_l$. In this case (see picture 8.8, left) the discontinuous solutions which satisfy the Rankine-Hugoniot condition are characterized because they get out of the shock instead of getting in. There are also continuous solutions: rarefaction shock waves. They are plotted in picture 8.8 and they are given by:

$$H(x,t) = \begin{cases} H_l \text{ if } x < H_l t \\ x/t \text{ if } H_l t < x < H_r t \\ H_r \text{ if } x > H_r t \end{cases} \tag{8.93}$$

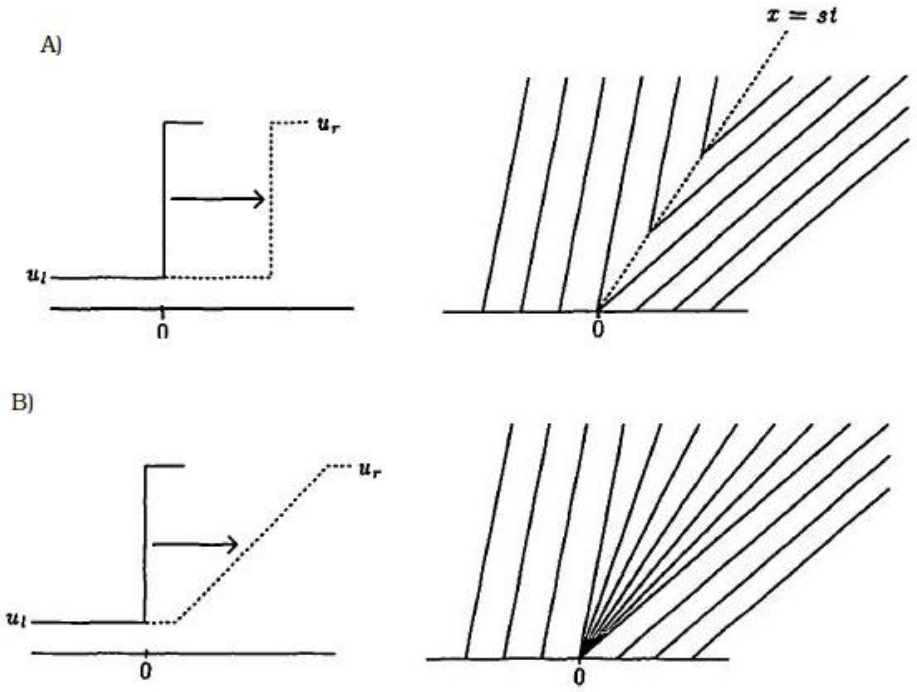

Figure 8.8: *Caso II: $H_r > H_l$ (left), and characteristics (right). There exist infinite solutions. Picture A represents a discontinuous wave. Picture B corresponds to a rarefaction wave. Taken from [92]*

The question that raises here is which of those weak solutions have a physical meaning. At this point it is needed to introduce the concept of **entropy** and **entropic solution**. In our case rarefaction waves will be the answer to that question, as they do not have any discontinuity.

Entropy is related with the propagation of the information in the domain and with the shape that discontinuity adopt. As it can be verified, all those families of rarefaction wave type solutions are continuous, weak, entropic and then stables. Resulting shock wave families will be weak solution only if they satisfy Rankine-Hugoniot condition (as it can be seen in the example 8.7). It can be noted additionally that they must satisfy several conditions to be

stable solutions (such as all characteristics have to get in the shock).

An effective and fast method to check the stability of a solution is to use the **entropy conditions**. The entropy conditions guarantee that a weak solution is also the "entropic solution" of the problem (which would be the solution of the hyperbolic problem with an additional regulating diffusive term in the limit at which the magnitude of the diffusive term tends to zero).

For the general case (even not convex flows), the entropy condition (defined by Lax and extended by Oleinik) establishes that a solution is an entropic solution if all the characteristics get inside of all the discontinuities present in the solution. An equivalent approach to this idea would be that all discontinuities in the solution must satisfy the following condition for all H between H_l y H_r:

$$\frac{F(H) - F(H_l)}{H - H_l} \geq s \geq \frac{F(H) - F(H_r)}{H - H_r} \tag{8.94}$$

For a conservation law (8.85) a numeric scheme is conservative if there exist a numeric flux function $f(x, y)$ such that:

$$\frac{H_i^{n+1} - H_i^n}{\Delta t} = \frac{f(H_{i+1}, H_i) - f(H_i, H_{i-1})}{\Delta x} \tag{8.95}$$

This definition confirms that all valid numeric schemes must satisfy the integral form of the hyperbolic equation with consistency constrain ($f(H, H) = F(H)$). However, to satisfy the entropy condition an additional constrain is required. It can be proved (see [92, 139] for more details) that if a conservative scheme is monotone then the entropy condition is satisfied.

These two conditions are the foundations of a wide group of discretization schemes developed to solve hyperbolic problems. A classic example of these schemes may be the " **Lax-Friedrich method**":

$$H_i^{n+1} = \frac{1}{2}[H_{i-1}^n + H_{i+1}^n] - \frac{\Delta t}{2\Delta x}[F_{i+1} - F_{i-1}] \tag{8.96}$$

However all methods try to minimize the dissipative effects on the solution, that is, to avoid the smoothing effect introduced by the discretization process which may lead to a wrong calculation of it.

Many strategies have been developed to perform that task. One of them was developed by **Godunov** (see [54] for more details). Godunov's idea

consist of reconstructing the exact solution for each time step $n+1$ by using the respective piece-wise constant function given as initial data from the previous time step n to solve a local Riemann problem for each discretized spatial interval in a middle point of the grid $i-\frac{1}{2}$ (picture 8.9):

$$H(x,0) = \begin{cases} H_l = H_{i-1}^n \text{ si } x < 0, \\ H_r = H_i^n \text{ si } x \geq 0. \end{cases}$$

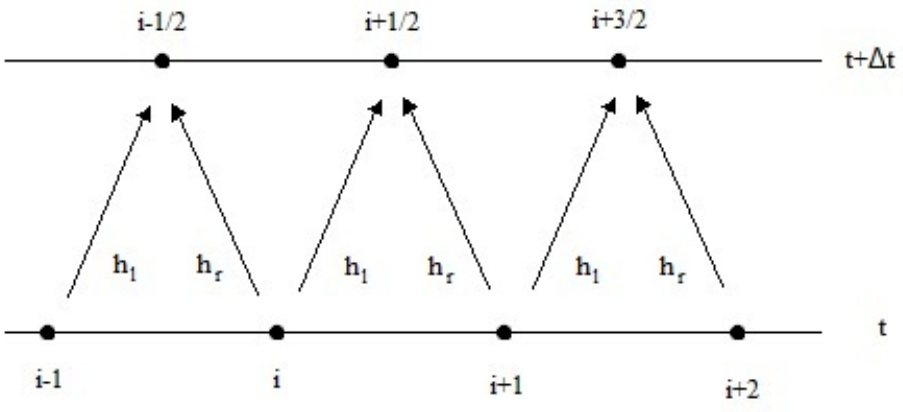

Figure 8.9: *Solution of the local Riemann problem from time t to time t+Δt*

Once all Riemann problems in the grid are solved, the solution in the i points is reconstructed by using an adequate average of the side points for each point.

This method is monotone itself. Godunov method may be also classified as a method with an accuracy order equal to one. At this point it is necessary to wonder if there exist other methods with an accuracy order larger than one (provided by Godunov) to obtain a more exact solution. The answer is positive, but with a restriction: Godunov show theoretically in a theorem ([54]) that monotone methods are at most order one of accuracy. But in spite of this inconvenient, several methods with larger accuracy have been developed by using different strategies which allow them to preserve the total variation and the conservative form during the solving process. This group of methods are called **TVD** (Total Variation Diminishing). As an example we will detail next the MUSCL algorithm.

MUSCL algorithm is a TVD method based on Godunov's idea, but reaching a second order accuracy (which improves the obtained solution).

The method proposes that piece-wise information from the previous step is not constant (as it considers Godunov) but a linear approximation with a slope interpolated from left and right states of the considered point (see picture 8.10)

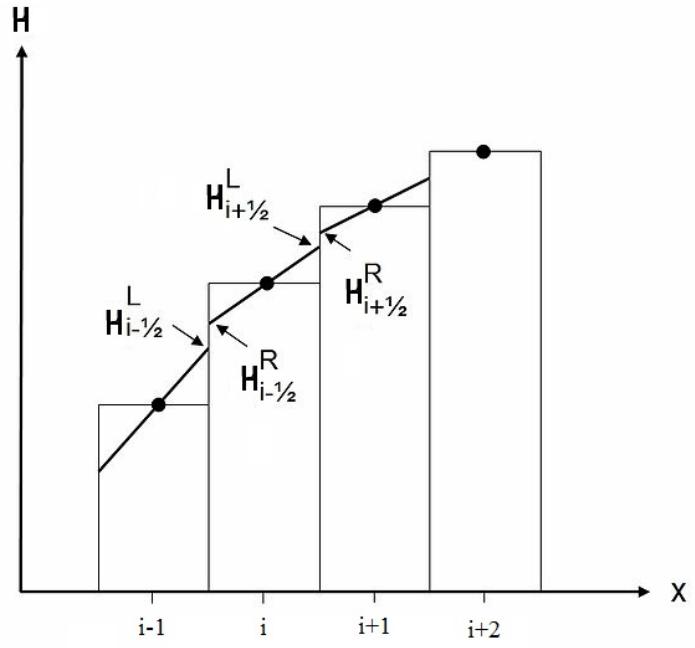

Figure 8.10: *Lineal approximation performed by MUSCL scheme with piece-wise information from the previous time step*

The full MUSCL algorithm is described next:

$$\frac{H_i^{n+1} - H_i^{n-1}}{\Delta t} + \frac{1}{\Delta x_i}\left[F(H^*_{i+\frac{1}{2}}) - F(H^*_{i-\frac{1}{2}})\right] = 0 \tag{8.97}$$

where $F(H^*_{i\pm\frac{1}{2}})$ is a second order approximation of the flux function, which depends on the values $u^L_{i+1}, u^R_{i+1}, u^L_{i-1}, u^R_{i-1}$ defined below as a lineal interpolation of the surrounding points:

$$H^L_{i+1} = H_i + 0.5\phi(r_i)(H_{i+1} - H_i)$$

$$H^R_{i+1} = H_{i+1} - 0.5\phi(r_{i+1})(H_{i+2} - H_{i+1})$$

$$H_{i-1}^{L} = H_{i-1} + 0.5\phi(r_{i-1})(H_i - H_{i-1})$$

$$H_{i-1}^{R} = H_i - 0.5\phi(r_i)(H_{i+1} - H_i)$$

$$r_i = \frac{H_i - H_{i-1}}{H_{i+1} - H_i}$$

r_i is the ration between gradients at both sides of i point. Notice that the slope of the lineal approximation ($\phi(r_i)$) is a function named "flux limiter": this function actually behaves as a flux limiter because it controls the slope of the gradients near the discontinuities to avoid spurious oscillations that otherwise could result into a non preserving calculation of the monotonicity (entropy condition). There exists numerous flux limiters in the literature and all of them must satisfy certain constrains to work properly, but the details of how do they work is out of the scope of this thesis. In our case a MINMOD limiter has been chosen:

$$\phi(u_i) = minmod\left(\theta\frac{u_j^n - u_{j-1}^n}{\Delta x}, \frac{u_{j+1}^n - u_{j-1}^n}{2\Delta x}, \theta\frac{u_{j+1}^n - u_j^n}{\Delta x}\right) \text{ con } \theta \in [0,1]$$

Flux functions are essential to develop this type of schemes. The central Kurganov and Tadmor **Kurganov and Tadmor** scheme is based on a centered difference development that can be considered as a variation of the Lax-Friedrich scheme, as it can be seen next:

$$F(u_{j+\frac{1}{2}}^*) = \frac{1}{2}\left[F(u_{j+\frac{1}{2}}^R) + F(u_{j+\frac{1}{2}}^L) - a_{j+\frac{1}{2}}\left[u_{j+\frac{1}{2}}^R - u_{j+\frac{1}{2}}^L\right]\right]$$

$$F(u_{j-\frac{1}{2}}^*) = \frac{1}{2}\left[F(u_{j-\frac{1}{2}}^R) + F(u_{j-\frac{1}{2}}^L) - a_{j-\frac{1}{2}}\left[u_{j-\frac{1}{2}}^R - u_{j-\frac{1}{2}}^L\right]\right]$$

where $a_{i\pm\frac{1}{2}}$ is the propagation speed, which can be defined as the spectral radius of the function F (maximum absolute eigenvalue of the Jacobian of the flux function F):

$$a_{j+\frac{1}{2}} = max\left[\rho\left(\frac{\partial F(u_j)}{\partial u}\right), \rho\left(\frac{\partial F(u_{j+1})}{\partial u}\right)\right]$$

$$a_{j-\frac{1}{2}} = max\left[\rho\left(\frac{\partial F(u_j)}{\partial u}\right), \rho\left(\frac{\partial F(u_{j-1})}{\partial u}\right)\right]$$

being $\rho(\cdot)$ the spectral radius. This is one of the schemes we will use in our simulations.

Lubrication term

The lubrication term $(\partial_x(H^3\partial_x^3 H))$ is a dissipative term which smooths the solution of the equation. The most important properties required for this term are the positivity preservation and entropy conservation.

This term has been discretized by using the scheme proposed by **Zhornistskaya** [180]:

$$\partial_x(H^3\partial_x^3 H) \approx \partial_x(a(H_j^n, H_{j-1}^n)\partial_x^3 H) \approx$$

$$\frac{a(H_{j+1}^n, H_j^n)\partial_x^3 H|_{j+1}^n - a(H_j^n, H_{j-1}^n)\partial_x^3 H|_j^n}{h} \tag{8.98}$$

with:

$$\partial_x^3 H|_j^n = \frac{H_{j+1}^n - 3H_j^n + 3H_{j-1}^n - H_{j-2}^n}{h^3}$$

$$\partial_x^3 H|_{j+1}^n = \frac{H_{j+2}^n - 3H_{j+1}^n + 3H_j^n - H_{j-1}^n}{h^3}$$

where a is a function which preserves positivity. According to [180], this function must have several properties to ensure positivity:

1. a(s,s) = f(s)
2. $a(s_1, s_2) = a(s_2, s_1)$
3. $a(s_1, s_2) \in C^4((0,\infty)\times(0,\infty)) \cap C([0,\infty)\times[0,\infty))$
4. $\forall\delta > 0$ there exist a $\gamma > 0$ such that $s1, s2 > \delta \longrightarrow a(s1, s2) \geq \gamma > 0$

Two examples may be:

$$a(s_1, s_2) = f(0.5(s_1 + s_2))$$
$$a(s_1, s_2) = 0.5(f(s_1) + f(s_2))$$

However, entropy preservation must be fulfilled and using the previous functions do not ensure it. In [180] a function which satisfy all the requirements is proposed. If we call $G''(s_i) = \frac{1}{f(s_i)}$, then:

$$a(s_1, s_2) = \begin{cases} \frac{s_1 - s_2}{G'(s_1) - G'(s_2)} \text{ if } s_1 \neq s_2 \\ f(s_1) \text{ if } s_1 = s_2 \end{cases}$$

This is the scheme that will be used in the simulations next.

Source term

The source term is a hyperbolic tangent function, a continuous smooth function which is bounded between zero and one for positive values of H. No special treatment will be applied to this function

After explaining how to discretize convection and lubrication terms, both schemes will be combined to obtain a full discretization of the whole equation.

8.3.2 Implementation

Recalling the evolution equation::

$$\partial_{\mathbf{T}}\mathbf{H} + \partial_{\mathbf{X}}\left[(\tau_{\mathbf{f}} + \partial_{\mathbf{X}}\mathbf{\Sigma})\left(\frac{\mathbf{1}}{\mathbf{2}}\mathbf{H^2} + \beta_{\mathbf{0}}\mathbf{H}\right)\right] - \partial_{\mathbf{X}}\left[\partial_{\mathbf{X}}\mathbf{P_b}\left(\frac{\mathbf{1}}{\mathbf{3}}\mathbf{H^3} + \beta_{\mathbf{0}}\mathbf{H^2}\right)\right]$$

$$= \frac{\mathbf{Da_U}}{\mathbf{K'}}\frac{\mathbf{1}}{\sqrt{\frac{\mathbf{Da_D}}{\mathbf{K'}}}}\tanh\left(\sqrt{\frac{\mathbf{Da_D}}{\mathbf{K'}}}\mathbf{H}\right) \tag{8.99}$$

This expression can be simplified by following the hypothesis already justified in previous chapters ($\Sigma = cte$, $\beta_0 = 0$ and substitution of $\partial_x P_b$):

$$\partial_{\mathbf{T}}\mathbf{H} + \frac{\tau_{\mathbf{f}}}{\mathbf{2}}\partial_{\mathbf{X}}\left[\mathbf{H^2}\right] - \frac{\partial_{\mathbf{x}}\mathbf{P_f}}{\mathbf{3}}\partial_{\mathbf{x}}\left[\mathbf{H^3}\right] + \frac{\mathbf{\Sigma}}{\mathbf{3}}\partial_{\mathbf{x}}\left[\mathbf{H^3}\partial_{\mathbf{x}}^{\mathbf{3}}\mathbf{H}\right] =$$

$$\frac{Da_U}{K'}\frac{1}{\sqrt{\frac{Da_D}{K'}}}tanh\left(\sqrt{\frac{Da_D}{K'}}H\right)$$

To simplify, some constants will be renamed:

$\alpha = \frac{Da_U}{K'} \frac{1}{\sqrt{\frac{Da_D}{K'}}}$

$\beta = \tau_f$

$P_f = \partial_x P_f$

$\epsilon = \sqrt{\frac{Da_D}{K'}}$

The final numeric expression is:

$$\partial_{\mathbf{T}}\mathbf{H} + \frac{\beta}{\mathbf{2}}\partial_{\mathbf{X}}\left[\mathbf{H^2}\right] - \frac{\mathbf{P_f}}{\mathbf{3}}\partial_{\mathbf{x}}\left[\mathbf{H^3}\right] + \frac{\mathbf{\Sigma}}{\mathbf{3}}\partial_{\mathbf{x}}\left[\mathbf{H^3}\partial_{\mathbf{x}}^{\mathbf{3}}\mathbf{H}\right] = \alpha\mathbf{tanh}\left(\epsilon\mathbf{H}\right) \tag{8.100}$$

This will be the discretized equation to compute the results. First the main parameters which control the simulation will be introduced and then some interesting values and ranges of parameters regarding perturbation and stability of the system will be looked for.

The convective term will be discretized by using a MUSCL algorithm with a second order centered difference scheme proposed by Kurganov and Tadmor:

$$H_t + f(H(x))_x = 0$$

$$(f(H(x))_x \approx \frac{1}{\Delta h}\left[F(u^*_{j+\frac{1}{2}}) - F(u^*_{j-\frac{1}{2}})\right]$$

where each term is defined as:

$$F(u^*_{j+\frac{1}{2}}) = \frac{1}{2}\left[F(u^R_{j+\frac{1}{2}}) + F(u^L_{j+\frac{1}{2}}) - a_{j+\frac{1}{2}}\left[u^R_{j+\frac{1}{2}} - u^L_{j+\frac{1}{2}}\right]\right]$$

$$F(u^*_{j-\frac{1}{2}}) = \frac{1}{2}\left[F(u^R_{j-\frac{1}{2}}) + F(u^L_{j-\frac{1}{2}}) - a_{j-\frac{1}{2}}\left[u^R_{j-\frac{1}{2}} - u^L_{j-\frac{1}{2}}\right]\right]$$

For more details, see the previous chapter.

The lubrication term ($\partial_x(H^3\partial_x^3 H)$) has been discretized by using Zhornistkaya's scheme ([180]):

$$\partial_x(H^3\partial_x^3 H) \approx \partial_x(a(H_j^n, H_{j-1}^n)\partial_x^3 H) \approx \frac{a(H_{j+1}^n, H_j^n)\partial_x^3 H|_{j+1}^n - a(H_j^n, H_{j-1}^n)\partial_x^3 H|_j^n}{h}$$

where a is a function which preserves the positivity of the scheme. The chosen a function for our case is that one used by [180] which also preserves the entropy:

$$a(s_1, s_2) = \begin{cases} \frac{s_1 - s_2}{G'(s1) - G'(s2)} \text{ if } s1 \neq s_2, \\ f(s_1) \text{ if } s_1 = s_2. \end{cases}$$

with $G''(v) = 1/f(v)$.

Numeric integration through the time will be performed by applying a second order explicit Runge - Kutta method:

$$U' = f(U)$$

$$U^* = U^n + \frac{1}{2}kf(U^n)$$

$$U^{n+1} = U^n + kf(U^*)$$

8.3.3 Key parameters

A description of the different numeric constants which control the evolution of each term in the interface evolution equation is shown next. Some comments about their effect over the solution and the system dynamics are also included:

- Shear stress parameter (β): It moves the interface in the flow direction. Different values of β will produce different geometries.
- Chemical reaction parameter (α): It pushes the interface in the vertical direction. As its value grows, the increment of the height in each iteration is larger. It promotes the amplification of small perturbations in the boundary if they are present, being able to destabilize the system.

- Surface tension parameter (Σ): It smooths the boundary by trying to reduce the volume of the whole surface. It may destabilize the code depending on its value.
- Pressure gradient parameter (P_f): It acts against wave propagation, reducing its propagation speed. It also modifies the shape of the wave, shaping it with a bell type geometry. It amplifies some perturbations, producing instability depending of its value respect to β value.
- Epsilon parameter (ϵ): It modifies the source term effect on the system.

Nevertheless this description is incomplete because not all parameters are independent among themselves when we consider stability effects: β, P_f and Σ are related so the stability of the code depends on the magnitude order of their ratios. The α term may destabilize the code if small perturbations are generated in the surface. Next a brief description of the different ratios of their effect in the numeric stability is given:

- P_f/β: This ratio controls the slope of the boundary in the wavefront tail. Values smaller than 6/8 generate a tail slope constant along the x axis. Values above this value tend to change the slope of it as a function of the position, generating a sea wave shape.
- Σ/β: This ratio controls the characteristic geometry of the biofilm. Higher values produce the appearing of "bell type shape" geometries. Smaller values will generate a wave geometry, with a positive slope in the tail and a peak in the upper part.
- P_f/Σ: This ratio controls the direction of the perturbation moving over the surface, promoting the formation of a wavefront in the back part of the biofilm. If its value is zero, then it has no influence on the system and the convective term domains.

8.3.4 Numerical results

In this section the numerical solutions of the evolution equation simulation are discussed for a different range of parameters. The different patterns observed are shown in the different pictures.

Figures 8.11, 8.12 and 8.13 show the effect of α,β and Σ in the numerical results. Each one has a singular effect in the code when they are analyzed separately.

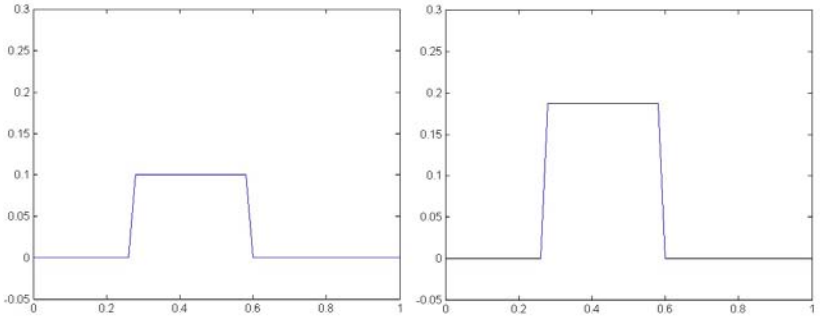

Figure 8.11: *Effect of α in the code. This term pushes the boundary in the positive z axis direction. $\alpha = 0$ (left) and $\alpha = 100$ (right). $H_0 = 0$. The remaining parameters are zero.*

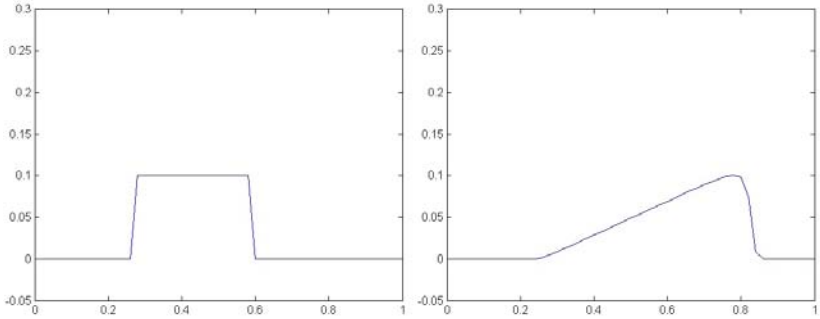

Figure 8.12: *Effect of β in the code. Convective term tends to drag the boundary in the positive x direction. $\beta = 0$ (left) and $\beta = 10$ (right). $H_0 = 0$. The remaining parameters are zero.*

Figures 8.14, 8.15 and 8.16 show the effect of previously described ratios.

H_0 has a significative influence in the stability of the code because depending on its value, the ranges of each parameter for which the code is stable vary. Its effect can be appreciated in the figure 8.17, where it is observed

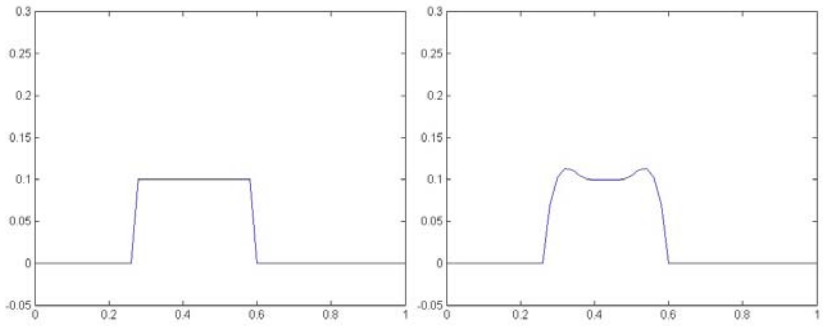

Figure 8.13: *Effect of* Σ *in the code.* Σ *promotes the reduction of exposed surface, trying to smooth sharp boundaries, as it behaves the physical surface tension.* $\Sigma = 0$ *(left) and* $\Sigma =$ *1E-2 (right).* $\beta = 80$. $H_0 = 0$. *The remaining parameters are zero.*

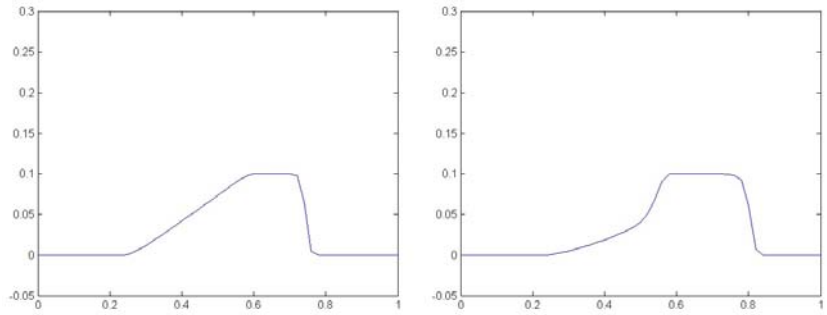

Figure 8.14: *Effect of* P_f/β *ratio on the code. Ratios smaller than* $6/8$ *tends to preserve the upper part of the wavefront with a constant slope. Larger values tend to curve the slope and generate a sea wave shape geometry.* $P_f/\beta = 4/8$ *(left) and* $P_f/\beta = 60/8$ *(right).* $H_0 = 0.1$. *The remaining values are zero.*

that by only modifying the initial value of the the biofilm heigh, the code diverges with the same parameter initial values.

α may destabilize the system if some perturbations would be present in the boundary, as it may increase the amplitude of these oscillations and eventually generate unstability in the code. Figure 8.18 show a case in which the presence of α term leads to the propagation and amplification of the oscillations.

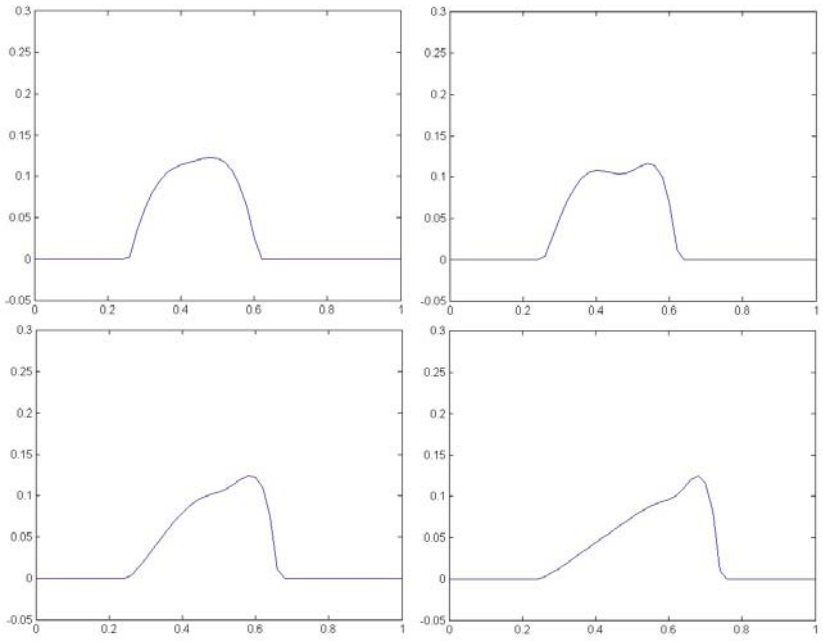

Figure 8.15: *Effect of* Σ/β *ratio in the code. Higher values tend to generate a "bell type" shape. Smaller values tends to generate a wave type shape. Figure A:* $\Sigma/\beta = 3E-2/1E0$. *Figure B:* $\Sigma/\beta = 3E-2/5E0$. *Figure C:* $\Sigma/\beta = 3E-2/8E0$. *Figure D:* $\Sigma/\beta = 3E-2/2E1$. $H_0 = 0.1$. *The rest of the parameters are zero.*

This last picture shows that the chemical reaction may destabilize the system by increasing the value of the height, which affects directly in the stability of the system by modifying the allowable range of parameters.

It has been observed as well an undesired effect in the code associated with numerical instability. For certain combinations of parameters the code show numerical spurious oscillations. By performing a deep analysis of these cases it has been observed that the instability does not depend on the spatial or temporal step, but it has to be considered as a natural answer of the algorithm itself against a multivalued solution. By observing the development of the image 8.19 it can been noticed that the solution tends to move to the right side of the wave peak. However, the inability of this mathematical formulation to provide multivalued solutions forces the code to answer by generating instability as a periodic wave pattern.

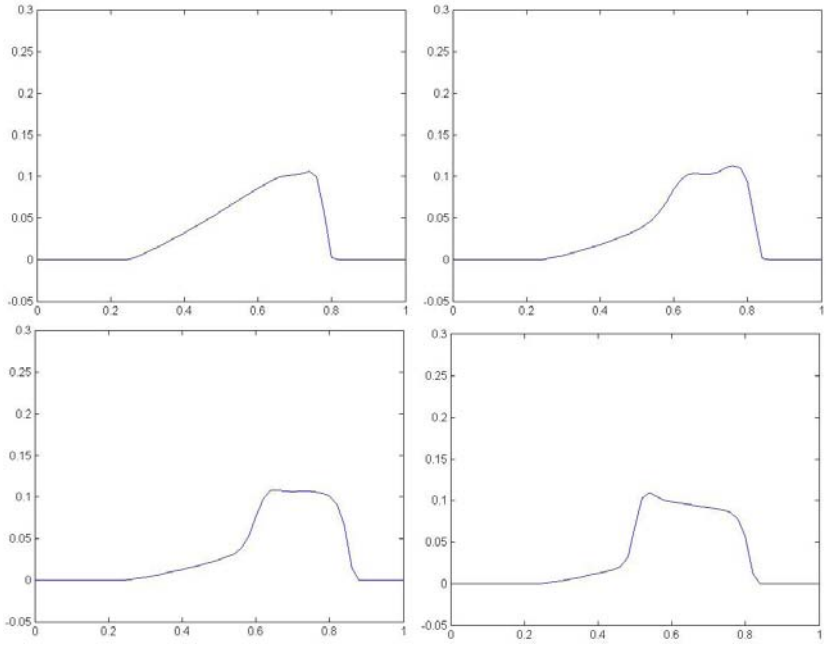

Figure 8.16: *Effect of P_f/Σ ratio in the code. This ratio controls the movement direction of the surface perturbation: larger values tend to generate a perturbation that moves in the opposite direction that the flow. Smaller values tend to propagate the perturbation in the flow direction. It can be observed certain geometric similarity with some geometries found in experiments (concretely some wave type and "streamer" type). Figure A: $P_f/\Sigma = 2E2/2E-2$. Figure B: $P_f/\Sigma = 7E2/2E-2$. Figure 3: $P_f/\Sigma = 8.5E2/2E-2$. Figura 4: $P_f/\Sigma = 1E3/2E-2$. $\beta = 1E2$. $H_0 = 0.1$. Rest of parameters are zero*

This fact forces us to look for an alternative formulation which allow us to represent multivalued solutions. This fact is consistent with experimental observations, because there are is an extensive bibliography with results concerning geometric configurations on biofilm colonies. Among them self-bended structures are usual: "streamer" type configurations, with a thread type structure, is a classic morphology adopted by biofilms.

8.3.5 Level-set formulation

The previous lubrication equation has the disadvantage that it does not allow multivalued solutions. If we want to obtain biofilm configurations as observed in the experiments we need to change the mathematical formulation. A way

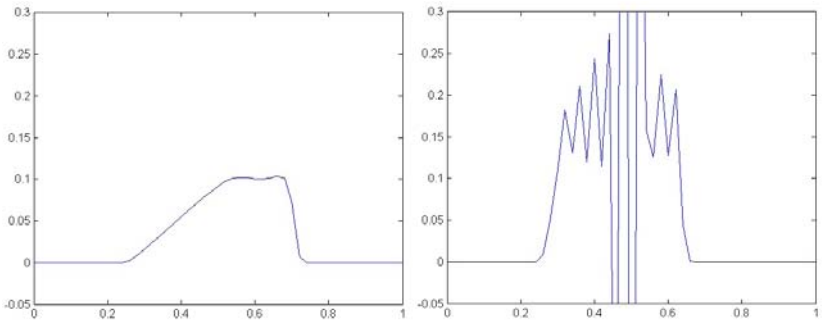

Figure 8.17: *Effect of H_0 in the code. The initial value of H will determine the range of parameters for which the code is stable. $H_0 = 0.1$ (left) and $H_0 = 0.2$ (right). $\alpha = 0$, $\epsilon = 0$,$\beta = 50$, $\Sigma = 1E-2$, $P_f = 10$*

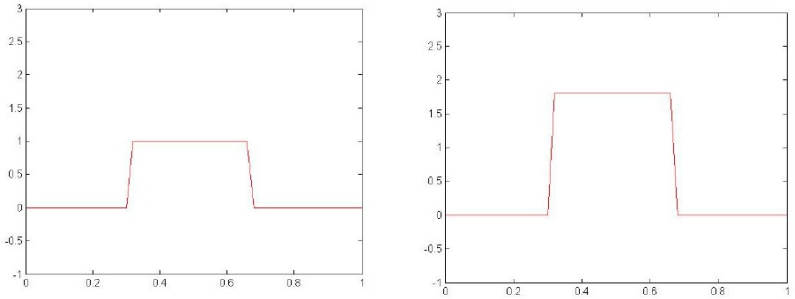

Figure 8.18: *Effect of α in the code. The picture on the left ($\alpha = 0$) show the result of an initial perturbation introduced by Σ. The presence of the chemical reaction (/α term) amplifies the perturbation and generate instability (picture on the left,$\alpha = 300$). Values: $\epsilon = 3.8E-1$, $\beta = 50E2$, $\Sigma = 4$, $P_f = 8E1$, $H_0 = 0.1$*

to solve the problem would be to use a free boundary description in terms of level-sets.

This family of methods has been effective to study free boundaries independently of the geometric shape that they adopt. This approach reformulates the original problem by defining a generic function ϕ such as its level-set equal zero match with the interface Γ to study:

$$\phi(\mathbf{x}, t) > 0 \text{ in } \Omega_{fluid}$$
$$\phi(\mathbf{x}, t) = 0 \text{ on } \Gamma$$

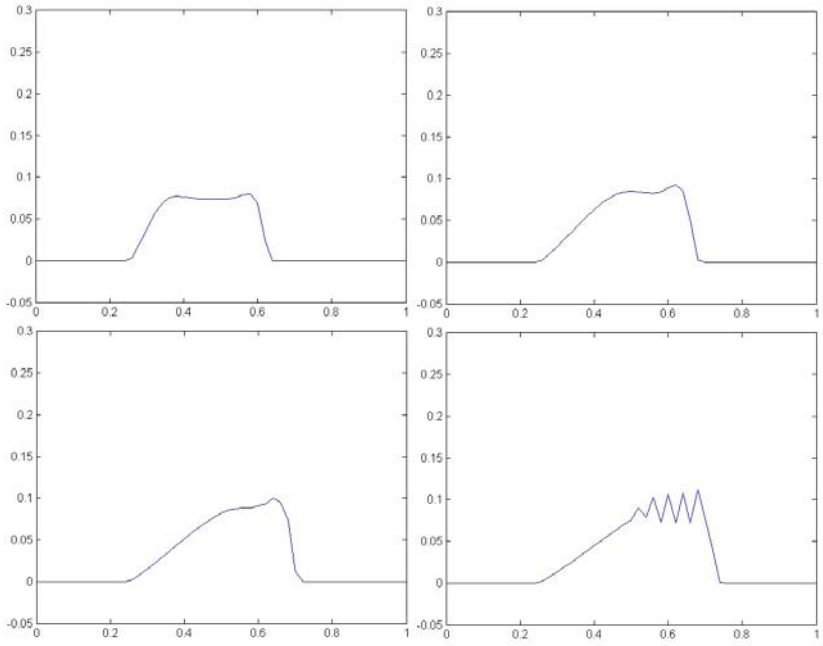

Figure 8.19: *Numerical answer of the algorithm against a combination of parameters which leads to a multivalued solution. Values:* $\alpha = 1E3$, $\epsilon = 3.8E-1$, $\beta = 50E2$, $\Sigma = 8$, $P_f = 8E1$, $H_0 = 0.07$

$$\phi(\mathbf{x}, t) < 0 \text{ in } \Omega_{biofilm}$$

As the function ϕ depends on the position of the boundary and the time, by differentiating this function in the target interface it is obtained:

$$\phi_t + \frac{d\mathbf{x}}{dt}\phi_x = 0 \tag{8.101}$$

or:

$$\phi_t + \vec{v}\phi_x = 0 \tag{8.102}$$

It can be observed that the resulting equation describes the position of the interface at each time step when it is exposed to a velocity field $\vec{v}$. This equation is easily integrable with each valid method to solve hyperbolic equations, giving as a result the position of the boundary without performing additional calculus. As an inconvenient, this method requires to know the shape of the function $\vec{v}$ which modifies the interface of the system.

It exist several methods to take advantage of the powerful metodology that Level-set techniques may offer. Among all of them, a proper method

could be the *"ghost cell method"*, which has already used successfully to describe the movement of interfaces in combustion systems [46]. This method could be applied in our case by splitting the system into two domains (fluid and biofilm) in which Navier-Stokes equations could be solved with their respective boundary conditions but considering that each domain occupy the whole domain (applying an extrapolation by using the boundary conditions given by the problem). Two solutions for each point will be obtained, but only one of them will be taken depending which sign adopt the Level-set function). The displacement of the Level-set function will be performed with the velocity data obtained at the interface as a result of solving Navier-Stokes equations, considering the sign of Level-set function to decide which solution is correct at each point.

This calculations are out of the scope of this work, being object of future implementation.

8.4 Conclusions

An analysis of a biofilm-water biphasic system is done with the aim of studying mathematically the behavior of the boundary when varying the different physical terms present.

A first description of biofilms as a solid material was tried, which implies the use of solid mechanics theory. Different similarities were found with biomaterials or hydrogels, but it was concluded that a simpler approach could be made by treating biofilms as a fluid. Some biofilms do indeed behave in that way.

With this approach, a coupled system of partial differential equations for both phases is obtained, including a chemical reaction term in the biofilm phase. This system is quite hard to handle because the position of the boundary is not described in an explicit way in the equations, but it is included implicitly through the boundary conditions at the interface. This reason and the fact that fluid biofilms tend to spread through the surface (being this length much larger than transversal height) led to a long-scale simplification, which assumes that perturbations in transversal direction are much larger than those given in longitudinal direction. In this way, an equation for the interface is found and analyzed.

Numerical solutions of this equation showed that the geometry of the in-

terface changes drastically when the different constant parameter ratios are modified. The source term has a destabilising effect over the system. This formulation is unable to reproduce multivalued interfaces which arise naturally in real biofilms.

Multivalued solutions are consistent with the geometrical behavior of the biofilms observed in the laboratory: thread and wave patterns have been observed that cannot be plotted using single valued profiles. This drawback forces us to plan as a future work the reformulation of the problem in terms of a level-set approach, which could yield all possible solutions.

Chapter 9

Summary, conclusions and perspectives

9.1 Summary

Biofilms are living organisms almost ubiquitous in nature which exert an undetermined influence in Nature and human systems. They are believed to be responsible for more than 80 per cent of infections in humans, ranging from deadly illnesses (cystic fibrosis, legionellosis...) to life threatening infections originated in artificial joints, pacemakers or catheters. Biofilms have also a huge impact in human made equipments. They may damage them generating substantial economic losses and decreasing overall efficiency. On the beneficial side, biofilms may be exploited to our advantage in bioremediation and industrial production. They are susceptible of being engineered to perform unusual tasks such as microsensing or micromanipulation of physical systems in nano and microscale.

There is a great interest in industry and science to control these biological systems to take advantage of their unique properties: the new possibilities offered by genetic manipulation and the characteristic dimensions of bacteria (in the order of microns) convert biofilms in a potential tool for a wide range of applications in many fields. As pointed out earlier, the origin of this thesis was an aeronautic project to design a new generation of heat exchangers for MEMs. With this idea in mind, we tested the behavior of biofilms in a real industrial system, leaving aside the controlled but impractical conditions in the laboratory. As many engineered systems involve rectangular ducts, we first checked the effect of several simple parameters (Reynolds numbers, concentration, type of nutrient) on biofilm growth. An industrial

device was designed and assembled to perform the experiments. The results showed that, depending on the Reynolds number, biofilms develop different spreading patterns. Images were taken with a Fluorescence microscope. We designed a statistical image treatment to quantify the information about cells concentration and distribution provided by the photographs. This provided some insight on the parameter regimes in which a biofilm may grow as a flat layer with an acceptable thickness. Pattern formation is to be avoided in industrial applications.

Biofilm dynamics is affected by many factors. Some of them known, others still unknown. Uncertainty in these system leads in a natural way to a stochastic description. The laws which govern the system are not given in a deterministic way, but in terms of probabilities. With this idea in mind, a hybrid approach was developed in chapter 3 to describe biofilm growth in a straight duct and exposed to a fluid flow. Bacteria were described as independent units which perform different metabolic activities (reproduction, spreading, erosion, attachment, EPS generation and deactivation) following different probabilistic laws informed by the state of continuous fields. Pattern formation is controlled by the collective behavior of cells acting according to these rules. The biofilm is seen both as a bacterial aggregate and a solid with certain cohesion. The flow is crudely taken into account through a couple of parameters measuring the shear strength and the thickness of the concentration layer. The nutrient concentration is evaluated devising a numerical strategy to solve simplified reaction-diffusion equations in this framework. Its evolution is governed by a parameter representing the ratio of the nutrient uptake by the cells to diffusional supply plus the constant background concentration. The simulations (both in 2D and 3D) show a variety of biofilms patterns for certain regimes of dimensionless parameters. A case study shows the influence of different parameters in the formation of these structures. Erosion and growth mechanisms alone are able to produce biofilm structures moving downstream. Strong erosion does not require large flows, small biofilm cohesion suffices.

Biofilm behavior is varied and complex. Although the analysis of simple cases (such as the model problem solved in 3) may yield useful predictions, it is not enough to reach a proper understanding of biofilm dynamics. The development of microfluidics has provided new detailed experimental information that can be used as guidance for improved models. Chapter 4 adapts the framework developed in Chapter 3 to the study of biofilm streamers in corner microflows, documented in a series of recent experiments by Stone and coworkers at Princeton University. The new hybrid model works in two time

scales: the shorter cell adhesion scale and the longer cell growth scale. In the short time scale, cell adhesion, motion and erosion due to the flow take place. New probabilistic rules for adhesion and motion are implemented. The adhesion mechanisms takes into account cell attachment to the wall past the corners due to secondary flows and adhesion of floating cells hitting the growing biofilm. The probabilities for motion and erosion are now informed by the true status of the flow around the biofilm. Shear forces exerted on the walls detach cells, whereas normal forces may move them. We have devised a numerical strategy to approximate the Navier-Stokes equation at a moderate computational cost in this framework. The flow is coupled to the concentration of nutrients, that informs the reproduction probability in a longer time scale. An initial biofilm seed past a corner develops into a streamer, that bends due to the corner flow. Eventually, it may reach the opposite corner and merge with the biofilm seed growing there, as observed in experiments, provided the adhesion rate and the biofilm cohesion are large enough to resist increased erosion when crossing the main stream.

There are situations in which biofilm dynamics has not been explored yet. One of these cases was selected as a target for Chapter 5 because of its relevance: the study of biofilm growth under a pulsatile flow. These flows are common in fields such as medicine, where peristaltic pumps are used to provide drugs, blood or other medical products. They are also the system chosen by Nature for circulatory systems in animals, including humans. A series of experiments led us to unexpected and previously unknown results. We have discovered that the combination of peristaltic pumping in a circuit made of tubular ducts with the presence of section variations triggers the formation of spiral biofilms. This seems to be the outcome of the combination of selective biofilm nucleation at stenosis points, guided attachment of planktonic bacteria driven by the oscillatory flow, and a competition between circular growth mechanisms and axial displacement and erosion due to the flow. Calculations with a simplified growth-flow model seem to sustain this theory. This mechanism for spiral formation might allow us to hypothesize with an unusual spreading mechanism for bacterial infections, which is out of the scope of this work.

Although the development of submerged biofilms in ducts is relevant in many fields, there are other aspects regarding biofilm evolution that should be studied for a broader picture. Biofilms grown on surfaces form a solid-air system (agar gel - biofilm - air). Additional bacterial behaviors such as cellular differentiation processes have to be considered. Bacteria specialize by generating chemical signals called "self-inductors" to perform specific tasks

which allow the whole colony to spread and survive more efficiently than without these processes. The simple but powerful dynamics of these systems and the hope of some scientist about establishing a direct relation between bacterial differentiation processes and the dynamic of human cells in illnesses like cancer motivate the modelization of differentiation processes. Chapter 6 adapts to biofilms on surfaces the hybrid framework developed in Chapter 3 for biofilms in flows, guided by experimental and theoretical observations made by Kolter's and Brenner's groups at Harvard University. The interaction with the external flow is suppressed. The presence of autoinductors and the differentiation of normal cells into specialized cells with certain characteristics is incorporated. Cells can differentiate in several types depending on chained probability laws informed by the status of nutrient and oxygen concentrations, and by the concentrations of chemicals secreted by different bacteria. Biofilm spread has to be modified to include the effect of water suctioned from the agar substratum according to adequate pressure fields. Numerical simulations show a good qualitative accordance with the observed development of the first stages of *B.Subtilis* colonies, which encourages us to keep working in a more accurate model valid for later stages where the dynamics becomes more complex.

The last chapter seeks for a simple continuum deterministic model able to describe a biofilm growth into a channel filled with a moving fluid. The approach consists in considering the biofilm as a fluid instead of a solid (which could be an interesting modelization in a prospective work). Under this assumption, lubrication theory and perturbation methods can be used to obtain an equation which describes the position of the interphase at each time step. Computational results show a behavior in accordance with previous models, but with several constrains for a range of parameters in which the numerical simulation cannot give a realistic solution due to the functional approach of the mathematical model, which forbids the biofilm boundary becoming multivalued and turning around. A level-Set formulation is proposed that might overcome that difficulty.

This work tries to offer a deep insight in the biofilm field, taking into account both theoretical and experimental approaches since a multidisciplinary point of view is required to establish a solid foundation for future works in this discipline. The complex relations between the different scientific disciplines involved in biofilm dynamics require a wide framework to permit a complete description that allows scientists and experts to handle them in the next generation of industrial and medical applications.

9.2 Perspectives

This thesis covers a significant part of biofilm dynamics, proposing different mathematical approaches in order to enlighten the complex physical-chemical dynamics involved in biofilm evolution. However, many poorly understood issues remain. This work focuses on some significant behaviors observed in experiments such as spread patterns or basic differentiation processes under certain conditions. There is then a need of scaling the problem up to more complex systems in accordance with industrial and medical situations, where the models are supposed to be useful.

One task to be done is the calibration of the models with real experiments. It is a fact that they cannot be a predictive tool if they are not tested in real systems. By using those calibration results, theoretical models such as the ones developed in this work might be improved by increasing the number of variables affecting the general dynamics: temperature, other bacterial strains, chemicals, turbulence. There are additional parameters that have a deep impact in the final result of the evolution of a biofilm, and it is neccesary to take them into account.

Our hybrid models can be extended by adding the effect of additional variables (i. e. temperature, quorum sensing signalling, etc.), or imposing non linear conditions in the external hydrodynamics such as vorticity, transient pulses or curvature in the substratum on which biofilms are attached to. The presence of chemical compounds or other bacterial competitors may also be extended easily.

Continuum models offer a good chance to study the complex structural mechanics behind the EPS matrix that develop most biofilms. This substance determines all physical properties regarding its natural resistance to external threats like shear stresses or chemicals. A proper modelization of this material taking into account experimental observations (using structural mechanics and mass transfer theories) would lead to understand in a better way how to control their presence by setting procedures to either remove them or grow them in a ordered way.

Additionally, the field demands a cheaper and faster way to quantify values that are critical to know the response of biofilms during the experiments. Although some methods developed by biologist such as GFP signalling have paved the way to non-invasive dynamic quantification methods, there is a lack of standardization in the gathering and processing work: reliable imag-

ing techniques are needed to process images in a systematic way, allowing to obtain the largest amount of information possible with microscopes.

Appendix A

Derivation of tangential and normal boundary conditions.

Taking the equation (8.23):

$$j(v_{b,n} - v_{f,n})\vec{n} - (\mathbf{T_b} - \mathbf{T_f}) \cdot \vec{n} = \kappa\sigma\vec{n} - \vec{\nabla}_s\sigma \longrightarrow$$

where $v_{b,n}\vec{n}$ and $v_{f,n}\vec{n}$ are the normal velocities at the interface. It is also known from equation (8.16) that:

$$j = \rho_f(\vec{v_f} - \vec{v_i}) \cdot \vec{n} = \rho_f(v_{f,n} - \vec{v_i}\vec{n})$$

$$j = \rho_b(\vec{v_i} - \vec{v_b}) \cdot \vec{n} = \rho_b(\vec{v_i}\vec{n} - v_{b,n})$$

Hence:

$$v_{f,n} = \frac{j}{\rho_f} + \vec{v_i}\vec{n} \tag{A.1}$$

$$v_{b,n} = \vec{v_i}\vec{n} - \frac{j}{\rho_b} \tag{A.2}$$

Substituting:

$$-j^2\left(\frac{1}{\rho_b} + \frac{1}{\rho_f}\right)\vec{n} - (\mathbf{T_b} - \mathbf{T_f}) \cdot \vec{n} = \kappa\sigma\vec{n} - \vec{\nabla}_s\sigma \longrightarrow \tag{A.3}$$

Now the equation (A.3) will be multiplied by normal and tangential vectors to obtain their respective projections of these stresses in their respective directions:

NORMAL COMPONENT

Performing a scalar product by $\vec{n}$, the next reduced expression may be obtained:

$$-j^2\left(\frac{1}{\rho_f}+\frac{1}{\rho_b}\right)\vec{n}\vec{n}-(\mathbf{T_b}-\mathbf{T_f})\vec{n}\vec{n}=k\sigma\vec{n}\vec{n}-\vec{\nabla}_s\sigma\vec{n} \tag{A.4}$$

Developing some tensorial algebra:

$$-j^2\left(\frac{1}{\rho_b}+\frac{1}{\rho_f}\right)-\frac{1}{1+(\partial_x h)^2}\cdot \tag{A.5}$$

$$\begin{pmatrix} -\partial_x h & 1 \end{pmatrix}\begin{pmatrix} p_b-p_f & \tau_{xy,b}-\tau_{xy,f} \\ \tau_{xy,b}-\tau_{xy,f} & p_b-p_f \end{pmatrix}\begin{pmatrix} -\partial_x h \\ 1 \end{pmatrix}$$

$$=\frac{\partial_x^2 h}{[1+(\partial_x h)^2]^{3/2}}\sigma$$

where:

$$-j^2\left(\frac{1}{\rho_b}+\frac{1}{\rho_f}\right)-\left[(p_b-p_f)-\frac{2(\tau_{xy,b}-\tau_{xy,f})(\partial_x h)}{1+(\partial_x h)^2}\right]=\frac{\partial_x^2 h}{[1+(\partial_x h)^2]^{3/2}}\sigma \tag{A.6}$$

TANGENTIAL COMPONENT:

Multiplying by $\vec{t}$ we get the following reduced expression:

$$-(\mathbf{T_b}-\mathbf{T_f})\vec{n}\vec{t}=-\vec{\nabla}_s\sigma\vec{t} \tag{A.7}$$

Operating:

$$\begin{pmatrix} 1 & \partial_x h \end{pmatrix}\begin{pmatrix} p_b-p_f & \tau_{xy,b}-\tau_{xy,f} \\ \tau_{xy,b}-\tau_{xy,f} & p_b-p_f \end{pmatrix}\begin{pmatrix} -\partial_x h \\ 1 \end{pmatrix}\frac{1}{1+(\partial_x h)^2} \tag{A.8}$$

$$= \vec{\nabla}_s \sigma \begin{pmatrix} 1 \\ \partial_x h \end{pmatrix} \frac{1}{[1+(\partial_x h)^2]^{1/2}}$$

Finally, we obtain:

$$(\tau_{xy,b} - \tau_{xy,f}) \frac{1-(\partial_x h)^2}{1+(\partial_x h)^2} = \frac{\partial_x \sigma + \partial_z \sigma \partial_x h + \partial_z \sigma (\partial_x h)^3 + \partial_x \sigma (\partial_x h)^2}{[1+(\partial_x h)^2]^{3/2}} \quad \text{(A.9)}$$

Having into account that j may be substituted as a function of the chemical reaction and the volume / surface ratio:

$$j = \gamma \frac{c_i}{c_i + K} \frac{V_b}{S_b} = \gamma \frac{c_i}{c_i + K} \frac{\int_0^L h dx}{\int_0^L \sqrt{1+(\partial_x h)^2} dx} \quad \text{(A.10)}$$

The nondimensionalization of the equations leads to:

NORMAL COMPONENTS

$$-\gamma^2 h_0^2 \left(\frac{\epsilon C}{\epsilon C + K'} \frac{\int_0^1 H dX}{\int_0^1 \sqrt{1+\epsilon^2 (\partial_X H)^2} dX} \right)^2 \left(\frac{1}{\rho_b} + \frac{1}{\rho_f} \right) \quad \text{(A.11)}$$

$$-\frac{\mu U_0}{h_0} \left[(P_b - P_f) - \frac{[2(\tau_b - \tau_f)(\partial_X H)]}{1+\epsilon^2 (\partial_X H)^2} \right] \epsilon = \frac{\frac{\mu U_0}{h_0} \partial_X^2 H \Sigma}{[1+\epsilon^2 (\partial_X H)^2]^{3/2}} \epsilon$$

Assuming $\rho_f \approx \rho_b = \rho$ we find:

$$-2 \frac{\gamma^2 h_0^2}{\rho} \left(\frac{\epsilon C}{\epsilon C + K'} \frac{\int_0^1 H dX}{\int_0^1 \sqrt{1+\epsilon^2 (\partial_X H)^2} dX} \right)^2 \quad \text{(A.12)}$$

$$-\frac{\mu U_0}{h_0} \left[(P_b - P_f) - \frac{[2(\tau_b - \tau_f)(\partial_X H)]}{1+\epsilon^2 (\partial_X H)^2} \right] \epsilon = \frac{\frac{\mu U_0}{h_0} \partial_X^2 H \Sigma}{[1+\epsilon^2 (\partial_X H)^2]^{3/2}} \epsilon$$

$$-2 \frac{\frac{\gamma^2 h_0^2}{\rho}}{\frac{\mu U_0}{h_0}} \left(\frac{\epsilon C}{\epsilon C + K'} \frac{\int_0^1 H dX}{\int_0^1 \sqrt{1+\epsilon^2 (\partial_X H)^2} dX} \right)^2 \quad \text{(A.13)}$$

$$-\left[(P_b - P_f) - \frac{2(\tau_b - \tau_f)(\partial_X H)}{1+\epsilon^2(\partial_X H)^2}\right]\epsilon = \frac{\partial_X^2 H\Sigma}{[1+\epsilon^2(\partial_X H)^2]^{3/2}}\epsilon$$

Defining $\xi = \frac{\frac{\gamma^2 h_0^2}{\rho}}{\frac{\mu U_0}{h_0}}$:

$$-2\xi\left(\frac{\epsilon C}{\epsilon C + K'}\frac{\int_0^1 H dX}{\int_0^1 \sqrt{1+\epsilon^2(\partial_X H)^2}dX}\right)^2 \tag{A.14}$$

$$-\left[(P_b - P_f) - \frac{2(\tau_b - \tau_f)(\partial_X H)}{1+\epsilon^2(\partial_X H)^2}\right]\epsilon = \frac{\partial_X^2 H\Sigma}{[1+\epsilon^2(\partial_X H)^2]^{3/2}}\epsilon$$

Now we can expand the main variables as a power series of ϵ and retain only the leading order ϵ:

$$(P_b - P_f) - 2(\tau_b - \tau_f)(\partial_X H) = -\partial_X^2 H\Sigma \tag{A.15}$$

$$P_b = P_f + 2(\tau_b - \tau_f)(\partial_X H) - \partial_X^2 H\Sigma \tag{A.16}$$

TANGENTIAL COMPONENT:

$$\frac{\mu U_0}{h_0}(\tau_b - \tau_f)\frac{1-\epsilon^2(\partial_X H)^2}{1+\epsilon^2(\partial_X H)^2} = \tag{A.17}$$

$$\frac{\mu U_0}{h_0}\frac{\partial_X\Sigma + \partial_Z\Sigma\partial_X H + \partial_Z\Sigma(\partial_X H)^3\epsilon^2 + \partial_X\Sigma(\partial_X H)^2\epsilon^2}{\left[1+\epsilon^2(\partial_X H)^2\right]^{3/2}}$$

Expanding the main variables and retaining only ϵ terms:

$$(\tau_b - \tau_f) = \partial_X\Sigma + \partial_Z\Sigma\partial_X H \tag{A.18}$$

$\partial_Z\Sigma\partial_X H$ term also cancels because surface tension is a force only present at the interface, being zero at any other point:

$$(\tau_b - \tau_f) = \partial_X\Sigma \tag{A.19}$$

Appendix B

Derivation of the chemical species conservation equation and respective boundary conditions.

We start with the equation (8.17)

$$\frac{\partial c_s}{\partial t} + \partial_x(uc_s) + \partial_z(wc_s) = D_s\nabla^2 c_s - \gamma\frac{c_s}{c_s + K_s} \tag{B.1}$$

with:

$$z = 0 \longrightarrow D_s\partial_z c_s = 0 \tag{B.2}$$

$$z = h \longrightarrow c_s = c_0 \tag{B.3}$$

All variables will be nondimensionalized as described in the main text. We will omit s subindex of the variable for simplicity:

$$\frac{c_0}{h_0/U_0}\epsilon^2\partial_T C + \frac{c_0}{h_0/U_0}\epsilon^2\partial_X(CU) + \frac{c_0}{h_0/U_0}\epsilon^2\partial_Z(CW) \tag{B.4}$$

$$= \frac{D_s c_0}{h_0^2}\epsilon^3\partial_X^2 C + \frac{D_s c_0}{h_0^2}\partial_Z^2 C\epsilon - \gamma\frac{C}{\epsilon C + K'}\epsilon$$

Sherwood and Damkohler dimensionaless numbers can be identified in the equation. Therefore:

$$\epsilon Sh\left[\partial_T C + \partial_X(CU) + \partial_Z(CW)\right] \tag{B.5}$$

$$= \left[\epsilon^2 \partial_X^2 C + \partial_Z^2 C\right] - Da_C Sh \frac{C}{\epsilon C + K'}$$

We define a new shape of Damkohler number to reduce the number of constants:

$$Da_D = Da_c Sh = \frac{\gamma}{c_0 D/h_0^2} \tag{B.6}$$

Let us substitute this expression in the equation:

$$\epsilon Sh\left[\partial_T C + \partial_X(CU) + \partial_Z(CW)\right] \tag{B.7}$$

$$= \left[\epsilon^2 \partial_X^2 C + \partial_Z^2 C\right] - Da_D \frac{C}{\epsilon C + K'}$$

We assume that convective transport is neglected (Sh ≈ 0). Expanding the main variables as a power series of ϵ and retaining only leading order ϵ:

$$0 = \left[\epsilon^2 \partial_X^2 C + \partial_Z^2 C\right] - Da_D \frac{C}{\epsilon C + K'} \tag{B.8}$$

The concentration is expressed as:

$$C = C_0 + C_1\epsilon + C_2\epsilon^2 + ... \tag{B.9}$$

The respective result for each order will be:

Order ϵ^0:

$$\partial_Z^2 C_0 - Da_D \frac{C_0}{K'} = 0 \tag{B.10}$$

Order ϵ^1:

$$\partial_Z^2 C_1 - Da_D \frac{C_1}{K'} = 0 \tag{B.11}$$

We remark that the concentration has been defined as $C = \frac{c}{c_0\epsilon}$, which is inconsistent with the boundary condition (B.3). In order to avoid that inconsistency, a magnitude order hypothesis about the concentration in the boundary condition on $z = h$ must be assumed:

$$z = h \longrightarrow c = c_0\epsilon \tag{B.12}$$

This correction assumes that C_0 must be a ϵ order term. As we are working within this order, next terms will be neglected (C_1,etc.). Thus, the boundary conditions may be expressed as follows:

$$Z = 0 \longrightarrow D_s\partial_Z(C_0 + \epsilon C_1 + ...) = 0 \longrightarrow \begin{cases} \partial_Z C_0 = 0 \\ \partial_Z C_1 = 0 \\ ... \end{cases} \tag{B.13}$$

$$Z = H \longrightarrow c_0\epsilon(C_0 + \epsilon C_1 + ...) = \epsilon c_0 \longrightarrow C_0 + \epsilon C_1 + ... = 1 \longrightarrow \begin{cases} C_0 = 1 \\ C_1 = 0 \\ ... \end{cases} \tag{B.14}$$

From the equation (B.10) and the boundary conditions we find:

$$C_0 = A_1 \exp\left(\sqrt{\frac{Da_D}{K'}}Z\right) + A_2 \exp\left(-\sqrt{\frac{Da_D}{K'}}Z\right) \tag{B.15}$$

By substituting the boundary conditions:

$$Z = 0 \longrightarrow D_s\partial_Z C_0 = 0 \longrightarrow A_1 = A_2 \tag{B.16}$$

$$Z = H \longrightarrow A_1 = \frac{1}{\exp\left(\sqrt{\frac{Da_D}{K'}}\right) + \exp\left(-\sqrt{\frac{Da_D}{K'}}\right)} \tag{B.17}$$

$$C_0 = \frac{1}{\exp\left(\sqrt{\frac{Da_D}{K'}}H\right) + \exp\left(-\sqrt{\frac{Da_D}{K'}}H\right)} \left[\exp\left(\sqrt{\frac{Da_D}{K'}}Z\right)\right. \tag{B.18}$$

$$+\exp\left(-\sqrt{\frac{Da_D}{K'}}Z\right)\Bigg]$$

Now we observe that:

$$C_0 = \frac{\exp\left(\sqrt{\frac{Da_D}{K'}}Z\right)+\exp\left(-\sqrt{\frac{Da_D}{K'}}Z\right)}{\exp\left(\sqrt{\frac{Da_D}{K'}}H\right)+\exp\left(-\sqrt{\frac{Da_D}{K'}}H\right)}$$

$$= \frac{\exp\left(\sqrt{\frac{Da_D}{K'}}Z\right)+\exp\left(-\sqrt{\frac{Da_D}{K'}}Z\right)}{\exp\left(\sqrt{\frac{Da_D}{K'}}H\right)+\exp\left(-\sqrt{\frac{Da_D}{K'}}H\right)} \longrightarrow$$

And finally:

$$C_0 = \frac{\cosh\left(\sqrt{\frac{Da_D}{K'}}Z\right)}{\cosh\left(\sqrt{\frac{Da_D}{K'}}H\right)} \tag{B.19}$$

This expression will be used (see appendix C) to obtain a final expression for boundary evolution.

Appendix C

Deduction of boundary evolution equation

We will use equations (8.30),(8.32), (8.33),(8.34) and (8.35).

Let us recall equation (8.30):

$$\epsilon(\partial_X U + \partial_Z W) = Da_U \frac{C}{\epsilon C + K'}\epsilon \tag{C.1}$$

If we integrate this expression with respect with Z and remove the low order terms it follows:

$$\partial_X U + \partial_Z W = Da_U \frac{C}{K'} \longrightarrow \int_0^H \partial_X U dZ + W(Z = H) - W(Z = 0) \tag{C.2}$$

$$= \frac{Da_U}{K'} \int_0^H C_0 dZ$$

Boundary conditions (8.32) and (8.34) will be used to develop the expression even more:

$$\int_0^H \partial_X U dZ + \partial_T H + U\partial_X H = \frac{Da_U}{K'} \int_0^H C_0 dZ \tag{C.3}$$

Taking into account that the upper integration term $(H(x,t))$ is not constant but it varies with x and t, we can just use the following relation:

$$\partial_X \left(\int_0^H U dZ \right) = \int_0^H \partial_X U dZ + U\partial_X H \tag{C.4}$$

Renaming $Q = \int_0^H U dZ$, the final equation yields:

$$\partial_X Q + \partial_T H = \frac{Da_U}{K'} \int_0^H C_0 dZ \tag{C.5}$$

This equation may be further simplified. By taking the results obtained in appendix B about the concentration expression, the right hand side of the equation can be integrated:

$$C_0 = \frac{\cosh\left(\sqrt{\frac{Da_D}{K'}} Z\right)}{\cosh\left(\sqrt{\frac{Da_D}{K'}} H\right)} \tag{C.6}$$

$$\int_0^H C_0 dZ = \frac{1}{\cosh\left(\sqrt{\frac{Da_D}{K'}} H\right)} \int_0^H \cosh\left(\sqrt{\frac{Da_D}{K'}} Z\right) dZ \tag{C.7}$$

Renaming for comfortability:

$$\gamma = \sqrt{\frac{Da_D}{K'}} \tag{C.8}$$

Applying this change and developing the expression:

$$\int_0^H C_0 dZ = \frac{1}{\cosh(\gamma H)} \frac{1}{\gamma} \sinh(\gamma Z) \,|_0^H \tag{C.9}$$

$$= \frac{1}{\gamma} \frac{\sinh(\gamma H)}{\cosh(\gamma H)} = \frac{1}{\gamma} \tanh(\gamma H) = \frac{1}{\sqrt{\frac{Da_D}{K'}}} \tanh\left(\sqrt{\frac{Da_D}{K'}} H\right) \tag{C.10}$$

Finally, the general expression can be written as:

$$\partial_X Q + \partial_T H = \frac{Da_U}{K'} \frac{1}{\sqrt{\frac{Da_D}{K'}}} \tanh\left(\sqrt{\frac{Da_D}{K'}} H\right) \tag{C.11}$$

Appendix D

Design of the CSTR

A mass balance for nutrient concentration and microorganism concentration at steady state were performed. Oxygen mass balance is also necessary to calculate the aeration demand of the system. Applying mass conservation:

Inflow - Outflow = Reaction (bacterial consumption)

Notice that bacterial consumption by the biofilm is performed out of the tank inside the recirculation loop. However, the setup is designed in such a way that the nutrient consumption of the biofilm will be much smaller than planktonic bacteria inside the tank. That is achieved by using a liquid volume in the tank (1 l) larger than the whole recirculation loop (0, 081 l), so changes in concentration produced out of the tank are going to be much smaller than changes produced inside it. The ratio between the volume of the CSTR and the volume of the circulation loop, which can be seen as a security factor (with a value for this case of 9), ensures that by controlling the conditions inside the tank, we are able to keep constant those variables through the rest of the setup.

The mass balance equation holds:

$$Q\left(C_i - C_w\right) = (-r_b)V \longrightarrow V = \frac{Q\left(C_i - C_w\right)}{-r_b} \tag{D.1}$$

where Q is the fresh nutrient flow that is equal that waste flow, C_i is the inflow concentration of nutrient, C_w is the waste nutrient concentration, V is the liquid volume inside the reactor and $-r_b$ is the bacterial reaction kinetics that can be defined as:

$$(-r_b) = \frac{k_2}{Y}\frac{C_w}{C_w + K_n}X_{EE} \tag{D.2}$$

with k_2 the bacterial growth constant (measured experimentally to be 0.17 h-1), X_{EE} the bacterial concentration at steady state and Y the biomass - nutrient yield factor. We conclude that:

$$X_{EE} = \frac{Q}{V} \frac{C_i - C_w}{\frac{k_2}{Y} \frac{C_w}{C_w + K_n}} \tag{D.3}$$

Bacteria reproduce over time and die due to different causes. Waste outflow also contributes to reduce the amount of bacteria. So the final balance in the CSTR will be:

$$V \frac{dX}{dt} = k_2 \frac{C_w}{C_w + K_n} XV - k_3 XV - QX \tag{D.4}$$

being k_3 the kinetic constant that represents bacterial death. This value with the rest of the kinetic parameters have been obtained from [61] and [115].

These two equations describe the whole system. As we have 2 equations and 5 unknown variables (V, C_w, Q, X_{EE} y C_i), we need to fix three of them. In this case the waste concentration (that is the concentration that will be pumped to biofilm flow cell to be the concentration tested in experiments at $Re = 0$, $C_i = 0.1$ g/l), the waste flow (is set to be Q = 1.7 ml/min) and the volume of the liquid in the reactor (is set to be V = 1 l) were the chosen variables. With these values, a table X_{EE} vs C_i can be done. Finally, we chose to be the inflow concentration $C_i = 1$ g/l, giving a steady state cell population around 0.45 g/l.

The minimum demand of oxygen needed to sustain the bacterial population was also considered. A balance between income of oxygen by mass transfer through the interphase, the amount dissolved on fresh nutrient fluid and the outcome corresponding to waste flow and chemical consumption was performed:

$$k_L a \left(C_{SAT} - C_O\right) + QC_I^{SAT} - QC_0 = \left(\frac{1-Y}{Y}\right) k_2 \frac{C_w}{C_w + K_N} \frac{C_O}{C_O + K_O} X_{EE} - k_3 X_{EE} \tag{D.5}$$

where k_L is the overall mass transfer constant fluid - air due to aeration, bubbling and mixing of the inner liquid in the CSTR, a is the ratio m^2/m^3 of water, C_{SAT} is the saturation concentration of oxygen on the atmosphere at room temperature, C_O is the oxygen concentration present on the fluid at

a certain time and K_O is the saturation constant for oxygen consumption of bacterial chemical reaction.

k_L value can be calculated by taking relations used for determine this value on liquid films on rivers, like this obtained from [93].

$$k_2' = \frac{k_L}{2.3H} \tag{D.6}$$

k_2' represents the re-oxygenation constant taken from [111] and H the depth of the liquid film. But in the other hand:

$$k_2' = \frac{294\,(D_o(T)v')^{1/2}}{H^{3/2}} \tag{D.7}$$

where D_o is the diffusion coefficient of oxygen depending on temperature value which has a value of (taken from [116]):

$$D_o(T) = D_o(20^oC) \cdot 1.037^{(T-20)} \tag{D.8}$$

$$D_o(20^oC) = 1.76E-4m^2/\text{day} \tag{D.9}$$

v' is the average velocity on the liquid film that can be calculated by knowing the rotation speed of the mixer ω_T :

$$v' = \omega_T \frac{R}{2} \frac{2\pi}{60} \tag{D.10}$$

being R the average radius of the tank.

By performing an iterative process looking for the zeros of equation it can be reached the minimum oxygen concentration needed to sustain the system and its value is 8.40 g/l.

Appendix E

Milling speeds table

In this appendix we show the different combinations of mill advance (in mm/min) and milling rotation (in r.p.m) that were used to create the different samples to make biofilm test samples.

Configuration	F(mm/min)	n(r.p.m)
1	1	3000
2	4	1000
3	10	833
4	12	600
5	14	500

List of Figures

Bibliography

[1] Aggarwal, S., and Hozalski, R. Determination of biofilm mechanical properties from tensile tests performed using a micro-cantilever method. *Biofouling 26* (2010), 479.

[2] Alpkvist, E., Picioreanu, C., Loosdrecht, M. C. M., and Heyden, A. Three-dimensional biofilm model with individual cells and continuum eps matrix. *Biotechnol. Bioeng. 94* (2006), 961.

[3] Anguige, K., King, J. R., and Ward, J. P. A multi-phase mathematical model of quorum sensing in a maturing pseudomonas aeruginosa biofilm. *Math. Biosci. 203* (2006), 240–276.

[4] Anseth, K. S., Bowman, C. N., and Brannon-Peppas, L. Mechanical properties of hydrogels and their experimental determination. *Biomoterials 17* (1996), 1647–1657.

[5] Apilanez, I., Gutierrez, A., and Diaz, M. Effect of surface materials on initial biofilm development. *Bioresource Technology 66* (1998), 225–230.

[6] Autrusson, N., Guglielmini, L., Lecuyer, S., Rusconi, R., and Stone, H. A. The shape of an elastic filament in a two-dimensional corner flow. *Phys. of fluids 23* (2011), 063602 1–7.

[7] Battin, T. J., Sloan, W. T., Kjelleberg, S., Daims, H., Head, I. M., Curtis, T. P., and Eberl, L. Microbial landscapes: new paths to biofilm research. *Nat. Rev. Microbiol. 5 (* (2007), 76.

[8] Berger, S. A., Talbot, L., and Yao, L. S. Flow in curved pipes. *Ann. Review of Fluid Mechanics 15* (1983), 461–512.

[9] Beyenal, H., and Lewandowski, Z. Combined effect of substrate concentration and flow velocity on effective diffusivity in biofilms. *Water research 34* (2000), 528–538.

[10] Beyenal, H., and Lewandowski, Z. Internal and external mass transfer in biofilms growth at various flow velocities. *Biotechnology progress 18* (2002), 55–61.

[11] Beyenal, H., and Lewandowsky, Z. Modelling mass transport and microbial activity in stratified biofilm. *Chemical Engineering Science 60* (2005), 4337–4348.

[12] Branda, S. S., Vik, S., Friedman, L., and Kolter, R. Biofilms: the matrix revisited. *Trends in microbiology 13* (2005), 20–26.

[13] Brown, D. L., Cortez, R., and Minion, M. L. Accurate projection methods for the incompressible navier-stokes equations. *J. Comput. Phys. 168* (2001), 464–499.

[14] Bruschi, P., and Piotto, M. Design issues for low power integrated thermal flow sensors with ultra-wide dynamic range and low insertion loss. *Micromachines 3* (2012), 295–314.

[15] Bryers, J. D. Modeling biofilm accumulation. *Physiological Models in microbiology.* (1998), 109–144.

[16] Cao, Y. S., and Alaerts, G. J. Influence of reactor type and shear stress on aerobic biofilm morphology, population and kinetics. *Water Research 29* (1995), 107–118.

[17] Castellon, E., Chavarra, M., de Lorenzo, V., Zayat, M., and Levy, D. An electro-optical device from a biofilm structure created by bacterial activity. *Adv. Mater. 22* (2010), 4846–4850.

[18] Celmer, D., Oleszkiewicz, J. A., and Cicek, M. Impact on shear force on the biofilm structure and performance of a membrane biofilm reactor for tertiary hydrogen-driven denitrification of municipal wastewater. *Water research 42* (2008), 3057–3065.

[19] Cense, A. W., Peeters, E. A. G., Gottenbos, B., Baaijens, F. P. T., Nuijs, A. M., and van Dongen, M. E. H. Mechanical properties and failure of streptococcus mutans biofilms, studied using a microindentation device. *Journal of Microbiological Methods 67* (2006), 63–472.

[20] Chai, L., Vlamakis, H., and Kolter, R. Extracellular signal regulation of cell differentiation in biofilms. *Materials research Society 36* (2011).

[21] Characklis, W. G. Attached microbial growths-ii. frictional resistance due to microbial slimes. *Water Research 7 (* (1973), 1249–1258.

[22] Characklis, W. G. Biofilm development and destruction. *Final report EPRI CS-1554 Project RP902-1. Palo Alto CA: Electric Power Research Institute* (1979).

[23] Chorin, A. J. A numerical method for solving incompressible viscous flow problems. *J. Comput. Phys. 2* (1967), 12–26.

[24] Christensen, B. E., and Characklis, W. G. Physical and chemical properties of biofilm. *Characklis WG Marshall KC editors. Biofilms New York: Wiley.* (1990), 93–130.

[25] Chudoba, J., Grau, P., and Ottova, V. Control of activated-sludge filamentous bulking - ii: selection of microorganisms by means of a selector. *Water Research 7* (1973), 1389–1398.

[26] Cogan, N. G., and Guy, R. D. Multiphase flow models of biogels from crawling cells to bacterial biofilms. *HFSP Journal 4 (* (2010), 11.

[27] Costerton, J. W. Introduction to biofilms. *International journal of Antimicrobial Agents 11* (1999), 217 – 221.

[28] Costerton, J. W., Geesey, G. G., and Cheng, G. K. How bacteria stick. *Sci. Am. 238* (1978), 86.

[29] Costerton, J. W., Lewandowski, Z., Caldwell, D., Korber, D., and Lappin-Scott, H. M. Microbial biofilms. *Annu. Rev. Microbiology 49* (1995), 711–745.

[30] Davey, M. E., and O'toole, G. A. Microbial biofilms: from ecology to molecular genetics. *Microbiol Mol Biol Rev. 64* (2000), 847–867.

[31] De Beer, D., Stoodley, P., and Lewandowski, Z. Liquid flow and mass transport in heterogeneous biofilms. *Water Res. 30* (1996), 2761.

[32] De Beer, D., Stoodley, P., and Lewandowski, Z. Measurement of local diffusion coefficients in biofilms by microinjection and confocal microscopy. *Biotechnol Bioengineering 53* (1997), 51–158.

[33] De Beer, D., Stoodley, P., Roe, F., and Lewandowski, Z. Effects of biofilm structures on oxygen distribution and mass transfer. *Biotechnology und Bioengineering 43* (1994), 1131–1138.

[34] de Carvalho, C. C. Biofilms: recent developments on an old battle. *Recent patents on biotechnology 1* (2007), 49–57.

[35] Donlan, R. M., and Costerton, J. W. Biofilms: Survival mechanisms of clinically relevant microorganisms. *Clin. Microbiol. Rev. 15* (2002), 167–193.

[36] Dos Santos, V. A., Heim, S., Moore, E. R., Stratz, M., and Timmis, K. N. Insights into the genomic basis of niche specificity of pseudomonas putida kt2440. *Environ Microbiol 6* (2004), 1264–1286.

[37] Drescher, K., Shen, Y., Bassler, B. L., and Stone, H. A. Biofilm streamers cause catastrophic disruption of flow with consequences for environmental and medical systems. *PNAS 110(11)* (2013), 4345–50.

[38] Duddu, D., Boradas, S., Chopp, D., and Moran, B. A combined extended finite element and level set method for biofilm growth. *International Journal for Numerical Methods in Engineering 74* (2007), 848–870.

[39] Dunsmore, B. C., Jacobsen, A., Hall-Stoodley, L., Bass, C. J., Lappin-Scott, H. M., and Stoodley, P. The influence of fluid shear on the structure and material properties of sulphate-reducing bacterial biofilms. *J. Ind. Microbiol. Biotechnol 29* (2002), 347.

[40] Dussan, V. E. B., and Davis, S. H. On the motion of fluid-fluid interface along a solid surface. *Journal of Fluid Mechanics 65* (1974), 1–95.

[41] Eberhard, J. P., Efendiev, Y., Ewing, R., and Cunningham, A. Coupled cellular models for biofilm growth and hydrodynamic flow in a pipe. *Int. J. Mult. Comp. Eng. 3 (* (2005), 499.

[42] Eberl, H. J., Picioreanu, C., Heijnen, J. J., and van Loosdrecht, M. C. M. A three-dimensional numerical study on the correlation of spatial structure, hydrodynamic conditions, and mass transfer and conversion in biofilms. *Chem. Eng. Sci. 55* (2000), 6209–6222.

[43] Edwards, K. J., Bond, P. L., Gihring, T. M., and Banfield, J. F. An archaeal iron-oxidizing extreme acidophile important in acid mine drainage. *Science 287* (2000), 1796–1799.

[44] Eguia, E., Trueba, A., Ro-Calonge, B., Giron, A., and Bielva, C. Biofilm control in tubular heat exchangers refrigerated by seawater using flow inversion physical treatment. *International Biodeterioration and Biodegradation 62* (2008), 79–87.

[45] Ehrlich, G. D., Stoodley, P., Kathju, S., Zhao, Y., and McLeod, B. R. Engineering approaches for the detection and control of orthopaedic biofilm infections. *Clinical orthopaedics and related research* (2005), 59–66.

[46] Fedkiw, R. P., Aslam, T., Merriman, B., and Osher, S. A non-oscillatory eulerian approach to interfaces in multimaterial flows (the ghost fluid method). *Journal of Computational Physics 152* (1999), 57–492.

[47] Finlayson, B. A. Introduction to chemical engineering computing. *Wiley* (2012).

[48] Flemming, H. C., Neu, T. R., and Wozniak, D. J. The eps matrix: the "house of biofilm cells". *Journal of bacteriology 189* (2007), 7945–7947.

[49] Flemming, H. C., and Wigender, J. The biofilm matrix. *Nat. Rev. Microbiol. 8* (2010), 623.

[50] Friedman, L., and Kolter, R. Two genetic loci produce distinct carbohydrate-rich structural components of the pseudomonas aeruginosa biofilm matrix. *Journal of bacteriology 186* (2004), 4457–4465.

[51] Fuqua, W. C., Winans, S. C., and Greenberg, E. P. Quorum sensing in bacteria: the luxr-luxi family of cell density-responsive transcriptional regulators. *J. Bacteriol. 176* (1994), 269.

[52] Garcia-Ybarra, P. L. Near-wall turbulent transport of large-schmidt-number passive scalars. *Phys. Rev. E 79* (2009), 067302.

[53] Ghannoum, M., and O'Toole, G. A. Microbial biofilms. *ASM Press* (2004).

[54] Godunov, S. K. A difference method for numerical calculation of discontinuous solutions of the equations of hydrodynamics. *Mat. Sb. 47* (1959), 71–306.

[55] Gong, C. Y., Shi, S., Dong, P. W., Zheng, X. L., Fu, S. Z., Guo, G., Yang, J. L., Wei, Y. L., and Qian, Z. Y. In vitro drug release behavior from a novel thermosensitive composite hydrogel based on pluronic f127 and poly(ethylene glycol)-poly(caprolactone)-poly(ethylene glycol) copolymer. *BMC Biotechnology* (2009), 9.

[56] Gottenbos, B., van der Mei, H. C., and Busscher, H. J. Models for studying initial adhesion and surface growth in biofilm formation on surfaces. *Methods Enzymol. 310* (1999), 523–533.

[57] Gross, M. J., Albinger, O., Jewett, D. G., Logan, B. E., and Bales, R. C. Measurement of bacterial collision efficiencies in porous media. *Water research 29* (1995), 1151–1158.

[58] Guglielmini, L., Rusconi, R., Lecuyer, S., and Stone, H. A. Three-dimensional features in low-reynolds-number confined corner flows. *J. Fluid Mech. 668* (2011), 33–57.

[59] Hahn, J., and Dubnau, D. Growth stage signal transduction and the requirements for srfa induction in development of competence. *J Bacteriol. 173* (1991), 7275–7282.

[60] Heijnen, J. J., van Loosdrecht, M. C. M., Mulder, A., and Tijhuis, L. Formation of biofilms in a biofilm air-lift suspension reactor. *Water Science and Technology 26* (1992), 647–654.

[61] Henze, M., Grady, C. P. L., Gujer, W., Marais, G. R., and Matsuo, T. Activated sludge model. *IAWQ, London 1* (1987).

[62] Hermanowic, S. W. A simple 2d biofilm model yields a variety of morphological features. *Math. Biosci. 169* (2001), 1–14.

[63] Heydorn, A., Ersboll, B. K., Hentzer, M., Parsek, M., and Givskov, M. Experimental reproducibility in flow-chamber biofilms. *Microbiology 146 (Pt 10)* (2000), 2409–2415.

[64] Heydorn, A., Nielsen, A. T., Hentzer, M., Sternberg, C., and Givskov, M. Quantification of biofilm structures by the novel computer program comstat. *Microbiology 146 (Pt 10)* (2000), 2395–2407.

[65] Hori, K., and Matsumoto, S. Bacterial adhesion: From mechanism to control. *Biochemical Engineering Journal 48* (2010), 424–434.

[66] Houaria, A., Picarda, J., Habaroub, H., Galasc, L., Vaudryc, H., Heimd, V., and Di Martinoa, P. Rheology of biofilms formed at the surface of nf membranes in a drinking water production unit. *Biofouling: The Journal of Bioadhesion and Biofilm Research* (2011), 235–240.

[67] Huh, C., and Scriven, L. E. Hydrodynamic model of a steady movement of a solid/liquid/fluid contact line. *J. Colloid Interface Sci. 35* (1971), 5–101.

[68] Humanes, E. Desarrollo de microbiosensores para aplicaciones aeroespaciales. *B. Eng. final project* (2008).

[69] Hung, T. K., and Brown, T. D. Solid-particle motion in two-dimensional peristaltic flows. *J. FLuid Mech. 73* (1976), 77–96.

[70] Jaffrin, M. Y., and Shapiro, A. H. Peristaltic pumping. *Ann. Rev. Fluid Mech. 3* (1971), 13–36.

[71] Jimenez, J. I., Minambres, B., Garcia, J. L., and Diaz, E. Genomic analysis of the aromatic catabolic pathways from pseudomonas putida kt2440. *Environ Microbiol 4* (2002), 824–841.

[72] Johnson, G., C. W. A constitutive model and data for metals subjected to large strains, high strain rates and high temperatures. *U.S air force and Honeywell independent program* (1983).

[73] Jones, H. C., Roth, I. L., and Saunders, W. M. I. . Electron microscopic study of a slime layer. *J Bacteriol 99* (1969), 316–325.

[74] Kim, S., and Lee, S. J. Measurement of dean flow in a curved microtube using micro digital holographic particle tracking velocimetry. *Exp. Fluids 46* (2009), 255–264.

[75] Kissel, J. C., McCarthy, P. L., and Street, R. L. Numerical simulation of mixedculture biofilm. *J. Environ. Eng. 110* (1984), 393.

[76] Klapper, I., Rupp, C., Cargo, R., Purevdorj, P., and Stoodley, P. Viscoelastic fluid description of bacterial biofilm material properties. *Biotechnol. Bioeng. 80* (2002), 289.

[77] Klopp, R. W., Clifton, R. J., and Shawki, T. G. Pressure-shear impact and the dynamic viscoplastic response of metals. *Mechanic of materials 4 (* (1985), 75–385.

[78] Koch, B., Jensen, L. E., and Nybroe, O. A panel of tn7-based vectors for insertion of the gfp marker gene or for delivery of cloned dna into gram-negative bacteria at a neutral chromosomal site. *Journal of microbiological methods 45* (2001), 187–195.

[79] Kojima, Y., Fujisawa, H., Nakazawa, A., Nakazawa, T., and Kanetsuna, F. Studies on pyrocatechase. *I. Purification and spectral properties. The Journal of biological chemistry 242* (1967), 3270–3278.

[80] Kolenbrander, P. E., and London, J. Adhere today, here tomorrow: oral bacterial adherence. *Journal of bacteriology 175* (1993), 3247–3252.

[81] Kolter, R., and Greenberg, E. P. Microbial sciences: the superficial life of microbes. *Nature 441* (2006), 300–302.

[82] Korstgens, V., Flemming, H. C., Wingender, J., and Borchard, W. Uniaxial compression measurement device for investigation of the mechanical stability of biofilms. *Journal of Microbiological Methods 46* (2001), 9–17.

[83] Kropfl, K., Vladar, P., Szabo, K., Acs, E., and Borsodi, A. K. Chemical and biological characterisation of biofilms formed on different substrata in tisza river (hungary). *Environmental pollution 144* (2006), 626–631.

[84] Kudo, H., Cheng, K.-J., and Costerton, J. W. Interactions between treponema bryantii and cellulolytic bacteria in the vitro degradation of straw cellulose. *Canadian Journal Microbiology 33* (1987), 244–248.

[85] Lambertsen, L., Sternberg, C., and Molin, S. Mini-tn7 transposons for site-specific tagging of bacteria with fluorescent proteins. *Environmental microbiology 6* (2004), 726–732.

[86] Langtangen, H. P., Mardal, K. A., Winther, R., and Stone, H. A. Numerical methods for incompressible viscous flow. *Adv. Water Resour. 25* (2002), 1125–1146.

[87] Lau, P. C. Y., Dutcher, J. R., Beveridge, T. J., and Lam, J. S. Absolute quantitation of bacterial biofilm adhesion and viscoelasticity by microbead force spectroscopy. *Biophysical Journal 96* (2009), 935–2948.

[88] Lecuyer, S., Rusconi, R., Shen, Y., Forsyth, A., Vlamakis, H., Kolter, R., and Stone, H. A. Shear stress increases the residence time of adhesion of pseudomonas aeruginosa. *Biophys. J. 100* (2011), 1381.

[89] Lee, M. W., and Park, J. M. One-dimensional mixed-culture biofilm model considering different space occupancies of particulate components. *Water Research 41* (2007), 4317–4328.

[90] Lembre, P., Lorentz, C., and di Martino, P. Exopolysaccharides of the biofilm matrix: A complex biophysical world. *DOI: 10.5772/51213* (2012).

[91] Lemon, K. P., Earl, A. M., Vlamakis, H. C., Aguilar, C., and Kolter, R. Bacterial biofilms. *Curr. Top. Microbiol. Immunol. 322* (2008), 1.

[92] Leveque, R. J. Numerical methods for conservation laws. *Lectures in Mathematics ETH-Zurich Birkhauser-Verlag Basel* (1990).

[93] Lewis, W. K., and Whitman, W. G. Principles of gas absorption. *Ind. Eng. Chem. 16* (1924), 1215–1220.

[94] Liu, H., and Fang, H. H. P. Extraction of extracellular polymeric substances (eps) of sludges. *J. Biotechnol. 95* (2002), 249.

[95] Lopez, D., Vlamakis, H., and Kolter, R. Biofilms. *Cold Spring Harbor Perspect. Biol. 2* (2010).

[96] Lopez, D., Vlamakis, H., Losick, R., and Kolter, R. Paracrine signaling in a bacterium. *Genes and Development 23* (2009), 1631–1638.

[97] Manuel, C. M., Nunes, O. C., and Melo, L. F. Dynamics of drinking water biofilm in flow/non-flow conditions. *Water Res. 41* (2007), 551–562.

[98] Marshall, K. C., Stout, R., and Mitchell, R. Mechanism of the initial events in the sorption of marine bacteria to surfaces. *Microbiology 68* (1971), 337–348.

[99] Massol-Deya, A. A., Whallon, J., Hickey, R. F., and Tiedje, J. M. Channel structures in aerobic biofilms of fixed-film reactors treating contaminated groundwater. *Applied and Environmental Microbiology 61* (1994), 769–777.

[100] McCabe, W. L., and Smith, J. C. Unit operations of chemical engineering. *McGraw-Hill Chemical Engineering Series* (1976).

[101] Moller, S., S. C. A. J. B. In situ gene expression in mixed-culture biofilms: evidence of metabolic interactions between community members. *Applied and Environmental Microbiology 64* (1998), 721–732.

[102] Monds, R. D., and O'Toole, G. A. The developmental model of microbial biofilms: ten years of a paradigm up for review. *Trends Microbiol. 17* (2009), 73–87.

[103] Morbiducci, U., Ponzini, R., Grigioni, M., and Redaelli, A. Helical flow as fluid dynamic signature for atherogenesis risk in aortocoronary bypass. a numeric study. *J Biomech. 40(3)* (2007), 519–534.

[104] Morgenroth, E., Van Loosdrecht, M. C. M., and Wanner, O. Biofilm models for the practitioner. *Water Sci. Technol. 41* (2000), 509–512.

[105] National Institute of Health, . Research on microbial biofilms. *National Heart* (2002).

[106] Nealson, K. H., Platt, T., and Hastings, J. W. The cellular control of the synthesis and activity of the bacterial luminescent system. *J. Bacteriol. 104* (1970), 313.

[107] Nelson, K. E., Weinel, C., Paulsen, I. T., Dodson, R. J., and Hilbert, H. Complete genome sequence and comparative analysis of the metabolically versatile pseudomonas putida kt2440. *Environ Microbiol 4* (2002), 799–808.

[108] Nichols, W. W., Dorrington, S. M., Slack, M. P., and Walmsley, H. L. Inhibition of tobramycin diffusion by binding to alginate. *Antimicrobial Agents Chemoter. 32* (1988), 518–523.

[109] Nicolella, C., van Loosdrecht, M. C. M., and Heijnen, J. J. Wastewater treatment with particulate biofilm reactors. *Journal of biotechnology 80* (2000), 1–33.

[110] Nielsen, M. W., Sternberg, C., Molin, S., and Regenberg, B. Pseudomonas aeruginosa and saccharomyces cerevisiae biofilm in flow cells. *J. Vis. Exp. 47* (2011), e2383.

[111] O'Connor, D., and Dobbins, W. Mechanism of reaeration in natural streams. *Proc. Amer. Soc. Cvil. 123* (1956), 641–684.

[112] Ohashi, A., Koyama, T., Syutsubo, K., and Harada, H. A novel method for evaluation of biofilm tensile strength resisting erosion. *Water Science Technology 39* (1999), 261–268.

[113] Oron, A., Davis, S. H., and Bankoff, S. G. Long-scale evolution of thin liquid films. *Reviews of modern physics 69* (1997), 31–980.

[114] Pereira, M. O., Kuehn, M., Wuertz, S., Neu, T., and Melo, L. F. Effect of flow regime on the architecture of a pseudomonas fluorescens biofilm. *Biotechnology and bioengineering 78* (2002), 164–171.

[115] Perez, J., Picioreanu, C., and Van Loosdrecht, M. Modelling biofilm and floc diffusion processes based on analytical solution of reaction-diffusion equations. *Water Research 39* (2005), 1311–1323.

[116] Perry, R. H., and Green, D. W. Perry's chemical engineers' handbook. *(7th Edition) McGraw-Hill 123* (1997), 641–684.

[117] Peyton, B. M. Effects of shear stress and substrate loading rate on pseudomonas aeruginosa biofilm thickness and density. *Water Research 30* (1996), 29–36.

[118] Picioreanu, C., Kreft, J. U., and Van Loosdrecht, M. C. M. Particle-based multidimensional multiespecies biofilm model. *Appl. and Env. Microbiology 70* (2004), 3024–3040.

[119] Picioreanu, C., van Loosdrecht, M. C., and Heijnen, J. J. A theoretical study on the effect of surface roughness on mass transport and transformation in biofilms. *Biotechnology and bioengineering 68* (2000), 355–369.

[120] Picioreanu, C., van Loosdrecht, M. C. M., and Heijnen, J. J. Mathematical modeling of biofilm structure with a hybrid differential-discrete cellular automaton approach. *Biotechnol. Bioeng. 58* (1998), 101.

[121] Picioreanu, C., van Loosdrecht, M. C. M., and Heijnen, J. J. Two-dimensional model of biofilm detachment caused by internal stress from liquid flow. *Biotechnol. Bioeng. 72* (2001), 205–218.

[122] Picologlou, B. F., Zelver, N., and Characklis, W. G. *Hydraulics Division ASCE 106* (1980), 33.

[123] Pizarro, G., Griffeath, D., and Noguera, D. R. Quantitative cellular automaton model for biofilms. *J. Environ. Eng. 127* (2001), 782–789.

[124] Poplawski, N. J., Shirinifard, A., Maciej, S., and Glazier, J. A. Simulation of single-species bacterial-biofilm growth using the glazier-graner-hogeweg model and the compucell3d modeling environment. *Math. Biosci. Eng. 5 (* (2008), 355.

[125] Purevdorj, B., Costerton, J. W., and Stoodley, P. Influence of hydrodynamics and cell signaling on the structure and behavior of pseudomonas aeruginosa biofilms. *Appl. Environ. Microbiol. 68* (2002), 4457–4464.

[126] Purevdorj-Gage, B. Pseudomonas aeruginosa biofilm structure, behavior and hydrodynamics. *Ph.D. thesis Montana State University* (2004).

[127] Putnam, E., and Spatafora, G. Investigating the effects of the gcrr gene product on streptococcus mutans biofilm architecture. *Phd Thesis* (2010).

[128] Ratner, B. Biomaterials science: An introduction to materials in medicine. *Academic Press* (2004).

[129] Rodgers, M., Zhan, X. M., and Prendergast, J. Wastewater treatment using a vertically moving biofilm system followed by a sand filter. *Process Biochemistry 40* (2005), 3132–3136.

[130] Rodriguez, D., Einarsson, B., and Carpio, A. Biofilm growth on rugous surfaces. *Physical review E 86* (2012), 061914.

[131] Rodriguez, D., Martinez, E., de Lorenzo, V., and Carpio, A. (unpublished).

[132] Rogers, S., van der Walle, C., and Waigh, T. A. Microrheology of bacterial biofilms in vitro: Staphylococcus aureus and pseudomonas aeruginosa. *Langmuir 24* (2008), 3549.

[133] Rusconi, R., Lecuyer, S., Autrusson, N., Guglielmini, L., and Stone, H. A. Secondary flow as a mechanism for the formation of biofilm streamers. *Biophys. J. 100* (2011), 1392–1399.

[134] Rusconi, R., Lecuyer, S., Guglielmini, L., and Stone, H. A. Laminar flow around corners triggers the formation of biofilm streamers. *J. R. Soc. Interface 7 (* (2010), 1293–1299.

[135] Sambrook, J., Maniatis, T., and Fritsch, E. F. Molecular cloning a laboratory manual.

[136] Schachter, B. Slimy business: the biotechnology of biofilms. *Nat. Biotechnol. 21* (2003), 361–365.

[137] Schembri, M. A., Hjerrild, A. L., Gjermansen, M., and Klemm, P. Differential expresion of echerichia coli autoaggregattion factor antigen 43. *J.Bacteriol. 185* (2003), 2236–2242.

[138] Seminara, A., Angelini, T. E., Wilking, J. N., Vlamakis, H., Ebrahim, S., Kolter, R., Weitz, D. A., and Brenner, M. P. Osmotic spreading of bacillus subtilis biofilms driven by an extracellular matrix. *Proc. Natl. Acad. Sci. USA 109* (2012), 1116.

[139] Sethian, J. A. Level set methods. evolving interfaces in geometry, fluid mechanics, computer vision, and materials science. *Cambridge Monograph on Applied and Computational Mathematics Cambridge University Press* (1996).

[140] Shapiro, A. H., Jaffrin, M. Y., and Weinberg, S. L. Peristaltic pumping with long wavelengths at low reynolds number. *J. Fluid Mech. 37* (1969), 799–825.

[141] Shaw, T., Winston, M., Rupp, C. J., Klapper, I., and Stoodley, P. Commonality of elastic relaxion times in biofilms. *Phys. rev. lett. 9314* (2004).

[142] Simoes, M., Simoes, L. C., and Vieira, M. J. Species association increases biofilm resistance to chemical and mechanical treatments. *Water research 43* (2009), 229–237.

[143] Singh, R., Paul, D., and Jain, R. K. Biofilms: implications in bioremediation. *Trends in microbiology 14* (2006), 389–397.

[144] Sinnot, M. D., Cleary, P. W., Arkwright, J. W., and Dinning, P. G. Investigating the relationships between peristaltic contraction and fluid transport in the human colon using smoothed particle hydrodynamics. *Comp. Biol. Med. 42* (2012), 492–503.

[145] Stewart, P. S., and Franklin, M. J. Physiological heterogeneity in biofilms. *Nat. Rev. Microbiol. 6* (2008), 199.

[146] Stonebridge, P. A., and Brophy, C. M. Spiral laminar flow in arteries? *Lancet 338* (1991), 1360–1363.

[147] Stonebridge, P. A., Buckley, C., Thompson, A., Dick, J., Hunter, G., Chudek, J. A., Houston, J. G., and Belch, J. J. Non spiral and spiral (helical) flow patterns in stenoses. in vitro observations using spin and gradient echo magnetic resonance imaging (mri) and computational fluid dynamic modeling. *Int. Angiol. 23(3)* (2004), 276–283.

[148] Stoodley, L. H., Costerton, J. W., and Stoodley, P. Bacterial biofilms: from the natural environment to infectious diseases. *Nat. Rev. Microbiol. 12* (2004), 95.

[149] Stoodley, P., Boyle, J. D., and Lappin-Scott, H. M. Influence of flow on the structure of bacterial biofilms. *Microbial Biosystems: New Frontiers. Proceedings of the 8th International Symposium on Microbial Ecology Bell Atlantic Canada Society for Microbial Ecology* (1999).

[150] Stoodley, P., Cargo, R., Rupp, C. J., Wilson, S., and Klapper, I. Biofilm material properties as related to shear-induced deformation and detachment phenomena. *J. Ind. Microbiol. Biotechnol. 29* (2002), 361–368.

[151] Stoodley, P., Dodds, I., Boyle, J. D., and Lappin-Scott, H. M. Influence of hydrodynamics and nutrients on biofilm structure. *Journal of Applied Microbiology 85* (1998), 19S–28S.

[152] Stoodley, P., Lewandowski, Z. and; Boyle, J. D., and Lappin-Scott, H. M. The formation of migratory ripples in a mixed species bacterial biofilm growing in turbulent flow. *Environmental Microbiology 1* (1999), 447–455.

[153] Stoodley, P., Lewandowski, Z., Boyle, J. D., and Lappin-Scott, H. M. Structural deformation of bacterial biofilms caused by short-term fluctuations in fluid shear: An in situ investigation of biofilm rheology. *Biotechnol. Bioeng. 65* (1999), 83.

[154] Sutherland, I. W. The biofilm matrix - an immobilized but dynamic microbial environment. *Trends Microbiol. 9 (* (2001), 222–227.

[155] Taherzadeh, D., Picioreanu, C., Kuttler, U., Simone, A., Wall, W. A., and Horn, H. Computational study of the drag and oscillatory movement of biofilm streamers in fast flows. *Biotech. and Bioeng. 105* (2010), 600–610.

[156] Takabatake, S., and Ayukawa, K. Numerical study of two-dimensional peristaltic flows. *J. Fluid Mech. 122* (1988), 439–465.

[157] Takabatake, S., Ayukawa, K., and Mori, A. Peristaltic pumping in circular cylindrical tubes: a numerical study of numerical transport and its efficiency. *J. Fluid Mech. 193* (1988), 267–283.

[158] Tien, C. J., Wu, W. H., Chuang, T. L., and Chen, C. S. Development of river biofilms on artificial substrates and their potential for biomonitoring water quality. *Chemosphere 76* (2009), 1288.

[159] van Loosdrecht, M. C. M., Heijnen, J. J., Eberl, H., Kreft, J., and Piciorenau, C. Mathematical modelling of biofilm structures. *Antonie van Leeuwenhoek 81* (2002), 245–256.

[160] van Swaay, D. Cell-free biofilm biosensor of catheter-related urinary tract infections, built using biobricks that exploit ahl signaling pathways in biofilms. *IET* (2008).

[161] Veening, J. W., Kuipers, O. P., Brul, S., Hellingwerf, K. J., and Kort, R. Effects of phosphorelay perturbations on architecture, sporulation, and spore resistance in biofilms of bacillus subtilis. *J. Bacteriol. 188* (2006), 3099.

[162] Velazquez, A., Arias, J. R., and Mendez, B. Laminar heat transfer enhancement downstream of a backward facing step by using a pulsating flow. *International Journal of Heat and Mass Transfer 51* (2008), 2075–2089.

[163] Verwey, E. J. W. Theory of the stability of lyophobic colloids. *The Journal of Physical and Colloid Chemistry 51* (1947), 631–636.

[164] Vincent, J. F. V. Structural biomaterials. *Princeton University Press.* (1990).

[165] Visick, K. L., and Ruby, E. G. Vibrio fischeri and its host: it takes two to tango. *Curr. Opin. Microbiol. 9* (2006), 632.

[166] Wanner, O., Eberl, H., Morgenroth, E., Noguera, D., Picioreanu, C., Rittmann, B., and van Loosdrecht, M. C. M. Mathematical modeling of biofilms. *IWA Publishing London* (2006).

[167] Weinan, E., and Lui, J. G. Gauge method for viscous incompressible flows. *Comm. Math. Sci. 1* (2003), 317–332.

[168] Weinberg, S. L., Eckstein, E. C., and Shapiro, A. H. An experimental study of peristaltic pumping. *J. Fluid Mech. 49* (1971), 461–479.

[169] Wilking, J., Angelini, T., Seminara, A., Brenner, M. P., and Weitz, D. A. Biofilms as complex fluids. *MRS Bull. 36* (2011), 385.

[170] Wilson, W. W., Wade, M. M., Holman, S. C., and Champlin, F. R. Status of methods for assessing bacterial cell surface charge properties based on zeta potential measurements. *Journal of microbiological methods 43* (2001), 153–164.

[171] Wu, J. A., Kusuma, C., Mond, J. J., and Kokai-Kun, J. F. Lysostaphin disrupts staphylococcus aureus and staphylococcus epidermidis biofilms on artificial surfaces. *Antimicrobial agents and chemotherapy 47* (2003), 3407–3414.

[172] Wuertz, S., Bishop, P. L., and Wilderer, P. A. Biofilms in wastewater treatment: An interdisciplinary approach.

[173] Xavier, J. B., and Foster, K. R. Cooperation and conflict in microbial biofilms. *Proc. Natl. Acad. Sci. USA 104* (2007), 876–881.

[174] Xiong, Y., and Liu, Y. Biological control of microbial attachment: a promising alternative for mitigating membrane biofouling. *Applied microbiology and biotechnology 86* (2010), 825–837.

[175] Yang, S., and Lewandowski, Z. Measurement of local mass transfer coefficient in biofilms. *Biotechnol. Bioeng. 48* (1995), 737.

[176] Yang, X., Beyenal, H., Harkin, G., and Lewandowski, Z. Quantifying biofilm structure using image analysis. *Journal of microbiological methods 39* (2000), 109–119.

[177] Yoruk, E., Ochs, M. F., Geman, D., and Younes, L. A comprehensive statistical model for cell signaling. *IEEE/ACM transactions*

on computational biology and bioinformatics / IEEE ACM 8 (2011), 592–606.

[178] Zaray, G., Kropfl, K., Szabo, K., Taba, G., Acs, E., Berlinger, B., Dogan, M., Bekir, S., and Akbulut, A. Comparison of freshwater biofilms grown on polycarbonate substrata in lake velence (hungary) and lake mogan (turkey). *Microchemical Journal 79* (2005), 145 – 148.

[179] Zhang, T. C., and Bishop, P. L. Density, porosity, and pore structure of biofilms. *Water Res. 28* (1994), 2267.

[180] Zhornitskaya, L., and Bertozzi, A. L. Positivity-preserving numerical schemes for lubrication-type equations. *SIAM Journal on Numerical Analysis 37* (2000), 23–555.

[181] Zobell, C. E. The effect of solid surfaces upon bacterial activity. *J Bacteriol. 46* (1943), 39–56.